Know thy star, know thy planet – disentangling planet discovery & stellar activity

Giles, Helen

Université de Genève
Département d'Astronomie

Faculté des Sciences
Dr Christophe Lovis
Professeur Stéphane Udry

Know Thy Star, Know Thy Planet

–

Disentangling Planet Discovery & Stellar Activity

Thèse

présentée à la Faculté des Sciences de l'Université de Genève
pour obtenir le grade de Docteur ès sciences,
mention Astronomie et Astrophysique

par

Helen Amanda Catriona GILES

de

Stirling (UK)

Thèse N° 5377

Genève
Observatoire Astronomique de l'Université de Genève
2019

UNIVERSITÉ DE GENÈVE

FACULTÉ DES SCIENCES

DOCTORAT ÈS SCIENCES, MENTION ASTRONOMIE ET ASTROPHYSIQUE

Thèse de Madame Helen GILES

intitulée :

«Know Thy Star, Know Thy Planet
-
Disentangling Planet Discovery
&
Stellar Activity»

La Faculté des sciences, sur le préavis de Monsieur C. LOVIS, docteur et directeur de thèse (Département d'astronomie), Monsieur S. UDRY, professeur ordinaire et codirecteur de thèse (Département d'astronomie), Madame M. DESSAUGES, docteure (Département d'astronomie), Madame H. CEGLA, docteure (Département d'astronomie), Madame A. VIDOTTO, docteure (School of Physics, University Trinity College Dublin, Ireland) et Monsieur D. BAYLISS, professeur (Department of physics, University of Warwick, Coventry, United Kingdom), autorise l'impression de la présente thèse, sans exprimer d'opinion sur les propositions qui y sont énoncées.

Genève, le 29 août 2019

Thèse - 5377 -

Le Doyen

N.B. - La thèse doit porter la déclaration précédente et remplir les conditions énumérées dans les "Informations relatives aux thèses de doctorat à l'Université de Genève".

For Women Everywhere
To Infinity and Beyond

Resumé

Depuis la découverte des planètes extrasolaires, ou *exoplanètes*, près de 4000 ont été confirmées. Cependant, cela n'a pas toujours été aussi simple. Les premières découvertes furent de grandes planètes similaires à Jupiter avec de petits orbites, donc assez proche de leur étoile, qui produisent un signal important et qui sont faciles à détecter. Nous sommes maintenant à la recherche de planètes de plus en plus petites, et, ultimement, une Terre 2.0, mais le signal de telles planètes est toutefois du même ordre que le bruit produit par leur étoile hôte. Par conséquent, pour arriver à cet objectif, il nous faut mieux comprendre l'étoile hôte.

Un effet important de l'activité stellaire est l'évolution et le comportement des *taches étoilées* (l'équivalent des taches solaires mais sur la surface d'autres étoiles). Une tache diminue la quantité de lumière émise par l'étoile lorsqu'elle traverse la surface de cette étoile, elle supprime le mouvement de convection sous sa surface et est souvent accompagnée par d'autres effets de surface additionnels, comme les *faculae* et *plage*. Lorsque l'on cherche une exoplanète avec les méthodes de *transit* et de *vitesse radiale*, les effets dus aux taches stellaires ne peuvent être ignorés. Les taches stellaires qui apparaissent et disparaissent de la surface dues à la rotation de l'étoile sont la source principale de la variation des courbes de lumière. La variation cyclique observée avec la méthode des vitesses radiales est causée par plusieurs effets, dont, encore une fois, les taches stellaires qui apparaissent à la surface de l'étoile et qui, dès lors, suivent la période de rotation de l'étoile. Cependant, les taches stellaires ne tracent pas seulement la période de rotation de l'étoile – sur une échelle temporelle plus grande, leur affaiblissement au cours du temps peut aussi affecter les observations. Cela peut être facilement déterminé en utilisant une méthode indirecte. En effet, en générant une *fonction d'auto-corrélation* de la courbe de lumière, le *temps de vie de l'affaiblissement* peut être mesuré. Cette propriété peut être utilisée pour mieux analyser l'étoile dans le but de trouver et caractériser des exoplanètes.

Lors de la recherche d'exoplanète, la question n'est plus de savoir *s'il est possible* d'en détecter, mais plutôt de *savoir auxquelles* s'intéresser. Au cours des 27 dernières années, plusieurs études ont utilisé des télescopes terrestres et spatiaux afin de chercher des exoplanètes. Bientôt, plusieurs nouvelles missions spatiales et nouveaux instruments seront également opérationnels. Avec ces récentes avancées en matière d'instrumentation et les astronomes qui en

apprennent davantage sur le sujet, le nombre potentiel d'exoplanète est en train d'exploser. Cela a conduit à l'expansion du domaine des exoplanètes, passant d'une poignée d'universités à un effort mondial, comprenant même des citoyens scientifiques. Après l'échec d'une deuxième roue à réaction, *Kepler* a été réaffecté d'une mission qui devait observée une petite partie du ciel pour quatre ans à une mission ayant pour objectif d'observer de nouvelles régions du ciel à chaque trois mois, la mission *K2*. Au contraire de la première mission, cette seconde mission (2014-2018) est complètement construite à partir de demandes de temps et les données sont également rendues publiques à la communauté. À Genève, nous avons analysé les courbes de rotation disponibles et conduit des observations additionnelles pour caractériser les candidates exoplanètes. Les compétences apprises et développées durant la recherche dans les courbes de rotation de la mission *K2* seront également appliquées à de futures missions, comme *TESS*, *CHEOPS* et *PLATO*.

Dans cette thèse, je décris et discute du travail que j'ai fait sur les deux côtés du problème: d'une part, nous devons caractériser l'activité stellaire, de l'autre, nous devons aussi continuer à trouver de nouvelles candidates exoplanètes et confirmer leur existence.

Foreword

Since the first discoveries of extrasolar planets, or *exoplanets*, more than 4000 have been confirmed. However, it has not always been easy. Early discoveries were of large Jupiter-like planets in close orbits, which meant they produced significant signals making them straightforward to discover. As we work towards finding smaller and smaller planets and, ultimately, Earth 2.0, the signals from these planets become hard to distinguish from the signals that emanate from the exoplanet's host star. Therefore, to keep advancing towards this quintessential goal, we must first truly understand the stellar host.

A significant contributor to stellar activity is the evolution and behaviour of *starspots* (the equivalent of sunspots on other stars). A spot decreases the amount of light emitted by the star as it passes across the stellar face, suppresses convective motion beneath it and is often accompanied by additional surface features such as *faculae* and *plage*. When searching for exoplanets using the *transit* and *radial velocity* methods, the effect of starspots cannot be ignored. In light curves, the primary source of long-term variation is due to the starspots passing into and out of sight as the star rotates. For radial velocity observations, the overall cyclical variation is made up of a series of components which includes one on the timescale of the stellar rotation period, again because spots come into and out of sight. However, starspots do not only trace out the stellar rotation period – on a longer timescale their evolution due to decay also dictates the behaviour observed. This can also be measured, but is much more easily done indirectly. By generating an *autocorrelation function* of light curves, a star's spot *decay lifetime* can be measured. This property can then be used for additional analyses of the star for the purpose of hunting for and characterising exoplanets.

When it comes to finding exoplanets, it is no longer a question of *'can we?'*, but rather *'which ones?'* Twenty-seven years on, there have been numerous ground- and space-based surveys dedicated to discovering exoplanets – with several new space missions and instruments coming online both in the near and distant future. But as telescopes get better, and astronomers learn more, the number of potentially discoverable exoplanets snowballs. This has led to the field of exoplanet discovery expanding from just a handful of well-equipped universities to a worldwide effort, including citizen scientists. With the failure of a second reaction wheel,

Kepler was repurposed from a mission which observed one small patch of sky for almost 4 years to a new mission which would observe new patches of sky roughly every three months – *K2*. Unlike the primary mission, the secondary mission (which ran from 2014 to 2018) was entirely led by guest observing proposals with all data available to the entire community. In Geneva, we analysed the publicly-available light curves and conducted follow-up observations of exoplanet candidates to characterise them. The skills learnt and developed during the search in *K2* light curves has and will be applied to future missions, such as *TESS*, *CHEOPS* and *PLATO*.

In this thesis, I describe and discuss the work I have done towards tackling both sides of the issue: on the one side, we need to characterise the stellar activity; the other side is to continue finding new and exciting exoplanet candidates and confirming their existence.

Sammanfattning

Sedan de första upptäckterna av extrasolära planeter, eller *exoplaneter*, har nästan 4000 bekräftats. Men det har inte alltid varit så lätt. Tidiga upptäckter var stora Jupiter-liknande planeter i nära banor, vilket innebar att de producerade signifikanta signaler som gjorde dem lättare att upptäcka. När vi arbetar på att hitta allt mindre planeter, och i till slut Earth 2.0, blir signalerna på dessa planeter lika stora som det 'brus' som kommer från exoplanetens värdstjärna. För att fortsätta utvecklingen mot det här målet, måste vi först förstå stjärnvärdarna.

Ett betydande bidrag till stjärnaktivitet är utvecklingen och uppförandet av stjärnfläckar (motsvarande solfläckar på andra stjärnor). En fläck minskar mängden ljus som emitteras av stjärnan när den passerar över stjärnans framsida, undertrycker konvektiv rörelse under den och åtföljs ofta av ytterligare ytfunktioner som *faculae* och *plage*.

När man söker efter exoplaneter med hjälp av *transit-* och *radialhastighetsmetoderna*, får effekten av stjärnfläckar inte ignoreras. I ljuskurvor är den primära källan till långvarig variation beroende av att stjärnfläckar passerar in och ur sikte när stjärnan roterar. För radialhastighetsobservationer består den totala cykliska variationen av en serie komponenter som innefattar en på tidsskalan för stjärnrotationsperioden. Återigen eftersom fläckar kommer in och ur sikte.

Stjärnfläckar spårar emellertid inte bara stjärnrotationsperioden, utan under en längre tidsperiod dikterar de dess utveckling genom förfall också det uppträdande beteendet. Detta kan också mätas, men är mycket lättare gjort indirekt. Genom att generera en *autokorrelationsfunktion* av ljuskurvor kan stjärnfläckars *nedbrytningslivstid* mätas. Denna egenskap kan sedan användas för ytterligare analyser av stjärnan i syfte att iaktta och karaktärisera exoplaneter.

När det gäller att hitta exoplaneter är det inte längre en fråga om *'kan vi?'*, men snarare *'vilka?'* Efter 27 år har det funnits många jord- och rymdbaserade undersökningar för att upptäcka exoplaneter – med flera nya rymduppdrag och -instrument som kommer online både snart och i en mer avlägsen framtid. Men samtidigt som teleskopen blir bättre, och astronomer lär sig mer, exploderar antalet potentiellt upptäckbara exoplaneter. Detta har lett till att exoplanetområdet växer från bara en handfull välutrustade universitet till en världsomspännande insats, inklusive lekmän som forskare.

Efter ett fel på ett reaktionshjul, fick *Kepler* vars uppdrag var att observera en liten bit av

himlen i nästan 4 år, ett nytt uppdrag att observera nya områden av himlen ungefär var tredje månad - *K2*. Till skillnad från det primära uppdraget leddes sekundäruppdraget (från 2014 till 2018) helt av gästobservatörers förslag, med all information tillgänglig för hela gruppen. I Genève analyserade vi de offentligt tillgängliga ljuskurvorna och genomförde uppföljningsobservationer av exoplanetkandidater för att karaktärisera dem. De färdigheter som lärts och utvecklats under sökandet av *K2s* ljuskurvor kommer att tillämpas på framtida uppdrag, t.ex. *TESS*, *CHEOPS* och *PLATO*.

I denna avhandling beskriver jag och diskuterar det arbete jag har gjort för att ta itu med båda sidor av frågan: å ena sidan behöver vi karaktärisera stjärnaktiviteten; å andra sidan gäller det att fortsätta hitta nya och spännande exoplanetkandidater och bekräfta deras existens.

Acknowledgements

They say it takes a village to raise a child, and the same is true for a PhD!

I wish to thank the *CHEOPS* mission and the University of Geneva for funding my PhD at the Observatoire de Genève. Thanks too, to my jury: Christophe Lovis, Stéphane Udry, Aline Vidotto, Mirka Dessauges, Daniel Bayliss and Heather Cegla; for their careful reading and critiquing of my thesis.

I am grateful to Christophe Lovis, Dan Bayliss and Stéphane Udry for sharing their vast exoplanet expertise. Also to the rest of the exoplanet group, thank you for the fascinating conversations. I will be eternally grateful to Christoph Mordasini for his mentoring, without which I am convinced that everything might have all ended differently.

Many thanks to my collaborators outside of Geneva; for inspiring and supporting me whilst I coded and cursed, helping me work on such exciting science. To Andrew Collier Cameron and Raphaëlle Haywood, for being such patient and supportive collaborators on my first project and paper. Thank you to the Astronomy Twitterverse where science and life, war stories and exciting discoveries brings us all together – impacting how science is done.

My friends and colleagues – we had so many ridiculous conversations over lunch, at bus stops and during conferences. Through good and bad, you made me laugh. Thank you to Marianne Girard, my co-thesis-writer – we battled deadlines and drank a lot of tea! Also my (virtual) tea-drinking friends: Annelies Mortier, Raphaëlle Haywood and Heather Cegla – three great women who made me want to be like them. And Javiera Rey – you still kick me to keep going and listen to me grumble!

Ian Giles (PhD in Scandinavian Studies), Helen Lawson (PhD in Early Medieval Exegesis) and Rohini Giles (DPhil in Planetary Physics) for showing me that it could be done. My parents, Ann and David Giles: for their practical help, for listening, my mother's frying pan jokes and my father's proof reading of this thesis. Thank you.

Last but not least, thanks to the best of role models: my fellow astrowomen and other women in science and beyond. You taught me that I could be whoever I wanted to be. For your efforts, I dedicate my thesis to you all.

Lastly, special thanks to David Ciardi for my thesis title – we'll all be using it for years!

Contents

Chapter 1

Introduction

1.1 The Big Picture

Since the first discovery of a planet outside of the Solar System, over 4000 have now been found. Therefore it can, perhaps, be assumed that astronomers now know how to find them. But one question to ask is, are we finding all of them? Are there any particular ones which are not being found? And if there are, why? What can we (or should we) be doing differently?

Another aspect to be considered when planet hunting, is how they are found. The majority are found by measuring their effect on the light from their stellar host. With that comes the concern of what other effects might be hidden within that light. The Sun has a variegated surface (with sunspots and other features). Other stars almost certainly have similar surfaces. How will these affect the stellar light that is depended on for conducting exoplanetary searches?

In this thesis, the work aims to investigate some of the questions considered.

‘One of the thrills of astronomy is its beauty. When you look up at a clear night sky, there is so much drama happening.’

Dr. Nirupama Raghavan

Know thy Star

Stellar activity has a significant impact on the process of exoplanet discovery and confirmation. Starspots and their effects play an important role in that activity.

1.2 History of Sun- & Starspots

Humans have been observing sunspots for many hundreds of years, and more recently they have begun to observe the same phenomenon on other stars with the aid of bigger and more modern telescope techniques.

1.2.1 Early Sunspot Observations

Whilst the Sun has played a significant role in human lives, dictating the seasons and the ability to grow food, observing blemishes on its surface was challenging. However, when the Sun was low in the sky or concealed by dust storms or smoke, the brightness of the Sun was diminished enough for features to be visible to the human eye. The first recorded reference to dark features on the Sun, or *sunspots*, comes from Theophrastus of Athens in 325 BC who was a student of Aristotle (Hardy 1991). Given the casual way he wrote about them hinted that these were not uncommon and had been observed regularly; and further observations were written about in China beginning in 165 BC (Wittmann & Xu 1987; Yau & Stephenson 1988). However, the teachings of Aristotle stated that the Sun was a perfect and immaculate object, so when Arab astronomers observed sunspots they were deemed to be transits of Mercury or Venus. Einhard and Kepler, in the 9th and 17th centuries respectively, made similar assumptions (Wittmann & Xu 1987).

One of the earliest drawings of sunspots came from John of Worcester in 1128 (Figure 1.1). Later, during fires in Russia some two hundred years later, the Sun was obscured by smoke and revealed "dark spots on the Sun as if nails were driven into it" (Wittmann & Xu 1987). With the invention of the telescope in 1608 in the Netherlands, many grasped at the opportunity to study the Sun much more closely. Galileo Galilei was one of the first to observe sunspots through a

Figure 1.1: From 1128, one of the earliest drawings of sunspots was by John of Worcester. They are represented by the two circles with different sizes on the northern and southern solar hemispheres. (Image credit: Corpus Christi College, Oxford)

telescope[a] in Padua. He was closely followed by Thomas Harriot in the United Kingdom, who recorded what he saw in his manuscripts and created drawings in 1610. However the first to publish their observations was Johann Fabricius in his book 'An Account of Spots Observed on the Sun and their Apparent Rotation with the Sun' published in Latin in 1611 (Fabricius 1611). It gives details of how he and his father observed sunspots, both with a telescope and a camera obscura. They also tracked how the sunspots appeared to come and go, as well as determining when the same sunspot or sunspot group reappeared, often showing foreshortening near the limb of the Sun. Fabricius therefore deduced that the sunspots must have been on the surface of the Sun, and that the Sun rotated (Hoyt & Schatten 1997; Casanovas 1997).

Around the same time as Fabricius and his father were observing sunspots, Christoph Scheiner conducted similar observations. He published his findings in three letters to a rich nobleman, Mark Welser. Scheiner later continued to observe the Sun, and further noted that the axis which the sunspots rotated on was slightly inclined to that of the ecliptic, by 7.5° (Scheiner 1630).

Welser, wishing to hear his comments, corresponded with Galileo who performed a series systematic observations of the Sun (an example drawing from his record of observations in Figure 1.2). By projecting the image of the Sun, he found that the sunspots were significantly foreshortened at the limb and suggested they were most likely formed of clouds, like Fabricius.

[a]Though I **strongly** advise that you do **not** observe the Sun directly, let alone with a telescope!

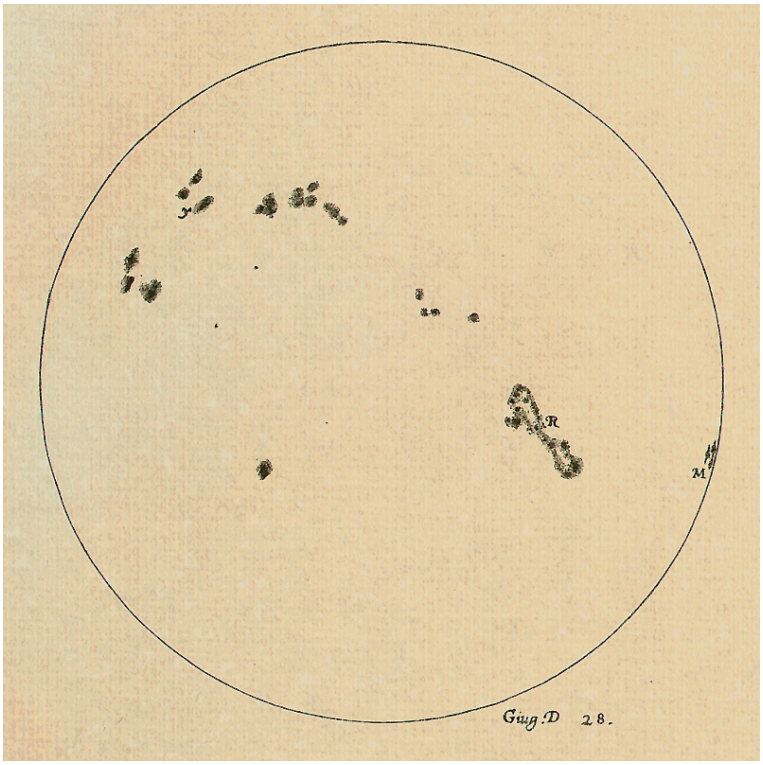

Figure 1.2: Drawn in 1612, an example of one of Galileo Galilei's systematic observations of the Sun. Galileo tracked spot groups as they crossed the solar face, e.g. group 'R' or 'M'. (Image credit: The Galileo Project, Rice University)

He also noticed several additional things: first, that sunspots often lay near the solar equator; second, that there were often bright blemishes near the sunspots (now known as *faculae*); and third, that the sunspots themselves were not in fact dark, but merely darker than the surrounding Sun. He reported his findings back to Mark Welser in a series of letters, which were later published as the book Galilei et al. (1613).

The next advance came from Alexander Wilson over 150 years later. Based in Glasgow, he noted how as a sunspot approached the limb of the Sun, the width of penumbra (the outer ring of the sunspot, see Section 1.3) changed. The part which was furthest away from the limb was smaller than that near the limb. Now known as the *Wilson effect* or *Wilson depression*, he hypothesised that this came about due to the sunspot being a depression in the solar surface. Wilson was also the first to suggest that these depressions could be revealing a cooler interior of the Sun. This idea was further adapted by William Herschel who suggested that the Sun is in fact a cooler object covered with hot clouds, where sunspots were spaces in the clouds.

1.2.2 Sunspot Cycle

During the 150-year gap between Scheiner and Wilson, there were several records from many observers who saw nothing of great significance. Whilst we now know that this period fell into the Maunder Minimum, this was not known at the time. Later, Herschel noted that between 1795 and 1800, there was a dearth in sunspots which he attributed to his concept of hot clouds covering a cooler Sun. But Herschel took his theory further, and he was the first to see a correlation with the climate, by showing that the price of wheat was higher during this quiet period on the Sun.

In 1826, Heinrich Schwabe started to study the Sun rigorously in the hope to see a transit of a planet sat within the orbit of Mercury. In the end, he had culminated over 40 years worth of detailed notes on features on the solar surface. Sadly, he never did see Mercury transit, but he did accidentally discover a cycle in the appearance in sunspots. Whilst Schwabe (1843) discussed the possibility of a 10-year cycle, the publication went mostly unnoticed. A few years later, it was given much more attention when a table of his observations appeared in *Kosmos* in 1851. Soon after, there was a rapid succession of further work carried out in the UK and Switzerland.

After Schwabe's discovery, Richard Carrington conducted a series of regular observations of the Sun for 8 years and from these he drew two key conclusions: first, that the movement of the sunspots over the course of a cycle was towards the equator in both the northern and southern hemispheres; and secondly, that sunspots at the latitudes closer to the equator appeared to travel much more quickly than those at higher latitudes. In particular, this second conclusion strongly suggested that the Sun could not be a rigid body with a constant rate of rotation – this detection of differential rotation was one of the first examples of direct evidence that the Sun had fluid-like outer layers.

With Schwabe's discovery of the sunspot cycle, Rudolf Wolf undertook an investigation into the existing sunspot records to see if it was possible to see the same cycle again. He also introduced a means for normalising the number of observed sunspots across different observers using different telescopes:

$$\mathcal{R} = k(10g + f) \tag{1.1}$$

where $\mathcal{R}$ was the *relative sunspot number*, g the number of visible sunspot groups, f the number of visible individual sunspots (inclusive of the sunspots in groups) and k was a correction factor which was different for each set of observations. Using this, and historical records, Wolf tracked sunspot cycles as far back as the 1755-66 decade. This has since been denoted as 'Cycle

1', and every 11-year cycle since follows this notation[b]. When Wolf became the director of the Observatory in Zurich, he started to keep a daily record of sunspots, enlisting assistance from other observatories for any days affected by poor weather or issues with instruments – this collaboration is still ongoing, involving over 30 different observatories.

Later it was rediscovered that the 1600s had had a significant lack of sunspots (Spörer 1889; Spörer & Maunder 1890; Maunder 1922). It was not widely acknowledged until Eddy (1976) revived the notion and made connections between the climatology of the 'Little Ice Age' and solar-activity of the Maunder Minimum (something which Herschel had deduced centuries earlier!). Further, Eddy suggested that the 'Medieval Warm Period' was down to the increased solar activity which occurred at the same time.

Whilst features on the surface of the Sun had been recorded as drawings and writings, it was not until 1845 when the first photograph was taken. At the Paris Observatory, Fizeau and Foucault produced an image which showed sunspots, but also evidence of limb darkening – a phenomenon which would not be explained for another 60 years (Schwarzschild & Villiger 1906). Around the same time, an advanced photography experiment was underway at Greenwich Observatory in London. The Greenwich photoheliographic records are (nearly) daily photographs of the solar surface taken between 1874 and 1976. In the 1970s, the responsibility of the records was transferred and continued by an observatory in Hungary. Using these images, it was possible to extract the area of sunspot coverage of the solar disc on an almost daily basis and therefore determine a highly detailed record of solar activity. From this, it is clear that there is a quasi-periodic variation with a mean period of $\sim$ 11 years. Spörer & Maunder (1890) and Maunder (1922) also devised the famous 'Butterfly' diagram, seen in Figure 1.3, showing the progression of sunspot latitudes over time.

1.2.3 A Brief History of Starspots

Given the breadth of detection and knowledge of sunspots, it is not unreasonable to assume that the same astronomers who theorised about their presence on the Sun also did so for other stars. In fact, Ismael Boulliau attributed a variability observed in the brightness of Mira Ceti to be similar to that of sunspots – a star which had dark patches, or *starspots*, that passed in and out of view of the observer as the star rotated. Similar observations were recorded by Rudolf Wolf (Tassoul & Tassoul 2006) and Pickering (1880). Alas, we now know that these are mostly due to pulsating stars and not starspots.

The first evidence for any form of stellar activity like that seen on the Sun came from spectroscopy. In 1891, Hale and Deslandres detected an increase in K-line emission which

[b]This thesis was written as Cycle 24 transitioned into Cycle 25

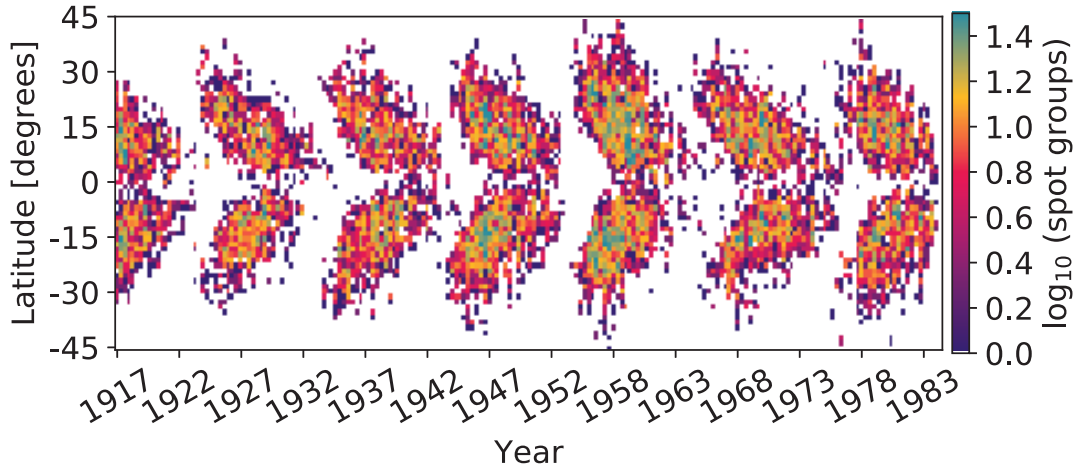

Figure 1.3: The 'Butterfly' diagram showing how the spot density varies over time (using archival data from Howard et al. 1984). At the beginning of a solar cycle, a small number of spots exist at high latitudes, and over time move closer to the equator and grow in number. (Credit: Brett Morris, UW)

correlated with the presence of sunspots. A similar effect was seen in the K-line emission for Arcturus by Eberhard in 1900, and subsequently for Aldebaran and σ Geminorum in Ca II emission (Eberhard & Schwarzschild 1913). In fact, Eberhard & Schwarzschild (1913) concluded that this behaviour must be the "same kind of eruptive activity that appears in sunspots". Decades later, over 400 stars with significant emission in Ca II H & K lines had been compiled (Joy & Wilson 1949), and from 1966 a systematic search was conducted at Mount Wilson to detect long-term variation in the intensity of the Ca II H & K emissions – this provided the first ever detection of magnetic variability for a star other than the Sun (Wilson 1978)!

But, the first true detection of spots on other stars came from Kron (1947). He detected patches of differing brightness on the star AR Lacertae B, a solar-like star, one of a pair of eclipsing binaries. Based on photometric observations from Lick Observatory, the brightness variations could be broken into two key components: the first, the usual features seen in eclipsing binaries; and the second, step-like changes in brightness during the stellar eclipse of the G5 star by the K0 star. Later, similar patterns were seen in the M-dwarf star YY Geminorum (Kron 1950). These variations were small, and could have only corresponded to a very small spot coverage. Sadly, at this time, the evidence for this being caused by starspots was not widely accepted.

Over the course of the 1960s, more attention was given to additional sources of periodic light and colour changes in late-type stars (Catalano & Rodonò 1967; Chugainov 1966; Godoli 1968). For HD 234677 (Chugainov 1966), the variability observed could not be explained by a

pulsating star or eclipses from a companion – there was only one likely culprit left, one (or more) starspots were on the stellar surface. It was around this time that it became accepted practice to measure stellar rotation period from the quasi-periodic variations observed in photometry. Additionally, photometric sinusoidal variations, with evolving phases and amplitudes, were seen in the binary stars CC Eridani (Evans 1959) and BY Draconis (Krzeminski & Kraft 1967), with accompanying spectroscopic variations. Krzeminski (1969) proposed this was due to starspots which were later modelled (Bopp & Evans 1973) for BY Dra – based on this, the star must have been covered in large spots which covered up to 20% of the stellar surface and they lived for several rotations. At the same time, like Bopp & Evans (1973), Hall (1972) studied the stellar variation observed in the binary system RS Canum Venaticorum. He reasoned that the cooler star had to have a significant spot coverage (±30 degrees in latitude and over 180 degrees longitude) and a cycle of over 20 years.

Up until the 1980s, it was hard to confirm starspots with absolute certainty. Since then, new methods, such as Doppler imaging, have enabled starspot detection to become standard procedure.

1.3 Sun- & Starspot Anatomy

Although early observations of sunspots were merely seen and described vaguely as dark smudges or shadows on the Sun, with telescopes and new techniques we now know a lot about their morphology. Spots are areas of the stellar photosphere where magnetic flux tubes have burst through (Figure 1.4), and are exposing the optically thick layers that lie beneath. Spots are darker than the surrounding photosphere because they are significantly cooler. Not because the layers beneath are actually cooler but because immediately below the spot, the magnetic flux is suppressing the convection; and convection is the primary source of heat transfer for Sun-like stars near the surface. This was first hypothesised by Biermann (1941) and has been shown to be relatively correct – though he initially suggested that a significant proportion of the convection is inhibited. In fact, a large amount of convective flux energy is still required to maintain the brightness of the spot. For whilst the spot appears very dark, they are in fact emitting a great deal of light[c].

Additionally, another byproduct of magnetic flux tubes generating spots is the reverse polarity of the ‘exit’ spot and the ‘entrance’ spot. A magnetic flux tube has a field direction, just like a bar magnet does, and manifests itself as a tube of parallel field lines. When the tube exits from the solar surface, the field lines are pointing outward. The tube then loops over and dives back into the surface, with the field lines now pointing inwards. Therefore, from an outside

[c]Fun fact: the average sunspot emits around the same amount of light as a full moon!

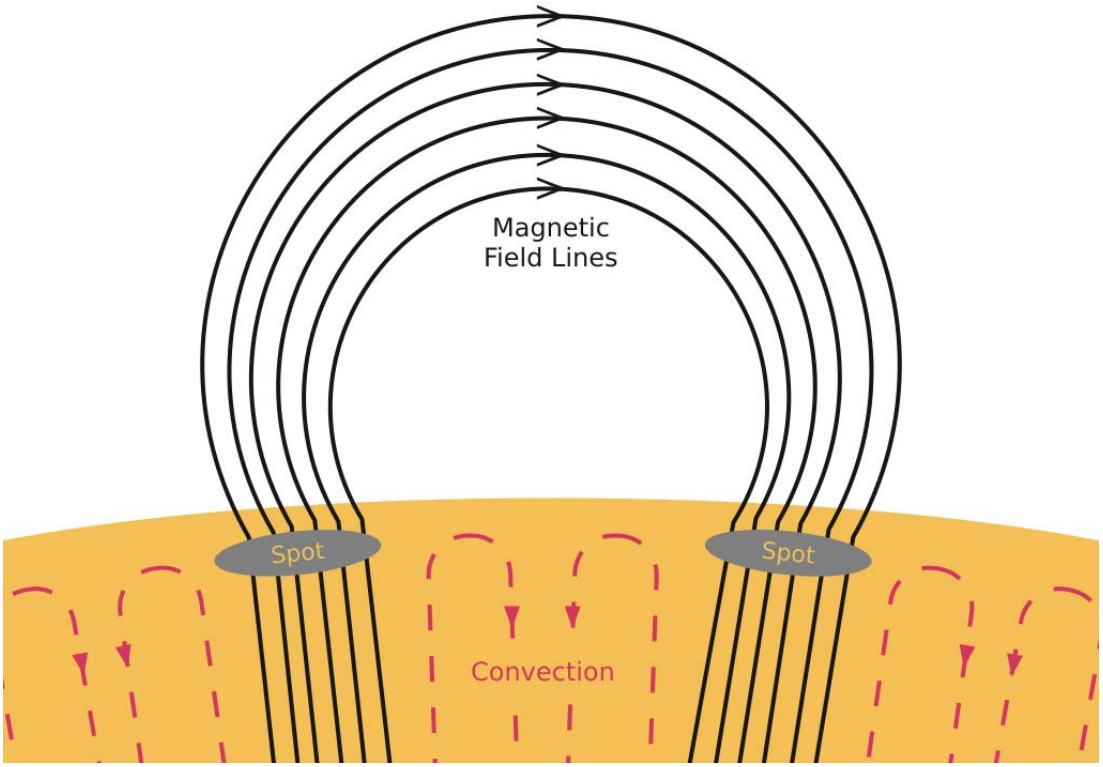

Figure 1.4: Illustration of spots with the magnetic field lines looping over the photosphere, with convection cells shown beneath. Magnetic flux tubes have burst through the stellar photosphere and expose the optically thick layers beneath. These appear as dark spots as the magnetic field lines suppress convection below the surface which is the main source of heat transfer near the surface. Additionally, each spot will have opposing magnetic polarities depending on the direction of the magnetic field lines.

observer's point of view, the two spots will have opposite polarities. For this reason, spots rarely appear alone and often manifest in groups of varying size, often with a distribution of sunspot sizes. Further, the strength of the magnetic field varies across the spot – in the centre, where the field lines are most vertical, the field strength of a sunspot can be as much as 2800 G. This slowly drops to less than 1000 G at the edge, where the field lines also become slightly more inclined (on average, 70°).

The range of spot sizes is significant: from tiny (on the Sun, diameters of ~3500km) to enormous (~60000km). Often, for sunspots, the size is described in units of millionths of the solar hemisphere surface area, described as

$$1 \times 10^{-6} A_{\odot/2} = 3.044 \times 10^{6}\ \mathrm{km}^2 \tag{1.2}$$

where

$$A_{\odot/2} = 2\pi R_{\odot}^2\ . \tag{1.3}$$

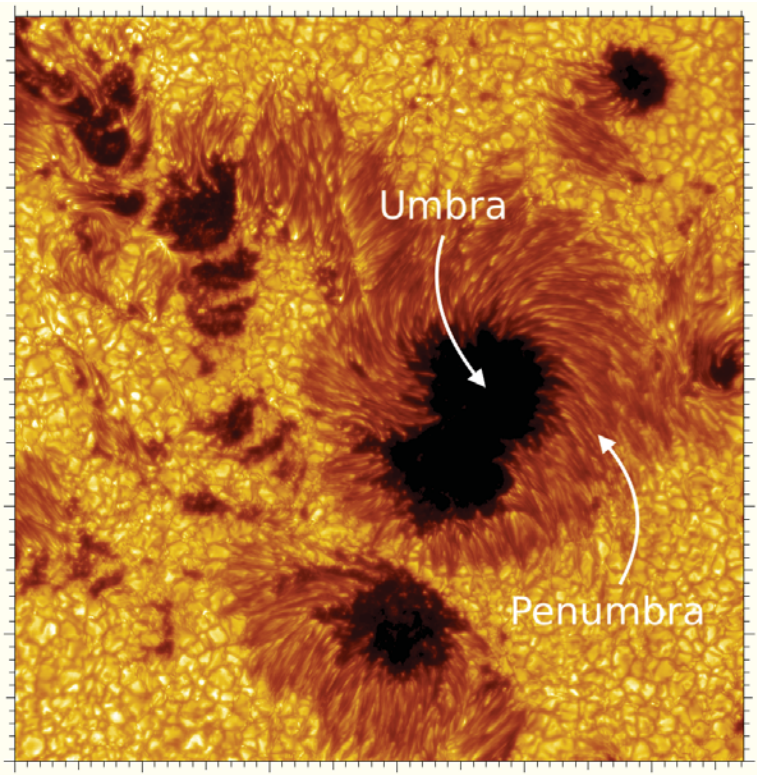

Figure 1.5: Image of sunspots, part of Active Region #10030, observed on 15 July 2002 by the Swedish Solar Telescope. Individual tics represent 1000 km on the Sun. Shown are the two key parts of a sunspot, the *umbra* (dark region) and the *penumbra* (outer ring around the umbra).
(Image credit: Swedish Solar Telescope, Royal Swedish Academy of Sciences)

The current record for the largest sunspot seen (since detailed records have been kept) was in March of 1947 (Newton 1955; Abetti 1957), where the spot had an area of $4300 \times 10^{-6} A_{\odot/2}$ (approximately a diameter of 130000km)! However, the distribution of spot sizes is not uniform. Bogdan et al. (1988) determined that for each solar cycle between 1917 and 1982 (and for all phases of a cycle) that the total area of sunspots were distributed lognormally – that there are a significant number of tiny and small spots, with much fewer larger spots.

This area within a spot is not a uniform space of darkness. Its anatomy can be split into two key portions: the central nucleus of the spot, the *umbra*; and an outer ring, the *penumbra* (see Figure 1.5). The radius of the spot is approximately split equally between the umbra and penumbra, and so the overall area of the umbra is much smaller than the penumbra. Additionally, there are differences in the brightness; for sunspots, the umbra emits around 20% of the average photosphere brightness, whilst the penumbra is brighter, around 75% – these would correspond to temperature differences of approximately 2000K and 400K, respectively, relative to the immaculate photosphere(Bray & Loughhead 1964; Thomas & Weiss 1992; Stix 2002). The penumbra can also be resolved further, and consists of a series of long, alternating bright and

dark filaments. Most of these filaments radiate outwards from the centre of the spot. Similar to the effect seen with the contrast of spots on the photosphere, the alternating brightness of the filaments is relative: a bright filament in one area of the penumbra may in fact be dimmer than a dark filament in another area. Attempts to measure their size (or distribution of sizes) in sunspots has been hindered by the available spatial resolution of observations and differing techniques. Observations have indicated preferred measurements of ~250km (Scharmer et al. 2002) to 150-180km (Sütterlin 2001), and more recently a suggestion that there is no preferred size (Rouppe van der Voort et al. 2004). But the behaviour of the length of the filaments is easier to resolve. Some filaments extend across the entire width of the penumbra, whilst others gradually disappear and with even more appearing part way through the penumbra. Consequently, due to the contrast with the umbra, the bright filaments are clearest at the umbra-penumbra boundary, with many seen reaching into the umbra itself. Each filament can range in length, from 3500-7000km in sunspots (Rouppe van der Voort et al. 2004; Langhans et al. 2005). And at the outer edge of the penumbra, when the spot meets the photosphere, the filaments become less distinct with bright and dark filaments harder to discern.

As described in Sect. 1.2.1, during the 1700s Alexander Wilson noticed that the widths of the penumbra changed as sunspots approached the limb of the Sun. He attributed this foreshortening to the sunspot not being a feature on the surface, but a depression *in* the surface. We now know that the *Wilson depression* is due to a decrease in optical depth, as the local pressure and temperature are lower around the spot, which allows the observer to see deeper into the star. The depth to which can be 'seen' in the case of the Sun has been debated in the literature: the oldest measurements (see Bray & Loughhead 1964 and Gokhale & Zwaan 1972) suggest depths of ~400-800km; whereas Balthasar & Woehl (1983) found depression depths of 500-2500. However, to determine the depths, different aspects of the morphology of the umbra and penumbra matter – their relative sizes (Wilson & Cannon 1968; Wilson & McIntosh 1969) and the raggedness of the umbra-penumbra boundary (Solanki & Montavon 1994) matter.

1.3.1 Other Stellar Surface Features

When observing the Sun in detail, there are not only spots which have been found. Surface-wide features include granulation which are a by-product of the convection originating from beneath the surface. There are also more localised features than spots. Pores, faculae and plages are often seen near spots and, as a collection, they are often called *active regions*. These active regions can be tens of thousands of kilometres wide and all the different constituents are all generated by a common source: magnetic activity. Active regions form from a bundle of magnetic field lines quickly rising buoyantly from the convective zone and out through the photosphere. This process then rapidly generates spots (for the Sun, within a few days) which

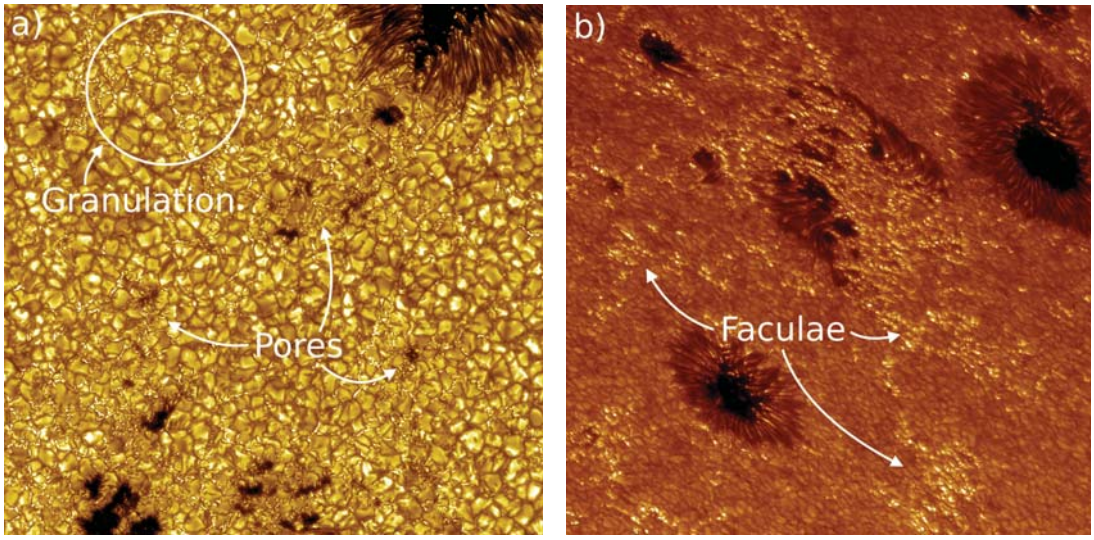

Figure 1.6: Images of other common surface features seen on the Sun:
a) Example of *granulation* (the bright cells and dark channels covering the whole image) and *pores* (the smaller, dark regions) taken with the Swedish Solar Telescope on 23 May 2010
(Image credit: Vasco Henriques, Institute for Solar Physics, Royal Swedish Academy of Sciences).
b) An active region near limb of the Sun, taken with the Swedish Solar Telescope on 29 June 2003; accompanying the spots in the photosphere are bright regions known as *faculae* within the chromosphere.
(Image credit: Dan Kiselman, Institute for Solar Physics, Royal Swedish Academy of Sciences).

slowly decay away (of the order of weeks and occasionally months) due to the fluid motions in the convective zone and photosphere. This indicates that the initial bundle of magnetic field lines was larger and more compact and coherent before being thrust out of the photosphere (Zwaan 1978, 1992), and at that point it splinters into smaller, more intense bundles to form the spots and pores (Keppens & Martinez Pillet 1996; Leka & Skumanich 1998).

1.3.1.1 Granulation

This global feature is generated by the convective motion of plasma beneath the photosphere and creates a cellular appearance across the entire star (each *granule* can range in size from 700-1500km on the Sun). Similar to a saucepan of boiling water, 'bubbles' of plasma are heated from further down in the star and rise to the surface as a cell (Figure 1.6). At the surface, the energy is dispersed into the photosphere and the plasma sinks back down through the darker, intergranual lanes surrounding the convection cells. The turnover time of a granule is only a few minutes.

Granulation has a complicated relationship with sunspots. Formed sunspots inhibit the

underlying convection, exposing and cooling the matter below. However, as will be seen in Chapter 5, granulation has a significant role in the evolution of spots on a stellar surface.

1.3.1.2 Pores

In essence, pores are tiny spots where there is only an umbra and no penumbra (see Figure 1.6). They are typically a similar size to an individual granule (~1000km), though pores on the Sun have been observed to reach sizes that rival the smallest sunspot. Often, pores are brighter in their umbrae than standard spots, but are darker than the intergranular lanes. Pores usually form when enough stray magnetic flux comes together through the action of convection, after being generated by convective collapse.

Whilst pores are not necessarily spot precursors, if several come together and coalesce a spot with a penumbra can begin to form. On average, they last for only 10-15 minutes when formed in the quiet photosphere; they can survive for up to a day when part of an active region.

1.3.1.3 Faculae & Plage

Spots appear as dark features, whereas faculae and plages appear close by as bright patches (faculae are only approximately 100K more than the local photosphere). In fact, when observing the Sun in white light, the most discernible features are the spots and faculae, with the faculae seen clearest at the limb of a star (Figure 1.6). Faculae consist of a large group of small facular points in the intergranular lanes, where the facular points are areas of magnetic flux concentration with diameters of roughly 200km on the Sun (Keller & von der Luehe 1992). Ordinarily faculae are associated with active regions, but it is possible to find small facular points dotted across a stellar surface. They can sometimes also cluster into little lines within the intergranular lanes and form *filigree* structures (Dunn & Zirker 1973). Faculae are difficult to see when not close to the limb of a star. But they can be much more easily detected via line radiation – chromospheric lines like Ca II H and K correspond to the brightening in the chromosphere due to the facular brightening, these chromospheric bright patches are *plages*. The pattern of the granulation beneath the plage regions is also altered – the convective cells are much smaller and the intergranular lanes are filled with strong magnetic field lines.

Within a facular region, elements form and decay with a time scale of a few hours; the regions themselves not only live longer, but exist much longer than spots. They also appear as much as several days before spots do, and will remain two or three times longer than the spot. Spots are rarely seen without neighbouring faculae, though facular regions can appear without accompanying spots. As faculae are generated by strong magnetic fields, their size are a good indicator of the overall active region size. They begin as small, more compact regions but evolve

into larger, broken groups as convection picks away at the magnetic field lines and redistributes them across the quiet stellar surface. The total number of faculae seen on the stellar surface varies with the spot cycle. Given all the the additional emission from large faculae, for the Sun the overall brightness is in fact greatest at sunspot cycle maximum even when the reduction in brightness due to the dark spots is taken into consideration.

1.4 Starspot Detection Methods & Measurable Starspot Features

For detecting and measuring the effect of starspots, there are a range of different techniques that can be used. For stellar physicists, their interest stems from wishing to understand better the processes ongoing within a star and how similar they are to one another and to the Sun. In more recent years, stellar activity has also become of interest for those who search for extrasolar planets (see 1.5 and onwards) where a very small signal needs to be found within a sea of stellar 'noise'.

1.4.1 Photometry

As has been seen for sunspots, spots cause brightness variations on the surface of a star. Therefore it is logical that it could be possible to detect their influence by studying the brightness of stars over a long baseline, such as a *light curve*. The variations expected within the light curve would be periodic and have the same period as the stellar rotation. This naturally depends on the lifetime of the active regions, where those with shorter lifetimes are hard to discern as they decay away too quickly to leave a repetitive trace. By modelling different coloured light curves, it is also possible to estimate likely temperatures and surface distributions of the spots.

To extrapolate properties of the spots from photometry, it is necessary to infer and use models. One example is to generate synthetic light curves using model stars with different sizes and distributions of spots, and compare those to the observed light curves. The models can be comprised of either circular, uniform spots (Budding 1977; Vogt 1981a; Poe & Eaton 1985) or spots with defined umbral/penumbral distributions (Dorren 1987); or the model can also be simple restrictions on the allowed latitude and longitudes of the spots (Bopp & Evans 1973; Eaton & Hall 1979). It is rarely possible for a single-spot model to fit the pattern in a light curve, and it is often unlikely to determine one, single result (with specific spot positions, sizes, temperatures etc.); additional measurements are needed, either photometry in different colours or other complementing techniques. Vogt (1981b,a) was able to determine the temperature and geometry of the spots from light curves in two colours (V and R) with a single, circular spot model with various properties. Since, more advanced computational codes have been developed as the wealth of photometric data has increased from various telescopes and

missions (e.g. Ribárik et al. 2003; Boisse et al. 2012; Oshagh et al. 2013a; Dumusque et al. 2014; Maxted 2016 and others).

Due to the variation in the light curve due to spots occurring at the same periodicity as the stellar rotation period, tracking the appearance of spots is a means to measuring the stellar rotation period. For more details, see Chapter 5.

1.4.2 Spectroscopy

There are various spectroscopic measurements which can aid in characterising spots; these include line-depth ratios and molecular lines.

Line-depth Ratios

The ratio in the line-depths is a reliable source of determining stellar atmosphere temperatures (with an accuracy of tens of degrees and changes less than 10K, Gray 1994). The same can be done for starspots (Gray 1996; Catalano et al. 2002). By tracking how the spot crosses the face of the star, it introduces depth variations in different lines which probe different temperatures; therefore by measuring how a temperature-dependent line changes with respect to one which is not temperature-dependent, it is possible to get an estimate of the temperature of the stellar surface feature. Examples can be seen in (Toner & Gray 1988) with respect to rotational modulation, and activity cycles in (Gray et al. 1996).

Molecular Lines

Stars with high effective temperatures have no molecular absorption lines, as they can only form in cooler stellar atmospheres. Therefore, for those stars, there may be molecular lines from starspots. The first time this effect was seen was by Vogt (1979) for the star HD224085. He studied the molecular lines for TiO and VO and concluded they were caused by spots. This was closely followed by similar detections on other stars from Ramsey & Nations (1980); Huenemoerder et al. (1989). Later, more developed techniques were proposed for more accurately measuring the temperature and filling-factor[d] of the spots themselves by comparing two or more molecular lines (Huenemoerder & Ramsey 1987; Neff et al. 1995; O'Neal et al. 1996, 1998, 2004). This method can also be extended to molecular lines in other bands; for example, in the near-infrared, where spots are significantly brighter than the rest of the photosphere and therefore have a larger effect on the molecular lines (O'Neal & Neff 1997).

As well as a means for detecting spots and determining their temperature and filling factor, the molecular lines can also be indicators of the spots' magnetic field strength. The TiO lines

[d]Filling-factor: the proportion of spot coverage on a star ($f = 0.1 \sim 10\%$).

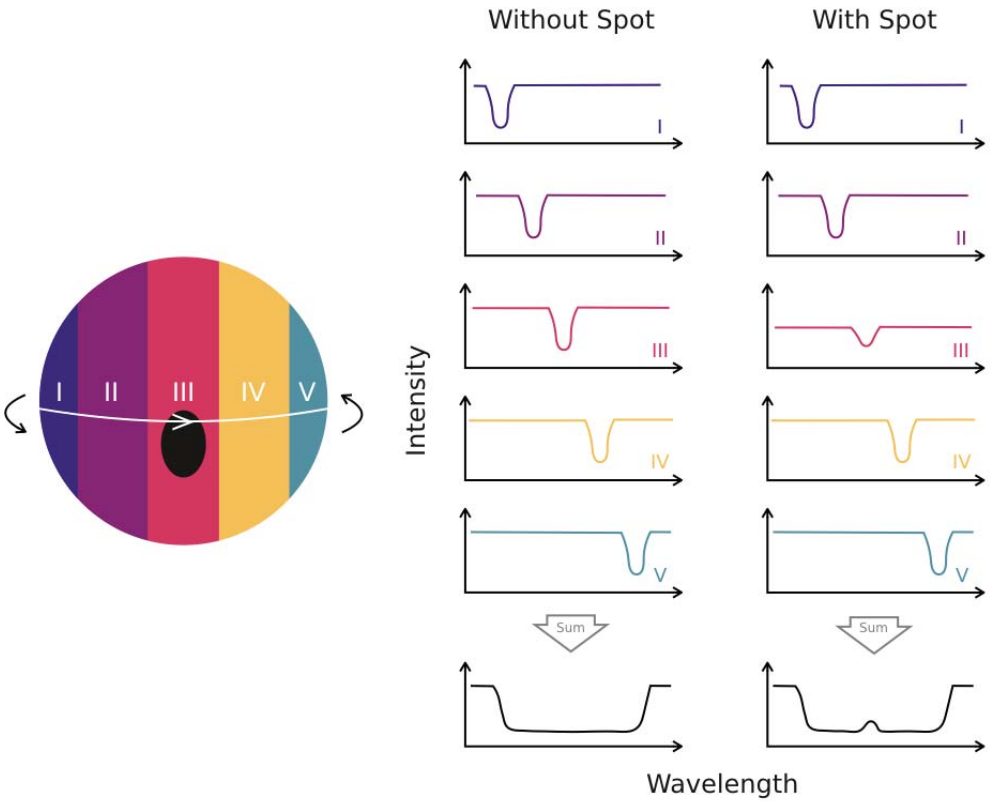

Figure 1.7: Illustration of the Doppler Imaging method. As a spot crosses the face of the star, it blocks light from portions of the stellar surface. Different areas of the star are red-/blue-shifted by different amounts. By tracking the amount of light blocked over the different shifts over time, it is possible to measure spot properties (adapted from Vogt & Penrod 1983).

at 7055Å are magnetically sensitive and will split by small amounts (Berdyugina & Solanki 2002; Berdyugina et al. 2003; Berdyugina 2002).

1.4.3 Doppler & Zeeman-Doppler Imaging

Ideally, when investigating starspots, knowing their location and size on the surface is important; as well as how all that evolves over time. Doppler imaging is able to determine that. The first uses of Doppler imaging come from its use for generating surface maps of Ap stars, to see anomalies in the magnetic field strength and element abundance (Deutsch 1958, 1970; Falk & Wehlau 1974; Goncharskii et al. 1977). If a star has surface features then these cause Doppler shifts as the star rotates, line profiles will change shape at certain phases when the surface inhomogeneity appears. The first time it was applied to "seeing" spots was by Vogt (1981c), Vogt & Penrod (1983) and Vogt et al. (1987). The theory behind Doppler imaging is shown in Figure 1.7. A rapidly rotating star is split into a number of sections (in line with the rotation

axis) where the Doppler shift induced by the rotating star is taken to be uniform; therefore absorption lines will be shifted by different (but known) amounts in each section. In the case of a non-spotted star, the sum of these line shifts are simply a Doppler-broadened version of the non-shifted line (which can be used to measure the stellar rotation period). However when placing a spot on the surface, as it enters each section, it will reduce the overall brightness of that section. Summing all sections will then reveal the Doppler-broadened line with an additional little 'bump'. Do this at regular intervals, and the movement of the spot can be tracked; and the size can be measured by the size of the bump in the line. The latitude of the spot can also be determined by establishing the range of wavelengths which were affected by it – a smaller range than the Doppler-broaded line would suggest higher latitudes, for example. Naturally, the reality of Doppler imaging is not as simple as the example in Figure 1.7 suggests. Additional noise in the stellar spectrum and stars with more than a single spot add complexity to this method. And a key precursor is that the star must rotate sufficiently rapidly that other sources of line broadening are dominated by the Doppler broadening. Additionally, it only functions well for fairly large spots – extrapolating the log-normal spot distribution seen on the Sun to stars with higher levels of activity (and therefore larger spots). Even the smaller spots cannot be resolved by Doppler imaging (Solanki & Unruh 2004) and that comparing the spot coverage observed via photometry and Doppler imaging for particular cases show that there are spots missing from imaging (Unruh et al. 1995).

Zeeman-Doppler imaging is just a further extension of Doppler imaging, and was first suggested by Semel (1989). It has since evolved to include more and more intricate magnetic forms and more detailed field properties by analysing more and more spectral lines at once (Donati & Brown 1997; Donati & Collier Cameron 1997). The Zeeman effect occurs when there is a magnetic field present within an area of stellar atmosphere, and causes the spectral lines to split into component lines at different wavelengths. The pattern of the splitting depends on the strength of the field and the properties of the atomic composition of the stellar atmosphere involved. In the case of a non-rotating star with a static spot, the spectra would show that some lines were split due to there being a magnetic field in the spot. But, add in stellar rotation, the same Doppler-effect will be seen – instead of it applying to simple spectral lines, it shifts the split lines. The same properties as measured through Doppler imaging can be measured, as well as the magnetic field strength by tracking the range of wavelengths involved.

1.4.4 Effect on Exoplanet Observations

Starspots are not just indicators of the behaviour of a star, they can also describe what the conditions are like in space surrounding that star. This is important when considering extrasolar planets (see Section 1.5), as their climate and habitability heavily depend on the level of activity

of the star. For Earth, there is evidence of a correlation between climate and the level of activity the Sun is experiencing at the time (see Section 1.2.2). Therefore, it can be understood that with higher levels of activity there may be climate effects on an Earth-like planet around a much more active, Sun-like star – and this could be further amplified for different stellar types and planets in closer orbits (and therefore closer to the 'action'). Furthermore, even the detection of such celestial bodies strongly relies on the ability to understand the stellar activity (and most significantly, the starspots) so that it can be removed as 'noise'. Details of this can be found in Sections 1.6.1 and 1.6.2 for the effect of starspots on radial velocities and photometry respectively, as well as Chapter 6.

'Science progresses best when observations force us to alter our preconceptions.'

Dr Vera Rubin

Know thy Planet

1.5 History of Exoplanets

Now making a regular appearance in both popular science media and new outlets, extrasolar planets are becoming a common concept. But what precisely defines an *extrasolar planet*? Extrasolar planets are actually well described through their name: '*extra-*' indicates something is beyond or external of the following conjunction; '*solar*' refers to the Sun (e.g. *solar system*). Therefore extrasolar planets are simply '*planets*' (a low-mass object) orbiting another star and they are typically abbreviated to *exoplanets*. But in essence, when considering what an exoplanet is, we are dealing with alien worlds.

The first true discovery on an exoplanet was by Wolszczan & Frail (1992), who found a multi-planet system around the pulsar PSR B1257+12 (Figure 1.8). It was detected when the time-of-arrival for regular bursts from the pulsar appeared to change regularly – the authors were able to determine that the variability was a combination of two sinusoidal signals, which indicated the star was being effected by the presence of two more objects potentially orbiting the

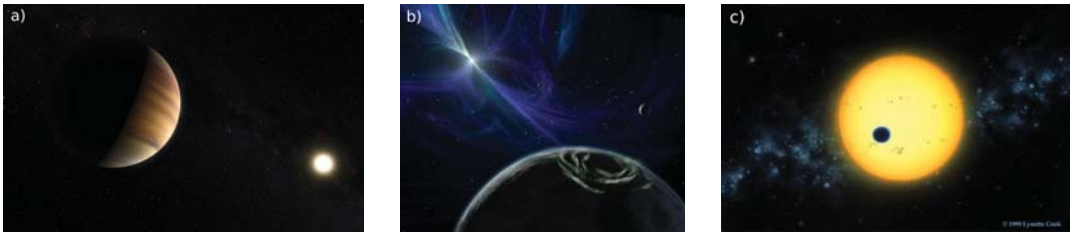

Figure 1.8: Artist impressions of the first three planet discoveries:
a) 51Peg b, the first exoplanet discovered around a solar-like star (Mayor & Queloz 1995) – a hot Jupiter in a 4.23-day orbit. This planet threw a 'spanner in the works' for astronomers thought they knew about planet formation and evolution. (Image credit: M. Kornmesser & Nick Risinger, ESO)
b) PSR B1257+12 was the first star to be discovered with planetary companions (Wolszczan & Frail 1992). The star is a pulsar and hosts two Super-Earths in 66.6- and 98.2-day orbits which were discovered due to their effect on the timings of regular electromagnetic pulses from the star. (Image credit: NASA/JPL-Caltech)
c) HD209458 b was the first planet to be observed transiting the stellar host (Charbonneau et al. 2000; Henry et al. 2000). Similar to 51 Peg b, the planet is a hot Jupiter with an orbit lasting 3.52 days. (Image credit: Lynette Cook)

star. Further analysis produced a system that contained two planets ($2.8M_\oplus$ $3.4M_\oplus$ in 98.2-day and 66.6-day orbits respectively, Wolszczan & Frail 1992).

However, the most common exoplanet given the title of 'first ever found' is attributed the first exoplanet discovered around a Sun-like star: 51 Pegasi b (Figure 1.8, Mayor & Queloz 1995). At just over 50 light years away, it was discovered via the radial velocity method (see Sect. 1.6.1). Using the ELODIE spectrogragh at the Haute-Provence Observatory in France, Michel Mayor and Didier Queloz discovered that the star was being orbited by a Jupiter-mass ($m\sin i = 0.47\pm0.02\ M_{Jup}$) planet. What added even further interest was that, at this time, it was in a highly-unusual short orbital period (4.23 days); something so short had never really been considered before, given all knowledge at the time about planet formation came from the Solar System!

With these two discoveries, research into exoplanet discovery began to be conducted world-wide, and it was not long until new methods of detecting these previously elusive exoplanets were being proposed and proven successful! Both Charbonneau et al. (2000); Henry et al. (2000) reported detecting an object transiting HD 209458 (Figure 1.8), which caused dips in measured intensity of the star (see Sect. 1.6.2). Like 51 Pegasi b, this was a Jupiter-mass planet ($0.69\pm0.017\ M_{Jup}$), but with a much larger radius ($1.38\pm0.018\ R_{Jup}$). The reason for this, is that the orbit is again quite short, at 3.52 days. Our Jupiter is quite far away from the Sun (it takes 11.86 years to orbit), which makes it quite cold as there is very little radiation from the Sun to heat it. For HD 209458b, it is very close to its host star meaning it gets a great deal of radiation; and this causes it to puff up like a popcorn kernel (Baraffe et al. 2010).

Since 1992, over 4000[e] exoplanets have been found and confirmed. They range from a series of different methods and instruments, with the most relevant described in Sect. 1.6. See Figure 1.9 to for a timeline of different discoveries and mission developments.

1.6 Detection Methods

Since the first discovery over 20 years ago, many methods for detecting exoplanets have been found; the majority of them depend on detecting changes in light or position of the stellar hosts.

1.6.1 Radial Velocity Method

Because of the individual galactic orbits of the stars in the Milky Way, every star is moving relative to the Solar System, which gives it a quantitative velocity. The radial velocity (the projection of the velocity along an observer's line of sight) is the bedrock of the radial velocity method.

[e] As of 1st August 2019, from the NASA Exoplanet Archive

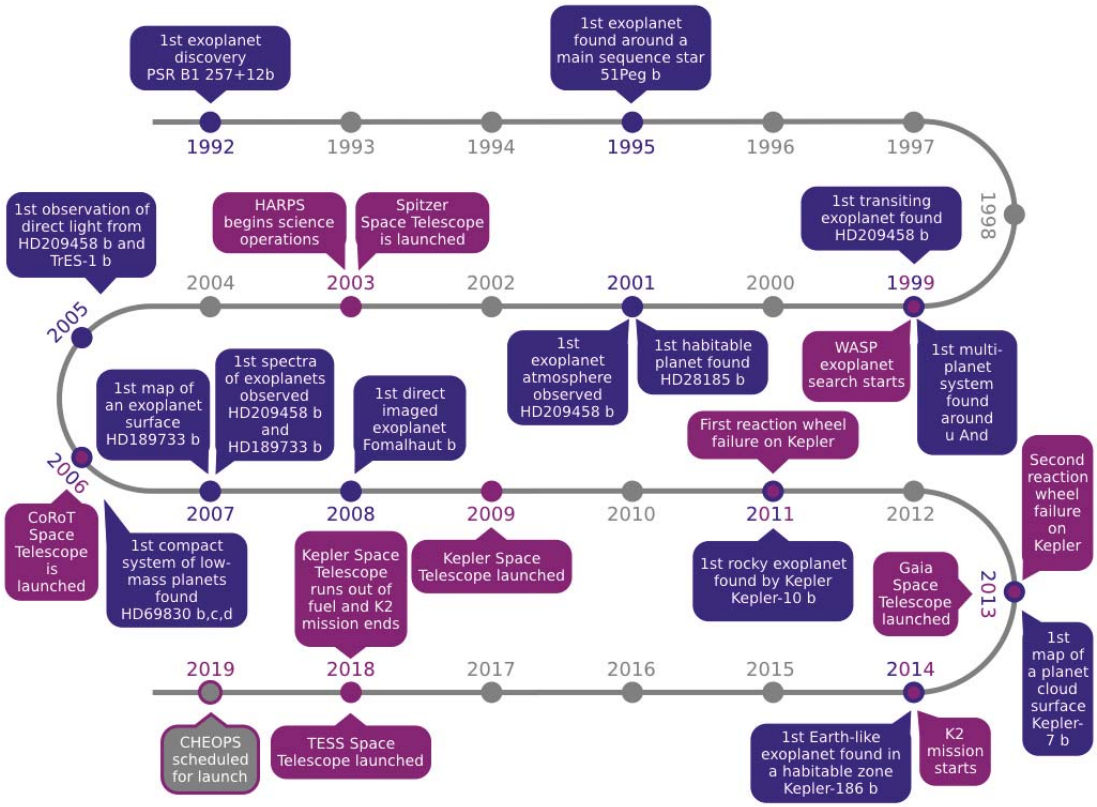

Figure 1.9: A timeline of key exoplanet discoveries (purple), mission launches and developments (plum).

As one of the first methods to find an exoplanet, it detects changes in the observed radial velocity of a star. As two or more bodies (i.e. star and planet[s]) co-orbit around the centre of mass (or barycentre) of the system, this causes a "wobble" effect in the radial velocity observed over time (Figure 1.11). This movement exerts an additional velocity to the star, thereby initiating the Doppler effect. When the star pulled away, the velocity is momentarily increased, whilst when the star is pulled towards the observer, the velocity is momentarily reduced. Due to being the radial velocity, an observer does not see this directly in the motion of the star – but the Doppler effect also affects the light escaping the star. Due to the presence of different elements in stellar atmospheres, absorption lines from the atoms absorbing stellar light are peppered throughout the spectrum of the star – and each of these lines occur at very specific wavelengths due to atomic properties (Figure 1.10). Therefore, every star has a very individual pattern of absorption lines but stars of the same spectral types share the same collection of absorption lines. Therefore, when the star accelerates to and from the observer and the Doppler effect affects all wavelengths of light, the same effect is seen for the dark absorption lines. This

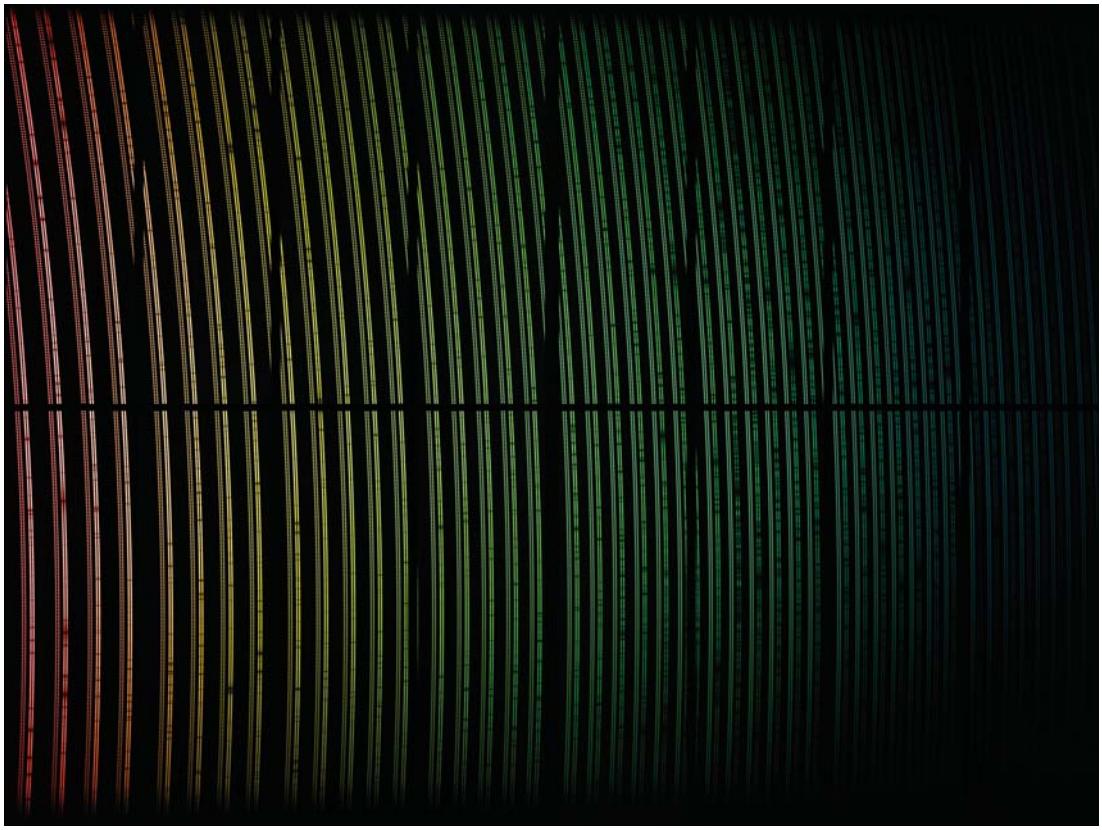

Figure 1.10: Taken during 'First Light' for the ESPRESSO instrument on the VLT in Paranal, Chile. The spectrum is of the star Tau Ceti. You can make out the small dark lines dotted along the coloured beams – these dark lines are the absorption lines from the star. (Image credit: ESO/ESPRESSO team)

means it is possible to measure the change in velocity by measuring the change in wavelength:

$$v_r = \frac{\lambda_0 - \lambda_{\rm obs}}{\lambda_0}\, c \tag{1.4}$$

where v_r is the radial velocity, λ_0 is the rest-frame wavelength, $\lambda_{\rm obs}$ is the observed wavelength and c is the speed of light.

So far, all that is known is that the observed radial velocity is changing over time (Figure 1.11). Now these radial velocities (or RVs) need to be converted to a planetary property. By having knowledge about how the geometry of the system evolves (i.e. a planet and star orbiting a shared barycentre) it is possible to reduce the orbit to

$$v_r(t) = K\,[\cos(2\pi\phi(t) + \omega) + e\cos\omega] + v_{r,*} \tag{1.5}$$

where

$$K = \left(\frac{2\pi G}{P_{\rm orb}}\right)^{1/3} \frac{M_p \sin i}{\left(M_* + M_p\right)^{2/3}} \frac{1}{\left(1 - e^2\right)^{1/2}}\,. \tag{1.6}$$

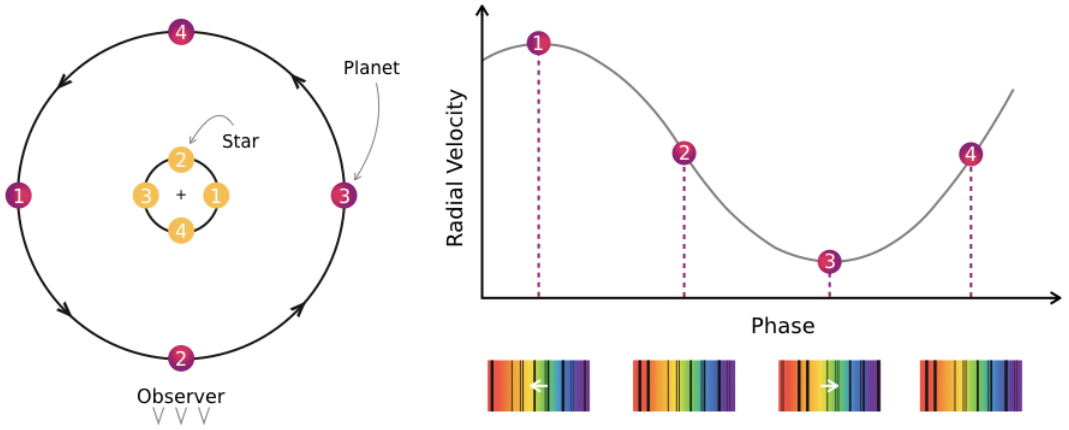

Figure 1.11: Illustration showing how a planet and star co-orbit around a shared barycentre, and how this alters the observed radial velocity measured from spectra. As the planet and star orbit the barycenter (+), the perceived radial velocity of the star changes (measured by measuring the wavelength of known absorption lines). This change appears, in an ideal case, as a sinusoid.

$\phi(t)$ is the true anomaly of the orbit, ω is the argument of pericentre (the angle from ascending node to the periapsis, with respect to the direction of motion), e is the eccentricity of the system and $v_{r,*}$ is the rest-frame radial velocity of the star. K is the radial velocity semi-amplitude which can then be related to planetary properties: $P_{\rm orb}$ is the orbital period of the planet around the star, M_* and M_p are the masses of the star and planet respectively, and i is the orbital inclination of the system with respect to the observer.

Therefore, by taking observations of the stellar spectrum regularly, it is possible to measure the RVs at different phases of the planetary orbital period. Following that, Eq. 2.1 and 2.2 can be fitted to the data points to determine planetary properties. However, from RVs, it is only ever possible to determine a value for $\mathrm{M_p \sin i}$ – a minimum mass of the planet(s). To accurately measure the planetary masses, another detection method needs to be brought in to define more orbital parameters, such as the orbital inclination.

In the years since the first radial velocity discovery, a lot of time has been dedicated to RV surveys with the specific aim to detect non-stellar companions of stars. This includes the ELODIE (later ELODIE–SOPHIE) search which found 51 Pegasi b (Mayor & Queloz 1995). Details of the ELODIE search can be found in Baranne et al. (1996); Perrier et al. (2003) and in Bouchy et al. (2009) for the SOPHIE search. Starting around the same time there was an ongoing search at the Lick Observatory which also produced several, early discoveries (e.g. 70 Virginis b, Marcy & Butler 1996) – see Fischer et al. (2014) for a full summary. A few years later, the Keck-HIRES spectrograph (Vogt et al. 1994) was on sky and initiated a radial velocity planet search using precise RVs – HIRES had a resolution of 85,000 – details of which can be found in Vogt et al. (2000).

Later, a new spectrograph was placed on the 1.2m Swiss-Euler telescope at ESO-La Silla site in Chile, named CORALIE, which also began exoplanet radial velocity searches (Queloz et al. 2000; Udry et al. 2000). Given the success of the installation, astronomers went on to develop a highly-stable, high-resolution spectrograph called HARPS (*High Accuracy Radial velocity Planet Searcher*), which was placed on the 3.6m telescope at the same site as CORALIE – HARPS also began a program of radial velocity searchs for exoplanets (Pepe et al. 2004). In 2012, the spectrograph HARPS-N started operations on the 3.58m Telescopio Nazionale Galileo (TNG) in La Palma. In essence, HARPS-N is an updated copy of HARPS which observes the northern hemisphere. It has improved image sharpness which means HARPS-N is able to achieve an accuracy less than 1 ms^{-1} for bright stars(Cosentino et al. 2012), however the skies in La Palma are not are good as those in La Silla. A significant proportion of the time on HARPS-N (80 nights per year) has been dedicated to the follow-up of *Kepler* and *K2* (Latham & HARPS-N Collaboration 2013; Hébrard et al. 2013; Berdiñas et al. 2016)

1.6.1.1 Stellar Activity Effects on RVs

Active regions in a stellar atmosphere can cause trouble when hunting for planets in RV curves, as well as other more continuous forms of stellar 'jitter' (e.g. stellar oscillations and granulation) which become an issue when attempting to measure changes in velocities of only a few ms^{-1}. Activity can effect RVs by altering the shapes of the spectral lines, or by introducing an additional signal in the curve. This stellar 'noise' is considered to be the main barrier when pushing down the precision on RVs to find an Earth-like exoplanet (Fischer et al. 2016).

Spots and plages are significant and occur on the timescale of the stellar rotation period, and induce signals in anywhere from $1ms^{-1}$ to 100 ms^{-1} (Saar & Donahue 1997). It is correlated with the level of the activity in the stellar chromosphere which can be tracked by measuring the emission in the core of the Ca H&K lines (Wilson 1978; Saar & Donahue 1997; Saar et al. 1998). Stellar oscillations have less of an effect on RVs, and cause most issues for giant and sub-giant stars. However, it can be combated by ensuring long enough exposures – for example it has been shown for HARPS that a 15-minute integration is sufficient for the oscillation effect to no longer be a significant issue, producing a signal less than $0.2ms^{-1}$ (Udry & Mayor 2008; Dumusque et al. 2011b). Granulation on the stellar surface can induce a 1-m/ s variation which needs to be averaged over many hours (Dumusque et al. 2011b; Meunier et al. 2015; Cegla et al. 2019).

The above can all be packaged into a term named 'jitter', which is treated as an excess in the RV error (see Saar et al. 1998; Wright 2005 for more details) and is different for each star (as each star has different proportions of each type of 'jitter'). There have been different methods and tools for combating the stellar activity effect in RVs. These include observing strategies

(Pepe et al. 2011; Dumusque et al. 2011b), simulating spots (Hatzes 2002) and bisector analysis (Boisse et al. 2011). There have also been attempts at modelling stellar-based, non-periodic and quasi-periodic signals, and removing them directly from the RVs by using: red-noise models such as those in Gregory (2011) and Tuomi et al. (2013); utilising simultaneous, complementary photometry (Aigrain et al. 2012; Haywood et al. 2014); and Gaussian Processes using different sources of stellar properties (Haywood et al. 2014; Rajpaul et al. 2015; Faria et al. 2016). This last technique, Gaussian Processes (or GPs) will be discussed further in Chapter 6.

However, even with these various techniques, one option many have chosen is to avoid 'noisy', active stars altogether and choose to hunt for planetary signals around 'quiet' stars (though, they are still effected by granulation and oscillation signals too).

1.6.2 Transit Method

A newer method than measuring RVs for detecting exoplanets is to detect dips in intensity of stars over time – these dips being indicators for a planet crossing the face of its host star. As a planet orbits a star, if the observer is positioned in such a way that the orbit is 'edge-on' (or almost) then it is possible that the shadow of the planet may be seen as it passes the face of the star. This is seen even within our own Solar System, when Venus and Mercury have transited across the Sun. However, we cannot easily resolve the stellar disc of other stars like we can for the Sun, therefore we do not see the actual shadow of the planet. But by measuring how bright the star appears to be over time, we can detect that brightness dropping due to the planet blocking some of the light. This was first demonstrated by Charbonneau et al. (2000); Henry et al. (2000) for the planet HD 209458b.

By monitoring a star for a significant length of time, there are four parameters which describe the transit (see Figure 1.12): ΔF, the transit depth in units of the intensity; t_T, the total duration of the transit; t_F, the duration of the flat portion of the transit; and $P_{\rm orb}$, the orbital period of the planet. Combinations of these and known stellar parameters can provide a great deal of insight into the system (Seager & Mallén-Ornelas 2003), so long as you have at minimum two transits (to accurately derive the orbital period, assuming the eccentricity is zero):

$$\frac{R_p}{R_*} = \sqrt{\Delta F}\,, \tag{1.7}$$

$$b \equiv \frac{a}{R_*}\cos i = \left(\frac{\left(1-\sqrt{\Delta F}\right)^2 - \left[\sin^2(t_F\pi/P_{\rm orb})/\sin^2(t_T\pi/P_{\rm orb})\right]\left(1+\sqrt{\Delta F}\right)^2}{1-\left[\sin^2(t_F\pi/P_{\rm orb})/\sin^2(t_T\pi/P_{\rm orb})\right]} \right)^{1/2}, \tag{1.8}$$

$$\frac{a}{R_*} = \left(\frac{\left(1+\sqrt{\Delta F}\right)^2 - b^2\left[1-\sin^2(t_T\pi/P_{\rm orb})\right]}{\sin^2(t_T\pi/P_{\rm orb})} \right)^{1/2}, \tag{1.9}$$

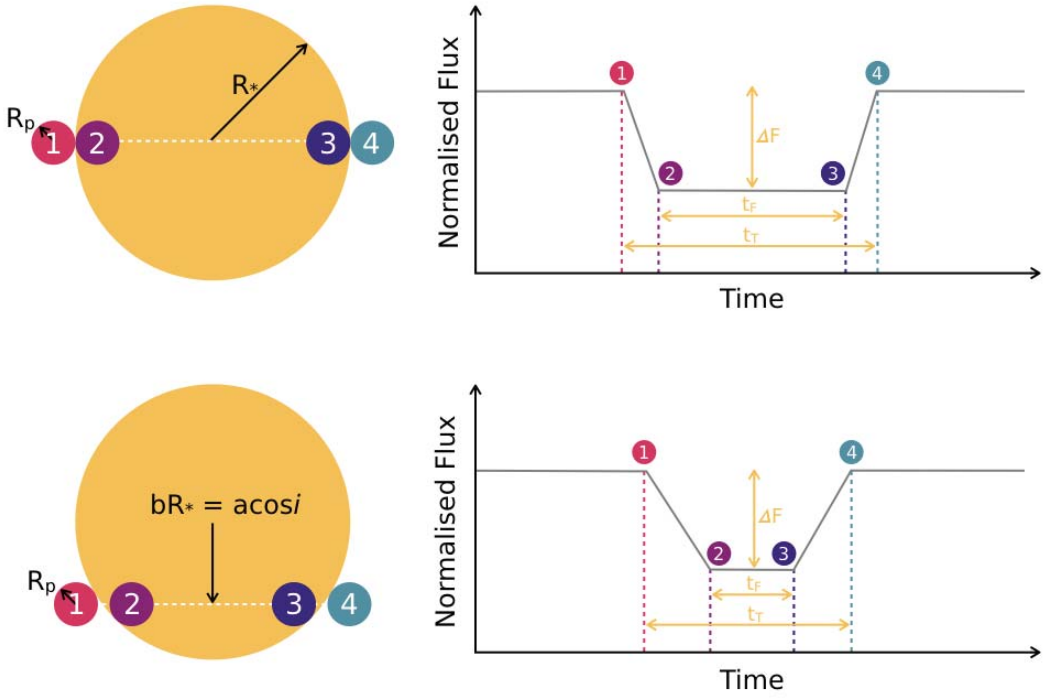

Figure 1.12: Illustration of the transit method, showing the key points of transit (marked 1-4) and definition of key transit parameters. The period of the planet is the time between each transit. As a planet crosses in front of the stellar face, a decrease in stellar brightness occurs. This will appear differently depending on the exact orbital properties of the planet with respect to the observer. This does not include the effects of stellar limb darkening.

$$\rho_* \equiv \frac{M_*}{R_*^3} = \left(\frac{4\pi^2}{P_{\rm orb}^2 G}\right)\left(\frac{\left(1+\sqrt{\Delta F}\right)^2 - b^2\left[1-\sin^2(t_T\pi/P_{\rm orb})\right]}{\sin^2(t_T\pi/P_{\rm orb})}\right)^{3/2}. \tag{1.10}$$

Equations 1.7 to 1.10 introduce seven new parameters: R_p, the planetary radius; a, the semi-major axis of the planet; b, the impact parameter; i, the orbital inclination (the same as for radial velocities); ρ_*, M_* and R_*, the stellar density, mass and radius respectively. However, Eq. 1.8-1.10 are relatively complex. They can be simplified by making one reasonable assumption (Seager & Mallén-Ornelas 2003) – that for the vast majority of planets, the transit duration will be significantly smaller than the orbital period, $t_T\pi/P_{\rm orb} \ll 1$ and $t_F\pi/P_{\rm orb} \ll 1$. This then allows $\sin x \approx x$, and if x is very small it also allows for $1 - \sin x \approx 1$. Therefore Eq. 1.8-1.10 can be transformed into

$$b = \left(\frac{\left(1-\sqrt{\Delta F}\right)^2 - (t_F/t_T)^2\left(1+\sqrt{\Delta F}\right)^2}{1-(t_F/t_T)^2}\right)^{1/2}, \tag{1.11}$$

$$\frac{a}{R_*} = \frac{2P_{\rm orb}}{\pi} \frac{\Delta F^{1/4}}{\left(t_T^2 - t_F^2\right)^{1/2}} \tag{1.12}$$

and

$$\rho_* = \frac{32}{G\pi} P_{\rm orb} \frac{\Delta F^{3/4}}{\left(t_T^2 - t_F^2\right)^{3/2}}. \tag{1.13}$$

These are significantly simpler, which also aids in analysing data. And as can be seen in Figure 1.12, it is possible to measure the majority of the orbital parameters from transits. One key measurement which cannot be determined is the planetary mass, which is why it is incredibly common to take targeted "follow-up" RV observations which can determine the mass.

The transit method has been heavily used since the first transiting planet was observed, both with telescopes on the ground and ones sent into space. Large ground-based programs such as the HATNet, the Hungarian Automated Telescope, a network of twelve telescopes (situated in both the northern and southern hemispheres), have discovered dozens of planets, such as HAT-P-11: a super-Neptune around a bright and active K star (Bakos et al. 2010). Similar networks were also deployed: TrES (Trans-Atlantic Exoplanet Survey, Alonso et al. 2004), a network of three 10cm telescopes; OGLE, originally designed for observing gravitational lensing (Udalski et al. 2002), can also detect planets like OGLE-TR-56 (Konacki et al. 2003); and WASP, the Wide-Angle Search for Planets (Pollacco et al. 2006) consists of two wide-field arrays of eight CCD cameras in both the northern and southern hemispheres and to date have well almost 200 planets to their name. There have also been a handful of single-site surveys such as MEarth (Nutzman & Charbonneau 2008; Irwin et al. 2009), the Siding Spring Observatory WFI (Bayliss et al. 2009) and NGTS, the Next Generation Transit Survey (Wheatley et al. 2013).

Transiting exoplanets have not only been discovered from the ground, but also from space. The first space-based mission to observe exoplanets was CoRoT (a 0.27m telescope) led by the CNES and other European partners (Auvergne et al. 2009), launched in 2006, and was able to observe individual stars for up to 150 days at a time. During its lifetime, CoRoT found almost 30 planets before suffering a fatal computer failure in 2012. Another space mission was *Kepler* (Borucki et al. 2010; Koch et al. 2010) – to date it is the mission that has discovered the largest number of exoplanets (over 2000!). Launched in March 2009, it began observations a coupe of months later and continued to observe a small patch of sky continuously for 4 years. However, during 2012 and 2013, two reaction wheels (in charge of controlling the stability of the telescope) failed, thereby stopping scientific operations. November 2013, *Kepler* was given a second chance – named *K2* – by balancing the remaining two reaction wheels with the solar

radiation pressure, though performing at a lower precision, it would be possible to observe transits for up to 80 days at a time (Howell et al. 2014).

1.6.2.1 Transit Timing Variations

Whilst planets typically orbit in their given period quite happily, if there is another body (or more), then the gravitational effect of that body (or bodies) can apply a small 'tug' to the observed planet. This will cause the time at which the transit should occur (using the centre of the transit as the reference point) to alter slightly (Miralda-Escudé 2002; Agol et al. 2005; Holman & Murray 2005). These transit-timing variations are known as TTVs. This effect becomes significantly more sensitive if the planets are in resonant orbits (i.e. the periods are integer or fraction multiples of one another). Commonly these will be confirmed similarly to standard transiting planets, by taking radial velocity measurements.

A system which experiences TTVs was Kepler-9 (Holman et al. 2010). Kepler-9b and c are two giant-planets which had TTVs of ~ 4 and ~ 39 minutes respectively, thereby their orbits are roughly in a 2:1 resonant orbit.

One of the first planet discoveries from TTVs was Kepler-19c – a system with a planet in a 9.3-day orbit which exhibited TTVs of five minutes. Ballard et al. (2011) demonstrated that the likelihood that this has an astrophysical cause is very unlikely, and showed with radial velocity measurements that the mass is of a planetary nature (it was then further characterised by Malavolta et al. 2017).

1.6.2.2 Stellar Activity Effects on Photometry

As for RVs, there are important stellar activity effects to acknowledge when planet hunting with light curves; these are a mix of short-term and long term variations, as well as uncertainties induced by lack of knowledge. Short-term variations are primarily from the stellar granulation and flicker. For the granulation, hydrodynamical models can be used to predict likely jitter observed (Svensson & Ludwig 2005; Ludwig 2006; Cegla et al. 2013; Norris et al. 2017). Flicker, photometric variability during an 8-hour scale, is a valuable stellar diagnostic and attributed to the stellar granulation (Bastien et al. 2013; Cranmer et al. 2014). It is directly correlated to the stellar surface gravity (Bastien et al. 2013) which is an advantageous stellar parameter to know for understand any star-planet system. This is, however, a continuous jitter term and therefore only introduces a uniform uncertainty.

The effect of starspots is considerable – they vary the brightness of the star which is needed to accurately determine sizes of the planets observed, as well as the transit duration. The planetary radius, measured from the change in brightness as it transits the star, is influenced

by how spotted the surface of the star is (Czesla et al. 2009; Carter et al. 2011; Walkowicz et al. 2013; Oshagh et al. 2016). In fact, using simulations, Oshagh et al. (2013b) determined that any unaccounted spots can lead to underestimating the size of the planet by up to 4%; and potentially introduce an error of ~4% in the transit duration and as much as 200s variation in the transit time (so after only a few transits, the time of transit may have an error as high as quarter-of-an-hour!). Additionally, due to changes in the the level of magnetic activity, the photometric radius of the star will change and this further induces more uncertainty in the transit duration (Loeb 2009; Cegla et al. 2012).

As well as having an effect on the overall brightness, which in turn affects the planet, spots can physically alter the observed transit shape. There have been cases where it was clear to see a spot being eclipsed by a planet as it eclipses the star. One of the most famous cases is HAT-P-11 which shows these spot-crossings in multiple transits (Southworth 2011). Because of so many crossings over a long baseline, as well as discovering and learning about the planet, a lot has been learnt about the spots as well; to the extent that we know HAT-P-11 exhibits similar preferential latitudes for spot formation as the Sun, and with similar spot sizes and distributions to the Sun, HAT-P-11 likely has a solar-like dynamo (Sanchis-Ojeda & Winn 2011; Morris et al. 2017).

1.6.3 Other Methods

1.6.3.1 Direct Imaging

Imagine someone told you that there was a tiny object next to the Sun in the sky. However, when you look, you were blinded by the glaring Sun. You place your hand up to the Sun to block it out, but it's still difficult to see anything because the sky around it is so bright. This, in essence, is the methodology behind direct imaging.

Direct imaging is one of the only methods which attempts to truly 'see' the planets, rather than the effect of the planet on the host star. This is achieved by taking an image of a system, where the bright host star is blocked by a coronagraph; thereby allowing fainter sources of light near to the star to be seen. The exoplanet, or in some cases the brown dwarf, will either reflect the starlight (in the visible light bands) or the small amounts of thermal emission (in the infrared) – a cartoon showing the concept of the method is shown in Figure 1.13. Sadly though, for a relatively simple idea there are significant caveats.

The difference in brightness between the light from the star and from the planet means that the stellar light needs to be efficiently blocked, and any additional effects extending beyond the coronagraph effectively detected and countered. This becomes more difficult again due to telluric atmospheric turbulence in Earth's atmosphere – reducing the star from a point source to

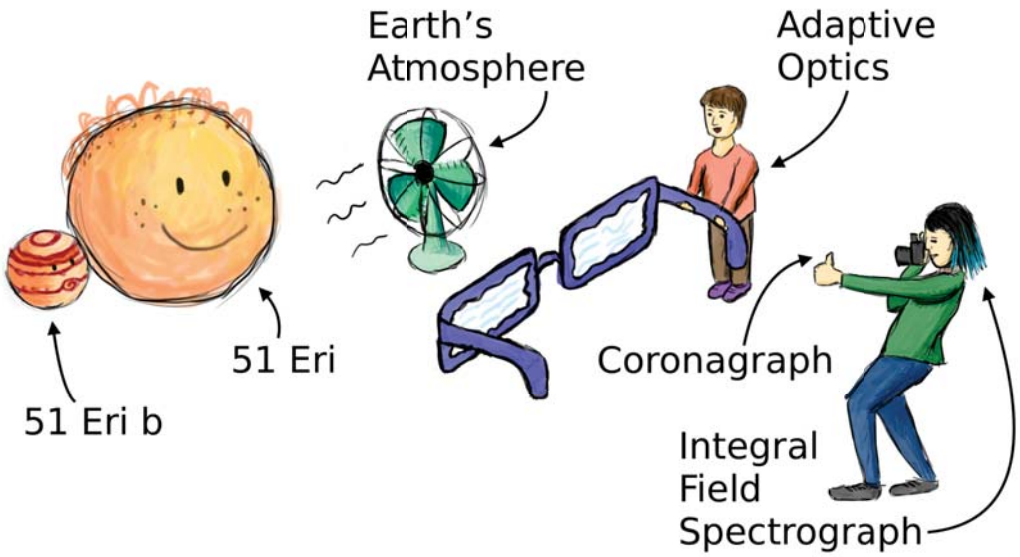

Figure 1.13: A cartoon of the discovery of 51 Eri b (Macintosh et al. 2015), describing the methodology behind the Direct Imaging method for detecting exoplanets. The CCD (or observer) places a coronagraph in front of the host star and takes an image, whilst monitoring the Earth's atmosphereic effect and removes it through adaptive optics. (Image credit: Jason Wang, GPI)

a larger, speckled mess. It can be compensated for by using adaptive optics (AO, see Davies & Kasper 2012). AO tracks changes in the Earth's atmospheric effects. It can do this by shooting a laser into the sky[f] to generate an artificial star or by following a bright guide star, where the wavefronts of the light is analysed. The wavefronts are altered by the atmosphere, and these alterations can be measured and countered with a deformable mirror; therefore, almost exactly in real time it is possible to 'undo' the atmospheric effect.

Once these hurdles have been overcome – and a small, faint point source detected – multiple images are taken over several months. As the planet orbits the star, its position in the sky will move. Tracking it over several images means it is possible to determine what the orbit would be.

The most common discoveries are large planets and brown dwarfs in very distant orbits. This is because they have a larger surface to emit light from, and are also far away enough from the stellar glare that they are easily detected as stand alone sources.

The first discovery of a planet from direct imaging was in fact a giant planet orbiting a brown dwarf. Chauvin et al. (2004) observed the brown dwarf 2MASSWJ 1207334-393254 with the NACO instrument on the VLT in Paranal, Chile. They detected a very faint and very red companion roughly 55 AU away, with further data and modelling indicating it had a mass of $\sim$ 5 Jupiter-masses.

[f] "Pew pew"!

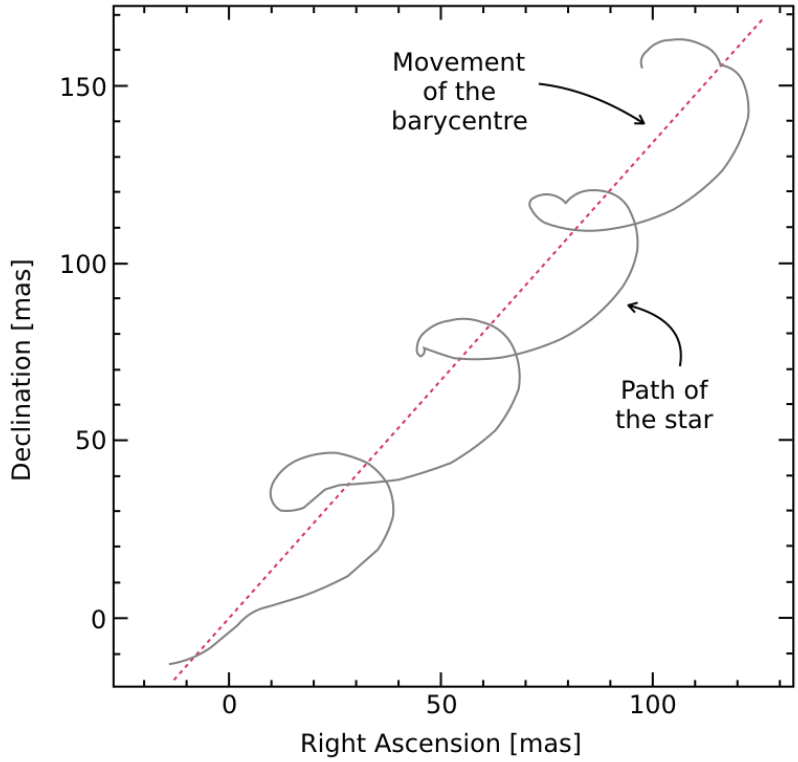

Figure 1.14: Illustration of the path of a star on the sky (solid line), at a distance of 50 pc and a proper motion of 50 mas/year. The astrometric 'corkscrew' is induced by a planet with a mass of $15M_{Jup}$ with an eccentricity of 0.2 and orbiting at 0.6AU. The straight line represents the path the star would have taken if there had not been a companion planet. (Adapted from Perryman 2018)

1.6.3.2 Astrometry

Astrometry follows a similar logic as the RV method, but rather than tracking the motion of the star via changes in the host star's spectra, you track the position of the star in the sky. All stars move across the sky in some direction depending on its location with respect to the Solar System; however adding in the gravitational pull of a planet around that star will cause that movement to change from a straight line to a 'corkscrew' motion (Figure 1.14).

Astrometry sadly comes with a long of history of false claims. As with others methods, the Earth's atmosphere plays a significant role in the accuracy obtainable from observatories on the ground – but this is not the only mistake seen. For almost a decade, it was believed that Barnard's Star (a low mass red dwarf 6 light-years away) possessed a Jupiter-like planet in a distant, slightly eccentric orbit (van de Kamp 1963). For the next 20 years, van de Kamp refined and revised the configuration of this system a further three times. Alas, in 1973 it was shown that the measured changes in position correlated with the timing of modifications and adjustments of the telescope's objective lens at Sproul Observatory, Swarthmore College

(Hershey 1973). And then, in November 2018, a revelation – Barnard's star was shown to in fact host a Super-Earth planet ($3.2M_{\oplus}$) in a 0.4AU orbit (Ribas et al. 2018). Whilst it was infinitely unlikely that van de Kamp would have ever been able to detect this planet without today's modern telescope and instruments; and certainly not with astrometry from the ground.

To date, this method solely has only successfully discovered one confirmed object, a low-mass companion of the ultracool dwarf DENIS-P J082303.1-491201. Using the VLT in Paranal, Chile, Sahlmann et al. (2013) successfully imaged and recorded the position of the ultracool dwarf with an accuracy of 0.2 milliarcseconds over the course of 2 years. These measurements indicated the presence of a low-mass object (~28 Jupiter masses) which orbits the star in 246.4 days.

However, much of this will change with the space mission *Gaia* (Perryman et al. 2001; Gaia Collaboration et al. 2016a,b). Launched in 2013 and with observations commencing early 2014, it has and will measure the positions, distances and motions of stars to very high precision. This will therefore detect the astrometric effects of planetary companions around stars observed by *Gaia*. Perryman et al. (2014), with some reasonable assumptions, predict over 20,000 high-mass (1-15M_{Jup}) long-period planets will be detected from the primary 5 year mission. This may increase up to over 70,000 during the 10 year mission.

1.6.3.3 Microlensing

The methods described up to this point often depend on a periodic signal of some sort, usually based on the orbital period of an exoplanet. Microlensing is different given that it is an event which typically only occurs once.

'Lensing' is a phenomenon which occurs due to general relativity, where the path of light (with respect to an observer) can be bent due to passing close to a massive object. A nearby star passes through the sky more quickly that a distant star, but if they align the perceived brightness of the background star would increase as it was lensed by the foreground star. If we now consider the foreground star has a planet orbiting it, given that the planet also has a mass (though smaller) it will also lens the background star (Figure 1.15). Therefore, monitoring the sky for such lensing events, and inspecting them more closely for smaller, similar increases in brightness close to the main incidence can indicate the presence of a planet. The first discovery from a microlensing survery was Bond et al. (2004) who detected the signature of a 2-body system for the star OGLE 2003-BLG-235, where two peaks were observed in the light curve of this star. However it was clear that the only possible solution was two bodies with a mass ratio of ~0.004. By assuming a the primary object was a main-sequence star, the inferred mass of the companion was ~ 1.5 Jupiter masses, with an orbital radius of roughly 3 AU.

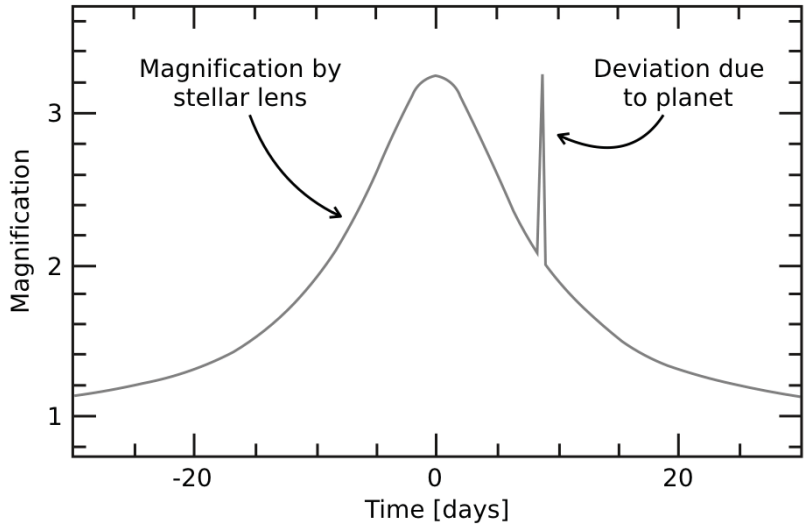

Figure 1.15: Illustration showing the concept of microlensing. As a background star passes behind a foreground star, the observed brightness increases as the foreground star lenses the background star's light. During the lensing, if there is a planet around the foreground star, there will be a sharp increase in brightness.

1.7 'Space – The Final Frontier'

As mentioned previously, there have been various attempts to detect exoplanets from both ground-based observatories and space telescopes. With over 4000[g] currently confirmed exoplanets, the detection rate is increasing almost exponentially (Figure 1.16).

However, many things can be extrapolated about this group of planets which boil down to how and where they were found. For example, each method typically finds planets within specific regions. As can be seen in Figure 1.17, Imaging tends to find exoplanets in distant orbits with higher masses; microlensing also finds planets with long-period orbits; whereas exoplanets discovered via RVs or transits have a much larger range of orbits and masses. However, it is clearer to see the distribution of periods and method of discovery in Figure 1.18a; transits dominate significantly, but the discoveries usually have slightly shorter periods than other methods. Additionally, of the transit discoveries, the majority were found with space-based telescopes. In fact, over 2680 came from the *Kepler* and *K2* missions alone.

The mission goal of *Kepler* was to find Earth-like exoplanets around solar-type stars. The importance of space- vs ground-based telescopes is significant for this goal, as Earth's atmosphere and day-night observing restrictions have serious effects on ground-based photometry. Going into space, these no longer matter and therefore near continuous viewing of targets is possible at high precision. In fact, a significant proportion of the Earth-like exoplanets dis-

[g] As of 1st August 2019, from the NASA Exoplanet Archive

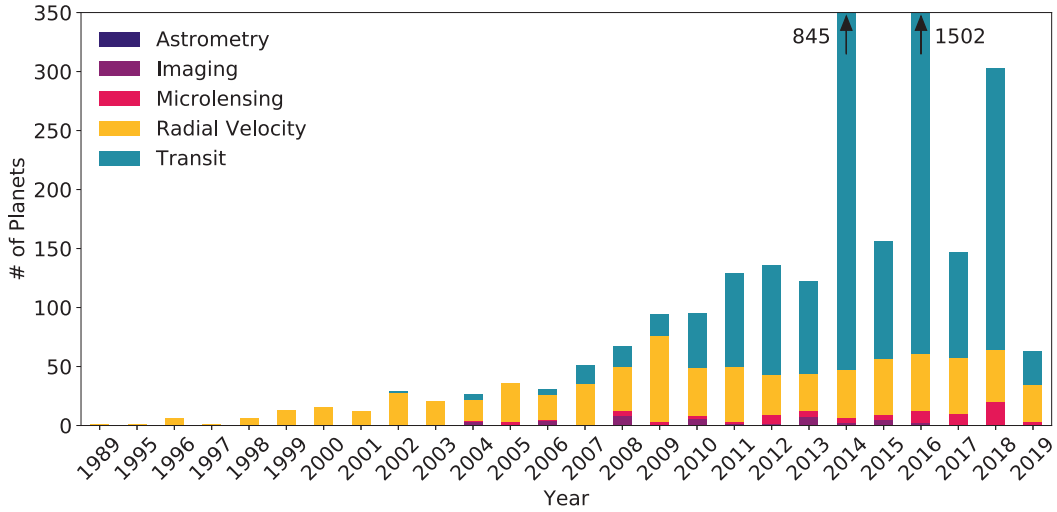

Figure 1.16: Number of confirmed discoveries per year for the five methods described in Section 1.6: RVs, transits, direct imaging, astrometry and microlensing. There is a near-exponential increase in the number each year.

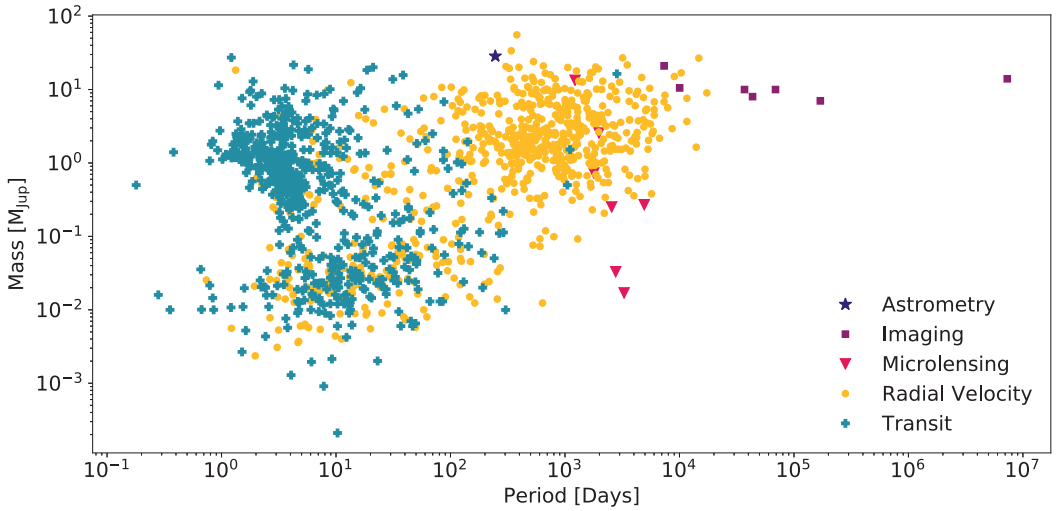

Figure 1.17: Distribution of the mass and period of confirmed discoveries, split by the discovery method (RVs, transits, direct imaging, astrometry and microlensing). Each method typically finds planets within different regions.

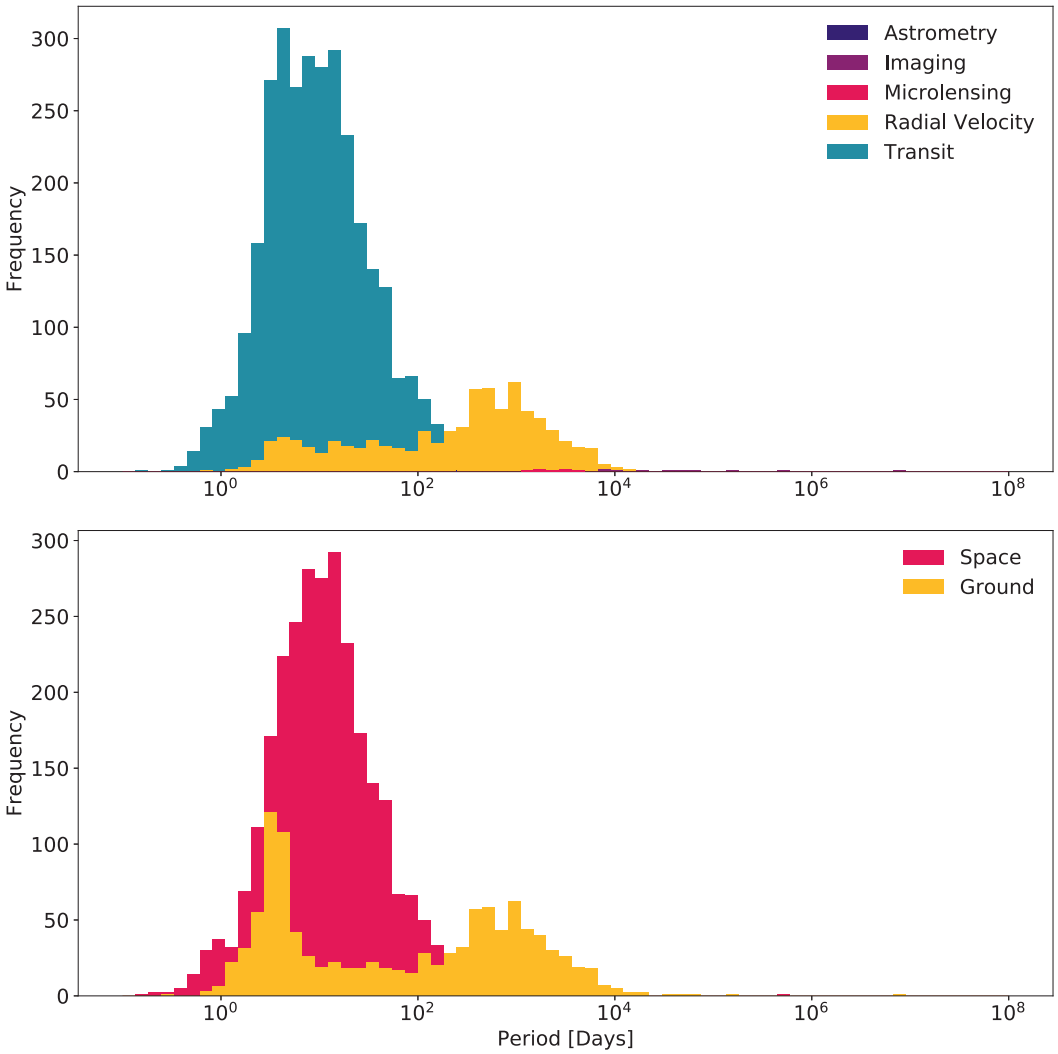

Figure 1.18: Distribution of the confirmed exoplanet periods, split by discovery method (a) and locale (b). A significant proportion of confirmed discoveries come from space-based telescopes targeting transiting exoplanets. The majority of those found from the ground were part of radial velocity searches, apart from a small peak between 1 and 10 days which came from ground-based transiting surveys .

covered so far have come from telescopes in space (Figure 1.19), usually in combination with ground-based follow-up efforts. The larger, Jupiter-like planets have been discovered by both space- and ground-based telescopes.

The most recent addition to the series of space-based telescopes is *TESS*, Transiting Exoplanet Survey Satellite, which will cover an area 400x larger than *Kepler* (85% of the sky). Launched April 18th, 2018, it has a 2-year primary mission; it is expected to find thousands of exoplanets (Stassun et al. 2018; Barclay et al. 2018). First light of *TESS* was August 7th, 2018 (Figure 1.20). Previous ground-based telescope surveys mainly found Jupiter-like exoplanets,

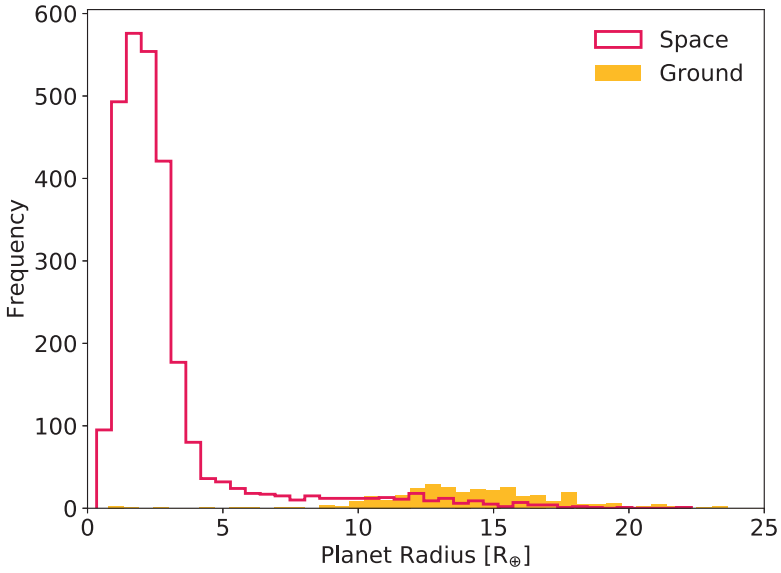

Figure 1.19: Distribution of the confirmed exoplanet radii, split by discovery locale. Nearly all Earth-like planets have been found by space-based telescopes, with ground-based telescopes primarily finding Jupiter-like, gas giant planets.

but *TESS* will find a large number of small planets around the nearest and brightest stars in the sky (which are the best for follow-up observations).

1.8 Thesis Outline

This thesis is organised in two main halves: one dedicated to the discovery of new transiting exoplanets; the other to the analysis of starspots.

Chapter 2 describes the key methods and tools used to discover and characterise exoplanets, which is generalised to no specific mission. This is followed by Chapters 3 and 4, which demonstrate how the toolkit from Chapter 2 was used in two different cases (specifically how the general methods from Chapter 2 were adapted).

In Chapter 5, details of how *Kepler* stars were analysed for the effect of starspots on their light curves can be found. Additionally in Chapter 5, there is also an attempt to analyse Solar data in the same way. The methodology detailed in Chapter 5 is then discussed with respect to its relevance for exoplanet discovery in Chapter 6, where there are two cases where the stellar activity work has been utilised in determining masses of exoplanets.

The final chapter, Chapter 7, concludes this thesis with a summary of the work done and thoughts for future work.

There are two appendices. Appendix A gives the full list of detected exoplanets by the

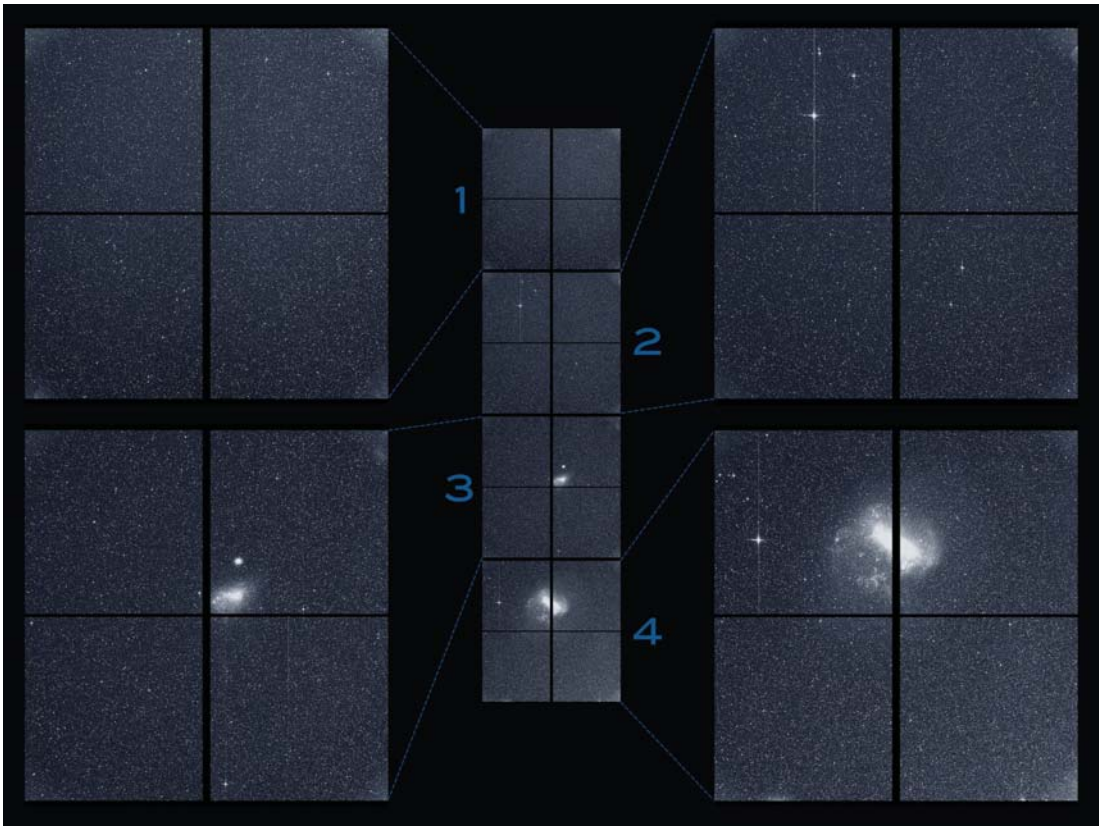

Figure 1.20: *TESS* (Transiting Exoplanet Survey Satellite) will cover an area 400x larger than *Kepler* and was launched April 18th, 2018. During its 2-year primary mission, it is expected to find thousands of exoplanets. This image is from a 30-minute cadence from August 7th, 2018. Key features seen include the Large and Small Magellanic Clouds and globular cluster NGC 104; and the brightest stars in the image are Beta Gruis and R Doradus. (Image credit: NASA/MIT/TESS)

method described in Chapters 2-4 (split into two tables, one for stellar properties and the other for planetary). In Appendix B, all publications to which I contributed, but were not directly connected to the work described in this thesis, are listed.

Chapter 2

Methodology & Toolkit

'I was taught that the way of
progress was neither swift nor easy.'

Dr Marie Skłodowska Curie

2.1 Transit Detection & Analysis

As described in Section 1.6.2, a transit is a dip in the brightness of a star as a planet orbiting that star crosses its face. Given the stellar parameters, it is possible to analyse a transit to determine properties of the system, such as planetary radius, orbital distance and inclination. But first it is necessary to detect one, and this must be based on observations of areas of the sky, using either ground-based or space-based telescopes. There must be a long baseline, so that multiple transits can be seen, and frequent observations (e.g. many exposures in an hour) so that the shape of the transit can be analysed.

2.1.1 Box-fitting Least Squares

There are several ways of detecting transits within a data set of light curves: they can be found by human inspection of individual light curves or computers can be trained to identify them using neural networks or other machine learning tools. One of the most popular is the **B**ox-fitting **L**east-**S**qaures (Kovács et al. 2002) approach (BLS). This is best suited to very large datasets which require an automated process for detecting transits. There are several stages to the BLS

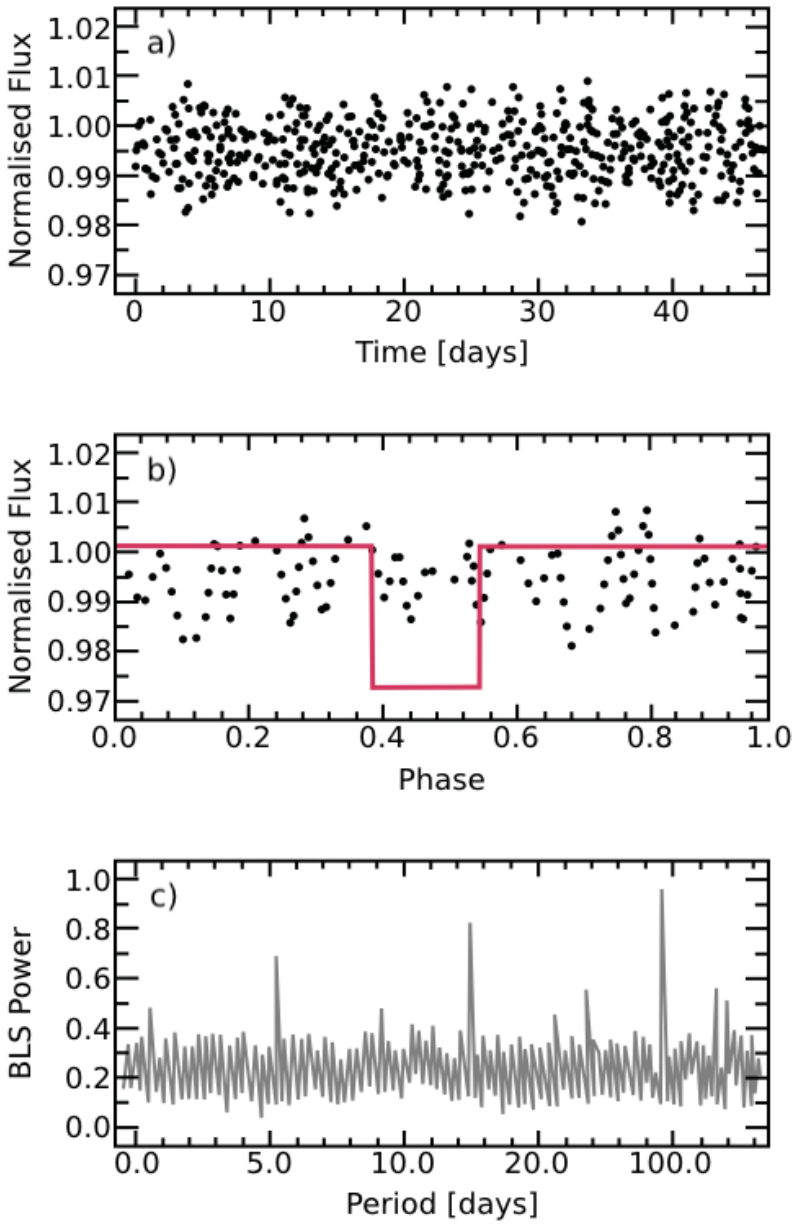

Figure 2.1: Illustration showing the methodology behind the Box-fitting Least Square technique. By taking a light curve and folding it at a series of trial orbital periods, a box (with varying widths) was fitted to the folded-light curve. This generates a power spectrum, where peaks represent the best fit at that location – the higher the power, the better the fit. (Adapted from Kovács et al. 2002)

method:

1) Before starting the BLS analysis, a series of different things need to be decided.
   a) a range of trial periods (e.g. periods ranging between 1 and 100 days), and how many steps within that range of periods (e.g. every 0.1 days or 1 day).
   b) decide what range of transit duration (in units of the period, q) to search for. In most cases for exoplanets, q is very small (<0.1).
   c) in the case of light curves with lots of exposures, it will become necessary to bin the light curve to speed up the process. Therefore it is necessary to know how many bins are wanted (e.g. 200 or 500 or more).
2) Take the light curve (Figure 2.1a) and fold it using the first trial period. This creates a phase-based light curve, where the time of observation has been converted to a phase of the trial orbital period (Figure2.1b). This phase curve is then binned into the number of bins decided in step 1.
3) A series of different sized boxes (based on the q defined in step 1) are fitted to the phased light curve with the best fitting box size (q) and the phase it was fitted at, reported back.
4) This box-fitting is performed for every trial period in the range defined in step 1. This generates a power spectrum of how well the box-fitting to the phased light curve was (Figure 2.1c). In this power spectrum, there will be random low value peaks. If there is a planet present in the light curve, a clear series of peaks will be present within the noisier random series, where one will be significantly higher than the neighbouring peaks. The highest value is statistically the likeliest solution for this planets, with the others occurring at harmonic values of this period.
5) Repeat this process for as many light curves as needed.

This method is both computationally simple and fast, but suffers from a number of caveats. Firstly, in order for it to be effective, the out-of-transit light curve behaviour must be as close to flat as possible. Trial orbital periods which match harmonics of the variability period of a variable star will produce false positives (they will yield realistic fits with the boxes, generating power spectra similar to those expected from a planet-like objects). Secondly, the speed and accuracy of the method depends on its parameters and on the definition of a significant result. Intensive sampling within a large range of periods will take much longer, and may not provide more accurate results. Similarly, too large a bin number will require more time to produce a result than a smaller number. But a small bin number will risk a transit being masked by the binning. Therefore it is crucial to have a good balance between the 'fineness' and computer time and the power needed.

One solution is to run the BLS analysis twice: first at a lower resolution and for any significant results, run again at the best solution in a higher resolution. For this a definition of

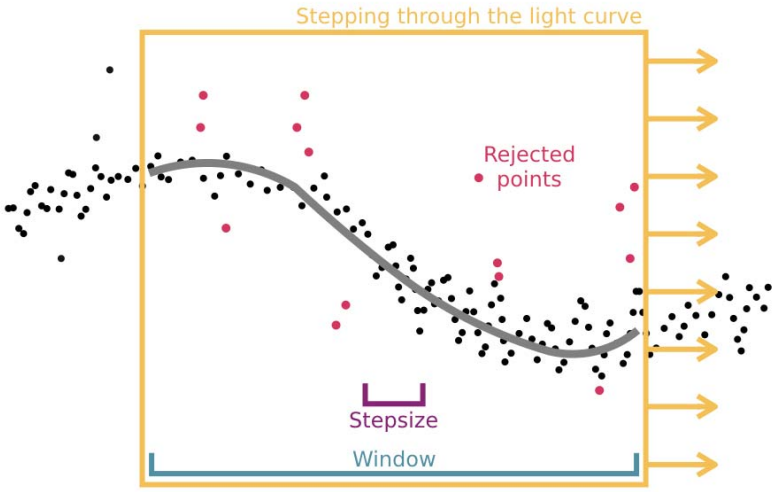

Figure 2.2: Illustration which shows the key components of the flattening tool: the 'window' (blue) section, the 'stepsize' (purple) section, a 'fitted' polynomial (grey line) with some points 'rejected' (in pink) from the fitting. The tool steps by 'stepsize' and fits a polynomial to the data points within the 'window'. Any points which are more than a threshold away are rejected and the process is repeated as many times as the tool specifies. Lastly, the only portion of the polynomial that is kept is the fit within the 'stepsize' area.

significance is necessary, and is often solved by setting a threshold on the signal-to-noise ratio (SNR). By taking an estimate of the out-of-peak noise around the period of interest, and the magnitude of the period signal, the SNR can be determined and compared to a predetermined threshold.

2.1.2 Light Curve Flattening

If the BLS routine is to work effectively the out-of-transit light curve must be as flat as possible: stellar, instrumental and Earth's atmospheric variations must be identified and adjusted for. One obvious way of doing this is to fit a polynomial to the overall light curve. However this may alter the shape of individual transits. It may also result in gradual change across the whole baseline. It is important to have a method which only acts locally. One option is to use an adapted polynomial which is only applied within a specific region of a light curve. The following parameters control the behaviour of the polynomial and ensure that its impact is local rather than global:

'stepsize' the size of the steps between each 'anchor' point in the polynomial fit (e.g. 0.1 days)

'window' the range within which the polynomial will be fitted to, where the polynomial 'anchor' point is in the centre (e.g. 5 days)

'poly_ord' the polynomial order to be fitted to the 'window' (e.g. 3)

'nsig' the number of σ, the standard deviation, to reject outliers (e.g. 3)

'niter' the number of iterations of outlier rejection and refitting that should be performed (e.g. 10)

The difference between this method and just fitting a standard polynomial is that it will react to how the local light curve behaves, and not on the global effect.

Figure 2.2 shows the method pictorially; the routine steps through a light curve in chunks with a size of 'stepsize', which are surrounded by the 'window' segment. A polynomial with the order 'poly_ord' is fitted to the data points in the window segment. The σ is calculated for the fit, and any points which lie further than 'nsig'$\times \sigma$ are rejected. This process is done 'niter' times, to ensure a convergence. The final step is to then accept the remaining polynomial fit, and determine the polynomial fit for the data points within the stepsize. These are recorded; and then repeated for each stepsize until the end of the light curve. This all produces a 'smoothed' version of the original light curve, which is then removed from the initial light curve through division. By rejecting outliers during the course of fitting a polynomial to a small area, this stops the transit from biasing the fit and therefore prevents it from being accidentally removed. That is dependent on correct use of the method – the most crucial rule for this is to ensure that 'window' >> 'stepsize'. If they are similar, then the polynomial will fit more and more the smaller structures – good for the noise seen, but could put any transits at serious risk.

2.2 Radial Velocity Follow-Up

The purpose of radial velocity follow-up is to complement the observations and knowledge already obtained from a light curve – primarily by determining a planetary mass by combining with the measured orbital inclination that can be found in photometry. And therefore enable the confirmation of exoplanetary candidates.

2.2.1 RV Sampling and Observational Strategies

To conduct RV follow-up, it is necessary to sample a full phase of the planetary orbit. This can be done by very regular, consistent follow-up over one orbit, or by less-regular sampling over several orbits of the planet. Whilst it is important to sample well the maximum and minimum of the RV phase curve, it is also important to sample the other areas to put constraints on the ellipticity of the orbit. Recently, it has become clear that the orbit of the planet is not the only thing that needs to be well-sampled. Due to the effect of stellar activity within RVs (see Section 1.6.1.1), it is necessary for low- and some high-mass planets to also have their stellar host's activity sampled (Dumusque et al. 2011b,a) – meaning at least one full stellar rotation and ideally also a whole starspot lifetime, as clear signals of these are necessary for advanced

machine learning methods (for fitting the RV curve with planetary parameters) to converge reliably.

2.2.2 RV Vetting & CCFs

Often, before performing intensive follow-up of an exoplanet candidate found from a transit survey, it is necessary to check that our candidate planet is not in fact another star orbiting the host or potentially another nearby star. This can be done by measuring two or three initial RV points and vetting their cross-correlation functions.

RV measurements are obtained by comparing the spectra obtained from the star (see Section 1.6.1) with a binary mask. A mask is merely an array where spaces within the mask match the location of the absorption lines in the spectrum. As the location of the absorption lines move due to the Doppler effect, and the size of this shift needs to be accurately measured, the mask is offset by small steps and cross-correlated with the spectrum. Once done over a range, this generates a function known as a cross-correlation function (CCF). The peak of the CCF gives the radial velocity of the star at the time of that observation.

To vet the initial CCFs, there are several things to be checked before continuing with more observations (see Figure 2.3 for an example):

1) **CCF Shape:** One simple check is the general shape of the CCF(s). They must be Gaussian in appearance and symmetric. Any large asymmetries can be an indicator of a stellar binary system.
2) **Check for Spectral Binaries:** A spectral binary is a binary system of stars where it is possible to detect both bodies via their individual spectra, which can change a CCF in two ways.
   - **SB1** Over two or more CCFs, the values of the RVs will dramatically change (e.g. many 100s of ms^{-1}). This indicates that the object orbiting our perceived host has a very high mass and is therefore not planetary (Figure 2.4).
   - **SB2** Within each CCF, there will be more than one peak. Most commonly it appears as one, large peak with an additional, smaller peak nearby. This shows that there is another stellar object in this system which has a different radial velocity compared to the perceived host, which would suggest the detected candidate may not be planetary (Figure 2.5).
3) **CCF Contrast:** The contrast ('depth') of the CCF should ideally be around 30-40%. Significantly less may suggest the wrong mask has been used for this star, and a different spectral type mask should be applied.
4) **CCF FWHM:** The **F**ull **W**idth at **H**alf **M**aximum can be used to determine the stellar rotational velocity ($v \sin i$). Whilst having a high $v \sin i$ does not 'kill' the exoplanet

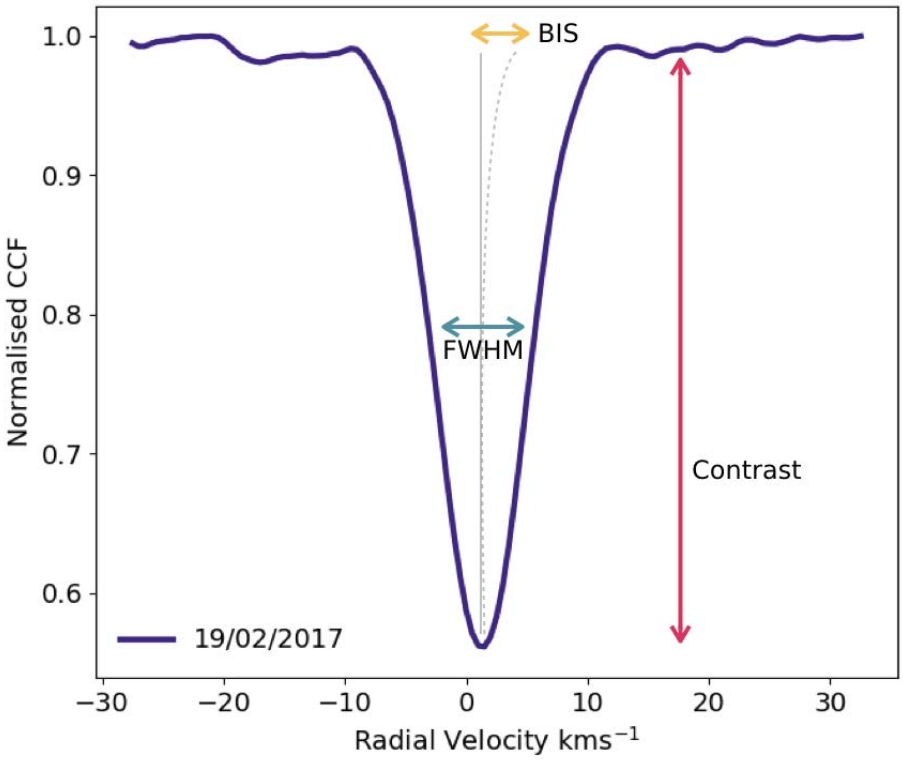

Figure 2.3: K2-140: an example of a good CCF, where the criteria are met. It has a contrast of 40%, a FWHM of 8.4kms^{-1} and a BIS close to zero (the BIS in the diagram has been exaggerated to ease of view).

candidate, if the $v \sin i$ is much greater than 7-8kms^{-1}, then it becomes more difficult to accurately measure the planetary mass.

5) **BIS:** Check the bisectors (BIS) of the CCF, which is an additional check of the CCF shape. The bisector describes the curvature of the line which tracks the midpoint of the CCF at different depths. For a perfect Gaussian, the value would be 0 (as it is symmetrical). However, given the CCF suffers from noise, the value is rarely exactly 0. But the BIS value, with its errors taken into account, should always be near 0. If a BIS value is significantly far from 0, this can suggest a non-planetary cause.
6) **Radial Velocity Value:** The actual value of the RV measurement should not be an extreme (either very small or large). Additionally, the error should be of the order of 10-20ms^{-1}. If the error is much larger than this, it would suggest a longer exposure is needed for the observation to improve the accuracy. Additionally there should be no correlation between the BIS values and RV values, as this may indicate an SB2 or stellar activity.

Many of the above criteria are there for vetting that the object is planetary in nature, rather

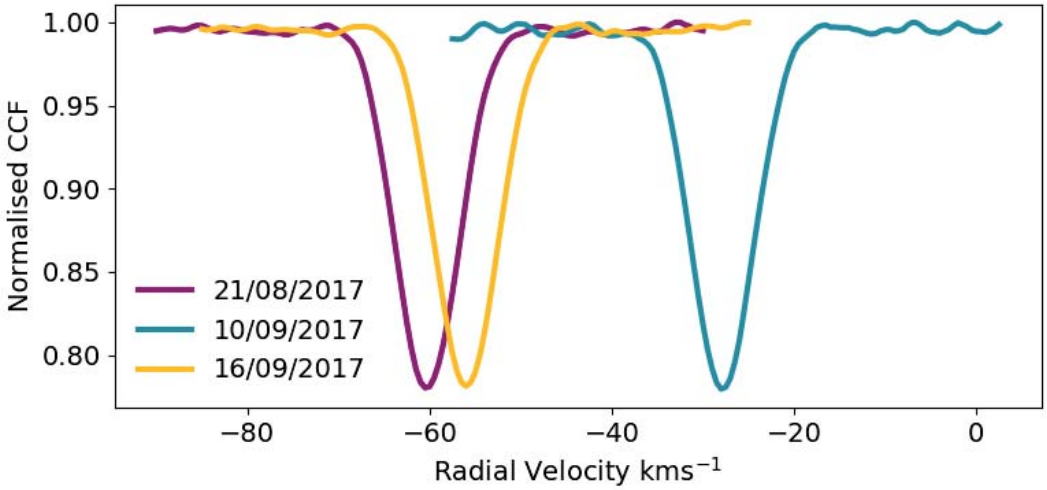

Figure 2.4: EPIC245946030: an example of an SB1, where the CCFs vary significantly between each exposure. This would indicate a non-planetary-like mass of the companion to the star.

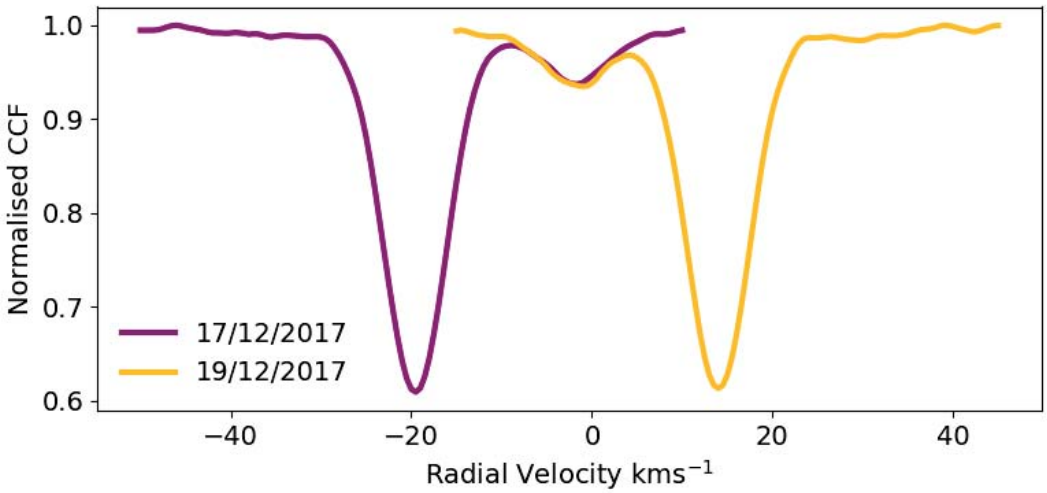

Figure 2.5: 1SWASPJ212938.68-032434.9: an example of an SB2 where there is a secondary CCF peak which also evolves over time. This would indicate that there is a stellar companion to the star of interest.

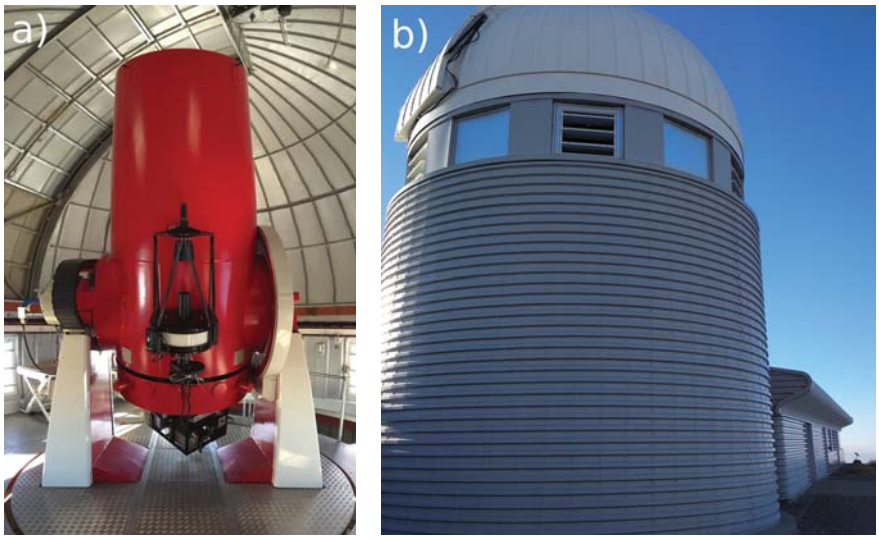

Figure 2.6: The very red Swiss Euler telescope (a) is housed within the dome of image (b), based at ESO's La Silla Observatory in Chile.

than a stellar companion. But of course, if candidates fail the vetting, this does not mean that there is not a planetary object which is in a more complicated system with two stars. For example a 'Tatooine'-like planet was found by the *Kepler* mission, Kepler-16b, which is a Saturn-like planet orbiting a pair of low-mass stars (Doyle et al. 2011). Therefore it is always worth comparing what has been seen in the initial CCFs and in the light curve.

2.2.2.1 Euler & CORALIE

For conducting RV follow-up, two things are needed: a telescope to gather the stellar light; and a spectrograph to split the light into a spectrum which is projected onto a CCD.

Run by the Observatoire de Genève, the Swiss Euler telescope is based at ESO's La Silla Observatory in Chile (Figure 2.6). Named after the famous Swiss mathematician, Leonhard Euler, the 1.2m reflecting telescope was first pointed at the sky in April 1998 and comes equipped with two instruments: EulerCam, a CCD for performing photometry; and CORALIE, an echelle spectrograph. CORALIE is fed by an optical fibre and has a resolution R=60,000 which can deliver an accuracy of 6ms^{-1} or less for the brightest targets (Queloz et al. 2000).

Euler and CORALIE have been heavily involved in exoplanet follow-up efforts since first-light, providing follow-up data for transiting exoplanet discoveries from missions like the ground-based *WASP* (Pollacco et al. 2006) and *NGTS* (Wheatley et al. 2013) projects; and space-based missions such as *K2* (Koch et al. 2010; Borucki et al. 2010), *K2* (Howell et al. 2014), and *TESS* (Ricker et al. 2015). Euler and CORALIE have also performed their own

long-term RV surveys to detect non-transiting planets (see Queloz et al. 2000; Udry et al. 2000; Santos et al. 2000, and others in the series).

2.2.3 Joint Fitting

Once RV follow-up has been obtained, covering the full phase of the exoplanet candidate's orbit (either by intense sampling during one planetary orbit or less-intense sampling over several orbits), the planetary properties need to be determined. This can be done individually for each set of data – modelling the light curve to obtain a set of parameters which can be fed as priors into the modelling of the RVs, whose results can then be fed back into the light curve model. Essentially iterating between the two until they converge to one set.

On the other hand, it is possible to tackle both the light curve and RVs simultaneously by joint-fitting. In essence, this takes both data sets, some known or estimated stellar properties and attempts to fit everything at once (for example with a Monte Carlo Markov Chain). By taking

$$v_r(t) = K\,[\cos(2\pi\phi(t) + \omega) + e\cos\omega] + v_{r,*} \tag{2.1}$$

where

$$K = \left(\frac{2\pi G}{P_{\rm orb}}\right)^{1/3} \frac{M_p \sin i}{\left(M_* + M_p\right)^{2/3}} \frac{1}{(1-e^2)^{1/2}} \tag{2.2}$$

which describes the planetary orbit through the changes in RVs and combines them with complex, analytic light curve models (such as those in Mandel & Agol 2002; Giménez 2006; Abubekerov & Gostev 2013; Kreidberg 2015). The light curve models take not only the transit shape (based on planetary radius, orbital distance and period etc.), but the models also consider the stellar properties such as limb darkening in different forms (these typically depend on the spectral type of the star).

There are various tools and packages for performing joint-fitting analysis, but two popular choices are the `EXONAILER` and `EXOFAST` (two versions available) packages. `EXONAILER` from Espinoza et al. (2016) is a straightforward python package which can fit either a light curve or RVs or both. `EXONAILER` is also able to fit using different telescope observations for both photometry and RVs, by allowing each to have their own set of instrument-based parameters (e.g. 'jitter' term, absolute radial velocity value μ etc.). It uses the light curve modelling provided by the package `BATMAN` (Kreidberg 2015) and RV fitting with RadVel (Fulton et al. 2018), all performed through an MCMC package, emcee (Foreman-Mackey et al. 2013). `EXONAILER` does not require stellar parameters or return any stellar parameters (though to assist in defining the transit shape you can provide the stellar density if known).

`EXOFAST` (Eastman et al. 2013) is different by not only performing joint-fitting between the light curve and radial velocity (though, like `EXONAILER` it is possible to fit each individually),

it also investigates and determines likely stellar parameters. To determine stellar parameters EXOFAST needs estimates of the stellar effective temperature and the metallicity, which can be measured from the stellar spectra. For the light curve modelling, EXOFAST uses the analytic calculation from Mandel & Agol (2002), with limb darkening defined by the work from Claret & Bloemen (2011). The stellar parameters are determined using the results of Torres et al. (2010). Although coded in IDL, a version of EXOFAST has been made available as an online resource at the NASA Exoplanet Archive[a]. More recently, a new version of EXOFAST has been made available (Eastman 2017) which has the added ability of handling multi-planet systems and analysing single-transit- event light curves.

[a] https://exoplanetarchive.ipac.caltech.edu/cgi-bin/ExoFAST/nph-exofast

Chapter 3

Application to *K2*

'Science is a quest for understanding.'

Prof. Dame Jocelyn Bell Burnell

3.1 Transit Detection for the *K2* Mission

The methods described in Chapter 2 were applied to the *K2* mission, the follow-up mission of *Kepler* after the second of four reaction wheels failed. *K2* observed in *Campaigns* of different regions of the sky along the ecliptic for 80 days at a time (as opposed to the 4 years which *Kepler* observed for continuously).

For the analysis of *K2* data, all of the steps detailed in Chapter 2 were followed. All targets labelled 'Stars' with *long cadence* light curves (i.e. 29.4 minute sampling) were downloaded when each Campaign had its public data release. The light curves were flattened (see Section 2.1.2) and had significant outliers removed (using the function which fitted the flattening polynomial) – the majority of these outliers were due to instrumental causes. The flattened light curves were then analysed by BLS (Section 2.1.1). For any which showed to have a significant SNR, they were reanalysed by the BLS at a higher resolution around the detected orbital period, and a diagnostic document was created (and stored) containing details such as: right ascension and declination; stellar magnitudes and other stellar properties such as radius and effective temperature (if known); the BLS output such as orbital period, transit duration

Table 3.1: A table detailing important details of each Campaign.

Campaign	RA	Dec	Length of Campaign [days]	Number of Targets†	Number of BLS Results	Number of Final Targets
11a/b*	17h21m33.1s	-23°58'33.45"	23.3/47.7	27080	1704/1695	6
12	23h26m38.1s	-5°6'8.4"	78.9	26392	4992	11
13	4h51m11.3s	20°47'13.47"	80.6	21339	3457	18
14	10h42m43.7s.	6°51'3.35"	79.7	18205	6466	16
15	15h34m28.2s.	-20°4'45.26"	88.0	22579	5136	31
16	8h54m50.3s.	18°31'31.42"	79.6	22880	5582	20
17	13h30m11.9s.	-7°43'15.87"	67.1	28551	5278	10
18	8h40m38.6s	16°49'40.31"	50.9	18482	4963	37

* C11 was split into two due to an error in the initial roll-angle used to minimise the solar effect.
† Number of 'Stars' observed with Long Cadence per Campaign.

and depth; as well as plots of the different stages of light curve analysis (raw, flattened, outliers removed), of the BLS power spectrum and the folded light curve showing the transit (including two zoom-ins of the odd and even transits). An additional step was included after the analysis was complete, which was to rank the results by their SNR – higher SNR (and therefore stronger candidates) were given higher ranks than those with low SNR. Also, to aid in the follow-up, stars which had *Kepler* magnitudes of 14 or less were deposited into an additional directory. For swift follow-up with the Swiss-Euler telescope, targets with magnitudes of 14 or less were the only instrumentally achievable options.

3.1.1 *K2* Campaigns

To date, *K2* has had 18 different campaigns. The process described in Section 3.1 was initiated for Campaign 11 and has been done for each data release since (details given of each campaign can be found in Table 3.1). Campaign 11 experienced issues due to an error with the initial roll-angle used to combat the torque effect from the Sun, and was therefore split into two sections (i.e. C11a and C11b).

3.1.2 Selection Criteria & Ranking of *K2* Exoplanet Candidates

Given that the follow-up performed would be conducted using the Swiss-Euler telescope (see Section 2.2.2.1), the planet size would have an important role in its detectability with the CORALIE instrument. With a resolution of R=60,000, low-mass planets would be difficult to detect. Therefore, the transit depth of any candidates had to be sufficient to indicate a higher-mass companion.

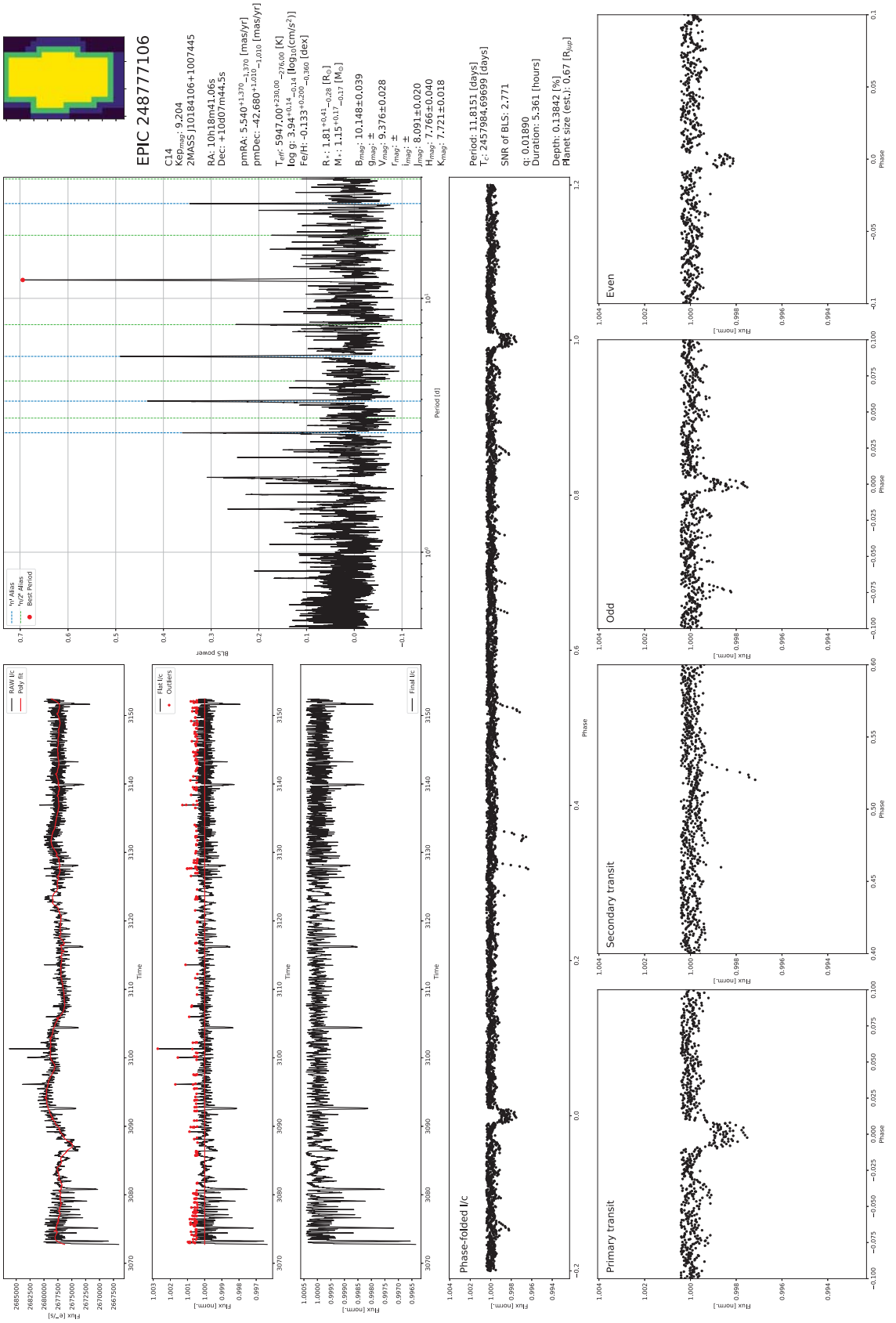

Figure 3.1: An example diagnostic document for the star EPIC 248777106 from Campaign 14. It has various diagnostic figures: each stage of the flattening and outlier removal tool to show how the light curve evolved during processing; the BLS power spectrum with the most favourable peak marked, and its harmonics; the full, phase-folded light curve; zoom-ins of the primary and secondary transit; the odd and even transits (i.e. every other transit, where if there is a difference, it can indicate a stellar companion); and also key parameters about the star and planet using initial estimates. For this case, the analysis suggests that this object has a $0.67 R_{Jup}$ planet around a $1.81 R_{\odot}$ star (given the stellar parameters from Huber et al. 2016). The small downward trends throughout the phase-folded light curve comes from the large, noisy scatter at the beginning of the *K2* light curve where the telescope is settling down at the beginning of the campaign.

Two criteria were used for the ranking of the *K2* objects.

1) The depths output from the BLS analysis had to be between 0.02% and 3% – given the potential stellar types observed (e.g. small stars like M-dwarfs to F-stars) this would cover the potential range necessary for gas giant planets.
2) A criteria was based on the BLS-determined transit duration; q (the ratio of transit duration to period) could not be too long or too short, as both scenarios would indicate statistically unlikely orbital dynamics. Therefore $0.005 < q < 0.2$ was set.

If any candidates failed either of these criteria, they were rejected from the pool of candidates to be ranked. Lastly, one final condition was included. Given the sheer number of instrumental effects seen in *K2* data, in particular the 6-hour roll effect, any candidates which regularly appeared at certain periods were also rejected. Given the unknown element of this, this was done by breaking the entire period range into a series of finely-set period blocks and counting the number of candidates which fell into each block. If any block had more than four candidates, they were all rejected.

Following on from this, all candidates still within the pool were accepted and ranked based on the SNR obtained from the BLS analysis. Every candidate in the ranked list was inspected by eye, with a significant majority still proving to be instrumental noise or stellar variability. Once all were inspected, every promising candidate received more individual attention for the flattening and outlier removal to clean each light curve as carefully as possible; with some still rejected due to the transit feature proving to still be a false positive once treated more thoroughly. The results which survived all these stages were considered for follow-up – though not all received follow-up due to observational procedures, as with some candidates from each campaign being better candidates than others. The follow-up observations were often started almost immediately, as the region of sky would often be currently visible with the Swiss-Euler telescope, or on the way to setting. The process for this is detailed in Section 2.2. Once the initial RV points had been vetted for non-planetary sources, the aim was to systematically sample the candidate's period over one or two orbits – however, given the heavy demand on the Swiss-Euler telescope, this was sometimes expanded to several orbits.

For Campaigns 11 to 18, please see Appendix A for full tables of candidate planets found and any details of their follow-up observations.

3.2 K2-140b – an eccentric 6.57 d transiting hot Jupiter in Virgo

Many candidates were detected and received follow-up observations with the Swiss-Euler telescope. One of the first was K2-140b (Giles et al. 2018a), a hot Jupiter in a 6.57-day orbit. Details of the discovery, follow-up and other analyses are described below.

Monthly Notices of the ROYAL ASTRONOMICAL SOCIETY

MNRAS **475,** 1809–1818 (2018) doi:10.1093/mnras/stx3300
Advance Access publication 2018 January 5

K2-140b – an eccentric 6.57 d transiting hot Jupiter in Virgo

H. A. C. Giles,[1⋆] D. Bayliss,[1] N. Espinoza,[2,3] R. Brahm,[2,3] S. Blanco-Cuaresma,[1,4] A. Shporer,[5] D. Armstrong,[6] C. Lovis,[1] S. Udry,[1] F. Bouchy,[1] M. Marmier,[1] A. Jordán,[2,3,7] J. Bento,[8] A. Collier Cameron,[9] R. Sefako,[10] W. D. Cochran,[11] F. Rojas,[2] M. Rabus,[2] J. S. Jenkins,[12] M. Jones,[13] B. Pantoja,[12,13] M. Soto,[12] R. Jensen-Clem,[14] D.A. Duev,[14] M. Salama,[15] R. Riddle,[14] C. Baranec[15] and N. M. Law[16]

[1]*Observatoire de Genève, Université de Genève, Chemin des Maillettes 51, CH-1290 Versoix, Switzerland*
[2]*Instituto de Astrofísica, Facultad de Física, Pontificia Universidad Católica de Chile, Av. Vicuña Mackenna 4860, 782-0436 Macul, Santiago, Chile*
[3]*Millennium Institute of Astrophysics, Av. Vicuña Mackenna 4860, 782-0436 Macul, Santiago, Chile*
[4]*Harvard–Smithsonian Center for Astrophysics, 60 Garden Street, Cambridge, MA 02138, USA*
[5]*Division of Geological and Planetary Sciences, California Institute of Technology, Pasadena, CA 91125, USA*
[6]*Department of Physics, University of Warwick, Gibbet Hill Road, Coventry CV4 7AL, UK*
[7]*Max-Planck-Institut für Astronomie, Königstuhl 17, D-69117 Heidelberg, Germany*
[8]*Research School of Astronomy and Astrophysics, Mount Stromlo Observatory, Australian National University, Weston, ACT 2611, Australia*
[9]*Centre for Exoplanet Science, SUPA School of Physics and Astronomy, University of St Andrews, North Haugh, St Andrews KY16 9SS, UK*
[10]*South African Astronomical Observatory, PO Box 9, Observatory 7935, South Africa*
[11]*McDonald Observatory and Department of Astronomy, University of Texas at Austin, Austin, TX 78712, USA*
[12] *Departamento de Astronomía, Universidad de Chile, Casilla 36-D, 7591245 Santiago, Chile*
[13]*European Southern Observatory, Alonso de Cordova 3107, Vitacura, Casilla 19001, Santiago, Chile*
[14]*Department of Astronomy, California Institute of Technology, 1200 E. California Blvd., Pasadena, CA 91101, USA*
[15]*Institute for Astronomy, University of Hawai'i at Mānoa, Hilo, HI 96720-2700, USA*
[16]*Department of Physics and Astronomy, University of North Carolina at Chapel Hill, Chapel Hill, NC 27599-3255, USA*

Accepted 2017 December 20. Received 2017 October 31; in original form 2017 June 21

ABSTRACT

We present the discovery of K2-140b, a $P = 6.57$ d Jupiter-mass ($M_P = 1.019 \pm 0.070 M_{\rm Jup}$) planet transiting a V = 12.5 (G5-spectral type) star in an eccentric orbit ($e = 0.120^{+0.056}_{-0.046}$) detected using a combination of *K2* photometry and ground-based observations. With a radius of $1.095 \pm 0.018\,R_{\rm Jup}$, the planet has a bulk density of $0.726 \pm 0.062\,\rho_{\rm Jup}$. The host star has a [Fe/H] of 0.12 ± 0.045, and from the *K2* light curve, we find a rotation period for the star of 16.3 ± 0.1 d. This discovery is the 9th hot Jupiter from *K2* and highlights *K2*'s ability to detect transiting giant planets at periods slightly longer than traditional, ground-based surveys. This planet is slightly inflated, but much less than others with similar incident fluxes. These are of interest for investigating the inflation mechanism of hot Jupiters.

Key words: techniques: high angular resolution – techniques: photometric – techniques: radial velocities – planets and satellites: detection – stars: individual: K2-140.

1 INTRODUCTION

Transiting exoplanets offer the best insight into worlds outside our Solar system, as we can determine the mass, radius, and obtain information regarding the planetary atmosphere. Traditional ground-based surveys such as HAT-Net (Bakos et al. 2004), WASP (Pollacco et al. 2006) and KELT (Pepper et al. 2007) are predominately sensitive to very short period transiting giant planets (P$\sim$ 3 d). Longer period transiting systems have proved much more difficult to detect. Some advantage has been gained using multisite surveys, with HAT-South (Bakos et al. 2013) detecting planets in periods as long as 16 d (Brahm et al. 2016b). However, the continuous monitoring enabled by space-based telescopes has allowed for a dramatic increase in the number of longer period transiting systems. The *Kepler* mission (Borucki et al. 2010; Jenkins et al. 2010; Koch et al. 2010), with 4 yr of near-continuous coverage, has uncovered a host of transiting planets with longer periods, however many of these transit stars that are too faint to allow for planetary mass determination via radial velocities. In 2013, after 4 yr of observations, the second of *Kepler*'s

⋆ E-mail: Helen.Giles@unige.ch

four reaction wheels failed. From this, the *K2* mission was born (Howell et al. 2014). Unlike the original mission, which observed a single region of the sky, *K2* observes proposed targets within a series of fields lying along the ecliptic, continuously, for ∼80 d. The adverse impact of the two failed reaction wheels has been minimized, but there is now a 6-h roll effect affecting *K2* light curves. This causes brightness changes as stars move from pixel to pixel on the CCD. However, there have been many different attempts to calibrate this effect and remove it from the light curves, allowing for transiting exoplanet searches (Vanderburg & Johnson 2014; Armstrong et al. 2015; Aigrain, Parviainen & Pope 2016). Further, the continuous observations for 80 d still allows for longer period systems to be discovered, e.g. EPIC 201702477b (40.736d, Bayliss et al. 2017b). Additionally, a number of more typical hot Jupiters have been discovered, e.g. K2-30b (4.099d), K2-34b (2.996d) (Lillo-Box et al. 2016), and K2-31b (1.258d, Grziwa et al. 2016).

In this paper, we report the discovery of K2-140b, a 6.57-d hot Jupiter on an eccentric orbit. In Section 2, we outline the observations that led to the discovery. In Section 3, we describe the analysis of the data that determined its properties. In Section 4, we discuss the properties and the planet's position with respect to other known hot Jupiters, and in Section 5, we summarize the discovery.

2 OBSERVATIONS

In this section, we set out the observations made to detect and characterize the transiting exoplanet K2-140b.

2.1 *K2* Photometry

The light curve for K2-140 came from Campaign 10 of the *K2* mission. This campaign observed 41 607 targets in long cadence (30 min) and 138 targets in short cadence (1 min) in the ecliptic plane centred around RA 12h 27m 07.07s Dec. −04° 01' 37.77″. Due to a pointing error (targets were off by 12 arcsec, meaning many fell outside their apertures), this campaign was split into two data releases, C10a and C10b. C10a lasted 6 d between 2016 July 6 19:45:29 UTC and 2016 July 13 01:19:55 UTC. The second release, C10b, was observed for 69 d. However, there was a data gap of 14 d after 7 d of observing due to module 4 of the telescope failing which powered off the photometer.

After the public release of the data on 2016 December 20, the light curves reduced by the *K2* Science team were downloaded and analysed for planetary signals (light-curve data listed in Table 2). This analysis required long-term variations to be removed from the light curve. This was done by fitting a sliding polynomial, which fits locally a polynomial to a small section ('step size') of the light curve using a significantly larger section ('window') of the surrounding light curve, and dividing it out. For the sliding polynomial, we used a third-order polynomial with a step size of 0.1 d and a window size of 5 d. To ensure the result is not jagged, the step size must be significantly smaller than the window size and to ensure that the transit is not accidentally fitted and removed by the process, to ensure the transit is left intact requires outlier rejection from the polynomial fit – this was done with a strict cut of positive outliers and a looser negative outlier cut. To search for planetary transits, we used a PYTHON-wrapped[1] version of the BLS routine (Kovács, Zucker & Mazeh 2002) to initially search for any significant signals and then a second time focused on the signal of interest to determine the transit parameters as accurately as possible. We then phase fold and output the light curve for visual inspection. This transit search found many candidates, which included K2-140 – a 6.57-d planet with a 1.26 per cent transit signal (Fig. 1).

Additionally, as can be seen in Fig. 1, there is some evidence of aliasing in the cadence. This is due to the observed rotation period being a half integer multiple of the cadence of *K2*.

2.2 Radial velocities

We observed K2-140 using the CORALIE spectrograph (Queloz et al. 2000) on the 1.2-m Euler Telescope at La Silla Observatory in Chile. CORALIE is a fibre-fed, high resolution ($R = 60\,000$) echelle spectrograph capable of delivering <6 m s^{-1} accuracy. Observations were made between 2017 February 20 and 2017 April 8. Additionally, K2-140 was observed using the High Accuracy Radial Velocity Planet Searcher (HARPS, Mayor et al. 2003) mounted on the ESO 3.6-m telescope in La Silla Observatory in Chile, on February 22 and between April 23 and 28. The spectra, which have a resolution $R = 115\,000$, were reduced using the Collection of Elemental Routines for Echelle Spectra (CERES, Brahm, Jordán & Espinoza 2017a).

The associated errors with each instrument vary significantly. In the case of CORALIE, the initial errors are higher than HARPS primarily because the star is relatively faint. As a test for the errors, we also calculated the root-mean-square of the data points from the fitted model (see Section 3.2) and they were comparable to the measured errors (see Table 1).

The radial velocities are plotted in Fig. 2, along with the best-fitting model determined by the joint fit described in Section 3.2. The radial velocities are also presented in Table 3.

In order to check radial velocity variation induced by a blended spectrum, we computed the bisector slope of the cross-correlation function for each observation in the manner described in Queloz et al. (2001). In Fig. 3, we find no correlation between the bisector slope and the measured radial velocity. If the signal detected was due to a blended eclipsing binary, then we may expect to see a strong correlation between the bisectors and radial velocity measurements. The bisector values are presented with the radial velocities in Table 3.

2.3 LCO photometry

In order to refine the ephemeris, check for TTVs, and check for a colour-dependent transit depth (signifying a probable blend), we performed ground-based photometric follow-up using the Las Cumbres Observatory (LCO) 1-m telescope network (Brown et al. 2013). On 2017 March 18, we monitored the transit in the *i*-band using the three LCO 1-m telescopes situated at South Africa Astronomical Observatory at Sutherland, South Africa (Fig. 4). The observations were taken using the 'Sinistro' camera with exposure times of 120 s and the telescope defocused (2.0 mm) to avoid saturation and spread the stellar point-spread function over more pixels – reducing the impact of flat-fielding uncertainties. The images were reduced using the standard LCO reduction pipeline (BANZAI), and then aperture photometry was performed using an automated pipeline (Espinoza et al., in preparation). These observations were made as part of a wider LCO Key Project[2] to characterize transiting planets using the

[1] https://github.com/dfm/python-bls

[2] http://web.gps.caltech.edu/shporer/LCOKP/

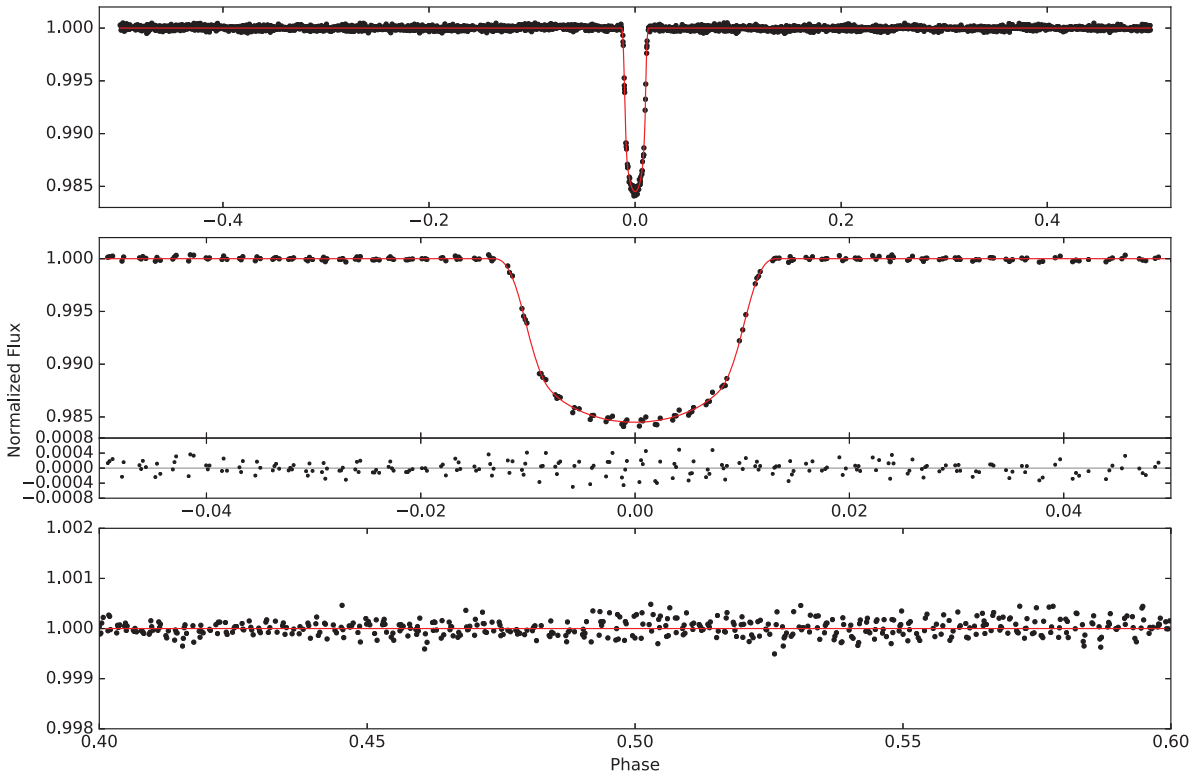

Figure 1. Phase-folded *K2* light curve of K2-140 (black points) with best-fitting model plotted as a solid red line (see Section 3.2). Top panel: Full phase light curve with the transit of K2-140b. There are no other significant dips indicating any other transits. Middle panel: Zoom-in of the transit of K2-140b and the resulting residuals from it and the model fit. Bottom panel: Zoom-in around phase 0.5. There is no indication of an observable secondary eclipse.

LCO 1-m network (see Bayliss et al. 2017b). They are listed in Table 2.

2.4 High angular resolution imaging

High angular resolution imaging of the target was obtained using the Robo-AO instrument (Baranec et al. 2013, 2014) mounted on the Kitt Peak 2.1-m telescope, on the night of 2017 April 15 using the long-pass '*lp600*' filter (Baranec et al. 2014) with a seeing of 1.5 arcsec and Strehl ratio of 2.7 per cent. The raw rapid read-out data from the Robo-AO visual camera were processed using Robo-AO's reduction pipelines described briefly below. A more detailed description can be found in Jensen-Clem et al. (2017).

First, the 'bright-star pipeline generates a windowed data cube centred on an automatically selected guide star. The windowed region is bi-cubically up-sampled and cross correlated with the theoretical PSF to give the centre coordinates of the guide star's PSF in each frame. The nightly dark and dome flat exposures are then used to calibrate the full-frame, unprocessed images. The calibrated full frames are aligned using the centre coordinates identified by the up-sampled, windowed frames, and co-added via the Drizzle algorithm.

Next, the 'high contrast imaging pipeline' generates a 3.5 arcsec frame windowed about the star of interest in the final science frame from the bright star pipeline. A high pass filter is applied to the windowed frame to reduce the contribution of the stellar halo. To whiten correlated speckle noise at small angular separations from the target star, a synthetic PSF generated by the Karhunen–Loève Image Processing (KLIP) algorithm is subtracted from the frame. The KLIP algorithm is based on the method of principal component analysis. The PSF diversity needed to create this synthetic image is provided by a reference library of Robo-AO observations – a technique called Reference star Differential Imaging.

The contrast curve was estimated using the VIP (Vortex Image Processing) package (Gomez Gonzalez et al. 2016) by measuring the residuals from resolution element-sized regions in the PSF-subtracted image.

The final Robo-AO image and contrast curve are shown in Fig. 5. The target is isolated down to $\Delta\text{mag} = 4$ at 0.5 arcsec and $\Delta\text{mag} = 4.5$ at 1 arcsec.

3 ANALYSIS

3.1 Stellar parameters

Initially, to determine the stellar parameters of K2-140, we built a pipeline for CORALIE spectra based on ISPEC[3] (Blanco-Cuaresma et al. 2014). This tool provides a large number of options to treat high-resolution spectra (e.g. co-addition, continuum normalization) and it can derive atmospheric parameters and chemical abundances using many different model atmospheres, atomic line lists,

[3] http://www.blancocuaresma.com/s/iSpec

Table 1. Parameters of K2-140.

Parameter	Units	Value	Source
EPIC ID		228735255	H16[a]
2MASS ID		2MASS J12323296-0936274	H16[a]
RA (α)	hh:mm:ss	12: 32: 32.96	H16[a]
Dec. (δ)	dd:mm:ss	−09: 36: 27.5	H16[a]
g_{GAIA}	mag	12.393	GAIA[b]
B	mag	13.349 ± 0.030	APASS[c]
V	mag	12.624 ± 0.030	APASS[c]
g	mag	12.930 ± 0.060	APASS[c]
r	mag	12.426 ± 0.020	APASS[c]
i	mag	12.292 ± 0.050	APASS[c]
J	mag	11.421 ± 0.026	APASS[c]
H	mag	11.068 ± 0.021	APASS[c]
K_s	mag	10.995 ± 0.021	2MASS[d]
Kep	mag	12.483	H16[a]
W_1	mag	10.985 ± 0.024	ALLWISE[e]
W_2	mag	11.030 ± 0.021	ALLWISE[e]
W_3	mag	10.891 ± 0.119	ALLWISE[e]
W_4	mag	$8.898 \pm -$	ALLWISE[e]
Distance	pc	340.24 ± 11.58	[f]
Age	Gyr	4.22 ± 0.95	[f]
Spectral type		G5	[f]
M_V	mag	$4.965^{+0.069}_{-0.066}$	[f]
[Fe/H]	dex	0.12 ± 0.045	[f]
$T_{\rm eff}$	K	5654 ± 55	[f]
log(g)	dex	$4.452^{+0.010}_{-0.009}$	[f]
$v \sin i$	km s^{-1}	3.8 ± 0.2	[f]
$P_{\rm rot}$	days	16.3 ± 0.1	[f]
M_*	$M_\odot$	$1.005^{+0.021}_{-0.020}$	[f]
R_*	$R_\odot$	$0.987^{+0.011}_{-0.011}$	[f]
ρ_*	$\rho_\odot$	1.048 ± 0.041	[f]
L_*	$L_\odot$	$0.893^{+0.049}_{-0.048}$	[f]
$\mu_{1,K2}$		$0.341^{+0.084}_{-0.079}$	[f]
$\mu_{2,K2}$		$0.441^{+0.111}_{-0.079}$	[f]
$\mu_{1,LCO}$		$0.56^{+0.18}_{-0.16}$	[f]
$\mu_{2,LCO}$		$0.38^{+0.20}_{-0.17}$	[f]
RV residuals (CORALIE)	km s^{-1}	0.0184	[f]
RV residuals (HARPS)	km s^{-1}	0.0097	[f]

[a]Huber et al. (2016), [b]Gaia Collaboration et al. (2016a,b),
[c]Henden & Munari (2014),[d]Skrutskie et al. (2006),
[e]Wright et al. (2010); Mainzer et al. (2011), [f] This work

radiative transfer codes, and spectroscopic techniques (i.e. equivalent width and synthetic spectral fitting). For this study, we executed the following steps:

(i) Align and co-add all the observations taken with CORALIE (see Section 2.2) to increase the S/N.
(ii) Reduce the spectrum to the optical wavelength range (480–680 nm).
(iii) Cross-correlate with a solar template to shift the observed spectrum to the rest frame.
(iv) Discard negative fluxes and estimate flux errors based on an estimated S/N.
(v) Convolve to a resolution of $R \sim 47\,000$ and homogeneously re-sample the spectrum.
(vi) Ignore regions affected by telluric lines.
(vii) Fit the pseudo-continuum and normalize the spectrum.
(viii) Derive atmospheric parameters using the synthetic spectral fitting technique, SPECTRUM (Gray & Corbally 1994) as radiative transfer code, atomic data obtained from VALD (Kupka, Dubernet & VAMDC Collaboration 2011), a line selection based on a $R \sim 47\,000$ solar spectrum (Blanco-Cuaresma et al. 2016, 2017) and the MARCS model atmospheres (Gustafsson et al. 2008).

As an output we obtained the effective temperature, surface gravity ($\log g$), and metallicity. From these, a series of isochrones were generated using stellar model generator SYCLIST[4] (Mowlavi et al. 2012). A grid of ages at a given metallicity ($Z = 0.040$) was generated and interpolated to determine the stellar age, mass, radius, and luminosity.

The results of the ISPEC analysis gave an effective temperature of 5732 ± 32K, a $\log g$ of 4.29 dex and [Fe/H] $= 0.32 \pm 0.03$ dex.

Following a similar procedure, the individual HARPS spectra were median combined in order to construct a higher SNR template.

[4] https://obswww.unige.ch/Recherche/evoldb/index/

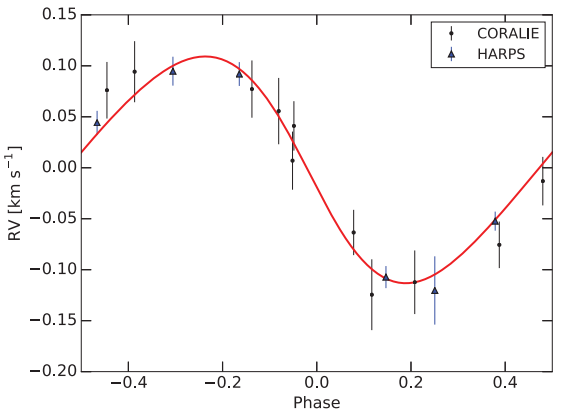

Figure 2. Phase-folded observations from CORALIE (black points) and HARPS (blue triangles) with the best-fitting model (red solid line) as described in Section 3.2. CORALIE observations were taken between 2017 February 20 and 2017 April 8 using the Swiss Euler telescope in La Silla, Chile. HARPS observations were taken between 2017 February 22 and 2017 April 28 using the ESO 3.6-m telescope in La Silla, Chile. The errors for HARPS have had the jitter added in quadrature.

Table 2. Photometry for K2-140.

BJD-2450000	Flux	Flux error	Filter	Instrument
7582.5906314203	1.000 020 94	0.000 083 99	*kep*	*K2*
7582.6110636177	1.000 065 07	0.000 083 93	*kep*	*K2*
7582.6314957142	1.000 003 89	0.000 083 85	*kep*	*K2*
7582.6519277110	1.000 017 66	0.000 083 76	*kep*	*K2*
7582.6723599071	1.000 004 62	0.000 083 69	*kep*	*K2*
7582.6927920026	0.999 985 20	0.000 083 62	*kep*	*K2*
7582.7132239980	1.000 019 08	0.000 083 51	*kep*	*K2*
7582.7336561931	0.999 929 69	0.000 083 42	*kep*	*K2*
7582.7540882872	1.000 152 49	0.000 083 31	*kep*	*K2*
7582.7745202812	0.999 933 07	0.000 083 23	*kep*	*K2*
–	–	–	–	–

**Note:* partial list – full table available in electronic form.

Table 3. Radial velocities for K2-140b in chronological order.

BJD-2450000	RV km s^{-1}	RV error km s^{-1}	BIS	Instrument
7804.751722	1.25803	0.02389	– 0.03886	CORALIE
7806.7167899	1.1231	0.0333	– 0.019	HARPS
7814.792453	1.20384	0.02344	– 0.08219	CORALIE
7815.668909	1.31119	0.02967	– 0.03487	CORALIE
7817.678137	1.27255	0.03227	– 0.06864	CORALIE
7818.723682	1.15348	0.02183	– 0.01804	CORALIE
7820.754834	1.14137	0.02247	0.02071	CORALIE
7821.852054	1.29300	0.02745	0.03278	CORALIE
7823.874191	1.29414	0.02778	0.02189	CORALIE
7832.714263	1.10465	0.03093	– 0.06040	CORALIE
7836.681188	1.31122	0.03383	0.00470	CORALIE
7850.717632	1.22394	0.02820	– 0.05072	CORALIE
7851.823385	1.09243	0.03450	– 0.00820	CORALIE
7866.6826602	1.1911	0.0086	0.02	HARPS
7867.699734	1.2876	0.0111	– 0.009	HARPS
7868.7574426	1.3382	0.0137	0.003	HARPS
7869.6828912	1.3354	0.0111	0.039	HARPS
7871.7285204	1.1362	0.0102	0.0	HARPS

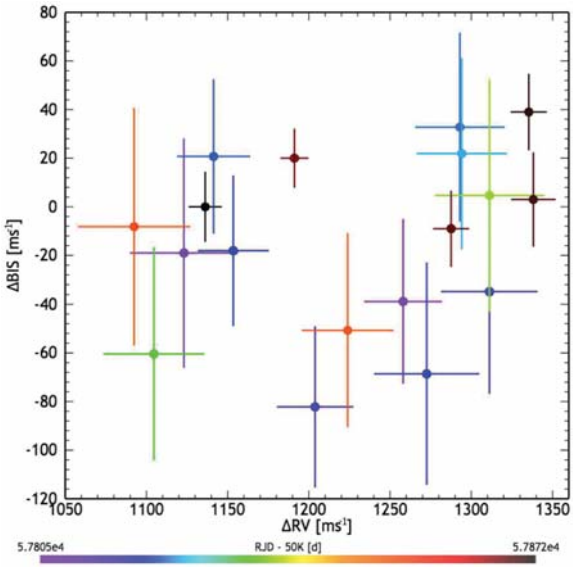

Figure 3. Distribution of the measured radial velocities and associated bisector slopes from CORALIE and HARPS. No evidence of correlation between the two can be seen. Colours represent date of observation between 2017 February 20 and 2017 April 28.

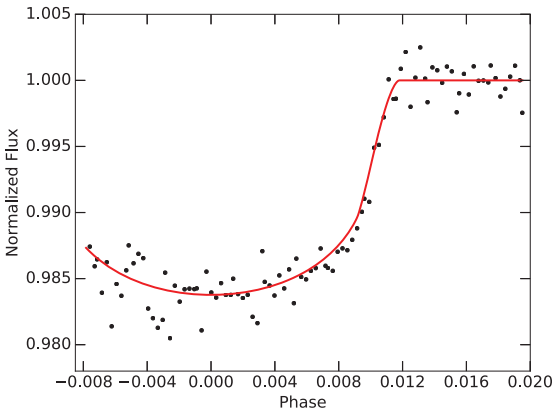

Figure 4. Phase-folded LCO light curve of K2-140 (black points) with best-fitting model plotted as a solid red line (see Section 3.2). Observations occurred the night of 2017 March 18 at the 1-m LCO telescope in Sutherland, South Africa, in '*i*' band.

The resulting spectrum was used as input of the Zonal Atmospheric Parameter estimator (ZASPE, Brahm et al. 2017b) for computing the stellar atmospheric parameters ($T_{\rm eff}$, $\log g$, [Fe/H] and $v_{\rm rot} \sin i$) by comparing it with a grid of synthetic spectra generated from the ATLAS9 model atmospheres (Kurucz 1993).

For estimating an initial guess of the physical parameters of the star, we used the Yonsei-Yale Isochrones (Yi et al. 2001) by searching for the M_* and stellar Age of the model that would produce the observed $T_{\rm eff}$ and a/R_* values for the given [Fe/H]. For obtaining the errors in the physical parameters, we performed Monte Carlo simulations where new values for $T_{\rm eff}$, a/R_*, and [Fe/H] were sampled from Gaussian distributions in each realization.

The resulting physical parameters were used to compute a more precise value for the stellar $\log g$ than the one obtained from

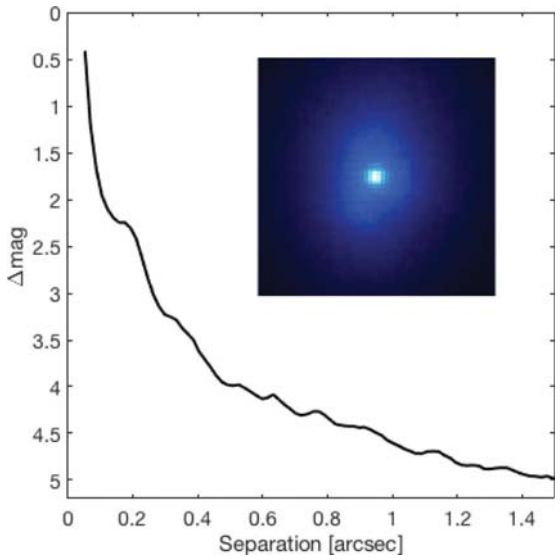

Figure 5. Contrast curve of K2-140 showing the upper limit on the magnitude difference between the target and a possible nearby star as a function of angular separation in arcsec. Data were taken by Robo-AO with the long-pass filter *lp600* covering a wavelength range from 600 nm to close to 1 μm (Baranec et al. 2014; Jensen-Clem et al. 2017). The inset shows the image of the target spanning 1 arcsec on the side.

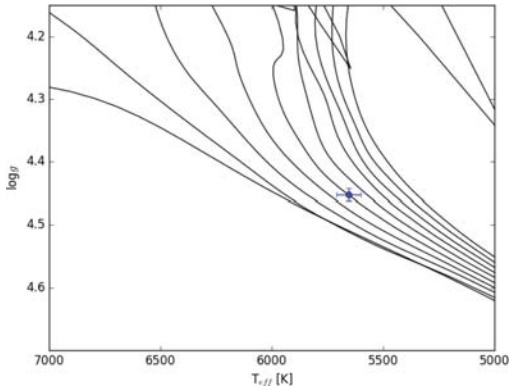

Figure 6. Yonsei-Yale isochrones (Yi et al. 2001) covering (from the left-hand to right-hand side) 0.1, 1, 2, 3, 4, 5, 6, 7, 8, and 9 Gyr based on the stellar parameters determined for K2-140.

spectroscopy. The new $\log g$ value was then held fixed in a new ZASPE execution, whose results are displayed in Table 1. The new atmospheric parameters were used to determine a new set of physical parameters from the Yonsei–Yale Isochrones (Fig. 6), obtaining a stellar mass of 1.005 ± 0.020 $M_{\odot}$, a stellar age of 4.2 ± 1.0 Gyr, and a corresponding stellar radius of 0.987 ± 0.011 $R_{\odot}$, making this host star a slightly metal-rich solar analogue.

Comparing the two results (ISPEC and ZASPE), a very similar effective temperature was measured. However, the ISPEC routine detected a smaller $\log g$ and higher metallicity. We attribute this discrepancy to the HARPS data having a significantly better signal-to-noise ratio than the reconnaissance spectroscopy, which was measured from CORALIE. For further analysis, the results from ZASPE using HARPS data were used.

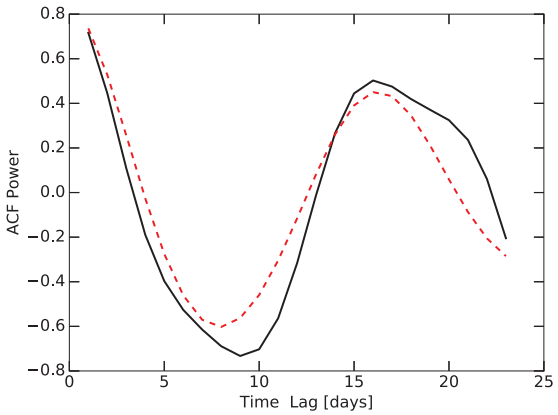

Figure 7. The autocorrelation function (black line) of the light curve for K2-140 with the transits omitted, fitted with a harmonic function (red dashed line) using method described in Giles et al. (2017). This measured a rotation period for K2-140 of 16.3 ± 0.1 d.

We measured the rotation period of K2-140 using an autocorrelation function of the polynomial fit of the *K2* light curve (with the transit omitted) as described in Giles et al. (2017). This determined a rotation period of 16.3 ± 0.1 d (Fig. 7). Given $R_* = 0.987^{+0.011}_{-0.011}$, this rotation should result in a $v \sin i \sim 3.1$ km s^{-1}, assuming stellar spin axis is perpendicular to the orbital plane of the planet. The spectroscopically derived $v \sin i$ is slightly larger than this value ($v \sin i = 3.8 \pm 0.2$), which may be due to non-equatorial spots and solar-like differential rotation. Such an effect has been seen in other *K2* transiting systems, e.g. HATS-36b (Bayliss et al. 2017a).

3.2 Joint fit

We fit the photometry data from Sections 2.1 and 2.3 jointly with the radial velocities from Section 2.2 using the `exonailer`[5] algorithm (Espinoza et al. 2016). The `exonailer` fitting was conducted with loose priors on the period, P, time of first transit, T_0, and planet-to-stellar-radii ratio, p (see Table 4 for priors used). These were determined directly from the *K2* light curve. In addition, extra (Gaussian) noise terms were added to the errors of the LCO and *K2* photometry (in order to empirically estimate extra photometric jitter), with a prior of $\mathcal{N}(1\,1000)$ for each. Extra Gaussian noise terms were also added to the CORALIE and HARPS radial velocities (in order to model radial-velocity jitter either instrumental or from stellar origin due to, e.g. activity).

Special care was taken in the modelling of the limb-darkening effect, as it is known that this can have a direct impact on the retrieved fitted transit parameters (Espinoza & Jordán 2015). In order to select the best limb-darkening law, we followed Espinoza & Jordán (2016) and ran the `ld-exosim` algorithm,[6] which gives the mean-square error on each of the retrieved transit parameters for a given limb-darkening law (given the noise, sampling and geometry of the transit). The quadratic law was chosen as it was the law that gave the minimum mean-square error on the planet-to-star radius ratio. For this case, this was the most important transit parameter because it defines the exoplanet's density. Additionally, the

[5] https://github.com/nespinoza/exonailer
[6] https://github.com/nespinoza/ld-exosim

Table 4. Parameters of K2-140b.

Parameter	Units	Value	Priors[a]
Period	days	$6.569300^{+0.000017}_{-0.000020}$	$\mathcal{N}(6.569, 0.01)$
T_0	days	$2457588.28380^{+0.00014}_{-0.00014}$	$\mathcal{N}(2457588.28544, 0.01)$
T_{14}	hours	4.56 ± 0.29	
T_{23}	hours	3.49 ± 0.26	
$T_{12=34}$	hours	0.53 ± 0.19	
R_P/R_*		$0.1140^{+0.0015}_{-0.0012}$	$\mathcal{U}(0.05, 0.2)$
b		0.33 ± 0.14	
i	$^\circ$	$88.51^{+0.69}_{-0.53}$	$\mathcal{U}(80, 90)$
a_*	au	0.0591 ± 0.0034	$\mathcal{U}(3.0, 30.0)$ [R_*]
K	km s^{-1}	$0.1112^{+0.0076}_{-0.0073}$	$\mathcal{N}(0.1, 0.1)$
$\gamma_{\rm CORALIE}$	km s^{-1}	$1.2170^{+0.0089}_{-0.0092}$	$\mathcal{N}(1.22, 0.05)$
$\gamma_{\rm HARPS}$	km s^{-1}	$1.2435^{+0.0068}_{-0.0070}$	$\mathcal{N}(1.24, 0.05)$
CORALIE jitter	km s^{-1}	$0.0041^{+0.0127}_{-0.0037}$	$\mathcal{J}(0.0001, 0.1)$
HARPS jitter	km s^{-1}	$0.0037^{+0.0144}_{-0.0033}$	$\mathcal{J}(0.0001, 0.1)$
Incident flux $\langle F \rangle$	10^8 erg s^{-1} cm^{-2}	2.565 ± 0.105	
e		$0.120^{+0.056}_{-0.046}$	$\beta(0.867, 3.03)$
ω	$^\circ$	$98.88^{+3.85}_{-4.16}$	$\mathcal{U}(0.0, 180.0)$
M_P	$M_{\rm Jup}$	1.019 ± 0.070	
R_P	$R_{\rm Jup}$	1.095 ± 0.018	
log g_P	dex (cgs)	3.324 ± 0.033	
ρ_P	$\rho_{\rm Jup}$	0.726 ± 0.062	
$T_{\rm eq.}$	K	1114 ± 34	

[a] $\mathcal{N}(\mu, \sigma)$ is a normal distribution with mean μ and standard deviation σ; $\mathcal{U}(a, b)$ is a uniform distribution between values a and b; $\mathcal{J}(a, b)$ is a Jeffrey's distribution with a lower limit of a and b; and $\beta(a, b)$ is a Beta distribution with parameters a and b as described by Kipping (2013a).

limb-darkening coefficients were individually fitted for the *K2* and LCO light curves, as they have different response functions and span different wavelength ranges. An initial fit assuming different planet-to-star radius ratios for each data set was also made, but both independently gave consistent parameters with no wavelength dependence. The final fit was made by using a common planet-to-star radius ratio for both data sets. Priors for the limb-darkening coefficients were set to be $\mathcal{N}(0, 1)$, an uninformative transformation of the quadratic limb-darkening parameters (see Kipping 2013b).

We tried fits assuming circular and non-circular orbits and the results favour the non-circular orbit, which gave an eccentricity of $0.120^{+0.056}_{-0.046}$ and an argument of periapsis of $98.88^{+3.85}_{-4.16}{}^\circ$.

The final fits for the *K2* and LCO light curves are shown in red in Figs 1 and 4, and for the radial-velocities in Fig. 2. The priors and posterior values of the fitted parameters with `exonailer` are listed in Table 4. As can be seen, the photometric jitter is significant only for the *K2* light curve; the LCO photometric jitter is consistent with zero. This is due to the fact that we decided to estimate the errors directly from the *K2* photometry, whereas the extra jitter was added in quadrature to the LCO errorbars given by the photometric pipeline. For the radial-velocity jitter, it can be seen that the extra term for both instruments is also consistent with zero.

3.3 Planet parameters

`exonailer` was able to determine various system parameters from the light curve transit shape: a/R_*, the semi-major axis-to-stellar radius ratio; R_p/R_*, the ratio of planetary to stellar radius (given as p in `exonailer`); t_0, the time of the first observed transit; P, the orbital period of the planet; and i, the inclination of the planet's orbit. Additionally, from the radial velocity curves: e, the eccentricity; ω, the periapsis argument; and K, the radial velocity semi-amplitude of the star. Through a combination of these parameters and the already determined stellar mass and radius from Section 3.1, further properties of the planet can be determined using the equations as described in Seager & Mallén-Ornelas (2003). We measured the planetary mass to be $1.019 \pm 0.070 M_{\rm Jup}$ with a radius of $1.095 \pm 0.018 R_{\rm Jup}$. This indicates a bulk density which is slightly less than that of Jupiter, $0.726 \pm 0.062 \rho_{\rm Jup}$. The planet has an incident flux of $2.565 \pm 0.105 \times 10^8$ erg s^{-1} cm^{-2}. The predicted equilibrium temperature is 1114 ± 34 K, with the assumption of a blackbody and an efficient transfer of energy from the day- to night-side. These are all listed in Table 4.

4 DISCUSSION

In this section, we compare the properties of K2-140b to the population of known hot Jupiters, and for this purpose, we use the NASA Exoplanet Archive[7] (Akeson et al. 2013) as accessed on 2017 June 6.

4.1 Orbital period

For warm and hot Jupiters, *Kepler* dominates the number of discoveries for planets with orbital periods equivalent to or longer than that of K2-140b. Therefore, to investigate the ability of *K2* to find longer period warm and hot Jupiters, we compare the *Kepler* and *K2* discoveries within a subset of all confirmed planets. They all have masses greater than $0.2 M_{\rm Jup}$ and have other significant parameters – such as eccentricity, planet density, and planet

[7] exoplanetarchive.ipac.caltech.edu

Table 5. *K2* discovered warm and hot Jupiters with precise measurements (20 per cent) on the masses and radii.

Planet	P_{orb} (d)	Mass (M_{Jup})	Radius (R_{Jup})	Reference
K2-29b	3.2588321 ± 0.0000019	0.73 ± 0.04	1.19 ± 0.02	Santerne et al. (2016)
”	3.2589263 ± 0.0000015	$0.613^{+0.027}_{-0.026}$	$1.000^{+0.071}_{-0.067}$	Johnson et al. (2016)
K2-30b	4.098503 ± 0.000011	$0.579^{+0.028}_{-0.027}$	$1.039^{+0.050}_{-0.051}$	Johnson et al. (2016)
”	4.098513 ± 0.000018	0.625 ± 0.030	1.197 ± 0.052	Lillo-Box et al. (2016)
”	$4.09849^{+0.00002}_{-0.00002}$	$0.589^{+0.023}_{-0.022}$	$1.069^{+0.023}_{-0.019}$	Brahm et al. (2016a)
K2-31b	1.257850 ± 0.000002	1.774 ± 0.079	$0.71 - 1.41$	Grziwa et al. (2016)
K2-34b	$2.9956675^{+0.0000075}_{-0.000071}$	1.649 ± 0.098	1.217 ± 0.053	Lillo-Box et al. (2016)
”	2.995654 ± 0.000018	1.773 ± 0.086	1.44 ± 0.16	Hirano et al. (2016)
”	$2.995629^{+0.000006}_{-0.000006}$	$1.698^{+0.061}_{-0.050}$	$1.377^{+0.14}_{-0.13}$	Brahm et al. (2016a)
K2-60b	3.00265 ± 0.00004	0.426 ± 0.037	0.683 ± 0.037	Eigmüller et al. (2017)
K2-97b	8.4016 ± 0.0015	1.10 ± 0.11	1.31 ± 0.11	Grunblatt et al. (2016)
K2-99b	18.249 ± 0.001	0.97 ± 0.09	1.29 ± 0.05	Smith et al. (2017)
K2-107b	3.31392 ± 0.00002	0.84 ± 0.08	1.44 ± 0.15	Eigmüller et al. (2017)

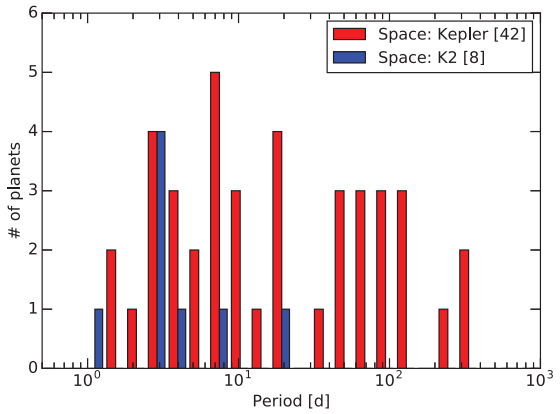

Figure 8. Distribution of confirmed planets found with *Kepler* and *K2* with masses $> 0.2M_{Jup}$. *Kepler* is in red and *K2* is in blue. K2-140b has been included into the *K2* distribution.

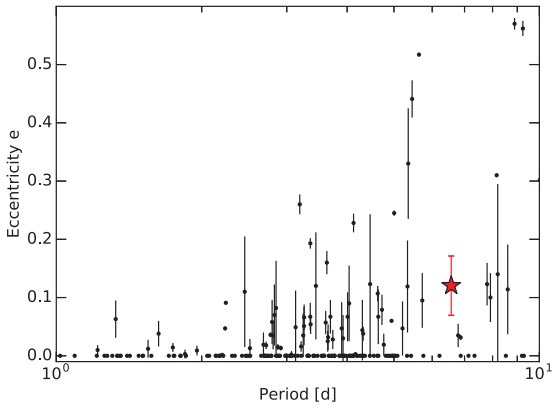

Figure 9. Eccentricities of transiting hot Jupiters (P = 1–10 d, $M_P > 0.2M_{Jup}$). K2-140b is plotted as a red star. Planets with undetermined eccentricities have been excluded.

radius – also measured. Currently, *K2* has only discovered eight planets within this subset where K2-140b is the third longest orbital period (see Table 5).

The number of planets discovered by *Kepler* and *K2* over the period range strongly reveals that, as expected, *K2* is less sensitive to long-period planets than *Kepler*, equally sensitive to short-period planets (Fig. 8). *Kepler* observed 156 000 stars and, to date, *K2* has observed a total of 171 610 (all stars observed by *K2* in long cadence from Campaigns 1–10). However, there will be a natural ramping down of the detection efficiency for planets with periods of ∼30–40d for *K2* as campaigns typically do not last longer than 80 d – whereas, for *Kepler*, there was almost 4 yr of continuous observation of the survey. Additionally, due to the necessary follow-up time required per planet (radial velocity, imaging etc.), the community has had much longer to confirm *Kepler* candidates compared with *K2* candidates – there are still regular announcements of discoveries from older *K2* campaigns as well as discoveries from the current campaign. Given more time, the distribution for planets with orbital periods of 40 d or less in *K2* may reach a similar distribution to *Kepler*. By the conclusion of the *K2* mission (assuming 19 full campaigns), we may expect *K2* will produce more than double the number of transiting giant planets with periods <10 d compared to *Kepler*.

Within the ranges of warm and hot Jupiters, ground-based surveys, in fact, dominate for shorter orbital periods. There are only 11 ground-based discoveries (NASA Exoplanet Archive, Akeson et al. 2013) with periods longer than that of K2-140b. This shows that, compared to ground-based surveys, *K2* is more effective at detecting longer period warm and hot Jupiters.

4.2 Eccentricity

Exoplanets that have non-zero eccentricities are bodies that have typically either been excited out of their orbits by other bodies or are migrating to a new orbit. The eccentric orbit of K2-140b has the potential to increase our understanding of these mechanisms.

In Fig. 9, we plot the measured eccentricities for transiting hot Jupiters with periods between 1 and 10 d. This was a subset of all confirmed planets with masses greater than $0.2M_{Jup}$ (and as previously, has other significant parameters measured). Below

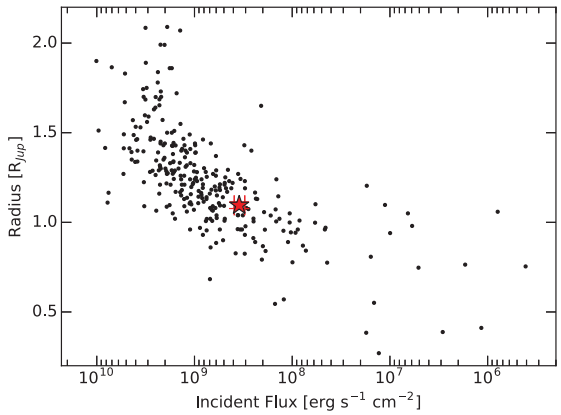

Figure 10. Distribution of incident flux and planet radii of confirmed planets found with measured masses (masses greater than $0.2M_{Jup}$) and other measured properties. This work is represented by the red star and all other warm, hot Jupiters by black points.

~5.5 d, approximately 70 per cent of hot Jupiters have measured eccentricity consistent with 0. However for systems with period greater than 5.5, this fraction drops below 50 per cent. It is therefore not surprising that we find a non-zero eccentricity for K2-140b ($e = 0.120^{+0.056}_{-0.046}$). If we assume a Q-factor of 10^6 (Wu 2005), we calculate (Goldreich & Soter 1966) a tidal circularization time-scale of τ_e =2.577 Gyr. Given our best estimate for the age of the system (4.22 ± 0.95Gyr), this means that the time-scale is of the same order of the age of the star.

4.3 Planet atmosphere inflation

A common avenue of investigation associated with warm and hot Jupiters is determining whether they are inflated or not. The distribution of the incident flux on a planet and its radii for warm and hot Jupiters is from a subset of confirmed planets with masses greater than $0.2M_{Jup}$ and with other significant parameters measured. Based on the mass and radius of K2-140b, it is slightly inflated compared with Jupiter, but not inflated with respect to other exoplanets with similar incident flux (see Fig. 10). The planet receives an incident flux of $2.565 \pm 0.105 \times 10^8$ erg s^{-1} cm^{-2}, which is very close to the empirical limit for inflation (2×10^8 erg s^{-1} cm^{-2} Demory & Seager 2011). Discovering exoplanet in this incident flux regime is important for studying the onset of the mechanism by which hot Jupiters are inflated.

5 CONCLUSIONS

We found a hot-Jupiter planet in data from *K2* Campaign 10 and followed it up with radial velocity measurements and high angular resolution imaging. K2-140b orbits a V = 12.624 ± 0.030, 4.22 ± 0.95 Gyr star with a [Fe/H] of 0.12 ± 0.045. The planet has a non-circular orbit with an eccentricity of $0.120^{+0.056}_{-0.046}$ and period of 6.57 d and a mass and radius of $1.019 \pm 0.070 M_{Jup}$ and $1.095 \pm 0.018 R_{Jup}$, respectively. It is the third longest period giant exoplanet discovered from *K2* and has a period longer period than 94 per cent of giant planets discovered from ground-based transit surveys.

ACKNOWLEDGEMENTS

HACG, DB, CL, SU, FB and MM thank the Swiss National Science Foundation (SNSF) and the Geneva University for their continuous support to our planet search programs. This work has been in particular carried out in the frame of the National Centre for Competence in Research 'PlanetS' supported by the Swiss National Science Foundation (SNSF).

NE acknowledges support from Financiamiento Basal PFB06. RB, NE, and AJ acknowledge support from the Ministry for the Economy, Development and Tourism Programa Iniciativa Científica Milenio through grant IC 120009, awarded to the Millenium Institute of Astrophysics. AJ acknowledges support by Fondecyt grant 1171208 and partial support by CATA-Basal (PB06, CONICYT). JSJ acknowledges support by Fondecyt grant 1161218 and partial support by CATA-Basal (PB06, CONICYT).

This work has made use of data from the European Space Agency (ESA) mission *Gaia* (https://www.cosmos.esa.int/gaia), processed by the *Gaia* Data Processing and Analysis Consortium (DPAC, https://www.cosmos.esa.int/web/gaia/dpac/consortium). Funding for the DPAC has been provided by national institutions, in particular the institutions participating in the *Gaia* Multilateral Agreement.

This research was made possible through the use of the AAVSO Photometric All-Sky Survey (APASS), funded by the Robert Martin Ayers Sciences Fund.

This publication makes use of data products from the Two Micron All Sky Survey, which is a joint project of the University of Massachusetts and the Infrared Processing and Analysis Center/California Institute of Technology, funded by the National Aeronautics and Space Administration and the National Science Foundation.

Some/all of the data presented in this paper were obtained from the Mikulski Archive for Space Telescopes (MAST). STScI is operated by the Association of Universities for Research in Astronomy, Inc., under NASA contract NAS5-26555. Support for MAST for non-HST data is provided by the NASA Office of Space Science via grant NNX09AF08G and by other grants and contracts.

This paper includes data collected by the *Kepler* mission. Funding for the *Kepler* mission is provided by the NASA Science Mission directorate.

This research has made use of the NASA Exoplanet Archive, which is operated by the California Institute of Technology, under contract with the National Aeronautics and Space Administration under the Exoplanet Exploration Program.

This work makes use of observations from the LCO network.

The Robo-AO team thanks NSF and NOAO for making the Kitt Peak 2.1-m telescope available. We thank the observatory staff at Kitt Peak for their efforts to assist Robo-AO KP operations. Robo-AO KP is a partnership between the California Institute of Technology, the University of Hawai'i, the University of North Carolina at Chapel Hill, the Inter-University Centre for Astronomy and Astrophysics (IUCAA) at Pune, India, and the National Central University, Taiwan. The Murty family feels very happy to have added a small value to this important project. Robo-AO KP is also supported by grants from the John Templeton Foundation and the Mt. Cuba Astronomical Foundation. The Robo-AO instrument was developed with support from the National Science Foundation under grants AST-0906060, AST-0960343, and AST-1207891, IUCAA, the Mt. Cuba Astronomical Foundation, and by a gift from Samuel Oschin. These data are based on observations at Kitt Peak National Observatory, National Optical Astronomy Observatory (NOAO Prop. ID: 15B-3001), which is operated by the

Association of Universities for Research in Astronomy (AURA) under cooperative agreement with the National Science Foundation. CB acknowledges support from the Alfred P. Sloan Foundation. ACC acknowledges support from STFC consolidated grant number ST/M001296/1. DA acknowledges support from STFC consolidated grant reference ST/P000495/1.

This research has made use of the SIMBAD data base and of the VizieR catalogue access tool operated at CDS, France, and used the DACE platform developed in the frame of PlanetS (https://dace.unige.ch).

REFERENCES

Aigrain S., Parviainen H., Pope B. J. S., 2016, MNRAS, 459, 2408
Akeson R. L. et al., 2013, PASP, 125, 989
Armstrong D. J. et al., 2015, A&A, 579, A19
Bakos G. Á. et al., 2013, PASP, 125, 154
Bakos G., Noyes R. W., Kovács G., Stanek K. Z., Sasselov D. D., Domsa I., 2004, PASP, 116, 266
Baranec C. et al., 2013, J. Visualized Exp., 72
Baranec C. et al., 2014, ApJ, 790, L8
Bayliss D. et al., 2017a, preprint (arXiv:1706.03858)
Bayliss D. et al., 2017b, AJ, 153, 15
Blanco-Cuaresma S., Soubiran C., Heiter U., Jofré P., 2014, A&A, 569, A111
Blanco-Cuaresma S. et al., 2016, How much can we trust high-resolution spectroscopic stellar atmospheric parameters? Zenodo
Blanco-Cuaresma S. et al., 2017, in Arribas S., Alonso-Herrero A., Figueras F., Hernández-Monteagudo C., Sánchez-Lavega A., Pérez-Hoyos S., eds, Highlights on Spanish Astrophysics IX. p. 334
Borucki W. J. et al., 2010, Science, 327, 977
Brahm R. et al., 2016a, PASP, 128, 124402
Brahm R. et al., 2016b, AJ, 151, 89
Brahm R., Jordán A., Espinoza N., 2017a, PASP, 129, 034002
Brahm R., Jordán A., Hartman J., Bakos G., 2017b, MNRAS, 467, 971
Brown T. M. et al., 2013, PASP, 125, 1031
Demory B.-O., Seager S., 2011, ApJS, 197, 12
Eigmüller P. et al., 2017, AJ, 153, 130
Espinoza N., Jordán A., 2015, MNRAS, 450, 1879
Espinoza N., Jordán A., 2016, MNRAS, 457, 3573
Espinoza N. et al., 2016, ApJ, 830, 43
Gaia Collaboration et al., 2016a, A&A, 595, A1
Gaia Collaboration et al., 2016b, A&A, 595, A2
Giles H., Collier Cameron A., Haywood R., 2017, MNRAS, 472, 1618
Goldreich P., Soter S., 1966, Icarus, 5, 375
Gomez Gonzalez C. A., Absil O., Absil P.-A., Van Droogenbroeck M., Mawet D., Surdej J., 2016, A&A, 589, A54
Gray R. O., Corbally C. J., 1994, AJ, 107, 742
Grunblatt S. K. et al., 2016, AJ, 152, 185
Grziwa S. et al., 2016, AJ, 152, 132
Gustafsson B., Edvardsson B., Eriksson K., Jørgensen U. G., Nordlund Å., Plez B., 2008, A&A, 486, 951
Henden A., Munari U., 2014, Contrib. Astron. Obs. Skalnate Pleso, 43, 518
Hirano T. et al., 2016, ApJ, 825, 53
Howell S. B. et al., 2014, PASP, 126, 398
Huber D. et al., 2016, ApJS, 224, 2
Jenkins J. M. et al., 2010, ApJ, 713, L87
Jensen-Clem R., Duev D. A., Riddle R., Salama M., Baranec C., Law N. M., Kulkarni S. R., Ramprakash A. N., 2017, AJ, 155, 32
Johnson M. C. et al., 2016, AJ, 151, 171
Kipping D. M., 2013a, MNRAS, 434, L51
Kipping D. M., 2013b, MNRAS, 435, 2152
Koch D. G. et al., 2010, ApJ, 713, L79
Kovács G., Zucker S., Mazeh T., 2002, A&A, 391, 369
Kupka F., Dubernet M.-L., VAMDC Collaboration, 2011, Baltic Astron., 20, 503
Kurucz R. L., 1993, VizieR Online Data Catalog, 6039
Lillo-Box J. et al., 2016, A&A, 594, A50
Mainzer A. et al., 2011, ApJ, 731, 53
Mayor M. et al., 2003, The Messenger, 114, 20
Mowlavi N., Eggenberger P., Meynet G., Ekström S., Georgy C., Maeder A., Charbonnel C., Eyer L., 2012, A&A, 541, A41
Pepper J. et al., 2007, PASP, 119, 923
Pollacco D. L. et al., 2006, PASP, 118, 1407
Queloz D. et al., 2000, A&A, 354, 99
Queloz D. et al., 2001, A&A, 379, 279
Santerne A. et al., 2016, ApJ, 824, 55
Seager S., Mallén-Ornelas G., 2003, ApJ, 585, 1038
Skrutskie M. F. et al., 2006, AJ, 131, 1163
Smith A. M. S. et al., 2017, MNRAS, 464, 2708
Vanderburg A., Johnson J. A., 2014, PASP, 126, 948
Wright E. L. et al., 2010, AJ, 140, 1868
Wu Y., 2005, ApJ, 635, 688
Yi S., Demarque P., Kim Y.-C., Lee Y.-W., Ree C. H., Lejeune T., Barnes S., 2001, ApJS, 136, 417

SUPPORTING INFORMATION

Supplementary data are available at *MNRAS* online.

Table 2. Photometry for EPIC 228735255.

Please note: Oxford University Press is not responsible for the content or functionality of any supporting materials supplied by the authors. Any queries (other than missing material) should be directed to the corresponding author for the article.

This paper has been typeset from a TEX/LATEX file prepared by the author.

Chapter 4

Detection & Follow-up of Monotransits

'Reserve your right to think, for even to think wrongly is better than not to think at all.'

Hypatia of Alexandria

Sometimes a search of long-baseline light curves may reveal an apparent single, non-repeating, transit – these events are called *monotransits*. Assuming that the monotransit is not in fact caused by a stellar companion or a freak instrumental error, these probe a new region of observed planet orbits (those with longer periods than ordinarily found via transit detection). Whilst many long period planets have been found via RV and Direct Imaging surveys, long-period planets which transit can mean that in the future, with highly precise instruments, they can be examined much more closely. This is of interest when considering how and why different types of planets form.

4.1 Monotransit Detection

Currently, there are very few confirmed monotransit exoplanets and monotransit candidates (e.g. Osborn et al. 2016; LaCourse & Jacobs 2018; Vanderburg et al. 2018). This is primarily due to them being difficult to detect in the first place – for example, the BLS method (Section 2.1.1) would fail to find them as it relies on folding light curves on trial periods; when the possible

periods for a monotransit roughly range from a small value to infinity, the algorithm would run forever.

However, there are three methods which are used to detect single-transit-events within a light curve:

By Eye Look at individual light curves and inspect them for any transits (e.g. Uehara et al. 2016). This method can be is slow and time consuming, but is relatively accurate. It can be made even more accurate by expanding the pool of people inspecting – this is the power behind citizen science projects like Zooniverse[a] where members of the public help identify and characterise exoplanets (e.g. Fischer et al. 2012; Wang et al. 2013; Schmitt et al. 2014; Wang et al. 2015).

Box-Car Search By taking a series of different sized box-car functions and attempting to fit them to light curves (e.g. Foreman-Mackey et al. 2016; Beichman et al. 2018). A very similar method to BLS, flagging when these fits occur, they can be inspected by eye. However, there can be spurious fits to breaks in data or astrophysical occurrences (e.g. stellar activity).

Machine Learning Instead of one or more people sifting through potentially thousands of light curves looking for transits, it is possible to teach a computer to do it, with self-organising mapping techniques (Armstrong et al. 2017) and neural networks (Osborn et al. 2019).

Multi-Planet Systems One method is to simply find them within multi-planet systems. A standard, multiple-transit planet may have been discovered through BLS or other methods; and within the light curve there can be a single transit of an additional planetary body (e.g. Vanderburg et al. 2015, 2016; Santerne et al. 2018).

Standard transit properties such as ΔF, t_C, t_T can be measured for a monotransit but planetary parameters cannot be determined as these depend on knowing the orbital period. Stellar parameters (such as surface gravity and stellar density) make it possible to model a transit shape and, using classic orbital dynamic relations, determine the likely orbital period. One such modelling tool is `Namaste` from Osborn et al. (2016).

[a] `https://www.zooniverse.org/`

4.2 Monotransit Follow-Up

In the absence of an orbital period, follow-up of such exoplanet candidates is a combination of patience and luck. It depends entirely on the length of the period – follow-up for a Jupiter-like planet in a 100 day orbit is much simpler than follow-up of a Jupiter-like planet in a 10 year orbit.

4.2.1 Photometric Follow-Up

An obvious option is to conduct additional follow-up photometric observations. However this has a couple of different issues with it. First, due to the unknown period, there is a delicate balance between dedicating enough sampling (i.e. observations during a period of time) that a transit can be detected and does not appear and disappear in between points. Whilst this may be possible from the ground (where there are a range of telescopes across the globe, such as NGTS), space-based telescopes are notoriously oversubscribed and it is unlikely that a longterm follow-up project would be successful. Second, if using a ground-based telescope network, no one telescope can continuously observe targets at a high sampling 24 hour a day. Therefore it would be necessary to have a network based around the world which could pick up targets as they are setting for another telescope. But this introduces additional issues of matching different instruments to reduce instrumental effects, and would require significant collaboration. Lastly, the quality of light curves which can be achieved from the ground is limited. As seen in Section 1.7, ground-based telescopes typically find Jupiter-like planets in slightly shorter periods. Finding smaller or more distant exoplanets becomes much more difficult due to Earth's atmospheric noise in the light curves.

4.2.2 Radial Velocity Follow-Up

The next simple solution is to conduct RV follow-up of these candidates. The same rules apply for this as for standard transiting exoplanet candidates, merely that the orbit that must be covered is significantly longer. But, unlike with photometry, it is possible to start to rule out the possibility of the candidate being a stellar companion rather than a planet; by checking the CCFs as discussed in Section 2.2.2. Also, once follow-up has been initiated after RV vetting, a star would quickly have an obvious effect on RV values whereas a planet-like object would have a much smaller RV signal (which becomes smaller as the mass of the planet decreases and the orbital period increases). In fact, for particularly long-period candidates having a 'flat' RV curve can be a positive sign as it indicates the mass of the object must be small and planet-like as opposed to the mass of a small, stellar companion. However, it can still indicate lack of companion at all, and needs to be interpreted carefully.

4.2.3 Astrometric Follow-Up

The space observatory Gaia is measuring the positions, distances and motions of millions of stars in the Milky Way to very high precision (Gaia Collaboration et al. 2016a,b, 2018). This has, and will have, a significant impact on exoplanet science, as we learn more and more about the stars with more accuracy, this feeds into the accuracy of planetary properties too. Gaia will also be highly advantageous for monotransit candidates. By measuring the positions and motions of stars, Gaia becomes the most advanced and most precise instrument for detecting planets with astrometry (Section 1.6.3.2). Large planets in distant orbits may have large enough reflexes upon their star that the Gaia mission can detect the shift in position.

4.3 Transiting planet candidate from *K2* with the longest period

A monotransit was found in the light curve of EPIC 248847494 in the data release for Campaign 14 of *K2*. Using `Namaste` (Osborn et al. 2016) and Gaia- and model-determined stellar properties, the period was estimated to be roughly 10 years – which once confirmed, would make it the longest transiting planet period known. Longterm RV follow-up is currently ongoing. Details of the discovery, vetting and follow-up, as well as other analyses, can found below. Initially known as EPIC 248847494, since summer 2019, this system has been assigned the name K2-311.

A&A 615, L13 (2018)
https://doi.org/10.1051/0004-6361/201833569

Astronomy & Astrophysics

LETTER TO THE EDITOR

Transiting planet candidate from K2 with the longest period

H. A. C. Giles[1], H. P. Osborn[2], S. Blanco-Cuaresma[3], C. Lovis[1], D. Bayliss[4], P. Eggenberger[1], A. Collier Cameron[5], M. H. Kristiansen[6,7], O. Turner[1], F. Bouchy[1], and S. Udry[1]

[1] Observatoire de Genève, Université de Genève, Chemin des Maillettes 51, 1290 Versoix, Switzerland
e-mail: Helen.Giles@unige.ch
[2] Aix Marseille Univ, CNRS, LAM, Laboratoire d'Astrophysique de Marseille, Marseille, France
[3] Harvard-Smithsonian Center for Astrophysics, 60 Garden Street, Cambridge, MA 02138, USA
[4] Department of Physics, University of Warwick, Gibbet Hill Road, Coventry, CV4 7AL, UK
[5] Centre for Exoplanet Science, SUPA, School of Physics and Astronomy, University of St. Andrews, North Haugh, St. Andrews KY16 9SS, UK
[6] DTU Space, National Space Institute, Technical University of Denmark, Elektrovej 327, 2800 Lyngby, Denmark
[7] Brorfelde Observatory, Observator Gyldenkernes Vej 7, 4340 Tølløse, Denmark

Received 5 June 2018 / Accepted 22 June 2018

ABSTRACT

Context. We present the transit and follow-up of a single transit event from Campaign 14 of K2, EPIC248847494b, which has a duration of 54 h and a 0.18% depth.
Aims. Using photometric tools and conducting radial velocity follow-up, we vet and characterise this very strong candidate.
Methods. Owing to the long, unknown period, standard follow-up methods needed to be adapted. The transit was fitted using `Namaste`, and the radial velocity slope was measured and compared to a grid of planet-like orbits with varying masses and periods. These used stellar parameters measured from spectra and the distance as measured by *Gaia*.
Results. Orbiting around a sub-giant star with a radius of $2.70 \pm 0.12\,R_{\rm Sol}$, the planet has a radius of $1.11^{+0.07}_{-0.07}\,R_{\rm Jup}$ and a period of 3650^{+1280}_{-1130} days. The radial velocity measurements constrain the mass to be lower than $13\,M_{\rm Jup}$, which implies a planet-like object.
Conclusions. We have found a planet at 4.5 AU from a single-transit event. After a full radial velocity follow-up campaign, if confirmed, it will be the longest-period transiting planet discovered.

Key words. planets and satellites: detection – stars: individual: EPIC248847494 – planetary systems – techniques: photometric – techniques: radial velocities – techniques: spectroscopic

1. Introduction

Detecting exoplanets via single-transit events (monotransits) will be crucial in the era of short-duration (27-day) campaigns with the Transiting Exoplanet Survey Satellite (TESS), with over 1000 monotransits estimated (Villanueva et al. 2018). To date, several monotransit candidates have been proposed (Osborn et al. 2016, and in prep.; LaCourse & Jacobs 2018; Vanderburg et al. 2018). LaCourse & Jacobs (2018) listed more than 160 candidates and also reported the detection of the monotransit we study here. However, only one monotransit has been confirmed and was reobserved (HIP116454b, Vanderburg et al. 2015). This transit is on a 9.1-day orbit.

We report the discovery of EPIC248847494b, a sub-stellar object on a very long-period orbit that exhibited a single transit in Campaign 14 of K2. In Sect. 2 we outline the observations that lead to and followed the detection. In Sect. 3 we describe the analysis of the data we performed to characterise the system, and the processes we used to eliminate possible causes other than a transit. In Sect. 4 we discuss the implications of this planet-like object, and in Sect. 5 we summarize the discovery.

2. Observations

The source EPIC248847494b was observed in Campaign 14 of the K2 mission with long-cadence (29.4-min) exposures. The campaign began on 1 June 2017 at 05:06:29 UTC and ended on 19 August 2017 at 22:11:02 UTC, lasting 79.7 days.

Following the public release of K2 reduced data on 20 November 2017, the light curves were searched for planetary signals following the same method as described in Giles et al. (2018). This method uses the K2 PDC_SAP-reduced light curves, which we detrended using a moving polynomial, and we removed significant outliers. Then we searched for transits using a box-fitting least-squares algorithm (BLS, Kovács et al. 2002). In addition to regular transit candidates, we detected a single-transit event in the light curve of EPIC248847494 (see Fig. 1). The transit depth is approximately 1.7 mmag, lasting over 53 h. No other transits or unusual systematics were seen in the light curve. From this we conclude that the event is of astrophysical origin.

In order to determine the nature of this very strong candidate, we observed EPIC248847494 with the 1.2 m Euler telescope at the La Silla Observatory in Chile using the CORALIE spectrograph (Queloz et al. 2000). CORALIE is a fibre-fed,

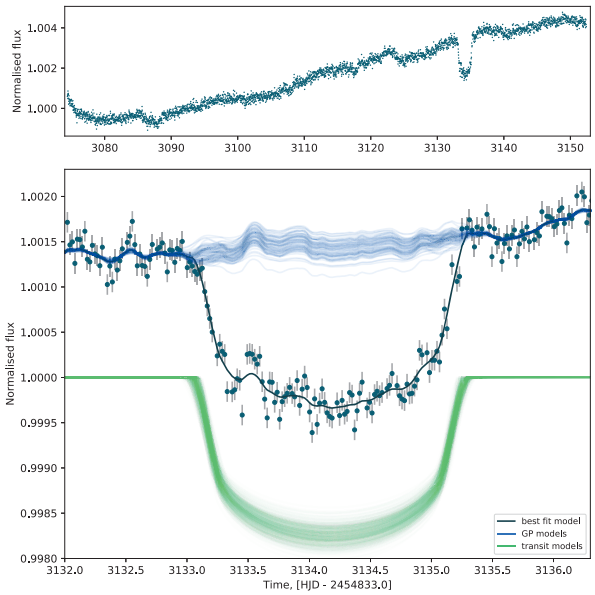

Fig. 1. Transit of EPIC248847494b observed by K2 and `Namaste` models. The *upper panel* shows the full light curve, and the *lower panel* shows a zoom of the transit together with the models. The black line shows the best-fit `Namaste` model. This is composed of the transit model (100 randomly selected models shown in green), and Gaussian process realisations (blue).

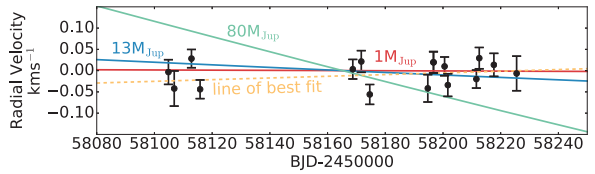

Fig. 2. Radial velocity observations from CORALIE (black points) compared with circular-orbit models of three objects: a Jupiter-mass planet (red), a 13 $M_{\rm Jup}$ brown dwarf (blue), and an 80 $M_{\rm Jup}$ low-mass star (green), assuming a period of 3650 days. The yellow dashed line is the best-fit line (see Sect. 2).

high-resolution ($R = 60\,000$) echelle spectrograph that is capable of high-precision (<6 m s^{-1}) radial velocity measurements (RVs). Fifteen observations were taken between 17 December 2017 and 17 April 2018 (see Table 1), where a 16th point was removed because of significantly high instrumental drift. These points give an RV slope of 0.19 ± 0.16 m s^{-1} day^{-1} (Fig. 2).

To check that RV variations were not due to a blended spectrum, we computed the bisector slope of the cross-correlation function for each observation as described by Queloz et al. (2001), see Table 1. We see no correlation between the bisector slope and radial velocities. We also recomputed this using different stellar masks but found no trends, which suggests that this is not a blended binary (Bouchy et al. 2009).

3. Analysis

3.1. Stellar parameters

To determine the stellar parameters of EPIC248847494, we followed the same method as Giles et al. (2018). A pipeline was built for the CORALIE spectra based on `iSpec`[1] (Blanco-Cuaresma et al. 2014a). All observations were aligned and co-added to increase the signal-to-noise ratio (S/N), were reduced and spectrally fitted using the code SPECTRUM (Gray & Corbally 1994) as the radiative transfer code. Atomic data were obtained from the *Gaia*-ESO Survey line list (Heiter et al. 2015b). We selected the line based on an $R \sim 47\,000$ solar spectrum (Blanco-Cuaresma et al. 2016, 2017), and we used MARCS model atmospheres (Gustafsson et al. 2008). The resulting errors were increased by quadratically adding the dispersions found when analysing the *Gaia* benchmark stars (Heiter et al. 2015a; Jofré et al. 2014; Blanco-Cuaresma et al. 2014b) with the same pipeline. This resulted in an effective temperature of 4877 ± 68 K, a log g of 3.41 ± 0.07 dex, and [Fe/H] = -0.24 ± 0.04 dex.

In the second data release of *Gaia* (Gaia Collaboration 2018), EPIC248847494 has a measured parallax (see Table 2) based on which we can determine an independent stellar radius using bolometric absolute magnitudes and the spectroscopically determined effective temperature for EPIC248847494 following the method detailed in Fulton & Petigura (2018). We took the K-band apparent magnitude (Skrutskie et al. 2006), the *Gaia* distance, and a bolometric correction (BC_K, from Houdashelt et al. 2000) of 1.91 ± 0.05, which was interpolated from the range within the coarse grid. We chose not to include an extinction correction as this only introduces an uncertainty of 0.5% (Fulton & Petigura 2018). This gave a radius of $2.70 \pm 0.12\,R_{\rm sol}$.

Taking the spectrally determined metallicity and effective temperature and the measured radius as observational constraints, we input them into the Geneva stellar evolution code (Eggenberger et al. 2008). This resulted in a stellar mass of $0.9 \pm 0.09\,M_{\rm sol}$. These values of mass and radius would therefore indicate a log g of 3.52 dex. When we fixed the iSpec analysis to this log g, the metallicity and effective temperature were very similar to the initial results (see Table 2). Log g is not well constrained spectroscopically, and changes have a very limited effect on other parameters. Therefore we adopt the parameters based on log g = 3.52.

Table 1. CORALIE radial velocities of EPIC248847494.

BJD-2450000	RV (km s^{-1})	RV Error (km s^{-1})	BIS
8104.845468	29.088	0.029	0.015
8106.856642	29.050	0.041	0.001
8112.830676	29.120	0.022	–0.061
8115.818047	29.048	0.022	–0.020
8168.748372	29.095	0.023	0.000
8171.685229	29.113	0.025	–0.061
8174.628598	29.036	0.023	–0.036
8194.743602	29.050	0.032	–0.034
8196.710862	29.111	0.025	–0.010
8200.554695	29.102	0.022	–0.004
8201.685863	29.058	0.027	–0.001
8211.576046	29.072	0.021	–0.011
8212.572145	29.121	0.025	–0.055
8217.646377	29.105	0.027	–0.037
8225.522768	29.085	0.041	–0.038

[1] http://www.blancocuaresma.com/s/iSpec

Table 2. Properties of the EPIC248847494 system.

Parameter	Units	Value
Stellar parameters		
2MASS		J10373341+1150338[a]
α	Right ascension [hh:mm:ss]	10:37:33.42[a]
δ	Declination [dd:mm:ss]	11:50:33.8[a]
Kep	[mag]	12.17[a]
V	[mag]	12.42[b]
K	[mag]	10.15[c]
g_{Gaia}	[mag]	12.17[d]
μ_α	Proper motion [mas yr^{-1}]	-38.74 ± 0.07[d]
μ_δ	Proper motion [mas yr^{-1}]	1.21 ± 0.06[d]
$\hat{\pi}$	Parallax [mas]	1.78 ± 0.04[d]
d	Distance [parsecs]	560 ± 13[†]
Fe/H	Metallicity [dex]	-0.23 ± 0.04[†]
$T_{\rm eff}$	Effective temperature [K]	4898 ± 68[†]
log(g)	Surface gravity [dex]	3.52 (fixed)[†]
R_*	Radius [$R_{\rm sol}$]	2.70 ± 0.12[†]
M_*	Mass [$M_{\rm sol}$]	0.90 ± 0.09[†]
ρ_*	Density [g cm^{-3}]	0.064 ± 0.007[†]
μ_1	Lin. limb-darkening coeff.	$0.562^{-0.001}_{+0.001}$
μ_2	Quad. limb-darkening coeff.	$0.149^{-0.001}_{+0.001}$
Planet parameters		
$P_{\rm orb}$	Period [days]	3650^{+1280}_{-1130}[†]
v'	Orbital velocity [R_* d^{-1}]	$0.61^{+0.08}_{-0.05}$[†]
$T_{\rm C}$	Transit centre [BJD]	$2457967.17^{+0.01}_{-0.01}$[†]
$T_{\rm D}$	Transit duration [h]	$53.6^{+5.9}_{-5.3}$[†]
$R_{\rm P}/R_*$	Planet-stellar radii ratio	$0.042^{+0.002}_{-0.002}$[†]
a	Semi-major axis [AU]	$4.5^{+1.0}_{-1.0}$[†]
b	Impact parameter	$0.79^{+0.04}_{-0.07}$[†]
i	Inclination [°]	$89.87^{+0.02}_{-0.03}$[†]
$R_{\rm P}$	Planet radius [$R_{\rm Jup}$]	$1.11^{+0.07}_{-0.07}$[†]
$<F>$	Incident flux [ergs s^{-1} cm^{-2}]	$2.6^{+1.7}_{-0.9} \times 10^5$[†]
$T_{\rm eq}$	Equilibrium temperature [K]	183^{+25}_{-18}[†]

Notes. [(a)] Huber et al. (2016), [(b)] APASS: Henden & Munari (2014), [(c)] 2MASS: Skrutskie et al. (2006), [(d)] Gaia Collaboration (2018), [(†)] This Work.

3.2. Eliminating the photometric systematics of K2

The possibility for false positives is high in monotransits. We therefore endeavored to eliminate all causes for false positives. All objects listed as "stars" with K2 light curves within 25 arcmin were checked for similar artefacts. Of the 61 objects, none showed odd behaviour at the same epoch as the monotransit. Additionally, the location of EPIC248847494 was not near the edge of the CCD, which suggests that no near-edge effects occurred. In the target pixel file of EPIC248847494, we checked the pixels for changes and failures before (both the star and background flux), during, and after the transit, but found none. We checked the centroid shifts of EPIC248847494 in the K2 release light curves. Pointing has three clear regimes (times given in BJD-2454833): ~3072–3087 days, which is when K2 settles into position after changing field; ~3087–3124 days, which is when K2 approaches optimum stability position; and ~3124–3153 days, when K2 leaves the optimum stability position. The optimum stability position is the moment when the balance between the remaining reaction wheels of K2 is most stably balanced against the solar radiation pressure (G. Baretsen, priv. comm.). The monotransit is away from this optimum stability position and other shifts in pointing. Furthermore, there is no evidence that the centroid position for the point spread functions (PSFs) or the flux-weighted centre have dramatically changed for any reason. Using the extracted light curve from Vanderburg & Johnson (2014), which is available from MAST[2], we checked the in-transit points along the measured arc caused by the movement of K2. When we inspected the change in flux that is due to arclength, no in-transit points were constrained to a single area, but the points covered the arc uniformly with no evidence for earlier or later points favouring certain arclength positions. No close neighbours are present in the *Gaia* DR2 data (Gaia Collaboration 2018).

3.3. Planet parameters

General transit-fitting methods are often not suitable for the modelling of monotransits, as intrinsic knowledge of the orbit is necessary (e.g. P and R_*/a), therefore a monotransit-specific fitting code (`Namaste`, Osborn et al. 2016)[3] was used to model the HLSP light curve from Vanderburg & Johnson (2014) of EPIC248847494 and explore the planetary characteristics. The code applies the transit models of Mandel & Agol (2002), taking the lateral velocity of the planet (scaled to stellar radius) as a parameter. Other transit parameters required are planet-to-star radius (uniform prior between 0.02 and 0.25), impact parameter (uniform prior between −1.2 and 1.2), transit centre, and limb darkening. Quadratic limb-darkening coefficients were estimated from $T_{\rm eff}$, log g, and metallicity for the *Kepler* bandpass (Sing 2010) and were fixed using a Gaussian prior.

The code `Emcee` (Foreman-Mackey et al. 2016) was used to explore the parameter space of the transit and Gaussian process (GP) models. To model the stellar and photon noise in the light curve, we used the `celerite` Gaussian process package (Foreman-Mackey et al. 2017). We fit two GPs, an exponential kernel for long-timescale trends ($\log a = -7.41 \pm 0.72$, $\log c = -10.9 \pm 0.7$), and a matern-3/2 kernel for short-timescale granulation ($\log \sigma = -10.0^{+0.23}_{-1.3}$, $\log \rho = -2.72^{+0.48}_{-0.38}$), alongside a fixed white-noise term (90 ppm, van Cleve & Caldwell 2009). We also tested the performance of a stellar rotation-like quasi-periodic kernel, an artificially high white-noise term to account for granulation, and fitting rather than fixing the white noise, all of which gave consistent results.

The best fit is a planet with an orbital velocity of $v' = 0.61^{+0.08}_{-0.05}$ R_* d^{-1}, which gives an orbital period of 3650^{+1280}_{-1130} days when converted using

$$\left(\frac{P_{\rm circ}}{\rm d}\right) = 18\,226 \frac{(\rho_\star/\rho_\odot)}{(v'/{\rm d}^{-1})^3}. \quad (1)$$

However, the model fitting revealed strong correlations between $R_{\rm P}/R_*$, b, and v'. This suggests that a slightly smaller planet with high velocity on a low-impact parameter transit fits the data almost as well as the larger R_P/R_* and b but lower v'. Because $R_{\rm P}/R_*$ only varied by a small amount, it did not significantly change the planetary radius.

The `Namaste` fit resulted in a planet-like object with a radius of $1.11 \pm 0.07\,R_{\rm Jup}$, orbiting its host star between 3.5 and

[2] https://archive.stsci.edu/prepds/k2sff/
[3] https://github.com/hposborn/namaste

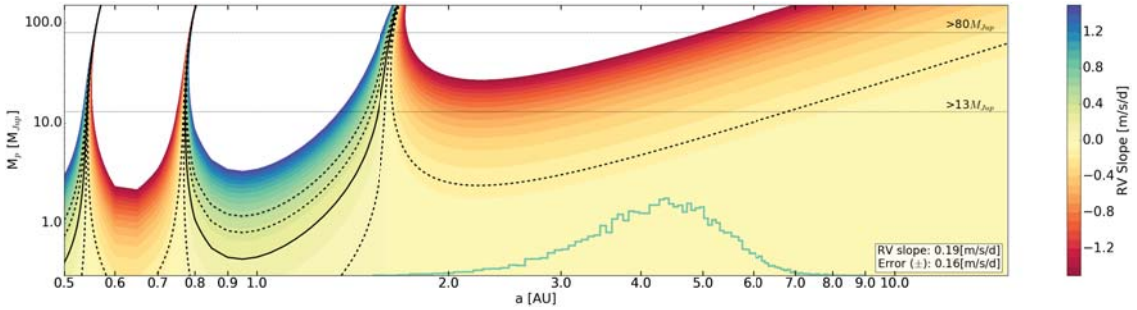

Fig. 3. Grid of semi-major axes and planetary masses and their corresponding RV slopes, using observations from CORALIE. The colour scale ranges −1.5 to 1.5 m s^{-1} day^{-1}, with all else set to white. The slope, with 1 and 2σ errors, of the CORALIE RVs (solid and dashed black lines) shows regions of likely solutions. We also show mass limits for low-mass stars and brown dwarfs (black dashed lines). The `Namaste` fit of the light curve (see Sect. 3) produces a distribution of semi-major axes (green histogram). The peaks in the grid scale at 0.55, 0.75, and 2 AU are due to RV quadrature for these orbits.

5.5 AU. This would indicate the planet has a temperature of approximately 183^{+25}_{-18} K (with the albedo set to 0). For simplicity, we assumed an eccentricity of 0, although we note that any orbital eccentricity would increase the spread on the velocity and therefore the period. For details, we refer to Osborn et al. (2016). We hope to constrain this as we gather more long-term RV data.

Knowing the time of transit means that we are in a unique position for RV follow-up. For all observations, it is possible to calculate the phase given an orbital period or semi-major axis, and an RV value given a planetary mass. Therefore we constructed a grid of semi-major axes, 0.5–15 AU, and planetary masses, 0.3–150 $M_{\rm Jup}$. Based on this, we calculated the orbital period and the semi-amplitude for the system, assuming that the eccentricity is zero. We calculated for each grid point the RVs that would occur at the times for which we have data and determined the RV slope, assuming a linear fit, in m s^{-1} day^{-1}. In Figure 3 we show the measured RV slope and the 1 and 2σ errors that cover the estimated semi-major axis range from `Namaste`. The peaks in the grid scale at 0.55, 0.75, and 2 AU are due to RV quadrature for these orbits. In combination with Fig. 2, it is clear that the RV signal would indicate a mass of 13 $M_{\rm Jup}$ or lower.

We also calculated the minimum RV slope we would expect to see for certain celestial body types in the 4.5 AU orbit from `Namaste`. For a low-mass star (>80 $M_{\rm Jup}$) and a brown dwarf (>13 $M_{\rm Jup}$), we would expect to see 1.88 m s^{-1} day^{-1} and 0.31 m s^{-1} day^{-1}, respectively. Therefore a planet-like object would be required to show a change over ∼120 days of less than ∼36 m s^{-1} (Fig. 2).

4. Discussion

If EPIC248847494b is indeed planetary in nature and confirmed with RVs, it will be the transiting exoplanet with the longest ever discovered period. A final confirmation would require three years of RV follow-up. Currently, there is only one confirmed transiting planet in the NASA Exoplanet Archive[4] (Akeson et al. 2013) with a period longer than 2500 days (our lower limit). With an occurrence rate of ∼4.2% (Cumming et al. 2008) for a planet with mass between 0.3 and 15 $M_{\rm Jup}$ in a 3–6 AU orbit and a transit probability of 0.12%, applied to the entire K2 catalogue (312 269 stars) that is observed for a maximum of 80 days, we would expect to detect about one object.

Based on a comparison with planets within the solar system, EPIC248847494b is similar to our gas giants, which strongly suggests that it possesses moons. The estimated equilibrium temperature of 183^{+25}_{-18} K would indicate that the planet is close to the snow line. Therefore, any moons may well be near the habitable zone, based on the stellar effective temperature and luminosity (Kopparapu et al. 2013, 2014), although it would have been much cooler for most of the main-sequence lifetime of this star.

The minimum observing windows for TESS are 27.4 days (assuming non-consecutive observing windows). This will apply a hard limit of ∼28-day periods for objects to have two or more transits. This has recently been investigated by Villanueva et al. (2018), who estimated that TESS will discover 241 monotransits from the postage stamps and a further 977 from the full-frame images. With the possibility of over 1000 new single-transit candidates, there may be many more EPIC248847494b-type planets to be discovered and characterised.

5. Conclusions

In Campaign 14 of the K2 mission, we detected a monotransit in the light curve of EPIC248847494 and performed follow-up observations. Based on the spectra we obtained as RV measurements, we determined that EPIC248847494b orbits a $2.70 \pm 0.12\,R_{\rm sol}$ star with a mass of $0.9 \pm 0.09\,M_{\rm sol}$, that is, a sub-giant star. EPIC248847494b is the first long-period planet to be vetted using RV, starting from a single monotransit. We estimate the orbital period to be 3650^{+1280}_{-1130} days, the radius to be approximately $1.11 \pm 0.07\,R_{\rm Jup}$, and we derive a lower and upper limit on the mass of 1 and ∼13 $M_{\rm Jup}$, respectively.

This is an excellent candidate for which to attempt detecting exomoons that may well be habitable. This would require extremely precise photometry (e.g. CHEOPS, Broeg et al. 2013, or PLATO, Rauer et al. 2014) for future transit events, however.

Additionally, given the shorter observation campaigns of TESS, the number of monotransit candidates will increase. We have shown that it is possible, given the parameters that can be measured from the transit, to characterise these candidates and potentially push detections to increasingly longer orbital periods.

[4] `exoplanetarchive.ipac.caltech.edu`

Acknowledgements. We would like to thank the referee for their comments and suggestions that were extremely valuable for the development of this Letter. We thank the Swiss National Science Foundation (SNSF) and the Geneva University for their continuous support of our planet search programs. This work has specifically been carried out in the frame of the National Centre for Competence in Research "PlanetS" supported by the Swiss National Science Foundation (SNSF). This paper includes data collected by the *Kepler* mission. Funding for the *Kepler* mission is provided by the NASA Science Mission directorate. HG acknowledges the assistance from L. Temple on measuring stellar radii.

References

Akeson, R. L., Chen, X., Ciardi, D., et al. 2013, PASP, 125, 989
Blanco-Cuaresma, S., Soubiran, C., Heiter, U., & Jofré, P. 2014a, A&A, 569, A111
Blanco-Cuaresma, S., Soubiran, C., Jofré, P., & Heiter, U. 2014b, A&A, 566, A98
Blanco-Cuaresma, S., Nordlander, T., Heiter, U., et al. 2016, in 19th Cambridge Workshop on Cool Stars, Stellar Systems, and the Sun (CS19), 22
Blanco-Cuaresma, S., Nordlander, T., Heiter, U., et al. 2017, in Highlights on Spanish Astrophysics IX, eds. S. Arribas, A. Alonso-Herrero, F. Figueras, et al., 334
Bouchy, F., Moutou, C., Queloz, D., & CoRoT Exoplanet Science Team 2009, in Transiting Planets, eds. F. Pont, D. Sasselov, & M. J. Holman, IAU Symp., 253, 129
Broeg, C., Fortier, A., Ehrenreich, D., et al. 2013, in Eur. Phys. J. Web of Conf., 47, 03005
Cumming, A., Butler, R. P., Marcy, G. W., et al. 2008, PASP, 120, 531
Eggenberger, P., Meynet, G., Maeder, A., et al. 2008, Ap&SS, 316, 43
Foreman-Mackey, D., Morton, T. D., Hogg, D. W., Agol, E., & Schölkopf, B. 2016, AJ, 152, 206
Foreman-Mackey, D., Agol, E., Angus, R., & Ambikasaran, S. 2017, AJ, 154, 220
Fulton, B. J., & Petigura, E. A. 2018, AJ, submitted [arXiv:1805.01453]
Gaia Collaboration (Brown, A. G. A., et al.) 2018, A&A, 616, A1
Giles, H. A. C., Bayliss, D., Espinoza, N., et al. 2018, MNRAS, 475, 1809
Gray, R. O., & Corbally, C. J. 1994, AJ, 107, 742
Gustafsson, B., Edvardsson, B., Eriksson, K., et al. 2008, A&A, 486, 951
Heiter, U., Jofré, P., Gustafsson, B., et al. 2015a, A&A, 582, A49
Heiter, U., Lind, K., Asplund, M., et al. 2015b, Phys. Scr., 90, 054010
Henden, A., & Munari, U. 2014, Contrib. Astron. Obs. S., 43, 518
Houdashelt, M. L., Bell, R. A., & Sweigart, A. V. 2000, AJ, 119, 1448
Huber, D., Bryson, S. T., Haas, M. R., et al. 2016, ApJS, 224, 2
Jofré, P., Heiter, U., Soubiran, C., et al. 2014, A&A, 564, A133
Kopparapu, R. K., Ramirez, R., Kasting, J. F., et al. 2013, ApJ, 765, 131
Kopparapu, R. K., Ramirez, R. M., Schottel Kotte, J., et al. 2014, ApJ, 787, L29
Kovács, G., Zucker, S., & Mazeh, T. 2002, A&A, 391, 369
LaCourse, D. M., & Jacobs, T. L. 2018, Res. Notes Am. Astron. Soc., 2, 28
Mandel, K., & Agol, E. 2002, ApJ, 580, L171
Osborn, H. P., Armstrong, D. J., Brown, D. J. A., et al. 2016, MNRAS, 457, 2273
Queloz, D., Mayor, M., Weber, L., et al. 2000, A&A, 354, 99
Queloz, D., Henry, G. W., Sivan, J. P., et al. 2001, A&A, 379, 279
Rauer, H., Catala, C., Aerts, C., et al. 2014, Exp. Astron., 38, 249
Sing, D. K. 2010, A&A, 510, A21
Skrutskie, M. F., Cutri, R. M., Stiening, R., et al. 2006, AJ, 131, 1163
van Cleve, J. E., & Caldwell, D. A. 2009, Kepler Instrument Handbook, 1st edn., KSCI-19033
Vanderburg, A., & Johnson, J. A. 2014, PASP, 126, 948
Vanderburg, A., Montet, B. T., Johnson, J. A., et al. 2015, ApJ, 800, 59
Vanderburg, A., Mann, A. W., Rizzuto, A., et al. 2018, AJ, 156, 46
Villanueva, Jr., S., Dragomir, D., & Gaudi, B. S. 2018, ArXiv e-prints [arXiv:1805.00956]

Chapter 5

Determining Starspot Lifetimes

'Do not look at stars as bright spots only – try to take in the vastness of the universe.'

Prof. Maria Mitchell

5.1 What are Starspot Lifetimes?

A lot can be observed and determined for Sunspots (see Sections 1.2-1.4.4), primarily because we can resolve the solar surface to relatively high resolution with modern-day instruments. It is also possible to learn some physical properties of starspots such as location, size and lifetimes. The lifetime of a starspot is the length of time which a spot or spot group take to decay (with the primary cause of this due to convection *eating* away at the edges, Simon & Leighton 1964). Lifetimes have been observed and studied rigorously on the Sun, both numerically (Petrovay & Moreno-Insertis 1997; Petrovay & van Driel-Gesztelyi 1997; Litvinenko & Wheatland 2015, 2017) and observationally (Moreno-Insertis & Vazquez 1988; Martinez Pillet et al. 1993; Petrovay & van Driel-Gesztelyi 1997; Petrovay et al. 1999; Hathaway & Choudhary 2008). But for stars other than the Sun, there were only a handful of cases where spot lifetimes had been determined, for example CoRoT-2 (Silva-Valio et al. 2010), CoRoT-6 (Lanza et al. 2011), Kepler-17 (Bonomo & Lanza 2012; Davenport 2015) and GJ 1243 (Davenport et al. 2015). Bradshaw & Hartigan (2014) compare these and a couple other cases with what is known on the Sun and concluded that they behave similarly to what we see on the Sun.

Prior to 2017, there had been no large-scale study of spot lifetimes. But with the *Kepler* mission, this became a possibility. Although *Kepler* was designed for finding planets around other stars (Borucki et al. 2010; Koch et al. 2010) it has revolutionised stellar physics by providing thousands on thousands of near-continuous, high-precision photometry for a variety of stellar types and ages. By having such a large sample of stars, large-scale statistical studies can be performed as opposed to individual case studies. In the case of measuring starspot lifetimes, this was done for over 2000 stars from the *Kepler* field (see Section 5.3, Giles et al. 2017). It has since been revisited by Namekata et al. (2019), whose results agreed well with those of Giles et al. (2017).

5.2 Methodology

5.2.1 Auto-Correlation Functions

To measure the lifetimes of starspots on a large sample of stars, a systematic method was needed – a technique which could be applied to each star without the need for tweaking parameters for each individual star. Such a method was developed for measuring stellar rotation rates of *Kepler* stars, by McQuillan et al. (2013), where they generated auto-correlation functions (ACFs) for each star. An ACF works by offsetting a light curve by a series of discrete time lags and cross-correlated with a non-offset version of the light curve. This generates a power spectrum like that seen in Figure 5.1.

As previously stated, the spot effect on light curves is very sinusoidal, which is why it is possible to measure stellar rotation periods from light curves. But due to spontaneous birth and decay, the phase and exact size of the sinusoid associated with each large spot changes. This means other, popular tools (e.g. Lomb-Scargle periodograms, Lomb 1976; Scargle 1982) for determining stellar rotation periods have always had uncertainties associated with them as there is no single result but a distribution of possible values.

This is the power of using ACFs, as they detect strong similarities between the two light curves without them having to be exactly the same (i.e. a sinusoid with constant amplitude and phase). Therefore, on either side of the central peak of the ACF (see Figure 5.1), there are sidelobes which occur at specific time lags with relatively fixed distances between each: at integer values of the stellar rotation period. After using this robustly, the use of ACFs by McQuillan et al. (2013) was applied to a much bigger sample – thousands of main-sequence stars from *Kepler* (McQuillan et al. 2014). McQuillan et al. (2014) determined the stellar rotation periods of over 34,000 stars.

The relevance of this work to spot lifetimes can be seen directly in an ACF (Figure 5.1). The occurrence of the sidelobes are not the only interesting feature seen – at each reappearance

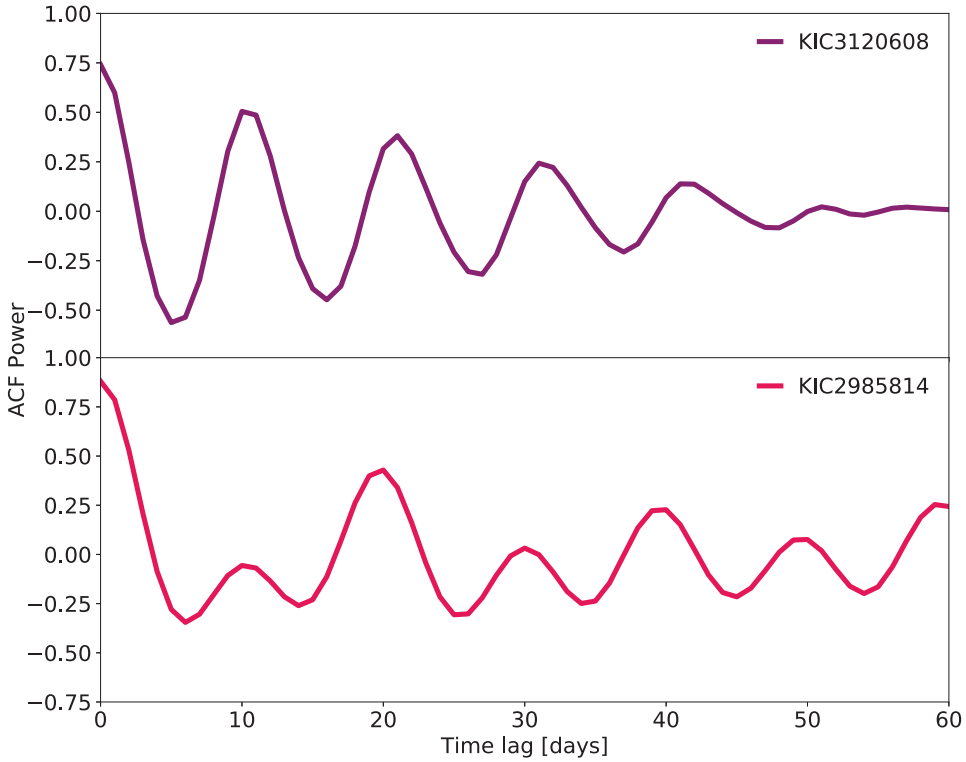

Figure 5.1: Examples of autocorrelation functions (ACFs) for two stars, KIC3120608 and KIC2985814 which were both observed by the *Kepler* mission. An ACF is able to pick up on quasi-periodic behaviour within a time series, such as the stellar rotational signal generated from spots coming in and out of sight on stellar surfaces. The period of the star can be measured as the time lags where peaks appear, and the decay of the spots being tracked can be measured from the decay of those peaks. Additionally, there is also evidence of an *interpulse* where there is a secondary spot half a rotation behind the larger primary spot; the second star, KIC2985814 shows an example of this.

of an integer value of the rotation period, the power has decreased. This decay in the sidelobes appears because the morphology of the spot, or spots, in question have dramatically changed – where the most significant change is the decay of spots (i.e. the lifetime). Therefore, it is possible to measure the lifetime of spots directly from an ACF.

5.2.2 Measuring Starspot Lifetimes

Given that it is possible to see the decay of spots within an ACF, the question is now how to measure that decay (which appears exponential) and determine the spot lifetime for any given star. The simplest method is to attempt to fit the ACF with a function with independent

parameters. The behaviour of an ACF is very similar to that of an underdamped simple harmonic oscillator (uSHO). However, there is one feature of many ACFs which do not match an uSHO. Since an ACF primarily tracks the largest contributing spot on the surface of a star, if there was a smaller spot half a rotation behind the primary spot, it would also contribute to the light curve as a smaller, secondary sinusoid which is also picked up in the ACF as an *interpulse* (example in Figure 5.1). Therefore, the function which was fitted had the same form as the uSHO with an additional term to account for the interpulse (a small amplitude, $2 \times P$ cosine term):

$$y(t) = \exp\left(-t/\tau_{\mathrm{AR}}\right)\left(A\cos\left(\frac{2\pi t}{P}\right) + B\cos\left(\frac{4\pi t}{P}\right) + y_0\right) \tag{5.1}$$

where t is the time lag of the ACF; y is the amplitude of the ACF as a function of t; τ_{AR} is the spot lifetime; P is the stellar rotation period; y_0 is an overall offset term; and A and B are the amplitudes of the central and interpulse peaks.

Equation 5.1 was fitted using a Monte Carlo Markov Chain (MCMC) which essentially 'random walks' its way to the optimal solution. It can be significantly aided by providing reliable priors for the different parameters. Amplitude A was simply set to the ACF power at time lag zero, whilst amplitude B was set to 0 with a non-zero error – therefore if an interpulse was present, it could be fitted, but if not the value for B remained close to zero. The stellar rotation period Gaussian prior was determined with peak finding, and an estimate of τ_{AR} was found by taking the ratio of the central peak and first sidelobe. Similarly to B, y_0 was set to 0 with a non-zero error to allow it to move freely. By fitting with an MCMC, it is also possible to determine an error on each parameter. The MCMC generates a posterior distribution for each of the model parameters, from which a best-fit value (e.g. the mean or median of the distribution) and uncertainty (e.g. 68% interval) can be derived.

5.3 A *Kepler* study of starspot lifetimes with respect to light-curve amplitude and spectral type

The above methods were applied to a sample of 2000+ stars from the results of McQuillan et al. (2014) to measure spot lifetimes and determine if and how those lifetimes depend on spectral type (Giles et al. 2017). Precise details of the methods and results are presented below.

Monthly Notices
of the
ROYAL ASTRONOMICAL SOCIETY

MNRAS **472,** 1618–1627 (2017)
Advance Access publication 2017 August 2

doi:10.1093/mnras/stx1931

A *Kepler* study of starspot lifetimes with respect to light-curve amplitude and spectral type

Helen A. C. Giles,[1,2]★ Andrew Collier Cameron[2] and Raphaëlle D. Haywood[3]†

[1]*Observatoire de Genève, Université de Genève, Chemin des Maillettes 51, Versoix CH-1290, Switzerland*
[2]*Centre for Exoplanet Science, SUPA, School of Physics and Astronomy, University of St Andrews, North Haugh, St Andrews KY16 9SS, UK*
[3]*Harvard–Smithsonian Center for Astrophysics, 60 Garden Street, Cambridge, MA 02138, USA*

Accepted 2017 July 26. Received 2017 July 25; in original form 2017 March 29

ABSTRACT

Wide-field high-precision photometric surveys such as *Kepler* have produced reams of data suitable for investigating stellar magnetic activity of cooler stars. Starspot activity produces quasi-sinusoidal light curves whose phase and amplitude vary as active regions grow and decay over time. Here we investigate, first, whether there is a correlation between the size of starspots – assumed to be related to the amplitude of the sinusoid – and their decay time-scale and, secondly, whether any such correlation depends on the stellar effective temperature. To determine this, we computed the auto-correlation functions of the light curves of samples of stars from *Kepler* and fitted them with apodised periodic functions. The light-curve amplitudes, representing spot size, were measured from the root-mean-squared scatter of the normalized light curves. We used a Monte Carlo Markov Chain to measure the periods and decay time-scales of the light curves. The results show a correlation between the decay time of starspots and their inferred size. The decay time also depends strongly on the temperature of the star. Cooler stars have spots that last much longer, in particular for stars with longer rotational periods. This is consistent with current theories of diffusive mechanisms causing starspot decay. We also find that the Sun is not unusually quiet for its spectral type – stars with solar-type rotation periods and temperatures tend to have (comparatively) smaller starspots than stars with mid-G or later spectral types.

Key words: techniques: photometric – stars: activity – stars: rotation – starspots. .

1 INTRODUCTION

The *Kepler* mission was designed to search for extrasolar planet transits in stars (within a single field of view), in particular small, Earth-like planets around Sun-like stars (Borucki et al. 2010; Jenkins et al. 2010; Koch et al. 2010). It has provided insight into planet formation as well as new exoplanet discovery, which also allowed us to determine occurrence rates (Howard et al. 2012; Petigura, Howard & Marcy 2013; Kane, Kopparapu & Domagal-Goldman 2014; Burke et al. 2015; Dressing & Charbonneau 2015; Santerne et al. 2016) and further probe the statistics of exoplanet population and system architectures.

Kepler has also revolutionized stellar physics. Tens of thousands of stars have 4 years worth of almost continuous, high-precision photometry, allowing for a thorough study of stellar brightness modulations across different stellar ages and types. From *Kepler*, fields such as asteroseismology (Bastien et al. 2013) and differential rotation studies (Reinhold, Reiners & Basri 2013; Aigrain et al. 2015; Balona & Abedigamba 2016) of main-sequence stars have evolved through the study of such a large sample of stars. McQuillan, Aigrain & Mazeh (2013) and McQuillan, Mazeh & Aigrain (2014) (hereafter known as McQ14) made the first large-scale surveys of stellar rotation by analysing the auto-correlation functions (ACF) of stellar light curves.

This unprecedented wealth of high-precision, continuous photometric data for thousands of main-sequence stars has enabled us to take a new look at our own Sun, resulting in comparisons between it and stars which are Sun-like. Gilliland et al. (2011) (and pre-*Kepler*; Radick et al. 1998) found that the Sun appears to be unusually inactive when compared to other solar-type stars, but it has since been suggested that this may in fact not be the case (Basri, Walkowicz & Reiners 2013). This is discussed in Section 4.3.1. In this paper our goal is to discover how Kepler observations can be used to infer the lifetimes of active regions on other stars, and to determine how the lifetime of an active region depends on its size and on the stellar photospheric temperature.

We define stellar activity, and active regions, in this context as meaning phenomena that introduce surface brightness

★ E-mail: helen.giles@unige.ch
† NASA Sagan Fellow.

inhomogeneities, giving rise to apparent flux modulation as the star rotates. Measurements of solar irradiance as a function of wavelength show that bright faculae and dark starspots are the main contributors to solar flux modulation on time-scales of the order of days to weeks (Foukal & Lean 1986). These modulations have a greater amplitude when the Sun is near the maximum of its 11-yr activity cycle. The solar irradiance variations are complex; solar active regions often comprise a bipolar spot group surrounded by an extended facular region of enhanced surface brightness. As an active region crosses the solar disc, the limb brightening of the faculae and foreshortening of the dark spots tend to cause a net initial flux increase. This is followed by a decrease as the spot visibility increases and the facular limb brightening declines (Fligge, Solanki & Unruh 2000). A similar pattern is seen in *Kepler* light curves. At times of high activity, the amplitude of variability is often seen to increase with no obvious change in the mean flux level in the *Kepler* bandpass. Solar irradiance measurements, however, clearly show that the facular flux increase outweighs the dark spot deficit at times of high activity (Lockwood et al. 2007).

For the Sun, a range of activity levels have been observed since telescopic records began (from the Maunder Minimum to large-amplitude cycles in the mid-20th century) and there are many differing opinions on what constitutes 'typical' solar activity levels (Krivova, Balmaceda & Solanki 2007; Livingston et al. 2007; Hanslmeier et al. 2013; Wehrli, Schmutz & Shapiro 2013; Inceoglu et al. 2015; Usoskin et al. 2016). The consensus appears to be that the average level of solar activity lies in between the extremes observed in the past 400 years. For our purpose, we will use the activity levels seen in the last three to four sunspot cycles as typical levels.

Furthering our understanding of stellar activity is not only important to the stellar community but is also crucial to many other areas of investigations, particularly in the exoplanet society. The presence of starspots and other magnetic active regions can induce quasi-periodic variations over time-scales of weeks to months. These activity signatures are seen as major sources of noise in the search for small exoplanets (Earths and super-Earths); spots can lead to wrong planet radius measurements (Barros et al. 2014). The presence of starspots and other magnetically active regions are a real nuisance in radial velocity (RV) exoplanet observations. As well as starspots, faculae and granulation produce signals modulated by the star's rotation. They evolve over time, giving rise to quasi-periodic signals with varying amplitudes and phases. This induces RV variations of 1–2 ms^{-1} even in the quietest stars (Isaacson & Fischer 2010). Stellar noise can conceal and even mimic planetary orbits in RV surveys, and has resulted in many false detections (e.g. CoRoT-7d, Haywood et al. 2014; Alpha Centauri Bb, Rajpaul et al. 2015; HD166435, Queloz et al. 2001; HD99492, Kane et al. 2016; HD200466, Carolo et al. 2014; TW Hydra, Huélamo et al. 2008; HD70573, Soto, Jenkins & Jones 2015; HIP13044, Jones & Jenkins 2014; Kapteyn's Star, Robertson, Roy & Mahadevan 2015; Gliese 667d, Robertson & Mahadevan 2014; and GJ 581d Robertson et al. 2014). It also significantly affects our mass estimates, which are routinely determined from RVs. A number of methods have been developed to account for activity-induced RV signals and have been quantitatively tested to review their performance (Rajpaul et al. 2015; Dumusque 2016; Haywood et al. 2016; Dumusque et al. 2017). Therefore, knowing the active region lifetimes can provide significant constraints for models used to determine exoplanet properties, such as mass (see López-Morales et al. 2016). Additionally, planet radii and masses are central to theoretical models of planet composition and structure (e.g. Zeng & Sasselov 2013) and are essential to interpreting observations of atmospheres (see Winn 2010). When it comes to studying atmospheric transmission spectroscopy of planet atmospheres, un-occulted spots serve to increase the ratio of the area of the planet's silhouette to that of the bright photosphere, making the transit look deeper than it really is. On the other hand, un-occulted faculae have the opposite effect. Since the contrast of both faculae and spots against the quiet photosphere depends on wavelength, particular care has to be taken in the interpretation of the atmospheric transmission spectroscopy (Pont et al. 2007; Oshagh et al. 2016; Chen et al. 2017). As the effects of starspots and suppression of the granular blueshift in faculae are expected to diminish towards longer wavelengths (Marchwinski et al. 2015), forthcoming infrared RV spectrometers such as CARMENES (Quirrenbach et al. 2014) and SPIRou (Delfosse et al. 2013) may help to separate planetary reflex motions from stellar activity signals. However, until recently only optical spectrometers were reaching the precision needed to determine the masses of super-Earth planets but CARMENES has been achieving 2 $m\,s^{-1}$ which is sufficient for measuring super-Earths (Quirrenbach et al. 2016). This would therefore suggest that others will be able to perform similarly, according to their specifications.

Sunspot (and by association, starspot) decay lifetimes have been a point of interest for decades, with many theories for the cause of their decay and what function it follows. Numerical investigations such as those by Petrovay & Moreno-Insertis (1997), Petrovay & van Driel-Gesztelyi (1997), and Litvinenko & Wheatland (2015, 2017) indicate that sunspot decay is consistent with a parabolic decay law, where the area of the spots decreases as a quadratic function of time. Observations of the Sun (Moreno-Insertis & Vazquez 1988; Martinez Pillet, Moreno-Insertis & Vazquez 1993; Petrovay & van Driel-Gesztelyi 1997; Petrovay, Martínez Pillet & van Driel-Gesztelyi 1999; Hathaway & Choudhary 2008) have similarly reflected the same behaviour. This relationship would imply that the main factor in spot decay is granulation, which was first hypothesized by Simon & Leighton (1964). Extrapolating the physics observed to occur on the Sun, only a few attempts have been made to measure starspot decay lifetimes. These studies would allow us to test our theories for sunspot decay on other Sun-like stars. As we cannot resolve the surfaces of others stars directly and at a high resolution like we can for the Sun, their sizes over time have to be inferred from indirect indicators. Bradshaw & Hartigan (2014), Davenport, Hebb & Hawley (2015) and Aigrain et al. (2015) have recovered the decay lifetime of starspots from both real and simulated *Kepler* data. However, there has not been a large-scale survey of starspot decay lifetimes until now.

In this paper, we determine the starspot lifetimes in a large sample of stars selected to have rotation periods close to 10 d and 20 d. Our technique, based on the Monte Carlo Markov Chains (MCMC) parameter estimation, allows us to determine estimates and uncertainties for the stellar rotation period and starspot lifetime of each star. We then investigate how the decay lifetimes relate to extrapolated spot sizes and whether the stellar spectral type has a role in this relationship. In Section 2, we justify the choice of stellar targets. In Section 3 we describe our improvements to the method used in McQ14 and how the representative measurements for spot sizes are determined. In Sections 4 and 5, we outline and discuss our results and the implications they have for stellar physics and exoplanetary discovery and characterization.

2 SAMPLE SELECTION

Our samples are drawn from the sample of stars analysed by McQ14. They analysed over 34 000 main-sequence stars taken from the *Kepler* mission stellar archive at the NASA Exoplanet Archive (Akeson et al. 2013). All of the stars in McQ14 were less than 6500 K

in temperature and excluded known eclipsing binaries (EBs) and *Kepler* Objects of Interest (KOIs). McQ14 utilized $T_{\rm eff} - \log g$ and colour–colour cuts used by Ciardi et al. (2011) to select only main-sequence stars. The boundary of 6500 K was selected by McQ14 to ensure that only stars with convective envelopes, which spin down during their lifetime, were included.

To keep computational time to manageable levels, two samples were drawn from the +34 000 McQ14 stars based on the measured rotation periods. Sample 1 has a range of periods between 9.5 and 10.5 d, and sample 2 with a range of 19.5 to 20.5 d. This resulted in 1089 and 1155 stars in each, respectively. Unlike in McQ14 where they used quarters 3–14 from the Exoplanet Archive, quarters 1 to 17 were used here. This was done to extend the temporal span of the light curves as much as possible.

3 METHODS

3.1 Auto-correlation function

We created ACFs in the same fashion as that of McQuillan et al. (2013, 2014) who cross-correlated each *Kepler* light curve with itself at a series of discrete time shifts (time lags). The correlation increases and decreases depending on the presence of a large dominant starspot. As a light curve can be approximated as sinusoidal in shape (Jeffers & Keller 2009), a time lag at an integer multiple of the stellar rotation period correlates strongly, meaning the first side lobe of an ACF corresponds to the stellar rotation period with further side lobes as harmonics of the period. The decrease in side lobe amplitude at higher time lags occurs as the light curve gradually varies in amplitude and phase due to starspot formation and decay. Therefore, the decay rate of the side lobes describes the decay rate of the starspots. By visual inspection, this appears to be comparable to an exponential decay. With this knowledge, ACFs were fitted with a simple analytical function. This is an improvement on what was reported by McQuillan et al. (2013, 2014) as it not only establishes further parameters of the stellar activity but also determines errors for them.

Many auto-correlation algorithms require the data to be uniformly sampled in time – *Kepler* data are close to uniformity but have variation in exact observation times and have significant data gaps. Therefore, to generate ACFs, the light curves were binned and weighted as described by Edelson & Krolik (1988), which has the added advantage of providing error estimates. Once the ACFs were generated, they were orthogonalized by subtracting the inverse variance-weighted mean, to ensure there were no unwanted correlations between the ACF power and the time lag.

The behaviour of an ACF at zero time lag $\geq$0 d resembles the displacement of an underdamped simple harmonic oscillator (*uSHO*), described by

$$y(t) = \mathrm{e}^{-t/\tau_{\rm AR}} \left(A \cos\left(\frac{2\pi t}{P}\right)\right) + y_0. \quad (1)$$

Many ACFs have an additional 'interpulse' close to half of the stellar rotation period (Fig. 1). This corresponds to there being another large but less dominant starspot on the opposite side of the star. Therefore the *uSHO* equation was adapted to include an inter-pulse term,

$$y(t) = \mathrm{e}^{-t/\tau_{\rm AR}} \left(A \cos\left(\frac{2\pi t}{P}\right) + B \cos\left(\frac{4\pi t}{P}\right) + y_0\right). \quad (2)$$

$\tau_{\rm AR}$ is the decay time-scale [days] of the ACF which represents the decay time-scale of the dominant starspot. P is the stellar rotation period [d^{-1}]. (Parameters A, B and y_0 do not represent physical properties of the star, but are needed to fit the *uSHO* equation.) A and B are the amplitudes of the cosine terms and y_0 is the offset of the *uSHO* from $y = 0$. The stellar rotation period is taken to be the time lag at which the largest side lobe occurs and is found by searching for all peaks in the ACF and establishing which is the highest (besides the peak at time lag = 0 d).

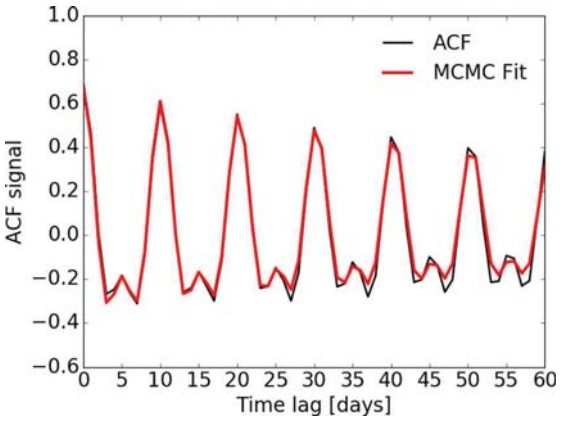

Figure 1. Example of a fitted ACF for *KIC 8869186* using equation (2). Selecting the positive time lag half of an ACF, it follows a similar pattern as a *uSHO*, which has a functional form that can be fitted using MCMC.

Brewer & Stello (2009) used a damped, stochastically driven harmonic oscillator model to emulate the quasi-periodic behaviour of solar p modes. They also computed the ACF of the resulting time series, obtaining an expression equivalent to equation (1). They used this as the kernel for a Gaussian-process regression analysis of the waveform. Because of the N^3 computational overhead involved in Gaussian-process regression, the large number of data points in each light curve and the large number of light curves analysed here, we elected instead to perform the parametric fit to the ACFs, as described by equation (2).

3.2 Monte Carlo Markov Chain

The *uSHO* equation was fitted to ACFs using a MCMC. An MCMC is a means to 'random walk' towards the optimal solution and to sample the joint posterior probability distribution of the fitted parameters. By estimating initial values for the parameters, X_θ, an initial fit of the *uSHO* equation is done and the likelihood, $\mathcal{L}$, measured through

$$\ln \mathcal{L} = -\frac{\chi^2}{2} - \sum_{i=1}^{N} \left(\ln \sigma_{y_i}\right) - \frac{N}{2} \ln(2\pi) \quad (3)$$

where

$$\chi^2 = \sum_{i=1}^{N} \left(\frac{y_i - \mu}{\sigma_{y_i}} \right)^2, \quad (4)$$

where N is the number of ACF points, y_i is the value of the ACF points with the error σ_{y_i}, and μ is the model ACF point value that corresponds to y_i. As the ACFs are often more distorted from the *uSHO* trend at higher time lags, due to interference from new starspots coming into effect, the MCMC only fits up to a time lag equivalent to 2.5 × P.

The parameter values are then perturbed by a small amount to a new position in parameter space and the fit and likelihood

calculations are repeated. If the likelihood is higher than the previous likelihood then the step is accepted and the next step takes place from the current location in parameter space. If the likelihood is worse than previous, it may be accepted under the Metropolis–Hastings algorithm (Metropolis et al. 1953; Hastings 1970), otherwise it will be rejected and the step is not completed and it goes back to the previous step and randomly steps again.

The Metropolis–Hastings algorithm enables occasional steps in the wrong direction to ensure that an MCMC does not become trapped at a local likelihood maximum, and to enable exploration of the entire likelihood landscape. An optimum acceptance rate for an N-dimensional MCMC is approximately 0.25 (Roberts, Gelman & Gilks 1997). Rates much lower or higher than this may struggle to converge. To achieve this, an optimal step size is calculated from the curvature of the χ^2-parameter space for each parameter α,

$$\sigma_{X_i} = \sqrt{\frac{2}{\partial^2\chi^2/\partial^2\alpha^2}}, \tag{5}$$

where the exact step size per MCMC step is a Gaussian distribution using σ_{X_i} and centred on the previous parameter value.

The initial inputs of the parameters for the MCMC are estimated from the ACF or given standard values: period in days, determined as the time lag of the largest side lobe of the ACF, representative of the rotation period; the decay time $\tau_{\rm AR}$ is based on the ratio of the first and second peaks of the ACF,

$$\tau_{\rm AR} = -\frac{P}{\log\left(\frac{y_i(P)}{y_i(0)}\right)}; \tag{6}$$

A is the ACF value at time lag = 0; and B and y_0 are taken to be zero.

As a means to encourage the MCMC to not search for solutions in the unlikely areas of parameter space, Gaussian priors were applied to three of the parameters: amplitude A, P and $\log\tau_{\rm AR}$. For $\tau_{\rm AR}$, having a Gaussian prior in log space reduces the risk of the MCMC wandering to unlikely high values. Also a hard lower limit of 1 d was included for $\log\tau_{\rm AR}$ to prevent a highly improbable $\tau_{\rm AR}$ value.

To determine whether convergence has been achieved, we adopt a likelihood rule as used by Charbonneau et al. (2008) and Knutson et al. (2008). Each calculated likelihood $\mathcal{L}$ was stored and the current likelihood compared to the median of all the previous likelihoods. When $\mathcal{L}$ falls below the median, the MCMC is considered to have achieved convergence. The MCMC then conducts another 5000 steps from which the mean and the standard deviation of each parameter are measured. This then launches a second MCMC routine using the mean and standard deviations as new initial parameters, X_θ, and step sizes ($\pm\sigma_{X_\theta}$). This second MCMC explores the likelihood maximum to find the optimal parameter values. Two final tests for convergence are applied to the final 5000 steps of the second MCMC chain: we calculate the correlation length of this chain (and check that it is less than ∼5 per cent of the total chain) and compute the Gelman–Rubin test (Gelman & Rubin 1992). Only stars that passed both of these tests are considered completed. These stars were then quickly visually inspected to remove any where the fitted functions were obviously wrong. Additionally, a check for correlations of all the fits of the ACFs for the targets was conducted by comparing all the parameter values to one another.

In Figs 2 and 3, it can be seen that there are no strong unexpected correlations. The small correlation between the two amplitude sizes is not concerning as when there is an interpulse present in an ACF

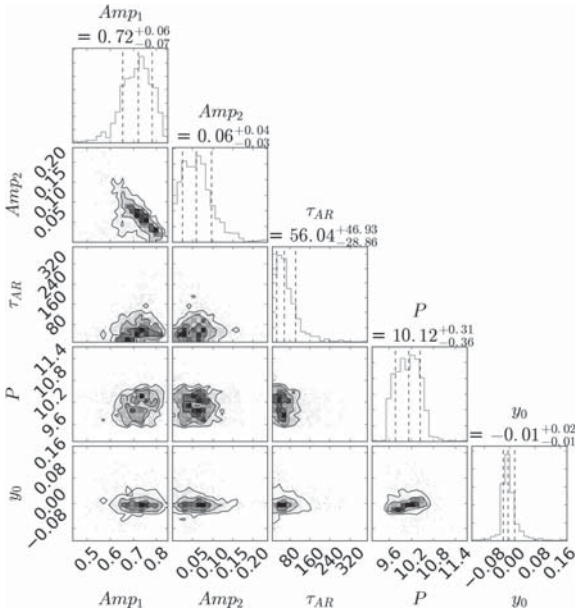

Figure 2. Correlation of all five MCMC parameters for the 10 d period sample. Most show Gaussian distributions apart from those associated with the offset – they indicate that the offset value is dependent on other parameters. There is also a correlation between the two ACF amplitudes, which is not surprising as typically if there was an interpulse present in a target's ACF then the larger the interpulse, the smaller the primary amplitude. Generated using routine from Foreman-Mackey, 2016.

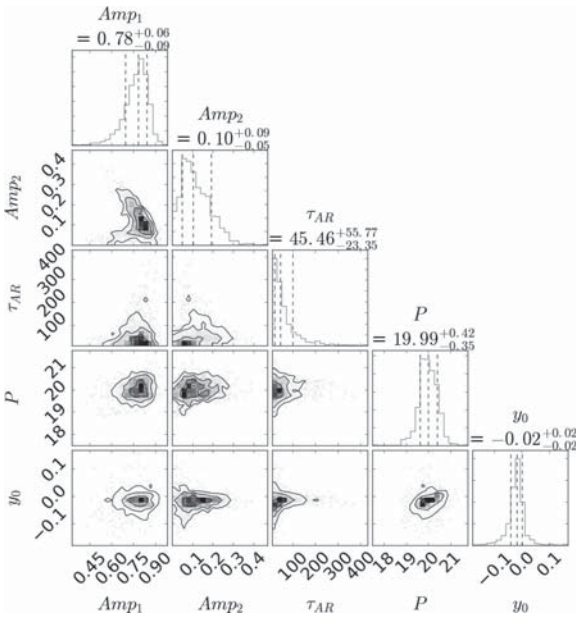

Figure 3. Correlation of MCMC parameters of the 20 d period sample. All have Gaussian distributions apart from the two ACF amplitudes, which typically have smaller primary amplitudes when the interpulse amplitude increases. Generated using routine from Foreman-Mackey, 2016.

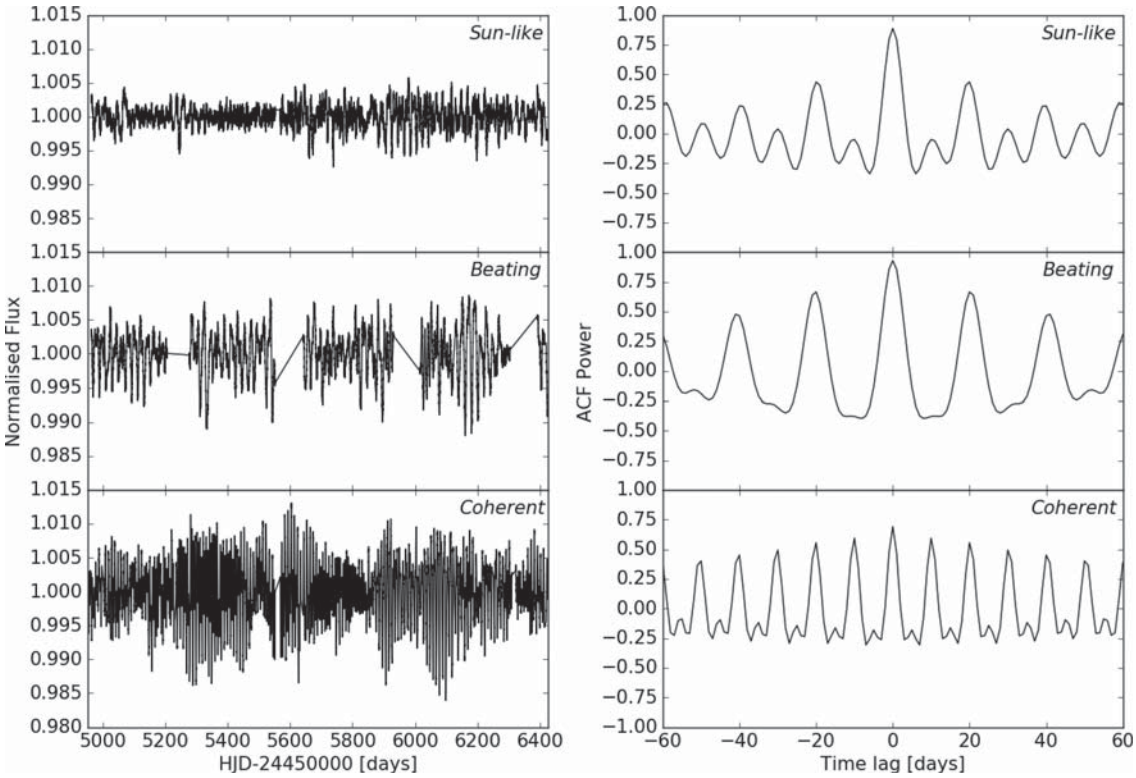

Figure 4. Three example light curves showing the three distinct light-curve morphologies often seen in *Kepler* data, and their ACFs. The Sun-like star, *KIC 2985814*, shows starspots which have a decay lifetime similar to the rotational period. The beating star ('beater'), *KIC 11802642*, has starspots which manage to survive a couple of stellar rotations and presents with a beating effect in the light curve. The long τAR star, *KIC 8869186*, is very coherent and has starspots which last many rotations. All of these decay lifetimes can be quite easily seen in how the peaks decay away in the ACFs. Taking a ratio of the decay lifetime over the rotational period, each morphology can be defined as $\sim$1, $>$1 and $\gg$1 for Sun-like, 'Beaters' and coherent stars, respectively.

this reduces the initial amplitude at zero time lag. Therefore, the larger the interpulse amplitude, the smaller the initial amplitude.

3.3 *Kepler* light-curve morphologies

There are three distinct types of light-curve morphologies (Fig. 4) that can be seen in the bulk of *Kepler* data – 'Sun-like', 'Beater' and 'Coherent'. These are purely qualitative descriptions. On the other hand, inspecting the ACFs, a distinction can be seen. 'Sun-like' stars appear to have starspot decay lifetimes that last approximately a rotational period, 'Beaters' have lifetimes that last a few rotations and the 'Coherent' stars have spots that persist for many rotations. Thereby taking the ratio of the activity starspot lifetime versus rotational period, $\tau_{\rm AR}/P_{\rm rot}$ (AR = Active Region, rot = rotation), we can define the ratio for each light-curve morphology as $\sim$1 for Sun-like stars, $>$1 for 'Beaters' and $\gg$1 for the 'Coherent' stars. It is known from Doppler imaging studies that many very active, fast-rotating stars have large, dark polar spots (Vogt & Penrod 1983; Strassmeier 2009, and references therein). Unless they are perfectly axisymmetric, such large polar features are likely to give rise to quasi-sinusoidal modulation. Since polar spots are generally large, we might expect them to have long lifetimes, producing modulations that would remain coherent for many rotation cycles. At the modest activity levels of most *Kepler* stars, however, such large polar spots are not expected to be widespread.

3.4 Determining the starspot sizes

Whilst it is possible to determine approximate spot sizes for F-, G-, K-stars from Doppler imaging (Collier Cameron 1995; Barnes, James & Collier Cameron 2002), there is currently no direct method to measure them from light curves. However, light curves do have continuous variations – these occur due to asymmetry between two sides of the star. It is worth making the point that the amplitude of solar photometric variability increases with overall activity levels through the magnetic cycle (Krivova et al. 2003). This implies that the power-law distribution of active region sizes is such that the largest individual active regions dominate the modulation. If all active regions were of similar size, an increase in the number of active regions at different longitudes would cause the light-curve modulation amplitude to decrease rather than increase (Bogdan et al. 1988). Therefore, as a proxy, the root-mean-square (rms) scatter of the light curve can be extrapolated to be representative of starspot size.

$$\mathrm{rms} = \sqrt{\frac{1}{N}\sum_{i=1}^{N} y_i^2}, \tag{7}$$

where N is the total number of points in the light curve and y_i the value of the flux at each data point. For a target, the 2σ range of the rms (which encompasses $\sim$95 per cent of points) is calculated, as this encompasses the majority of the sinuous structure of the light

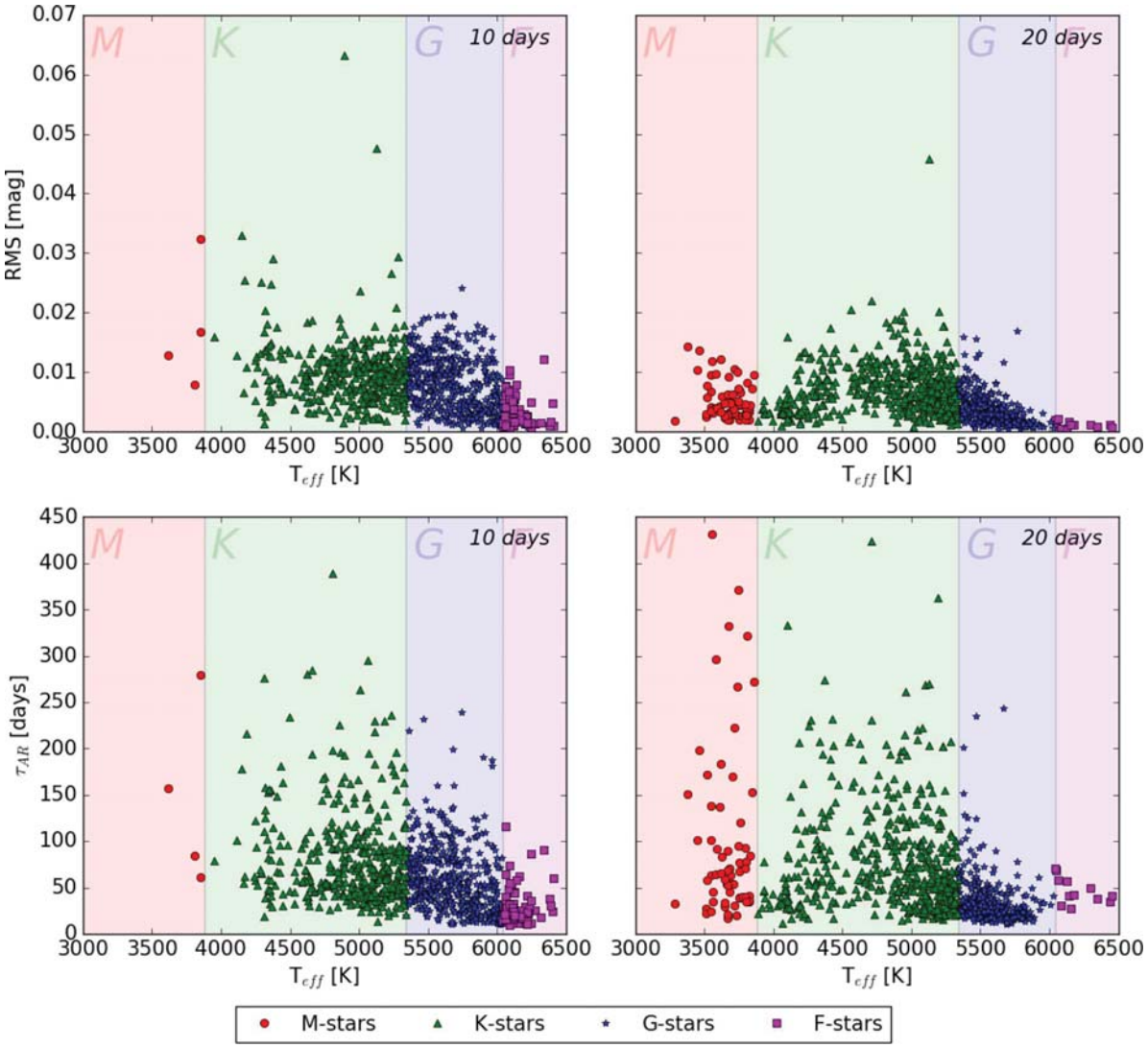

Figure 5. Plot series showing both data sets in two configurations. Upper level: effective temperature of targets (as stated by McQ14) versus the rms of the targets' light curve. Lower level: effective temperature of targets versus the measured decay lifetime. All targets have been split in colour and symbol based on their spectral type (from M- to F-stars) determined from Pecaut & Mamajek (2013). For both data sets, the average spot size (rms) and decay lifetime decrease the hotter the star.

curve but ought not to include the erroneous outliers which may not have all been removed during post-observation processing.

4 RESULTS

Generally, the quality of the fits produced by the MCMC routine was good, though some were poorer and a couple were entirely spurious fits. Therefore, all of the results were also inspected by eye and those with significantly different fits, therefore not representative, were rejected from the sample.

With 1089 stars for the 9.5–10.5 d (i.e. 10 d) period sample and 1154 stars for the 19.5–20.5 d (i.e. 20 d) period sample, the ACF-fitting program returned 913 (83.8 per cent success rate) and 861 (74.6 per cent success rate) acceptable ACF fits for the 10 and 20 d sample, respectively.

In Fig. 5, the targets have been partitioned by spectral type (from M- to F-stars) as determined from Pecaut & Mamajek (2013), and are represented by different colours and symbols which are detailed in the attached key. The first row shows how the rms amplitude of the rotational modulation (proxy for the starspot size for a star) varies with the stellar effective temperature for each of the two samples. The second row displays how the decay lifetime depends on the effective stellar temperature.

4.1 Comparison of rotation periods

In McQ14, the periods were determined using an ACF routine, and these were used during sample selection. Comparing the periods from McQ14 and those generated by the MCMC (Fig. 6), there is some variation with the 10 d sample varying less than the 20 d

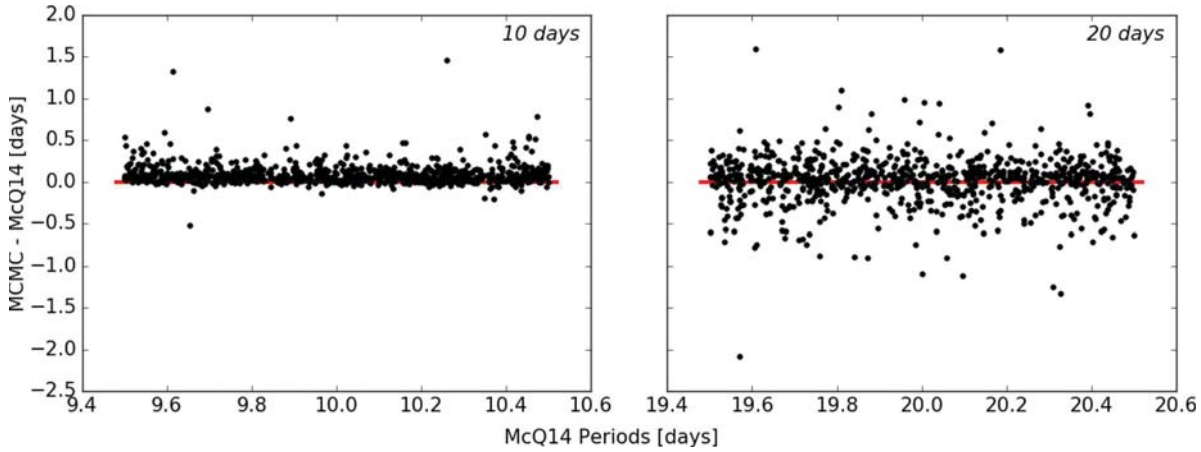

Figure 6. Comparison of the MCMC-measured stellar rotation period and the period determined by McQ14. The red line represents the line where the MCMC-measured period is the same as those from McQ14. For both the 10 d period sample and in particular the 20 d period sample, there is a large range of differences in periods. However, something to note is the difference in ACF generation from McQ14 and that an MCMC was then applied to the different ACF.

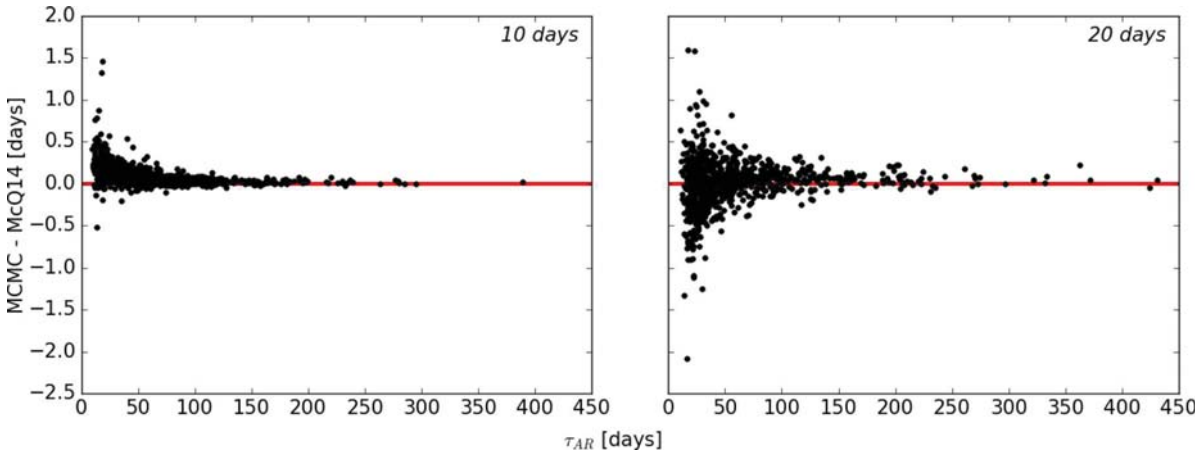

Figure 7. Comparison of the MCMC-measured stellar rotation period and the period determined by McQ14 with respect to τAR. The red line indicates where the MCMC-measured period is the same as McQ14. The 10 d period sample shows an asymmetry in the residuals indicating that for the smaller decay lifetimes $\tau_{\rm AR}$ there is a larger disagreement between the two measured periods. This is most likely due to McQ14 underestimating the true period as they did not consider the decay envelope. In the 20-d sample, short active region lifetimes degrade the precision with which the rotation periods can be determined, leading to a more symmetric distribution in the differences between periods determined with the two methods.

sample. This range will reflect upon the difference in ACF generation as the routines used in McQ14 and this paper are different, meaning variation in stellar rotation periods is to be expected. Further, as a point of interest, the residuals for the 10 d sample are asymmetric, with our algorithm generally finding longer periods than McQ14. Due to not fitting the decay envelope, McQ14 will have underestimated the period, biasing the first sidelobe to a lower time lag. Therefore, the shorter the decay lifetime, the larger a discrepancy seen in Fig. 7. Interestingly, this becomes symmetric for the 20 d sample, but with the same trend that shorter decay lifetimes have larger range.

4.2 10-d period sample

For this sample, in Fig. 5 (left-hand side), there is a distinct distribution of starspot sizes and decay lifetimes. Hotter stars with $T_{\rm eff}$ greater than 6200 K have a smaller range of spot sizes than cooler stars. These stars also have spots which do not survive for very long. At effective temperatures above the ∼6200 K boundary, the limit on decay lifetime is less than 100 d. This is up to a third of starspot lifetimes on much cooler stars.

For ease of viewing, the comparison between spot size and decay lifetime has been split into four observed spectral types in Fig. 8. The coolest stars (M-stars) have a large range of spot size versus decay time-scale but given the very small stellar population this is not representative. However, there are a great many more K-stars and G-stars which show a strong trend of longer decay lifetimes for larger spots. The gradient of the trend is greater for the K-stars, indicating that the hotter the star, the shorter the lifetime. Additionally, the range of the spot sizes associated with the G-stars is less than the K-stars. This limits spots to have no larger effect on the light curve than an rms of 0.025 mag. The F-stars, like the

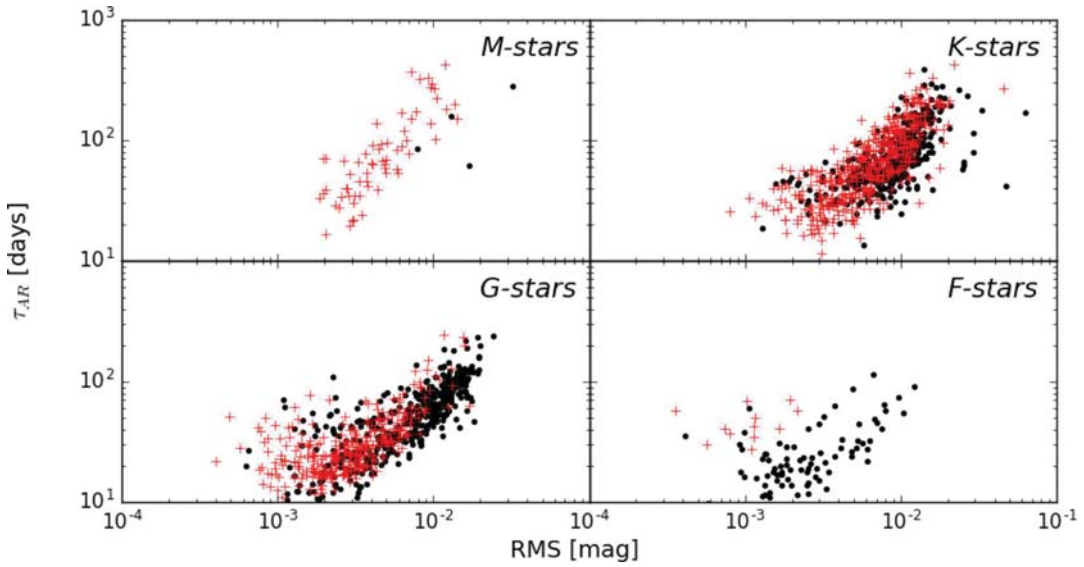

Figure 8. Distribution of decay time-scales and rms of target light curves, split by spectral type (based on temperature boundaries from Pecaut & Mamajek (2013)) for the 10 (•) and 20 (red+) day period sample. There is a slight increase in trend gradient as stellar temperature increases. There is a strong relationship between the day lifetime and rms – the larger the rms of the light curve, the larger the decay lifetime. For the hottest stars, the size of spots possibly appears to be very small, and they often do not survive very long.

M-stars, are not very numerous in this sample. However, they do all cluster together at low decay lifetimes and small spot sizes suggesting that for the hottest of all the targets, spots rarely reach a large size or survive very long. This would also suggest spots survive longer the bigger they are.

4.3 20-d period sample

The 20 d sample is similar to the previous sample with a few small differences (Fig. 5): the temperature above which the range of spot sizes dramatically decreases is at a lower temperature ∼5700 K and spots can survive longer on cooler stars than in the 10 d sample.

As for the 10-d sample, when we partition the stars by spectral type for the relationship between decay lifetime and spot size (Fig. 8), the coolest stars again are not well represented. For the K- and G-stars there is again a positive relationship with increasing decay lifetime and larger spots, with the trend gradient appearing to just be slightly steeper for the K-stars. However, the range of decay lifetimes and spot sizes is much more limited for these G-stars than in the other sample. The F-stars similarly cluster in the lower decay lifetime, smaller spot size area, but have a little more range than the 10-d period sample of F-stars.

4.3.1 Solar comparison

From investigations on stars observed by *Kepler* and previous surveys, there was discussion about the activity of the Sun and whether it was unusually quiet (Radick et al. 1998; Gilliland et al. 2011). Comparing it to the 20 d sample (solar rotation period ∼27 d), stars with Sun-like temperatures (∼5800 K) all have small light-curve amplitudes indicating small spots. The amplitudes of solar variability measured by Krivova et al. (2003) through the solar cycle are very similar to those measured in this work for stars with solar-like rotation periods and effective temperatures. This would (as discussed in Basri et al. 2013) indicate that the Sun is not suspiciously inactive.

4.4 Spot size and distribution

4.4.1 rms as a proxy for spot size

We find that stars with large rms variations indicate spots with longer lifetimes. This could lead to two interpretations: large variations could mean that there are a few big spots dominating with smaller rms variations meaning there are only small spots. But it could theoretically be possible that there are many spots of a similar size. There is good physical reasoning behind the hypothesis that diffusive decay takes longer to destroy big active regions than small ones. If indeed the lifetime is short for stars that have many spots of similar size, short lifetimes would also be associated with small light-curve amplitudes. Implementing Occam's Razor, the simpler explanation is, however, that the solar spot size and spot-lifetime power laws can be extrapolated to other stars, and that the same physical processes operate.

4.4.2 Active-region lifetime as a function of spot size and effective temperature

Using the two data sets together, it is possible to generate a function using the rms (as a spot size proxy) and effective temperature to generate an expected active region lifetime which can be used for an individual star. Orthogonalizing the data by removing the mean value of each distribution and fitting a quadratic through regression to the data in log–log space, the following relation is determined:

$$\log_{10}\tau_{\rm AR} = 10.9252 + 3.0123\log_{10}{\rm rms} + 0.5062\left(\log_{10}{\rm rms}\right)^2 - 1.3606\log_{10}T_{\rm eff}, \quad (8)$$

where *rms* is the root mean square scatter of individual *Kepler* light curves which were normalized to a mean flux of unity, $T_{\rm eff}$ is the stellar effective temperature in K, and $\tau_{\rm AR}$ is the resultant decay lifetime in days. If this is used as an estimate for the mean of a Gaussian prior probability distribution for $\log \tau_{\rm AR}$ then the standard deviation σ of the residuals from the fit should be used as the standard deviation σ of the prior: $\sigma(\log_{10}\tau_{\rm AR}) = 0.178623$.

4.4.3 Active longitudes

When considering active longitudes, evidence from the *Kepler* light curves suggests that even if spots persistently recur at active longitudes, they would tend to preserve the coherence of the light curve on time-scales longer than the lifetimes of an individual active region. We cannot explicitly say whether such an effect is present; however we note that the decay time-scales we obtain from the light curves of the solar-like stars are comparable with the lifetimes of the large solar spot groups.

5 CONCLUSION

The aim of this paper was to determine whether there is a relationship between the sinusoidal amplitude seen in *Kepler* light curves, as a proxy for starspot size, and the decay time-scale of starspots. Furthermore, we sought to determine whether the lifetimes of spots of a given size depend on the stellar effective temperature.

As can be seen within the two samples (9.5–10.5 d and 19.5–20.5 d period stars) drawn from McQ14, there are three main conclusions.

(i) Big starspots live longer on any given star,
(ii) Starspots decay more slowly on cooler stars,
(iii) The Sun is not unusually quiet for its spectral type.

Our observation that big spots generally survive longer on any given star is consistent with models of spot decay in which turbulent diffusion is eating the edges of the spots (Simon & Leighton 1964; Litvinenko & Wheatland 2015, 2017). This is also consistent with our finding that spots generally survive longer on cooler stars. As the vigour of convection is temperature dependent, the turbulent diffusivity, and hence the rate of spot decay, will increase with the convective heat flux and hence with effective temperature. An analogy would be food colouring being dispersed more slowly in cool water than in boiling water.

The work presented in this paper has deepened our knowledge of the connection between the light-curve morphologies of Kepler stars and the physics that determine active region lifetimes in convective stellar photospheres. This in turn can be applied to many areas which rely on light from stars, in particular when searching and analysing exoplanet host candidates.

ACKNOWLEDGEMENTS

We would like to thank our referees for their constructive comments that have improved the quality of this work.

This paper includes data collected by the *Kepler* mission. Funding for the *Kepler* mission is provided by the NASA Science Mission directorate. This research has made use of the NASA Exoplanet Archive, which is operated by the California Institute of Technology, under contract with the National Aeronautics and Space Administration under the Exoplanet Exploration programme.

HACG acknowledges the financial support of the National Centre for Competence in Research 'PlanetS' supported by the Swiss National Science Foundation (SNSF) and the financial support of the University of St Andrews; and the computer support from the University of St Andrews. ACC acknowledges support from STFC consolidated grant number ST/M001296/1. RDH gratefully acknowledges support from STFC studentship grant ST/J500744/1, a grant from the John Templeton Foundation, and NASA XRP grant NNX15AC90G. This work was performed in part under contract with the California Institute of Technology (Caltech)/Jet Propulsion Laboratory (JPL) funded by NASA through the Sagan Fellowship Program executed by the NASA Exoplanet Science Institute. The opinions expressed in this publication are those of the authors and do not necessarily reflect the views of the John Templeton Foundation. Sections of this research was submitted as part of a Masters project for HACG supervised by ACC at the University of St Andrews in 2015 April. HACG gratefully thanks for all supervision from ACC and support from RDH and other members of the astronomy group.

REFERENCES

Aigrain S. et al., 2015, MNRAS, 450, 3211
Akeson R. L. et al., 2013, PASP, 125, 989
Balona L. A., Abedigamba O. P., 2016, MNRAS, 461, 497
Barnes J. R., James D. J., Collier Cameron A., 2002, Astron. Nachr., 323, 333
Barros S. C. C. et al., 2014, A&A, 569, A74
Basri G., Walkowicz L. M., Reiners A., 2013, ApJ, 769, 37
Bastien F. A., Stassun K. G., Basri G., Pepper J., 2013, Nature, 500, 427
Bogdan T. J., Gilman P. A., Lerche I., Howard R., 1988, ApJ, 327, 451
Borucki W. J. et al., 2010, Science, 327, 977
Bradshaw S. J., Hartigan P., 2014, ApJ, 795, 79
Brewer B. J., Stello D., 2009, MNRAS, 395, 2226
Burke C. J. et al., 2015, ApJ, 809, 8
Carolo E. et al., 2014, A&A, 567, A48
Charbonneau D., Knutson H. A., Barman T., Allen L. E., Mayor M., Megeath S. T., Queloz D., Udry S., 2008, ApJ, 686, 1341
Chen G., Guenther E. W., Pallé E., Nortmann L., Nowak G., Kunz S., Parviainen H., Murgas F., 2017, A&A, 600, A138
Ciardi D. R. et al., 2011, AJ, 141, 108
Collier Cameron A., 1995, MNRAS, 275, 534
Daniel Foreman-Mackey, 2016, Scatterplot Matrices in Python. The Journal of Open Source Software 24. doi:10.21105/joss.00024
Davenport J. R. A., Hebb L., Hawley S. L., 2015, ApJ, 806, 212
Delfosse X. et al., 2013, in Cambresy L., Martins F., Nuss E., Palacios A., eds, SF2A-2013: Proceedings of the Annual Meeting of the French Society of Astronomy and Astrophysics. Société Francaise d'Astronomie et d'Astrophysique, p. 497
Dressing C. D., Charbonneau D., 2015, ApJ, 807, 45
Dumusque X., 2016, A&A, 593, A5
Dumusque X. et al., 2017, A&A, 598, A133
Edelson R. A., Krolik J. H., 1988, ApJ, 333, 646
Fligge M., Solanki S. K., Unruh Y. C., 2000, A&A, 353, 380
Foukal P., Lean J., 1986, ApJ, 302, 826
Gelman A., Rubin D. B., 1992, Stat. Sci., 7, 457
Gilliland R. L. et al., 2011, ApJS, 197, 6
Hanslmeier A. et al., 2013, A&A, 550, A6
Hastings W. K., 1970, Biometrika, 57, 97
Hathaway D. H., Choudhary D. P., 2008, Solar Phys., 250, 269
Haywood R. D. et al., 2014, MNRAS, 443, 2517
Haywood R. D. et al., 2016, MNRAS, 457, 3637
Howard A. W. et al., 2012, ApJS, 201, 15
Huélamo N. et al., 2008, A&A, 489, L9
Inceoglu F., Simoniello R., Knudsen M. F., Karoff C., Olsen J., Turck-Chiéze S., Jacobsen B. H., 2015, A&A, 577, A20
Isaacson H., Fischer D., 2010, ApJ, 725, 875

Jeffers S. V., Keller C. U., 2009, in Stempels E., ed., AIP Conf. Ser. Vol. 1094, 15th Cambridge Workshop on Cool Stars, Stellar Systems, and the Sun. Am. Inst. Phys., New York, p. 664
Jenkins J. M. et al., 2010, ApJ, 713, L87
Jones M. I., Jenkins J. S., 2014, A&A, 562, A129
Kane S. R., Kopparapu R. K., Domagal-Goldman S. D., 2014, ApJ, 794, L5
Kane S. R. et al., 2016, ApJ, 820, L5
Knutson H. A., Charbonneau D., Allen L. E., Burrows A., Megeath S. T., 2008, ApJ, 673, 526
Koch D. G. et al., 2010, ApJ, 713, L79
Krivova N. A., Solanki S. K., Fligge M., Unruh Y. C., 2003, A&A, 399, L1
Krivova N. A., Balmaceda L., Solanki S. K., 2007, A&A, 467, 335
Litvinenko Y. E., Wheatland M. S., 2015, ApJ, 800, 130
Litvinenko Y. E., Wheatland M. S., 2017, ApJ, 834, 108
Livingston W., Wallace L., White O. R., Giampapa M. S., 2007, ApJ, 657, 1137
Lockwood G. W., Skiff B. A., Henry G. W., Henry S., Radick R. R., Baliunas S. L., Donahue R. A., Soon W., 2007, ApJS, 171, 260
López-Morales M. et al., 2016, AJ, 152, 204
McQuillan A., Aigrain S., Mazeh T., 2013, MNRAS, 432, 1203
McQuillan A., Mazeh T., Aigrain S., 2014, ApJS, 211, 24 (McQ14)
Marchwinski R. C., Mahadevan S., Robertson P., Ramsey L., Harder J., 2015, ApJ, 798, 63
Martinez Pillet V., Moreno-Insertis F., Vazquez M., 1993, A&A, 274, 521
Metropolis N., Rosenbluth A. W., Rosenbluth M. N., Teller A. H., Teller E., 1953, J. Chem. Phys., 21, 1087
Moreno-Insertis F., Vazquez M., 1988, A&A, 205, 289
Oshagh M., Dreizler S., Santos N. C., Figueira P., Reiners A., 2016, A&A, 593, A25
Pecaut M. J., Mamajek E. E., 2013, ApJS, 208, 9
Petigura E. A., Howard A. W., Marcy G. W., 2013, Proc. Natl Acad. Sci., 110, 19273
Petrovay K., Moreno-Insertis F., 1997, ApJ, 485, 398
Petrovay K., van Driel-Gesztelyi L., 1997, Sol. Phys., 176, 249
Petrovay K., Martínez Pillet V., van Driel-Gesztelyi L., 1999, Sol. Phys., 188, 315
Pont F. et al., 2007, A&A, 476, 1347
Queloz D. et al., 2001, A&A, 379, 279
Quirrenbach A. et al., 2014, Proc. SPIE, 9147, 91471F
Quirrenbach A. et al., 2016, Proc. SPIE, 9908, 990812
Radick R. R., Lockwood G. W., Skiff B. A., Baliunas S. L., 1998, ApJS, 118, 239
Rajpaul V., Aigrain S., Osborne M. A., Reece S., Roberts S., 2015, MNRAS, 452, 2269
Reinhold T., Reiners A., Basri G., 2013, A&A, 560, A4
Roberts G. O., Gelman A., Gilks W. R., 1997, Ann. Appl. Probab., 7, 110
Robertson P., Mahadevan S., 2014, ApJ, 793, L24
Robertson P., Mahadevan S., Endl M., Roy A., 2014, Science, 345, 440
Robertson P., Roy A., Mahadevan S., 2015, ApJ, 805, L22
Santerne A. et al., 2016, A&A, 587, A64
Simon G. W., Leighton R. B., 1964, ApJ, 140, 1120
Soto M. G., Jenkins J. S., Jones M. I., 2015, MNRAS, 451, 3131
Strassmeier K. G., 2009, A&AR, 17, 251
Usoskin I. G., Gallet Y., Lopes F., Kovaltsov G. A., Hulot G., 2016, A&A, 587, A150
Vogt S. S., Penrod G. D., 1983, PASP, 95, 565
Wehrli C., Schmutz W., Shapiro A. I., 2013, A&A, 556, L3
Winn J. N., 2010, Exoplanet Transits and Occultations. Univ. Arizona Press, p. 55
Zeng L., Sasselov D., 2013, PASP, 125, 227

SUPPORTING INFORMATION

Supplementary data are available at *MNRAS* online.

full_results

Please note: Oxford University Press is not responsible for the content or functionality of any supporting materials supplied by the authors. Any queries (other than missing material) should be directed to the corresponding author for the article.

This paper has been typeset from a TEX/LATEX file prepared by the author.

5.3.1 Important Takeaway Messages

From Giles et al. (2017), there are three key takeaway points which stemmed from this being one of the first statistical studies about spot lifetimes.

1) For a given spectral type, large spots have longer lifetimes than smaller spots.
2) For spots of a given size, they have a longer lifetime on cooler stars than hotter ones. This directly connects to the cause of spot decay, as hotter stars will have more vigorous granulation than cooler stars.
3) When compared to other stars similar to the Sun, the Sun shows similar behaviour to its peers. It has been previously suggested that the Sun demonstrated unusually quiet stellar activity, which is not found in Giles et al. (2017).

Additionally, a relationship between the stellar effective temperature, spot size and and spot lifetime was calculated,

$$\log_{10}\tau_{\mathrm{AR}} = 10.9252 + 3.0123\log_{10}\mathrm{rms} + 0.5062\left(\log_{10}\mathrm{rms}\right)^2 - 1.3606\log_{10}T_{eff} \quad (5.2)$$

thereby enabling anyone with a need for an estimate of the spot lifetime for a given star to determine one.

5.4 The Solar Benchmark: Rotational Modulation of the Sun Reconstructed from Archival Sunspot Records

Morris et al. (2019) used the same methodology as in Giles et al. (2017) to attempt to measure sunspot lifetimes using a light curve generated from extrapolating surface flux from archival spot coverage records of the Sun. To measure sunspot lifetimes, the ACF was analysed; however the form of the ACF was slightly different to that used in Giles et al. (2017) as the longer-term stellar activity due to the magnetic cycle introduced an additional trend which combated the uSHO function. Therefore it was not possible to quantitatively determine the lifetimes. Qualitatively, it was possible to establish that the sunspot lifetime from the ACF would be of the order of the rotation period – this would be in agreement with previous observations and publications. Further details of the methods used and additional results from the analysis of the newly-generated solar light curve can be found in Morris et al. (2019).

Monthly Notices
of the
ROYAL ASTRONOMICAL SOCIETY

MNRAS **484,** 3244–3250 (2019)
Advance Access publication 2019 January 18

doi:10.1093/mnras/stz199

The solar benchmark: rotational modulation of the Sun reconstructed from archival sunspot records

Brett M. Morris [1]★ James R. A. Davenport,[1]† Helen A. C. Giles [2] Leslie Hebb,[3] Suzanne L. Hawley,[1] Ruth Angus,[4] Peter A. Gilman[5] and Eric Agol[1]

[1]*Astronomy Department, University of Washington, Seattle, WA 98195, USA*
[2]*Observatoire de Genève, Université de Genève, Chemin des Maillettes 51, CH-1290 Versoix, Switzerland*
[3]*Physics Department, Hobart and William Smith Colleges, Geneva, NY 14456, USA*
[4] *American Museum of Natural History, New York, NY, 10024 USA*
[5]*High Altitude Observatory, National Center for Atmospheric Research, Boulder, CO, 80307-3000 USA*

Accepted 2019 January 15. Received 2019 January 15; in original form 2018 November 27

ABSTRACT

We use archival daily spot coverage measurements from Howard et al. to study the rotational modulation of the Sun as though it were a distant star. A quasi-periodic Gaussian process measures the solar rotation period $P_{\rm rot} = 26.3 \pm 0.1$ d, and activity cycle period $P_{\rm cyc} = 10.7 \pm 0.3$ yr. We attempt to search for evidence of differential rotation in variations of the apparent rotation period throughout the activity cycle and do not detect a clear signal of differential rotation, consistent with the null results of the hare-and-hounds exercise of Aigrain et al. The full reconstructed solar light curve is available online.

Key words: sun: activity – sun: rotation – sunspots – stars: activity.

1 INTRODUCTION

For decades astronomers have endeavoured to study the 'Sun as a star', measuring properties of the Sun that we typically measure on distant stars, with the goal of putting the Sun into context (e.g. Livingston 1991; Tayler 1996; Chaplin et al. 2004; Livingston et al. 2007; Hall et al. 2009; Bertello, Pevtsov & Pietarila 2012; Hall 2015; Egeland et al. 2017). These efforts are valuable, for example, for understanding the Sun's activity through time, by observing Sun-like stars of different ages or at different phases in their activity cycles.

We are entering a new era for the study of rotational modulation of stars. *Kepler* has measured rotational modulation of tens of thousands of stars for four consecutive years, and K2 has measured rotation periods for many more stars, albeit over a shorter baseline. *TESS* will measure precision light curves for bright nearby stars, for a maximum duration of 355 consecutive days near the ecliptic poles in the primary mission (Ricker et al. 2014; Sullivan et al. 2015). *Gaia* will measure rotation periods for $>10^5$ stars (see e.g. Lanzafame et al. 2018). ESA's PLAnetarty Transits and Oscillations (PLATO) mission may observe targets for up to 8 yr (Rauer et al. 2014), potentially allowing us to probe variations in the stellar rotational modulation of stars as a function of phase in their activity cycles. Having a solar benchmark light curve to compare these future, long-term light curves will be an important data product for the community.

Morris et al. (2018) developed tools for measuring the apparent stellar centroid offsets due to starspots that affect *Gaia* astrometry. In particular, a framework was developed for reconstructing archival spot maps of the Sun using the Mount Wilson Observatory (MWO) spot coverage catalogue published in Howard, Gilman & Gilman (1984). The MWO spot catalogue is a digitized representation of 'white light' photographic plate images of the solar disc taken from 1917 to 1985, denoting the apparent positions (latitude and longitude) and areas of penumbrae in sunspot groups. In this work, we use the same software and spot coverage archive as Morris et al. (2018), to reconstruct artificial time-series photometry of the Sun with one day cadence.

In Section 2, we introduce our approximation of the solar rotational light curve, and measure its properties as though it were a distant star. We will then recover several properties of the Sun using the reconstructed light curve. First and foremost we seek to recover the solar rotation period and activity cycle period, which are 25–34 d and 10.9 yr, respectively (Howe et al. 2000; Hathaway 2015).

We also follow the technique of Giles, Collier Cameron & Haywood (2017) to estimate the sunspot lifetimes. High-resolution observations of sunspots show that they have lifetimes ranging from hours to months (Solanki 2003). There is a roughly linear relationship between active region areas and their lifetimes, as described by Gnevyshev (1938) and Waldmeier (1955) (see also, e.g. Petrovay & van Driel-Gesztelyi 1997).

★ E-mail: morrisbrettm@gmail.com
† DIRAC Fellow.

The broad range of possible rotation periods for the Sun is the result of differential rotation – the Sun rotates faster at the equator than at the poles (Miesch 2005). The pursuit to detect differential rotation from photometric rotational modulation of Sun-like stars in *Kepler* light curves has proven very difficult (Aigrain et al. 2015). Setting the perils aside, we will naively attempt to search for differential rotation by its effect on the solar light curve in Section 3.

2 THE SOLAR LIGHT CURVE

2.1 Constructing the light curve

As in Morris et al. (2018), we integrate the total flux of the unspotted, limb-darkened Sun,

$$F_{\odot,\mathrm{unspotted}} = \frac{1}{d^2}\int_0^{R_\star} 2\pi r\, I(r)\,\mathrm{d}r, \tag{1}$$

where $I(r)$ is a quadratic limb-darkening law, d is the distance to the target, and r is in units of angle, so that $2\pi r\mathrm{d}r$ is solid angle.

We define Cartesian sky-plane coordinates (x, y), with the origin placed at the centre of the star, $\hat{x}$ aligned with the stellar equator, and $\hat{y}$ aligned with the stellar rotation axis. We describe each starspot with an ellipse with centroid $\boldsymbol{r}_i = (x_i, y_i)$, and $r_i = |\boldsymbol{r}_i|$. We can compute the negative flux contribution from each spot by computing the approximate spot area and contrast. A circular spot will be foreshortened near the stellar limb. The foreshortened circular spot can be approximated with an ellipse with semimajor axis R_{spot} and semiminor axis $R_{\mathrm{spot}}\sqrt{1-(r_i/\mathrm{R}_\odot)^2}$.

Since these spots are small compared to the solar radius ($R_{\mathrm{spot}}/\mathrm{R}_\odot < 0.1$), we adopt one limb-darkened contrast for the entire spot, $c_{ld} = (1-c)I(r)$, where c is the flux contrast in the spot relative to the photosphere flux.

The integrated spot flux is

$$F_{\mathrm{spot},i} = -\frac{\pi}{d^2}R_{\mathrm{spot}}^2 c_{ld}\sqrt{1-(r_i/\mathrm{R}_\odot)^2}, \tag{2}$$

and accounting for all N spots, the spotted flux of the star is

$$F_{\odot,\mathrm{spotted}} = F_{\odot,\mathrm{unspotted}} + \sum_{i=1}^{N} F_{\mathrm{spot},i}. \tag{3}$$

This approximation is valid for spots that are small compared to the solar radius, or small compared to the scale of limb-darkening variation across the solar disc.

The spot group coverage catalogue of Howard et al. (1984) describes the daily areas and positions of sunspot groups from 1917 to 1985, see Fig. 1. We approximate each spot group as a single circular spot with the area of the entire spot group. We fix the spot contrast in the *Kepler* band at $c = 1 - I_{\mathrm{spot}}/I_{\mathrm{phot}} = 0.7$, which is the mean sunspot intensity averaged over the penumbra and umbra, assuming their typical penumbra covers a factor of 5 more area than the umbra (Solanki 2003).

The reconstructed solar light curve is shown in Figs 2 and 3. This very long-term view of the solar light curve shows periods of high variance separated by relatively quiet times, corresponding to the phase in the activity cycle. During solar maximum, there can be as many as 14 spot groups on the visible hemisphere of the Sun at once, leading to typical dips in flux of order ∼500 ppm. Near solar minimum, the spotless solar surface had no spot groups, and we have filled in those dates with no spot group entries with flux equal to unity.

The full reconstructed solar light curve is available online (Morris 2018).[1]

2.2 Constraining the effects of faculae

The Mount Wilson Observatory sunspot catalogue only tracked the positions and areas of dark sunspots, but did not measure the positions or sizes of faculae, which are small *bright* regions of concentrated magnetic flux. We reconstruct the solar light curve due to facular brightening using the same technique as in the previous section, but this time using faculae positions and areas from the Greenwich Photo-Heliographic Plate archive, digitized in 1999 by the NOAA Environmental Data Rescue Program, which provides facular positions and areas.

Unlike the starspots, we do not choose a fixed contrast for the faculae, since facular intensity varies as a function of position on the Sun. Therefore, we compute a contrast for each facula individually given their position according to

$$\Delta T_{\mathrm{fac}} = 250.9 - 407.7\mu + 190.9\mu^2, \tag{4}$$

where ΔT_{fac} is the temperature excess of the faculae relative to the local photosphere, $\mu = \cos\theta$, and θ is the angle between the stellar surface normal and the observer's line of sight (Meunier, Desort & Lagrange 2010; Dumusque, Boisse & Santos 2014). The contrast of each facula is thus the integrated blackbody flux with the photospheric temperature plus the temperature excess, normalized by the blackbody flux with the temperature of the photosphere (5777 K). We integrate the blackbodies over the *Kepler* bandpass, but the choice of bandpass has little effect on the results (see e.g. fig. 2 of Morris et al. 2018).

The resulting light curve of excess solar flux due to faculae is shown in Fig. 4. Typical brightening in the *Kepler* band due to faculae is small ($\lesssim$20 ppm) compared to the darkening due to sunspots ($\lesssim$200 ppm). Despite their large relative area coverage compared to starspots, the typical facular intensity contrast ($c \sim 1.05$) is relatively small compared with sunspots ($c \sim 0.7$), so we expect spots to dominate the rotational modulation of the Sun in the *Kepler* band, in agreement with Shapiro et al. (2016), for example.

The dominance of sunspots over faculae in the rotational light curve of the Sun is not to be confused with the fact that the Sun is considered 'faculae dominated' on time-scales of the activity cycle. That is, near solar maximum the Sun is bolometrically brighter than it is at solar minimum (Solanki, Krivova & Haigh 2013). What we refer to as the solar light curve in this work is *not* the bolometric flux of the Sun, rather it is the flux integrated over a bandpass like those of *Kepler*, *TESS*, or *Gaia*. As such, we choose to ignore the effects of faculae in the remainder of this work, since spots dominate the rotational modulation, which is our primary focus.

2.3 Measuring the solar rotation and activity cycle periods

An astronomer's first instinct is likely to measure periodicities upon seeing a light curve such as Fig. 2. In this section, we examine the autocorrelation function and Lomb–Scargle (LS) periodogram of the solar light curve to establish benchmark measurements of the rotation and activity cycle periods.

[1] https://doi.org/10.5281/zenodo.1476637

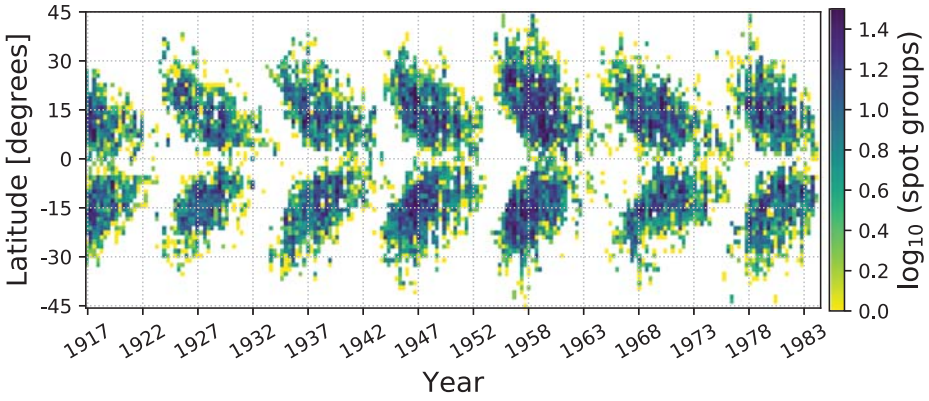

Figure 1. Butterfly diagram (after Maunder 1904) showing spot density as a function of time and solar latitude with the spot archive of Howard et al. (1984).

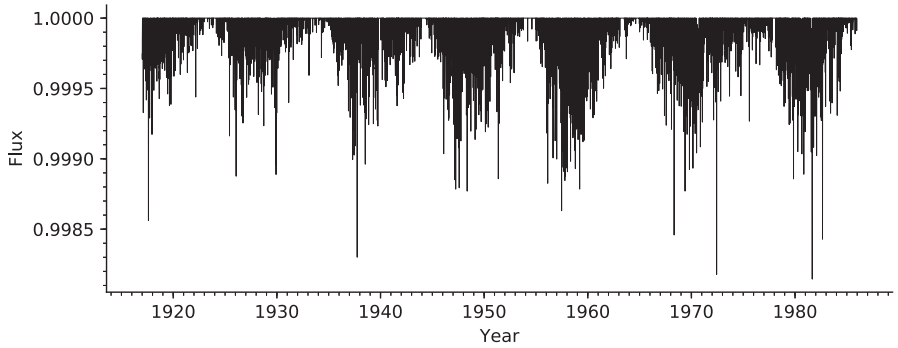

Figure 2. Reconstructed solar light curve from the spot area coverage archive of Howard et al. (1984). The standard deviation of the full light curve is 150 ppm. The mean flux is 80 ppm less than the maximum flux. See Fig. 3 for a close-up view of one cycle and further description.

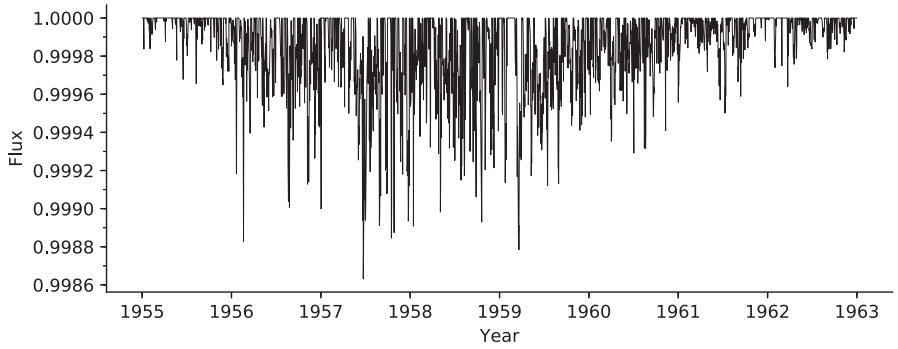

Figure 3. Reconstructed solar light curve zoomed into cycle 19 to show fine structure. This light curve is unlike *Kepler* light curves for several reasons: our reconstruction has no photon noise, no p-mode oscillations, no granulation 'flicker', and no instrumental artefacts. In addition, unlike *Kepler* targets, we know the true unspotted flux of the Sun in these reconstructed light curves (i.e. we know when the Sun was truly spotless), so the light curve has a maximum of unity, rather than a median of unity.

2.3.1 Gaussian process regression

The autocorrelation function of the solar light curve is shown in Fig. 5. There is short-term variation peaking at 26 d – approximately the rotation period of the Sun at the photosphere near the active latitudes (Howe et al. 2000). There is also a long-term decaying cosine-shaped correlation with its first peak at 10.6 yr, corresponding to the magnetic activity cycle period of ∼11 yr (Hathaway 2015). Finally, there is a cosine-shaped correlation with a period of 365 d, corresponding to the orbital period of the Earth. This systematic crops up because the Earth's orbit is inclined with respect to the solar equator by 7.25° (Meeus 1991), causing starspots to drift slightly towards and away from the solar equator throughout each year, injecting a small correlated signal into the reconstructed light curve.

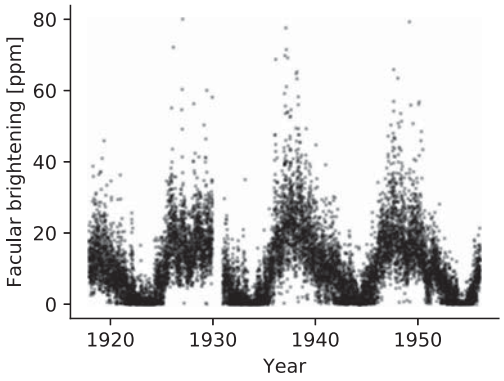

Figure 4. Facular brightening of the Sun from the Greenwich Photo-Heliographic archive spanning three activity cycles. Note that the scale of facular brightening in the *Kepler* band is small ($\lesssim$20 ppm) compared to the darkening due to sunspots ($\lesssim$200 ppm).

For a more rigorous measurement of the solar rotation and activity cycle period (Angus et al. 2018), we model the light curve with a quasi-periodic Gaussian process with a kernel of the form:

$$k(\tau) = a_0 \mathrm{e}^{-c_0\tau} \cos\left(\frac{2\pi\tau}{P_{\rm cyc}}\right) + a_1 \cos\left(\frac{2\pi\tau}{P_{\oplus}}\right) + a_2 \mathrm{e}^{-c_2\tau}\left[\cos\left(\frac{2\pi\tau}{P_{\rm rot}}\right) + 1\right], \quad (5)$$

τ is the difference in times (units of days). The exponential term allows for deviations from a perfectly periodic activity cycle signal with decay time-scale $c_0 > 0$. $P_{\rm rot}$ is the rotation period and $P_{\rm cyc}$ is the activity cycle period. $P_{\oplus}$ is the orbital period of the Earth, which imprints itself on these data because the Earth's inclination with respect to the solar equator gives rise to a periodic systematic shift in the positions of sunspots. We fit for a_0, a_1, a_2, c_0, c_2, $P_{\rm rot}$, $P_{\rm cyc}$ using Markov Chain Monte Carlo via EMCEE with CELERITE (Foreman-Mackey et al. 2013, 2017). We measure $P_{\rm rot} = 26.3 \pm 0.1$ d – see the posterior distributions in Fig. 5. We note that this is consistent with the asteroseismic rotation period of the solar photosphere at $\sim$15° latitude (Howe et al. 2000) – as one would hope, it seems the quasi-periodic Gaussian process properly recovers the rotation period at the active latitudes where the most spots are emerging. Thus, at high enough S/N, a light curve will show the rotation period at the active latitudes, rather than the equatorial rotation period, as has been potentially observed in tidally synchronized binaries (see e.g. Lurie et al. 2017).

We also measure activity cycle period $P_{\rm cyc} = 10.61 \pm 0.23$ yr. This is consistent with canonical cycle period measured by taking the dates of the minima of cycle 1 and cycle 23 and dividing by 22, yielding an average cycle period of 10.9 yr (131.7 months, Hathaway 2015).

2.3.2 Lomb–Scargle periodogram

Next, we use the LS periodogram to compare its ability to pick out the quasi-periodic peak – see Fig. 6. The dominant period is 27 d, just longer than the rotation period measured by Gaussian process regression in the previous section. The difference in rotation periods measured with each technique is an artefact of the intrinsically quasi-periodic nature of the Gaussian process kernel in the previous section, and the strict periodicity enforced by the LS periodogram. In addition, the uncertainty in the periodicity measured with the LS periodogram is not well defined, so it is not possible to do a robust comparison between the LS and Gaussian process period measurements. Turning to longer periods, the activity cycle peak is prominent at 10.6 yr – this result is consistent with the Gaussian process regression measurement.

We prefer the value from the quasi-periodic Gaussian process analysis for the apparent rotation period rather than the LS period because (1) we know from high-resolution observations that there's more than one frequency at play – for example, starspots emerge and decay on time-scales similar to the stellar rotation period and (2) the Gaussian process regression provides us with robust uncertainties on the apparent rotation period. For these reasons, we encourage observers of distant stars to consider using Gaussian process regression over the LS periodogram when searching for the rotation period at the mean active latitudes (VanderPlas 2018).

2.4 Measuring active region evolution time-scales

The autocorrelation function in Fig. 5 has a peak at the rotation period of the star, and smaller peaks at integer multiples of the rotation period with decreasing amplitudes. Giles et al. (2017) developed a technique for measuring active region evolution time-scales by modelling the autocorrelation functions of active stars with a underdamped simple harmonic oscillator (uSHO), which we apply here to the autocorrelation function of the reconstructed solar light curve to estimate active region lifetimes.

We attempt to measure the sunspot lifetimes from the autocorrelation function. However, the form of the autocorrelation function (Fig. 5) is slightly different to those seen in Giles et al. (2017), which typically follow the pattern of a uSHO. In Fig. 5, there is an additional decreasing trend which causes the subsequent peaks to be significantly lower than the central peak, which arises from the much longer time-scale activity cycle pattern. This effect is persistent whether we generate the autocorrelation function for the light curve as a whole, or cut it up into smaller portions and combine the autocorrelation functions.

Although the uSHO fits were unsuccessful, we can still make some qualitative statements from inspection of the autocorrelation function at short lags. The signal of rotation peaking at 26 d has repeated aliases at twice and possibly at three times the rotation period, each with diminished amplitude, before the aliases of the rotation signal appear to decay away at large lags ($\gtrsim 3P_{\rm rot}$). This suggests that the typical spot decay time-scale is similar to the rotation period, and only occasional spots survive more than one or two solar rotations. This observation is in agreement with spatial resolved observations which show that the longest-lived sunspots live of order several rotations (Pettit 1951; Howe et al. 2000), but most only survive for less than one rotation (Petrovay & van Driel-Gesztelyi 1997).

3 DIFFERENTIAL ROTATION

Many efforts have been made to quantify differential rotation in *Kepler* light curves of stars, most notably in Aigrain et al. (2015), where several groups of observers attempted to measure the differential rotation rate in synthetic light curves. The authors found that there was little relation between the injected and recovered differential rotation rates, indicating that *Kepler* detections of solar-like differential rotation ought to be treated with caution.

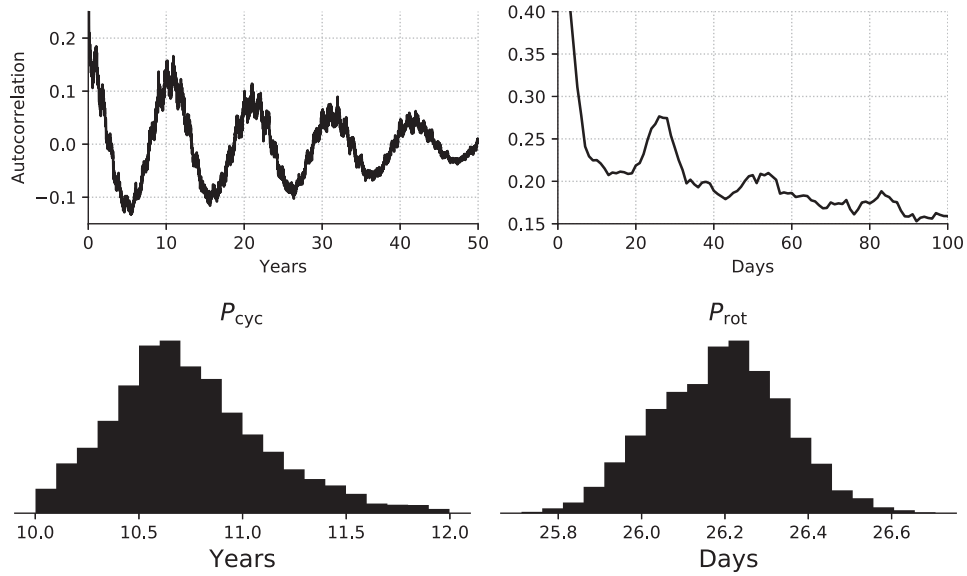

Figure 5. *Upper left*: Long-term autocorrelation function of the solar light curve in Fig. 2. The first peak is ∼10.5 yr. *Upper right*: Short-term signals in the autocorrelation function of the solar light curve, with a peak at 26 d. This estimate of the rotation period is approximately consistent with the rotation period at the active latitudes (Howe et al. 2000). See Section 2.3 for a more robust rotation period measurement using Gaussian process regression with a quasi-periodic kernel. *Lower*: Posterior distributions for the magnetic activity cycle period P_{cyc} and the solar rotation period P_{rot} measured with a quasi-periodic Gaussian process regression to the synthetic photometry from 1917 to 1985 (see Fig. 2). We measure $P_{rot} = 26.32 \pm 0.14$ d and $P_{cyc} = 10.61 \pm 0.23$ yr.

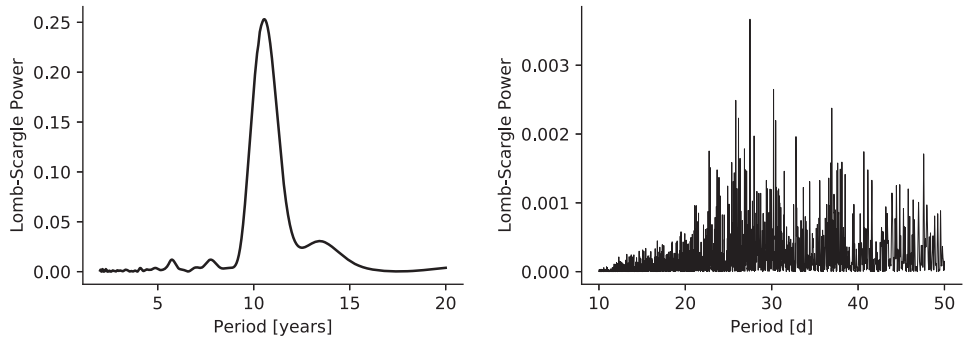

Figure 6. Lomb–Scargle periodogram of the solar light curve in Fig. 2 on long (*left*) and short (*right*) time-scales. Like the autocorrelation function in Fig. 5, the Lomb–Scargle periodogram has a peak at the oft-quoted activity cycle period of 11 yr, and the rotational peak at 27 d.

In this section, we set out to mimic this perilous exercise by measuring the solar rotation period in consecutive one year bins, using the quasi-periodic Gaussian process technique that we used in Section 2.3 to measure the rotation period of the full light curve. We choose one year bins so that there is sufficiently long baseline to get a fit for the period, but the duration is short compared to the activity cycle period (11 yr). If the rotational modulation contains the signature of differential rotation, we expect to find that the apparent rotation period changes slightly from one year to the next, as spots emerge at different latitudes throughout the activity cycle, and due to differential rotation, the spots rotate with slightly different periods.

Ideally, we would observe that at the beginning of each activity cycle, the spots emerge at high latitudes and therefore the apparent rotation period is long. Then as the activity cycle progresses, spots emerge at lower latitudes, revealing shorter rotation periods.

The rotation period recovered from fitting the quasi-periodic Gaussian process to one year bins of the solar light curve is shown in black points in Fig. 7. The red curve shows the rotation period at the mean area-weighted spot latitude averaged into yearly bins, and shows the small differential rotation signal imparted by the activity cycle which we are attempting to measure. In practice, we observe a spread in measured rotation periods much larger than the variance due to the activity cycle, with similarly large uncertainties. Activity minima can be identified in this figure by the large uncertainties on the rotation period, when few spots are present to drive rotational modulation. In between these points of large uncertainties are intervals where the rotation period is measured more precisely,

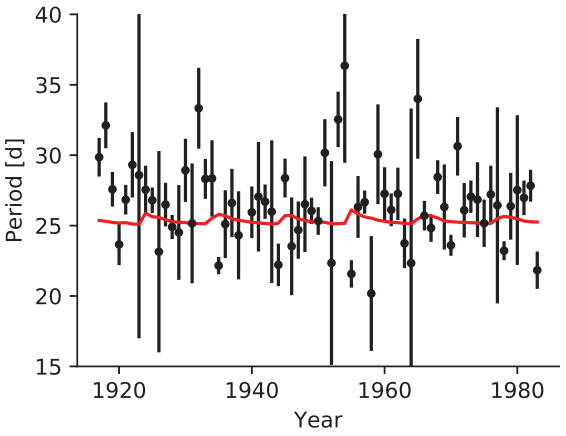

Figure 7. Measured solar rotational period inferred from quasi-periodic Gaussian process regression to 1-yr-long bins of the solar light curve (black circles), compared with the rotation period at the mean area-weighted spot latitude averaged in 1 yr bins (red curve). As spots emerge at different latitudes with differential rotation, we hoped to find that the rotation period varied from year to year with the phase of the activity cycle – with spots emerging at high latitudes and long rotation periods, and the rotation period appearing to decrease as spots emerge closer to the solar equator. It appears that due to spots emerging at a broad range of latitudes at all phases of the activity cycle, the apparent rotation period remains largely constant, irrespective of the activity cycle phase.

though it is roughly consistent with a 26.3 d rotation period throughout all phases of the activity cycle. Assuming the rotation period is 26.3 d throughout, the reduced $\tilde{\chi}^2 = 8$, indicating that the variance is indeed greater than expected for Gaussian-distributed errors. However, the stochastic nature of the measurements makes it impossible to recover the true differential rotation rate from these rotation measurements. Therefore even at 'infinite' signal to noise, we arrive at the same conclusion as Aigrain et al. (2015) – measuring differential rotation shear from rotational modulation alone is a fraught exercise.

4 DISCUSSION

The detection of differential rotation from the solar light curve eludes us in Section 3. One reason for this is made clear by the butterfly diagram in Fig. 1 – the distribution of spots within active latitudes of the Sun are broad; spots are distributed within $\pm 8^\circ$ of the mean 'active latitude' at each phase of the activity cycle. The spots at multiple latitudes each contribute to the rotational modulation with their own rotation period, imprinting the mean rotation period on the light curve, rather than the specific rotation period at a high or low latitude. We are encouraged by recent work by Benomar et al. (2018) which may hold the key to measuring differential rotation from stellar photometry via asteroseismology for at least a small subset of stars.

One limitation of this reconstruction approach is that the Howard et al. (1984) spot archive only catalogued spots within 60° longitude of the central solar meridian, meaning that spots on the limb were not logged. If spots near the limb were included in this time series, the overall flux trends might be smoother, and there would be fewer days with flux equal to unity. However, the net effect on the rotation period and activity cycle measurements is likely small, since spots on the limb are geometrically foreshortened, and due to the Wilson depression, they have smaller contrasts than spots at disc centre (Solanki, Walther & Livingston 1993).

5 CONCLUSION

We reconstructed a one day cadence light curve of the Sun using the sunspot archive of Howard et al. (1984). We compared the amplitude of variability due to dark sunspots to the amplitude of brightening from faculae, and found that the dark sunspots dominate the rotational modulation.

With the noise-free light curve, we measured rotation period and activity cycle period of the Sun with both the LS periodogram and a quasi-periodic Gaussian process regression. The rotation periods and activity cycle periods measured with both techniques are consistent with the rotation period at the active latitudes, and the duration of a typical activity cycle. We showed that differential rotation cannot be detected even from this idealized reconstructed light curve.

ACKNOWLEDGEMENTS

We gratefully acknowledge the following software packages which made this work possible: ASTROPY (Astropy Collaboration 2013; The Astropy Collaboration 2018), IPYTHON (Perez & Granger 2007), NUMPY (Van Der Walt, Colbert & Varoquaux 2011), SCIPY (Jones et al. 2001), MATPLOTLIB (Hunter 2007), CELERITE (Foreman-Mackey et al. 2017), GATSPY (Vanderplas 2015), EMCEE (Foreman-Mackey et al. 2013). Some of this work has been carried out in the frame of the National Centre for Competence in Research 'PlanetS' supported by the Swiss National Science Foundation (SNSF).

JRAD acknowledges support from the DIRAC Institute in the Department of Astronomy at the University of Washington. The DIRAC Institute is supported through generous gifts from the Charles and Lisa Simonyi Fund for Arts and Sciences, and the Washington Research Foundation. This research has made use of NASA's Astrophysics Data System.

REFERENCES

Aigrain S. et al., 2015, MNRAS, 450, 3211
Angus R., Morton T., Aigrain S., Foreman-Mackey D., Rajpaul V., 2018, MNRAS, 474, 2094
Astropy Collaboration, 2013, A&A, 558, A33
The Astropy Collaboration, 2018, ApJ, 156, 123
Benomar O. et al., 2018, Science, 361, 1231
Bertello L., Pevtsov A. A., Pietarila A., 2012, ApJ, 761, 11
Chaplin W. J., Appourchaux T., Elsworth Y., Isaak G. R., Miller B. A., New R., 2004, A&A, 424, 713
Dumusque X., Boisse I., Santos N. C., 2014, ApJ, 796, 132
Egeland R., Soon W., Baliunas S., Hall J. C., Pevtsov A. A., Bertello L., 2017, ApJ, 835, 25
Foreman-Mackey D., Hogg D. W., Lang D., Goodman J., 2013, PASP, 125, 306
Foreman-Mackey D., Agol E., Ambikasaran S., Angus R., 2017, AJ, 154, 220
Giles H. A. C., Collier Cameron A., Haywood R. D., 2017, MNRAS, 472, 1618
Gnevyshev M. N., 1938, Izv. Gl. Astron. Obs. Pulkove, 16, 36
Hall J. C., 2015, in IAU General Assembly, Vol. 29. p. 2256949
Hall J. C., Henry G. W., Lockwood G. W., Skiff B. A., Saar S. H., 2009, AJ, 138, 312
Hathaway D. H., 2015, Living Rev. Solar Phys., 12, 4
Howard R., Gilman P. I., Gilman P. A., 1984, ApJ, 283, 373

Howe R., Christensen-Dalsgaard J., Hill F., Komm R. W., Larsen R. M., Schou J., Thompson M. J., Toomre J., 2000, Science, 287, 2456
Hunter J. D., 2007, Comput. Sci. Eng., 9, 90
Jones E., Oliphant T., Peterson P. et al., 2001, SciPy: Open source scientific tools for Python
Lanzafame A. C. et al., 2018, A&A, 616, A16
Livingston W., 1991, in Tuominen I., Moss D., Rudiger G., eds, Proc. IAU, The Sun and Cool Stars. Activity, Magnetism, Dynamos. Springer-Verlag, Berlin, p. 246
Livingston W., Wallace L., White O. R., Giampapa M. S., 2007, ApJ, 657, 1137
Lurie J. C. et al., 2017, AJ, 154, 250
Maunder E. W., 1904, MNRAS, 64, 747
Meeus J., 1991, Astronomical Algorithms, Richmond, Willmann-Bell
Meunier N., Desort M., Lagrange A. M., 2010, A&A, 512, A39
Miesch M. S., 2005, Living Rev. Solar Phys., 2, 1
Morris B. M., 2018, bmorris3/solarlightcurve v0.1, zenodo
Morris B. M., Agol E., Davenport J. R. A., Hawley S. L., 2018, MNRAS, 476, 5408
Perez F., Granger B. E., 2007, Comput. Sci. Eng., 9, 21
Petrovay K., van Driel-Gesztelyi L., 1997, Sol. Phys., 176, 249
Pettit E., 1951, Astron. Soc. Pac. Leaflet , 6, 146
Rauer H., et al., 2014, Exp. Astron., 38, 249
Ricker G. R. et al., 2014, in Proc. SPIE Conf. Ser. Vol. 9143, Space Telescopes and Instrumentation 2014: Optical, Infrared, and Millimeter Wave. SPIE, Bellingham, p. 914320
Shapiro A. I., Solanki S. K., Krivova N. A., Yeo K. L., Schmutz W. K., 2016, A&A, 589, A46
Solanki S. K., 2003, A&AR, 11, 153
Solanki S. K., Walther U., Livingston W., 1993, A&A, 277, 639
Solanki S. K., Krivova N. A., Haigh J. D., 2013, Annu. Rev. Astron. Astrophys., 51, 311
Sullivan P. W. et al., 2015, ApJ, 809, 77
Tayler R. J., 1996, The Sun as a Star, Cambridge University Press, Cambridge, UK. p. 256
Van Der Walt S., Colbert S. C., Varoquaux G., 2011, preprint (arXiv:e-prints)
Vanderplas J., 2015, gatspy: General tools for Astronomical Time Series in Python, zenodo
VanderPlas J. T., 2018, ApJS, 236, 16
Waldmeier M., 1955, Ergebnisse und Probleme der Sonnenforschung , Leipzig, Geest & Portig

This paper has been typeset from a TEX/LATEX file prepared by the author.

Chapter 6

Use of Starspot Lifetimes in Exoplanet Follow-Up

> 'While we cannot maintain that in everything woman is man's equal, yet in many things her patience, perseverance, and method make her his superior.'
>
> *Williamina Fleming*

Whilst knowing starspot lifetimes is of interest to stellar physicists, it can also be of use for those who search for exoplanets.

6.1 Starspot Lifetimes & Gaussian Processes

As mentioned previously (Section 1.6.1.1), spots have a significant effect on the RV measurements used for measuring exoplanet masses. One method for combating their effect is to fit for the spot signal using Gaussian Processes (GPs). A GP is a method which uses a correlated noise model to describe the correlation between all the data points, all contained within a covariance kernel. It is a non-parametric, Bayesian approach to fitting data. Instead of deciding how a certain model or function works and what measurements are required to obtain this, a GP starts with the data and uses it to test a theory. And since the model is non-parametric, the observations determine the behaviour of the model or function. The only input is deciding

how the data might be correlated. For the details on how GPs work, please see Haywood et al. (2014); Haywood (2015); Rajpaul et al. (2015); Faria et al. (2016).

Spot lifetimes play a useful role in the efficient use of GPs. GPs use covariance kernels to fit for correlated behaviour in a series, with the most common kernel, the quasi-periodic kernal, having the form

$$k(t,t') = \theta_1^2 \exp\left[-\frac{(t-t')^2}{2\theta_2^2} - \frac{2\sin^2\left(\frac{\pi(t-t')}{\theta_3}\right)}{\theta_4^2}\right] \tag{6.1}$$

where θ_1 is the amplitude of correlated noise; θ_2 is the lifetime of features which induce activity variations in RVs; θ_3 is a periodic signal; and θ_4 is the level of high-frequency structure in the GP model. Out of these hyperparameters for the quasi-periodic covariance kernel, there are two which can be reliably estimated prior to using the kernel: θ_2 and θ_3. The physical quantities they relate to are the spot lifetimes and stellar rotation period, which can both be found from an ACF of a light curve. Taking these and using them as priors for GP regression, it will give a more physically-motivated solution and spend less time investigating other possibilities which have values for the hyperparameters which are significantly different from the suggested prior.

6.1.1 Sampling of Radial Velocity Measurements

Whilst GPs are designed to infer the behaviour of stellar activity during gaps in RV observations, for them to work most effectively, there needs to be an observational strategy in place to ensure the sampling is adequate enough to cover the different aspects at play within RV observations.

There are three key signals which exist: (1) the quasi-periodic variation due to stellar rotation, (2) periodic variation – i.e. a planetary signal – and (3) the decay of spots. Given that all three need to be modelled, the effects of all three need to be well sampled. Often, a lot of focus is applied to sampling well the orbit of the planet in question, with a secondary goal of sampling well the stellar rotation. However, if the observing strategy was intensive sampling with a baseline only covering one or two stellar rotations (assuming $P_{orb}<P_{rot}$) then the GP will struggle to settle on the true spot lifetime. Therefore, when performing RV surveys or RV follow-up, it is vital to ensure the baseline of observations covers approximately an entire spot lifetime (which can be estimated from a light curve).

6.2 Starspot Lifetimes Used in Transiting Exoplanet RV Follow-Up

Starspot lifetimes have been used several times for constraining GP regression, either via the methods described in Giles et al. (2017) or by using the formula calculated (Equation 5.2).

Below are two cases where the ACF of the light curve was fitted to determine the stellar rotation period and spot lifetime.

6.2.1 Kepler-21b: A Rocky Planet Around a V = 8.25 Magnitude Star

A bright star observed by *Kepler*, Kepler-21 was found to host a $1.6R_{\oplus}$ planet in a 2.78-day orbit by Howell et al. (2012). However they were only able to impose an upper limit on the mass, at $10M_{\oplus}$. López-Morales et al. (2016) were able to constrain the mass by obtaining a further 82 RV observations with HARPS-N and, in conjunction with the pre-existing 14 RV observations from HIRES, use GP regression to obtain a mass of $5.1M_{\oplus}$. For the GP regression, an ACF was generated from the *Kepler* light curve to determine the spot lifetimes and stellar rotation periods. More details of the method and results can be found in López-Morales et al. (2016) whose first page is included below.

The Astronomical Journal, 152:204 (16pp), 2016 December doi:10.3847/0004-6256/152/6/204

KEPLER-21b: A ROCKY PLANET AROUND A $V = 8.25$ mag STAR*

Mercedes López-Morales[1], Raphaëlle D. Haywood[1], Jeffrey L. Coughlin[2], Li Zeng[3], Lars A. Buchhave[4], Helen A. C. Giles[5], Laura Affer[6], Aldo S. Bonomo[7], David Charbonneau[1], Andrew Collier Cameron[8], Rosario Consentino[9], Courtney D. Dressing[10,19], Xavier Dumusque[5], Pedro Figueira[11], Aldo F. M. Fiorenzano[9], Avet Harutyunyan[9], John Asher Johnson[1], David W. Latham[1], Eric D. Lopez[12], Christophe Lovis[5], Luca Malavolta[13,14], Michel Mayor[5], Giusi Micela[6], Emilio Molinari[9,15], Annelies Mortier[8], Fatemeh Motalebi[5], Valerio Nascimbeni[13], Francesco Pepe[5], David F. Phillips[1], Giampaolo Piotto[13,14], Don Pollacco[16], Didier Queloz[5,17], Ken Rice[12], Dimitar Sasselov[1], Damien Segransan[5], Alessandro Sozzetti[7], Stephane Udry[5], Andrew Vanderburg[1], and Chris Watson[18]

[1] Harvard-Smithsonian Center for Astrophysics, 60 Garden Street, Cambridge, MA 01238, USA; mlopez-morales@cfa.harvard.edu
[2] SETI Institute, 189 Bernardo Avenue Suite 200, Mountain View, CA 94043, USA
[3] Department of Earth and Planetary Sciences, Harvard University, 20 Oxford Street, Cambridge, MA 01238, USA
[4] Centre for Star and Planet Formation, Natural History Museum of Denmark & Niels Bohr Institute, University of Copenhagen, DK-1350 Copenhagen, Denmark
[5] Observatoire Astronomique de l'Université de Genéve, Chemin des Maillettes 51, Sauverny, CH-1290, Switzerland
[6] INAF—Osservatorio Astronomico di Palermo, Piazza del Parlamento 1, I-90124 Palermo, Italy
[7] INAF—Osservatorio Astrofisico di Torino, via Osservatorio 20, I-10025 Pino Torinese, Italy
[8] SUPA, School of Physics & Astronomy, University of St. Andrews, North Haugh, St. Andrews Fife, KY16 9SS, UK
[9] INAF—Fundación Galileo Galilei, Rambla José Ana Fernandez Pérez 7, E-38712 Breña Alta, Spain
[10] Division of Geological and Planetary Sciences, California Institute of Technology, Pasadena, CA 91125, USA
[11] Instituto de Astrofísica e Ciências do Espaço, Universidade do Porto, CAUP, Rua das Estrelas, PT4150-762 Porto, Portugal
[12] SUPA, Institute for Astronomy, University of Edinburgh, Royal Observatory, Blackford Hill, Edinburgh, EH93HJ, UK
[13] Dipartimento di Fisica e Astronomia "Galileo Galilei," Universita'di Padova, Vicolo dell'Osservatorio 3, I-35122 Padova, Italy
[14] INAF—Osservatorio Astronomico di Padova, Vicolo dell'Osservatorio 5, I-35122 Padova, Italy
[15] INAF—IASF Milano, via Bassini 15, I-20133, Milano, Italy
[16] Department of Physics, University of Warwick, Gibbet Hill Road, Coventry CV4 7AL, UK
[17] Cavendish Laboratory, J J Thomson Avenue, Cambridge CB3 0HE, UK
[18] Astrophysics Research Centre, School of Mathematics and Physics, Queens University, Belfast, Belfast BT7 1NN, UK
Received 2016 August 15; revised 2016 September 14; accepted 2016 September 22; published 2016 December 2

ABSTRACT

HD 179070, *aka* Kepler-21, is a $V = 8.25$ F6IV star and the brightest exoplanet host discovered by *Kepler*. An early detailed analysis by Howell et al. of the first 13 months (Q0–Q5) of *Kepler* light curves revealed transits of a planetary companion, Kepler-21b, with a radius of about $1.60 \pm 0.04\ R_\oplus$ and an orbital period of about 2.7857 days. However, they could not determine the mass of the planet from the initial radial velocity (RV) observations with Keck-HIRES, and were only able to impose a 2σ upper limit of $10\ M_\oplus$. Here, we present results from the analysis of 82 new RV observations of this system obtained with HARPS-N, together with the existing 14 HIRES data points. We detect the Doppler signal of Kepler-21b with a RV semiamplitude $K = 2.00 \pm 0.65$ m s^{-1}, which corresponds to a planetary mass of $5.1 \pm 1.7\ M_\oplus$. We also measure an improved radius for the planet of $1.639\ +0.019/-0.015\ R_\oplus$, in agreement with the radius reported by Howell et al. We conclude that Kepler-21b, with a density of 6.4 ± 2.1 g cm^{-3}, belongs to the population of small, $\lesssim 6\ M_\oplus$ planets with iron and magnesium silicate interiors, which have lost the majority of their envelope volatiles via stellar winds or gravitational escape. The RV analysis presented in this paper serves as an example of the type of analysis that will be necessary to confirm the masses of TESS small planet candidates.

Key words: planets and satellites: formation – planets and satellites: individual (Kepler-21b) – stars: individual (HD 179070) – techniques: photometric – techniques: radial velocities – techniques: spectroscopic

Supporting material: machine-readable table

1. INTRODUCTION

Results from NASA's *Kepler* Satellite Mission have revealed an abundance of planets smaller than $2\ R_\oplus$ with orbital periods less than 100 days (Howard et al. 2012; Dressing & Charbonneau 2013; Fressin et al. 2013; Petigura et al. 2013a, 2013b; Foreman-Mackey et al. 2014; Dressing & Charbonneau 2015; Silburt et al. 2015). Although only a few of those planets have measured masses, and therefore densities, those measurements have started to unveil an interesting picture. Below a radius of about $1.6\ R_\oplus$ most planets are consistent with bare rocky compositions without any significant volatile envelopes (Rogers 2015). Moreover, when considering only planets with masses measured with precisions better than 20% via RVs, planets with masses smaller than about $6\ M_\oplus$ appear to be rocky and have interiors composed mostly of iron and magnesium silicates in Earth-like abundances (26% Fe, 74% $MgSiO_3$, on average, based on Zeng et al. 2016), while planets more massive than about $7\ M_\oplus$ show a wider range of densities (Dressing et al. 2015; Gettel et al. 2016). Such dichotomy suggests the possible existence of mechanisms by

* Based on observations made with the Italian Telescope Nazionale Galileo (TNG) operated on the island of La Palma by the Fundación Galileo Galilei of the INAF (Istituto Nazionale di Astrofisica) at the Spanish Observatorio del Roque de los Muchachos of the Instituto de Astrofísica de Canarias.
[19] NASA Sagan Fellow.

6.2.2 An Accurate Mass Determination for Kepler-1655b, a Moderately Irradiated World with a Significant Volatile Envelope

A $2.2R_{\oplus}$ planet in a 11.87-day orbit was discovered around a Sun-like star from the *Kepler* mission. The follow-up consisted of 95 RV points with the HARPS-N spectrograph on the Telescopio Nazionale Galileo. The mass was measured using GP regression, and determined to be $5.0M_{\oplus}$. For the GP, the light curve was split into three pieces and analysed with an ACF to determine the spot lifetimes and stellar rotation periods – with the average of the three used for the GP regression. More details of the method and results can be found in Haywood et al. (2018) whose first page is included below.

The Astronomical Journal, 155:203 (19pp), 2018 May https://doi.org/10.3847/1538-3881/aab8f3

An Accurate Mass Determination for Kepler-1655b, a Moderately Irradiated World with a Significant Volatile Envelope

Raphaëlle D. Haywood[1,20], Andrew Vanderburg[1,2,20], Annelies Mortier[3], Helen A. C. Giles[4], Mercedes López-Morales[1], Eric D. Lopez[5], Luca Malavolta[6,7], David Charbonneau[1], Andrew Collier Cameron[3], Jeffrey L. Coughlin[8], Courtney D. Dressing[9,10,20], Chantanelle Nava[1], David W. Latham[1], Xavier Dumusque[4], Christophe Lovis[4], Emilio Molinari[11,12], Francesco Pepe[4], Alessandro Sozzetti[13], Stéphane Udry[4], François Bouchy[4], John A. Johnson[1], Michel Mayor[4], Giusi Micela[14], David Phillips[1], Giampaolo Piotto[6,7], Ken Rice[15,16], Dimitar Sasselov[1], Damien Ségransan[4], Chris Watson[17], Laura Affer[14], Aldo S. Bonomo[13], Lars A. Buchhave[18], David R. Ciardi[19], Aldo F. Fiorenzano[11], and and Avet Harutyunyan[11]

[1] Harvard-Smithsonian Center for Astrophysics, 60 Garden Street, Cambridge, MA 01238, USA; rhaywood@cfa.harvard.edu
[2] Department of Astronomy, The University of Texas at Austin, 2515 Speedway, Stop C1400, Austin, TX 78712, USA
[3] Centre for Exoplanet Science, SUPA, School of Physics and Astronomy, University of St Andrews, St Andrews, KY16 9SS, UK
[4] Observatoire Astronomique de l'Université de Genève, Chemin des Maillettes 51, Sauverny, CH-1290, Switzerland
[5] NASA Goddard Space Flight Center, 8800 Greenbelt Road, Greenbelt, MD 20771, USA
[6] Dipartimento di Fisica e Astronomia "Galileo Galilei," Universita' di Padova, Vicolo dell'Osservatorio 3, I-35122 Padova, Italy
[7] INAF—Osservatorio Astronomico di Padova, Vicolo dell'Osservatorio 5, I-35122 Padova, Italy
[8] SETI Institute, 189 Bernardo Avenue, Suite 200, Mountain View, CA 94043, USA
[9] Division of Geological Planetary Sciences, California Institute of Technology, Pasadena, CA 91125, USA
[10] Astronomy Department, University of California, Berkeley, CA 94720, USA
[11] INAF—Fundación Galileo Galilei, Rambla José Ana Fernandez Pérez 7, E-38712 Breña Baja, Tenerife, Spain
[12] INAF—Osservatorio Astronomico di Cagliari, via della Scienza 5, I-09047, Selargius, Italy
[13] INAF—Osservatorio Astrofisico di Torino, via Osservatorio 20, I-10025 Pino Torinese, Italy
[14] INAF—Osservatorio Astronomico di Palermo, Piazza del Parlamento 1, I-90134 Palermo, Italy
[15] SUPA, Institute for Astronomy, Royal Observatory, University of Edinburgh, Blackford Hill, Edinburgh EH93HJ, UK
[16] Centre for Exoplanet Science, University of Edinburgh, Edinburgh, UK
[17] Astrophysics Research Centre, School of Mathematics and Physics, Queen's University Belfast, Belfast, BT7 1NN, UK
[18] Centre for Star and Planet Formation, Natural History Museum of Denmark, University of Copenhagen, DK-1350 Copenhagen, Denmark
[19] NASA Exoplanet Science Institute, Caltech/IPAC-NExScI, 1200 East California Boulevard, Pasadena, CA 91125, USA
Received 2017 July 10; revised 2018 March 16; accepted 2018 March 18; published 2018 April 20

Abstract

We present the confirmation of a small, moderately irradiated ($F = 155 \pm 7\,F_{\oplus}$) Neptune with a substantial gas envelope in a $P = 11.8728787 \pm 0.0000085$ day orbit about a quiet, Sun-like G0V star Kepler-1655. Based on our analysis of the *Kepler* light curve, we determined Kepler-1655b's radius to be $2.213 \pm 0.082\,R_{\oplus}$. We acquired 95 high-resolution spectra with Telescopio Nazionale Galileo/HARPS-N, enabling us to characterize the host star and determine an accurate mass for Kepler-1655b of $5.0 \pm^{3.1}_{2.8}\,M_{\oplus}$ via Gaussian-process regression. Our mass determination excludes an Earth-like composition with 98% confidence. Kepler-1655b falls on the upper edge of the evaporation valley, in the relatively sparsely occupied transition region between rocky and gas-rich planets. It is therefore part of a population of planets that we should actively seek to characterize further.

Key words: stars: individual (Kepler-1655, KOI-280, KIC 4141376, 2MASS J19064546+3912428) – planets and satellites: detection – planets and satellites: gaseous planets

1. Introduction

In our own solar system, we see a sharp transition between the inner planets, which are small ($R_p \leqslant 1\,R_{\oplus}$) and rocky, and the outer planets that are larger ($R_p \geqslant 3.88\,R_{\oplus}$), much more massive, and have thick, gaseous envelopes. For exoplanets with radii intermediate to that of the Earth ($1\,R_{\oplus}$) and Neptune ($3.88\,R_{\oplus}$), several factors go into determining whether planets acquire or retain a thick gaseous envelope. Several studies have determined statistically from radius and mass determinations of exoplanets that most planets smaller than $1.6\,R_{\oplus}$ are rocky (i.e., they do not have large envelopes but only a thin, secondary atmosphere, if any at all; Lopez & Fortney 2014; Weiss & Marcy 2014; Dressing & Charbonneau 2015; Rogers 2015; Buchhave et al. 2016; Gettel et al. 2016; Lopez 2017; Lopez & Rice 2016). Others have found that planets in less irradiated orbits tend to be more likely to have gaseous envelopes than more highly irradiated planets (Hadden & Lithwick 2014; Jontof-Hutter et al. 2016). However, it is still unclear under which circumstances a planet will obtain and retain a thick gaseous envelope and how this is related to other parameters, such as stellar irradiation levels.

The characterization of the mass of a small planet in an orbit of a few days to a few months around a Sun-like star (i.e., in the incident flux range $\approx$1–5000 $F_{\oplus}$) is primarily limited by the stellar magnetic features acting over this timescale and producing RV variations that compromise our mass determinations. Magnetic fields produce large, dark starspots and bright faculae on the stellar photosphere. These features induce RV variations modulated by the rotation of the star and varying in amplitude as the features emerge, grow, and decay. There are two physical processes at play: (i) dark starspots and bright faculae break the Doppler balance between the approaching blueshifted stellar hemisphere and the receding redshifted half of the star (Saar & Donahue 1997; Lagrange et al. 2010;

[20] NASA Sagan Fellow.

6.3 Generating Simulated Light Curves with `CHEOPSim`

Early results of the work described in Giles et al. (2017) were used for generating simulated stellar light curves[a], a code developed by Rodrigo Díaz, for the software `CHEOPSim`. `CHEOPSim` is a tool which is designed to simulate light curves of stars which will be observed by the *CHEOPS* mission, a satellite telescope which will perform high-cadence, incredibly-precise photometric follow-up of known transiting planets.

For `CHEOPSim` to accurately simulate expected light curves, the stars needed to behave like stars – this meant introducing realistic stellar effects. Similar to how GPs were used to model the different aspects of RV curves (i.e. stellar rotation, spot decay and a Keplerian orbit), GPs can also be used to generate stellar signals which behave with certain criteria based on the spectral type which a simulated light curve is needed for. This uses the spot lifetimes and stellar rotation periods measured from 2000+ stars observed by *Kepler* and the spectral type of those stars (based on the stellar effective temperature). Inserted into the GP, the GP constructs a light curve with the characteristics expected for a star of that spectral type.

6.4 Determining the Effect on Transit Depths from Unocculted Starspots

The depth of a transit is directly proportional to the ratio of the planetary and stellar radii. As mentioned in Section 1.6.2.2, there are various sources for uncertainty in the transit depth. One of those are the effects of unocculted starspots on the observed stellar surface (Carter et al. 2011); their presence cause the overall brightness of the star to decrease. This effectively reduces the observed size of the star which in turn would increase the ratio of radii, leading to an overestimate of the planetary radius. This overestimation can be accounted for by the spot coverage, ϵ, described by

$$\frac{R_p}{R_*} = \sqrt{\delta(1-\epsilon)}. \tag{6.2}$$

Whilst the absolute spot coverage of most stars remains unknown, Giles et al. (2017) determined the root-mean-square scatter of a large data set of stars observed by *Kepler*; and were used as proxies for spots sizes (the larger the root-mean-square scatter, the larger the spot). The same can be applied for determining the effect of spots on transit depths. By determining a relationship between the stellar effective temperature and root-mean-square, it is possible to estimate the overestimation on planetary radii for a given star where the stellar effective temperature is known (and ideally, also the stellar activity behaviour).

[a] `https://github.com/exord/lcspotter`

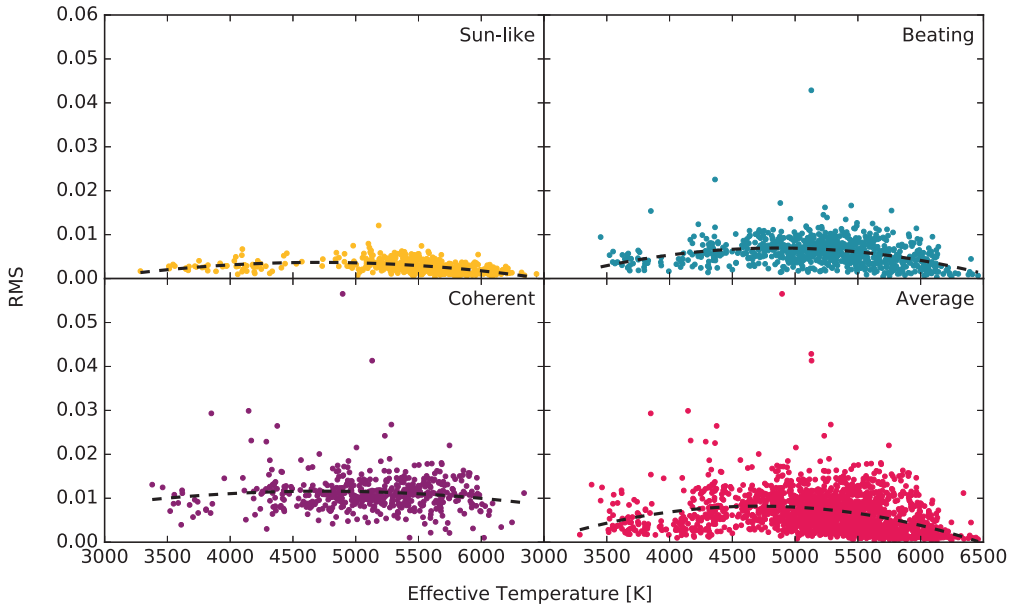

Figure 6.1: The stellar effective temperature vs spot size results of Giles et al. (2017) split by their stellar activity type and with a quadratic function fitted. The fourth panel shows the full results to generate an 'average' function for the case when a stellar activity type is not known.

Using Equation 6.2, the $\sqrt{\delta}$ can be treated as the measured observational term, transit depth. This leaves the $\sqrt{1-\epsilon}$ term to be determined.

Splitting the results from Giles et al. (2017) into the three regions of stellar activity behaviour described in the publication, by studying the ratio of the spot lifetimes and stellar rotational period. The three regions are as follows: 'Sun-like', where $\tau/P \sim 1$; 'Beating', where $\tau/P > 1$; and 'Coherent', where $\tau/P >> 1$.

For each region, a quadratic function was fitted to give a relationship for the root-mean-square of a given stellar effective temperature (as demonstrated by the black lines in Figure 6.1). Using the root-mean-square as the proxy for spot coverage, the quadratic functions fitted to each region can be inputted into the relationship between planetary radius and spot coverage (Equation 6.2). This generates a factor, or percentage, which the observed ratio of radii can be corrected to give the true, unocculted planet radius (see Figure 6.2). Errors for each type can be determined by examining the residuals and measuring the standard deviation of those residuals – 'Sun-like', 'Beating', 'Coherent' and Average have uncertainties of 0.13%, 0.29%, 0.43% and 0.43% respectively. For comparison, taking $T_{eff} \sim 5800$K, the values for each type of stellar activity behaviour are 0.12%, 0.25%, 0.52%, 0.25% (in the same order as before).

Stars with longer spot lifetimes will typically have larger over-estimates of their transit

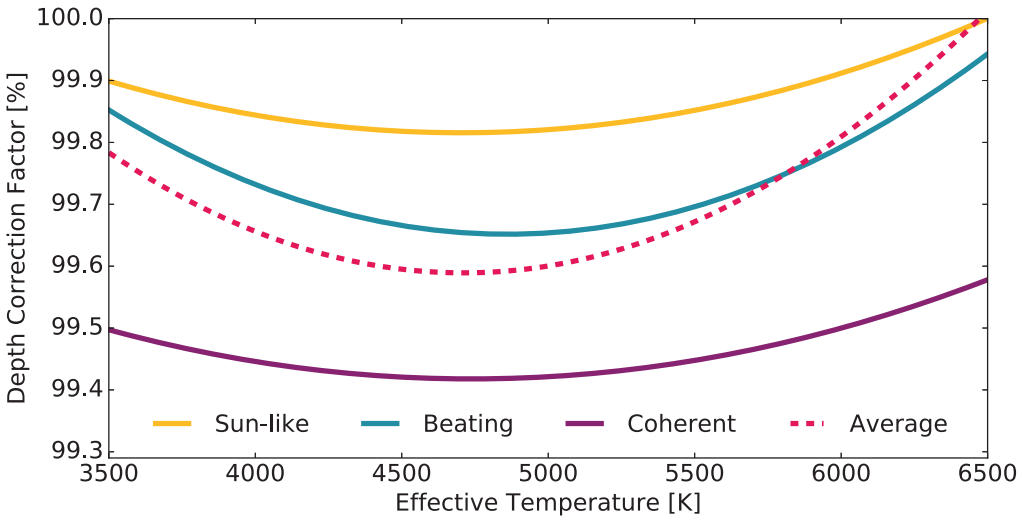

Figure 6.2: The estimated percentage transit depths should be corrected for, given a stellar effective temperature and stellar activity behaviour type. The pink dashed line represented the function which was fitted on the entire data sample from Giles et al. (2017) and can be used as an average for the case where stellar activity type is not known.

depths, whilst the more 'Sun-like' lifetimes have much less. Additionally, the hotter stars have less effect from spots. A similar effect is seen for the lowest temperature stars as well, however this is more likely to be due to there being less data for the cooler stars. The errors are of the order of the values themselves. This would mean the maximal effect expected, for any given star, can be as much as $\sim 1\%$.

This will be of interest for precise transit surveys, such as *CHEOPS* (Broeg et al. 2013). *CHEOPS* will perform high-precision, high-cadence follow-up photometry of known exoplanets and exoplanet candidates. In the case of an individual transit, the unocculted spot coverage will be one of the key observational uncertainties. For targets which are observed more than once, the spacing between each observed transit should be considered. If the spacing is of the order or less than the lifetime of the spots, then the level of spot coverage can be expected to be different from the previous transit. However, if the spacing is greater than the spot lifetime, then each transit can essentially be treated as a stand-alone transit.

Chapter 7

Conclusion & Future Prospects

'The more you know, the more you know you don't know.'

Dr. Jessie Christiansen

7.1 Where are we?

Over the course of this thesis the most important advance in research into exoplanets and their stellar hosts has been the development of new methodologies and skills. Astronomers have coded better tools, formed larger collaborations and developed better and better instruments. *K2* received its final "goodnight" commands; *TESS* was launched and started operations; and *ESPRESSO* successfully saw first light.

7.1.1 Know Thy Star

The work discussed in Chapters 5 and 6 addresses a crucial aspect of both stellar physics and exoplanet discovery which needs careful attention as more and more precise instruments come online. Treating the stellar effect in RVs and light curves simply as a 'noise' term will become less and less effective as smaller planets are discovered in more distant orbits. It will become essential to understand the behaviour of the star and the way this behaviour affects the light observed.

In Chapter 5, the first large-scale survey of starspots, Giles et al. (2017), showed that the lifetime of starspots can be measured and that it has a strong dependence on the spectral type and size of spots. This was done by generating autocorrelation functions (ACFs) of over 2000 stars and measuring how the side lobes decayed away from the central peak.

Giles et al. (2017) provides statistical evidence that:

1) larger starspots live longer;
2) starspots of a given size on a cooler star live longer than starspots of the same size on a hotter star;
3) the Sun is not unusually quiet for its spectral type.

These are conceptually reasonable expectations, and perhaps could have been established in individual cases: this large-scale survey is the first confirmation that they are true across the board.

As well as the large survey of *Kepler* stars, the method was also adapted and applied to a light curve generated from archival data of the spot coverage of the Sun. However, due to additional signals present in the ACF (such as the long-term activity cycle and a signal which appeared to be a seasonal), it was not possible to apply the same quantitative tools. Whilst it was not possible to quantitatively measure the lifetimes of the sunspots, it was possible to establish qualitatively that the lifetimes would be of the order of a solar rotation, which matches previous measurements. This does however raise the question as to why it was not possible to perform the same test – does the fact that the Sun is observed in significantly more detail than a distant star is make a difference? Or is there something about the Sun which is intrinsically different from other stars?

As discussed in Chapter 6, one current method for modelling the RVs of planets involves GPs which have a term that behaves like the starspot lifetime (López-Morales et al. 2016; Haywood et al. 2018). Measuring starspot lifetimes from one source of data can significantly benefit a different source and improve our abilities to find exoplanets. This means that for transiting exoplanets from surveys which contain a long baseline (such as *Kepler*) then the measured starspot lifetime can be determined and utilised for performing RV follow-up of that candidate; especially if the star is particularly active and therefore needs a significant amount of analysis to extract the planetary signal.

Additionally, the results of Giles et al. (2017) could be used photometrically. As part of the planning for the *CHEOPS* mission, software to simulate the type of light curves expected from the mission was created. For this to be as exact as possible, it was necessary to include a stellar activity aspect. To do so, early results of Giles et al. (2017) were used to determine the typical spot sizes and lifetimes of different stellar types, which were decided when generating light curves for specific uses.

Furthermore, it was possible to demonstrate initial estimates of the effect of unocculted starspots on the observed transit depth of an exoplanet. As starspots decrease the overall stellar brightness, this also in effect reduces the perceived stellar radius. By underestimating the stellar radius, this would overestimate a planet's radius. As part of Giles et al. (2017), the starspot size proxy can also be considered as a typical starspot coverage – and this can be split with regards the stellar effective temperature and also starspot lifetime type. Ultimately, the effect was quite small, with the largest overestimation of a planet radius being of the order of 1% (typical uncertainties on a planet radius from multiple transits will be larger than this). But knowing that the effect would be minimal is valuable information, and whilst the 1% overestimation is currently a 'small' value with future instruments and advances it may become a point of concern in the future.

7.1.2 Know Thy Planet

The techniques described in Chapter 2 were successfully applied to the second half of the *K2* mission, C11-18 (Chapter 3 and 4). This included downloading, 'cleaning' and processing of the publicly available light curves. Given the population of stars observed by each campaign (see Table 3.1) and the final candidates eligible for RV follow-up with CORALIE, the following is determined:

- for C11-18,185,508 stellar light curves were downloaded for analysis;
- 37,578 were deemed to have transit-like signals ($\sim$ 20.26%);
- from those 37,578, only 18,654 ($\sim$ 49.64%) met magnitude requirements for CORALIE, and the BLS criteria for the ranking;
- of the remaining candidates from the BLS, only 149 ($\sim$ 0.80%) were deemed of good enough quality to be passed as potential candidates for CORALIE follow-up after being inspected by-eye.

Whilst there was a large number of candidates outputted from the BLS, they were only approximately 20% of the total number of stars observed, where only half of those met the criteria that were necessary for follow-up with CORALIE. More rigorous criteria could have been used, but given the risk of missing good candidates due to the ever evolving behaviour of *K2* on the light curves, it was safer to allow 'poorer' candidates to be put forward and allow the human eye to save the less robust, but still strong candidates from being lost (e.g. the long-period monotransit candidate discussed in Chapter 4).

As for the 149 final candidates eligible for CORALIE follow-up (see Table A.2 for more details), 32 were either already discovered and confirmed or were confirmed by other teams as follow-up was ongoing or pending. In fact, of the 149 final candidates, 47 candidates have

received RV observations (either as just initial points or intensive follow-up), and 11 were since confirmed (or part of a previous follow-up effort e.g. WASP-151 b). Of the remaining 36 candidates, 15 were found to be spectral binaries or other stellar contaminant flags which ruled them to be false-positives. Currently, 21 candidates are receiving RV follow-up. This includes the continued follow-up of K2-311b (Giles et al. 2018b), in the hope to characterise its mass.

From this two planets were found and confirmed. K2-140b (Giles et al. 2018a): a slightly inflated, Jupiter-sized planet in a 6.57-day orbit around a V=12.5 star. This planet was a proof of concept confirmation for the new pipeline in place in Geneva, from taking the light curves from the publicly available data, performing analysis and conducting follow-up with the Swiss telescope and other instruments.

K2-311b (Giles et al. 2018b) is the second discovery from the new Geneva-based pipeline. It is a monotransit candidate which, after extensive analysis of its transit, RV follow-up and stellar properties, was deemed to be a Jupiter-like planet with an estimated orbital period of $\sim$ 10 years, orbiting an evolved sub-Giant star. Once finally confirmed, this would be the longest known transiting exoplanet.

7.2 And where are we going?

Invariably, the fields of exoplanets and stars are intensely intertwined. As the planets discovered get smaller, the stellar contribution to the light observed becomes more and more problematic. On the other side are those who embrace the 'noise' from exoplanet searches. *Kepler* was revolutionary for the stellar physics field as it was (and arguably still is) one of the best sources of high-cadence, very-precise photometry of stars.

This will naturally continue for future exoplanet surveys, for example *TESS* (Ricker et al. 2015). *TESS* will observe 400 times more sky than *Kepler*, over the course of 26 different segments (where the celestial poles will be observed continuously!). It will also observe the stars in a different wavelength and typically much brighter stars than *Kepler* – this is of interest for both understanding the stellar host and discovering exoplanets. For planets, brighter host stars improve the follow-up, as the brighter they are the easier it is to observe spectra to high precision. Whereas for the stars, it opens up a new avenue of research – do the starspot lifetimes behave the same way in a different wavelength? Do the lifetimes apply to the activity indicators within simultaneous RV follow-up? Learning about these are not just applicable to stellar physics but also feedback into exoplanet discovery.

Additionally, *TESS* will be of significant importance for the future of monotransit candidates. Villanueva et al. (2019) predict that more than 1000 single-transit events will be seen by *TESS* (from either postage-stamps or full-frame-images). Currently, there are limited tools designed

specifically for monotransit candidates (see Chapter 4), and detailed knowledge of the star is needed. The standard techniques used for exoplanet follow-up can be applied to monotransits, but are only ideally applicable to those which still have relatively short periods (e.g. 50 days) as they can have their orbits observed and constrained within a season. Candidates which exhibit signs of having periods significantly longer (e.g. K2-311b at ~10 years, Giles et al. 2018b) cannot be treated in the same way. Whilst the methodology utilised in Giles et al. (2018b) may well prove effective, it will require several years worth of follow-up – new techniques and tools may well reduce the need for such a long baseline. The development of new approaches will be well worth the effort, as long-period transiting planets is a still relatively unexplored area of research due to those already known having faint host stars (making it very difficult to conduct any follow-up). This may, and almost certainly will change with *TESS*.

Another telescope which will come on-sky soon is *CHEOPS* (Broeg et al. 2013). A space-based telescope, organised as a collaboration between ESA and Switzerland, which is the first S-class mission being launched by ESA. The primary mission of *CHEOPS* is to perform follow-up photometry of known transiting planets with high precision. This will be of particular interest to the monotransit candidates, as they will require not only additional orbits to constrain the transit shape but also precise transit ephemeris. A collaboration between the science teams of *CHEOPS* and *TESS* has been organised, with this and other scientific goals in mind, named *CHESS*.

A little further afield is the *PLATO* mission (Rauer et al. 2014) – a space-based mission with an expected launch by 2026. It will observe large areas of sky for long periods of time – similar to *Kepler* and *K2* but with higher precision and more stars. The first goal of *PLATO* (PLAnetary Transits and Oscillations of stars) is to detect terrestrial exoplanets and characterise their bulk properties, in particular planets which fall in the habitable zone of Sun-like stars. *PLATO* will, like *Kepler* produce high quality light curves that will allow for further stellar physics studies – this ability to study the stars was in fact a crucial component of the mission proposal. *PLATO* will not only continue to discover previously undiscovered exoplanets, but also provide additional, more precise transits of those already known and deeper understanding of their stellar hosts.

When it comes to discovering and understanding exoplanets, we have advanced beyond what was perhaps expected when the first planets were being found. We have found a menagerie of exoplanets of all type of orbit shapes and radii. But the most elusive is finding something that looks familiar to the place which we call Home. However, to find another Earth, or another Solar System, we must *Know Thy Star to Know Thy Planet*.

Appendix A

Appendix: List of Planet Candidates Detected from *K2*

This Appendix lists the planet candidates detected from *K2* light curves for Campaigns 11 to 18. They have been split into two tables: the first table shows each candidate's key stellar properties (e.g. coordinates, brightness, radius); the second lists the parameters for the planet as determined by the BLS routine, and includes additional comments and gives the current status of the RV follow-up.

Table A.1: Table of *K2* Candidates – Stellar Properties

EPIC #	Campaign #	RA	Dec	*Kepler* Mag	V Mag	*Gaia* Radius ($R_\odot$)
232172024	11	17:09:18.58	-26:58:10.93	12.12	12.53	9.13
204403554	11	16:55:50.15	-22:28:16.01	13.22	13.50	1.11
224999193	11	17:32:47.12	-23:17:22.7	13.75	-	3.17
229426032	11	16:55:04.53	-28:42:38.03	11.47	11.60	1.30
242207980	11	17:38:09.82	-30:03:21.48	13.67	-	-
231275397	11	17:11:41.96	-23:35:32.82	12.83	13.08	9.57
245946030	12	23:40:54.27	-10:59:07.19	11.70	12.10	1.51
246063952	12	23:25:41.54	-07:56:05.11	12.32	12.45	1.07
246067459	12	23:10:49.04	-07:51:27	13.55	13.75	-
246088339	12	23:34:52.87	-07:23:38.82	13.47	13.57	1.04

Table A.1 continued from previous page

EPIC #	Campaign #	RA	Dec	*Kepler* Mag	V Mag	*Gaia* Radius ($R_\odot$)
246120070	12	23:20:01.14	-06:42:07.83	10.47	10.68	0.97
246261316	12	23:34:49.84	-03:50:05.64	13.55	13.73	0.78
246326057	12	23:35:42.6	-02:32:37.02	13.74	13.91	1.80
246375295	12	23:34:27.88	-01:34:48.13	11.93	12.14	9.57
246389308	12	23:21:25.31	-01:17:50.75	10.84	11.01	1.87
246441449	12	23:16:15.23	00:18:24.27	12.67	12.80	1.19
246485787	12	23:20:18.07	01:40:58.77	12.47	12.47	1.27
246628376	13	04:50:32.07	13:36:48.59	12.51	12.71	-
246698204	13	04:58:57.21	14:32:58.48	7.53	7.42	-
246712205	13	04:57:20.85	14.:43:30.39	11.94	12.09	2.50
246769933	13	05:03:43.43	15:24:38.98	11.74	12.54	0.86
246851721	13	05:15:40.74	16:16:43.47	11.26	11.24	1.87
246911830	13	05:07:28.16	16:52:03.78	12.47	12.69	1.81
247028425	13	04:43:10.7	17:59:19.67	11.35	11.60	0.85
247085413	13	04:52:44.73	18:31:43.57	12.14	12.43	4.15
247098361	13	04:55:03.96	18:39:16.33	9.79	9.82	1.26
247142564	13	05:19:00.98	19:04:32.74	12.22	12.72	16.19
247476672	13	04:54:29.14	22:00:54.98	12.18	12.46	1.99
247548566	13	04:44:05.43	22:34:03.62	13.38	13.25	1.08
247576642	13	05:04:00.00	22:47:07.33	10.39	10.15	3.48
247689275	13	04:44:05.8	23:38:02.84	12.94	13.25	-
247740694	13	04:55:28.24	23:59:44.91	13.50	14.05	5.31
247773181	13	05:03:15.38	24:13:23.98	11.03	10.84	1.56
247887989	13	04:40:35.66	25:00:36.02	13.33	14.06	-
247956487	13	04:28:29.72	25:29:24.92	12.64	12.85	3.47
248545986	14	10:42:22.63	04:26:28.9	13.55	14.55	-
248874928	14	10:57:30.28	12:32:08.3	12.57	12.86	0.76
201498078	14	10:52:07.78	00:29:36.1	10.45	10.61	1.83
248777106	14	10:18:41.06	10:07:44.5	9.20	9.38	1.76
248758353	14	10:56:45.49	09:40:26.3	12.12	12.36	0.95
248847494	14	10:37:33.42	11:50:33.8	12.17	12.42	2.55
248651022	14	10:34:56.66	07:08:50.5	12.30	12.49	0.87

Table A.1 continued from previous page

EPIC #	Campaign #	RA	Dec	*Kepler* Mag	V Mag	*Gaia* Radius ($R_\odot$)
248779118	14	10:37:43.75	10:10:45.1	11.38	12.81	1.14
248527709	14	10:13:24.01	03:57:36.7	12.92	13.37	0.74
248827616	14	10:19:07.61	11:20:47.0	11.60	11.92	1.66
248783679	14	10:22:19.29	10:17:19.4	12.61	12.76	1.68
248621597	14	10:45:48.45	06:25:09.9	12.87	13.03	1.26
201701882	14	10:59:21.44	03:40:17.5	12.69	12.81	-
248740871	14	10:46:46.09	09:15:38.8	13.89	14.40	0.68
248618202	14	10:44:37.60	06:20:00.9	9.60	9.84	0.83
248659495	14	10:42:28.10	07:21:21.7	13.35	13.60	2.36
249788281	15	15:07:34.31	-18:03:09.1	12.98	13.17	1.18
249928278	15	15:24:30.22	-16:18:22.6	12.70	12.90	1.52
249703125	15	15:30:33.08	-19:11:20.4	12.88	13.12	0.91
249559552	15	15:24:17.97	-20:59:57.62	12.85	13.19	0.69
249451861	15	15:32:17.84	-22:21:29.74	11.06	11.41	1.18
249833762	15	15:46:41.69	-17:27:40.86	11.02	11.50	-
249884266	15	15:49:48.06	-16:49:51.97	12.80	13.07	1.23
249846890	15	15:20:07.51	-17:17:42.21	12.48	12.65	1.19
249378363	15	15:31:59.5	-23:20:34.94	12.66	11.98	1.60
249707254	15	15:34:56.55	-19:08:06.05	13.86	14.13	0.76
249401470	15	15:05:57.19	-23:02:10.51	12.11	12.37	1.18
249447551	15	15:35:14.6	-22:24:57.15	13.53	13.81	1.13
249921188	15	15:46:32.26	-16:23:20.34	13.89	14.08	1.72
249541048	15	15:39:23.83	-21:13:27.02	12.32	12.51	1.29
249259371	15	15:46:34.37	-24:54:01.92	13.30	13.75	4.86
249865296	15	15:38:10.18	-17:03:49.47	12.85	12.96	1.35
249223471	15	15:23:32.96	-25:22:14.69	9.59	9.47	1.02
249624646	15	15:39:25.87	-20:11:55.74	10.78	11.11	1.58
249133524	15	15:48:22.15	-26:30:58.41	12.87	13.06	1.81
204440872	15	15:59:41.7	-22:19:30.26	12.93	13.22	1.04
249883966	15	15:21:38.78	-16:50:06.06	11.04	11.36	2.28
249217698	15	15:42:14.79	-25:26:43.57	12.61	12.84	2.76
249675967	15	15:09:23.79	-19:32:40.46	12.18	12.40	0.97

Table A.1 continued from previous page

EPIC #	Campaign #	RA	Dec	*Kepler* Mag	V Mag	*Gaia* Radius ($R_\odot$)
249569027	15	15:30:24.54	-20:53:00.62	12.48	12.70	0.76
249401939	15	15:32:13.33	-23:01:47.28	13.46	-	0.67
249483417	15	15:31:37.16	-21:56:48.9	10.83	11.23	0.71
249252791	15	15:26:21.96	-24:59:11.07	13.59	13.88	2.48
249344320	15	15:06:47.1	-23:47:22.99	12.98	13.18	1.14
249830881	15	15:46:15.93	-17:29:50.45	13.82	14.02	0.95
249708923	15	15:32:12.32	-19:06:47.99	10.93	10.96	2.31
249893012	15	15:12:59.57	-16:43:28.29	11.36	11.43	1.82
212110888	16	08:30:18.90	22:14:09.3	11.44	11.45	1.40
212036875	16	08:58:45.67	20:52:08.7	10.94	10.95	1.49
211432167	16	08:51:27.31	12:07:40.5	8.55	8.24	2.38
212040382	16	09:04:40.79	20:55:53.2	12.52	12.63	2.11
211730024	16	09:05:57.47	16:19:32.1	11.40	11.84	1.46
211812935	16	08:52:35.49	17:29:59.4	12.64	12.85	2.13
211920604	16	08:43:50.99	19:02:02.6	12.26	12.37	2.45
211741619	16	08:47:35.29	16:29:23.7	13.56	14.22	0.67
251408535	16	08:56:06.41	25:16:40.3	13.73	14.01	0.94
212204403	16	08:43:30.80	24:25:23.2	12.48	12.56	0.88
211945201	16	09:06:17.75	19:24:08.1	10.12	10.15	1.40
211647930	16	09:07:09.45	15:12:20.5	11.98	11.56	1.18
211919004	16	08:39:06.49	19:00:36.1	13.13	13.37	0.87
211830293	16	09:04:33.58	17:44:49.5	11.92	12.13	1.79
211397844	16	09:01:27.35	11:36:27.5	13.29	13.53	5.61
211604981	16	09:13:18.93	14:36:24.7	12.73	12.78	2.36
211816003	16	08:50:29.07	17:32:32.8	13.65	13.84	0.80
211886472	16	09:08:31.81	18:31:42.8	11.13	11.28	2.19
212048748	16	08:58:52.35	21:04:33.8	12.77	13.82	-
212165050	16	08:44:58.82	23:22:16.6	10.74	10.65	-
212651234	17	13:55:42.76	-09:25:04.0	11.14	11.31	2.87
212697709	17	13:26:37.25	-08:19:03.2	12.19	12.91	1.13
212705192	17	13:30:25.31	-08:07:48.9	11.73	12.20	2.24
212735333	17	13:29:34.48	-07:22:26.4	11.98	12.16	0.98

Table A.1 continued from previous page

EPIC #	Campaign #	RA	Dec	*Kepler* Mag	V Mag	*Gaia* Radius ($R_\odot$)
212779563	17	13:47:23.44	-06:08:12.7	9.95	10.36	0.61
212803289	17	13:55:05.70	-05:26:32.9	11.01	11.15	2.71
212628254	17	13:41:30.30	-09:56:45.9	9.78	9.88	1.17
212689874	17	13:19:19.56	-08:30:34.1	12.33	12.50	0.95
212672300	17	13:38:26.14	-08:55:37.7	12.85	12.91	1.31
212691422	17	13:21:49.52	-08:28:18.2	11.92	12.06	1.93
211309648	18	08:55:27.99	10:02:43.04	13.85	13.97	1.65
211317649	18	08:35:42.18	10:12:23.91	13.21	13.36	1.02
211391507	18	08:29:40.38	11:30:30.97	13.61	13.77	1.68
211393988	18	08:55:16.31	11:32:55.94	13.86	13.87	1.61
211417387	18	08:28:58.84	11:54:10.21	13.05	13.08	1.89
211432167	18	08:51:27.31	12:07:40.51	8.55	8.24	2.38
211480861	18	08:18:10.5	12:51:45.66	9.96	9.90	2.12
211705502	18	08:17:58.23	15:59:16.48	13.22	13.36	1.47
211713099	18	08:20:53.73	16:05:27.41	13.64	13.83	0.93
211736671	18	08:13:31.65	16:25:10.59	12.16	12.33	1.80
211800191	18	08:51:32.35	17:19:11.4	12.44	12.62	1.03
211808055	18	08:36:08.27	17:25:48.3	13.74	-	1.08
211817572	18	08:12:23.05	17:33:54.55	11.39	11.13	1.62
211818569	18	08:27:44.81	17:34:45.83	12.94	13.32	0.64
211962097	18	08:53:36.86	19:39:26.19	13.57	13.61	2.07
211993818	18	08:24:49.18	20:09:10.78	7.22	7.34	10.62
212110888	18	08:30:18.91	22:14:09.27	11.44	11.45	1.40
212099230	18	08:32:17.66	22:00:21.64	10.51	10.79	1.00
211490999	18	08:43:11.72	13:00:34.53	13.42	13.60	0.94
211424769	18	08:35:24.64	12:00:41.94	9.44	9.39	1.41
212164470	18	08:39:15.27	23:21:26.93	12.70	12.65	1.18
211816003	18	08:50:29.07	17:32:32.8	13.65	13.84	0.80
211921220	18	08:44:06.62	19:02:34.14	13.83	13.95	2.08
211920604	18	08:43:50.99	19:02:02.61	12.26	12.37	2.45
211506851	18	08:37:01.38	13:14:09.62	13.45	13.30	0.92
211442297	18	08:26:12.83	12:16:54.97	13.19	13.36	0.83

Table A.1 continued from previous page

EPIC #	Campaign #	RA	Dec	*Kepler* Mag	V Mag	*Gaia* Radius ($R_\odot$)
211342524	18	08:32:23.69	10:40:38.06	12.41	12.42	1.74
211919528	18	08:43:57.59	19:01:05.36	13.29	13.50	0.78
211730267	18	08:47:45.29	16:19:44.12	13.46	13.63	0.89
211401787	18	08:27:35.27	11:40:02.91	9.71	9.61	1.47
211391664	18	08:25:57.19	11:30:40.12	12.10	12.17	1.37
211733267	18	08:40:02.26	16:22:20.66	12.15	12.40	0.90
211644764	18	08:30:44.87	15:09:45.31	13.11	13.16	1.73
211822389	18	08:41:53.39	17:38:04.66	13.64	13.81	1.46
211892898	18	08:43:34.63	18:37:19.93	11.77	12.09	6.85
211390677	18	08:30:48.91	11:29:40.45	13.31	13.57	7.10
212009578	18	08:40:24.64	20:24:47.56	13.28	13.44	2.57

Table A.2: Table of *K2* Candidates – Planetary Properties & Status)

EPIC #	Campaign #	P_{orb} (days)	t_C (days)	t_T (hrs)	Δ F (%)	# of RVs	Comments	Flag*
232172024	11	8.67	57690.68137	3.26	0.37	17	Long-term variation seen in RVs	CanP
204403554	11	2.69	57695.31899	3.87	0.12	-		pFP
224999193	11	3.15	57694.78864	3.61	0.07	-		pFP
229426032	11	2.18	57691.35532	1.79	1.42	1	Confirmed: K2-237 b (Soto et al. 2018)	ConP
242207980	11	10.47	57715.97638	5.78	1.07	-		
231275397	11	2.65	57729.64461	3.76	0.10	-		
245946030	12	26.53	57773.47931	3.52	1.39	6	Significant movement in RV values – SB1	pFP
246063952	12	8.12	57749.30832	2.55	0.06	-		pFP
246067459	12	3.20	57811.01157	2.63	0.68	16	Confirmed: K2-238 b (Soto et al. 2018)	ConP
246088339	12	2.99	57740.60439	2.13	0.10	-		CandP
246120070	12	40.57	57804.57582	4.93	1.72	-		pFP
246261316	12	4.70	57741.72826	2.33	0.10	-		CandP
246326057	12	13.45	57762.24207	2.35	1.21	-		CandP
246375295	12	3.41	57806.12913	2.08	1.39	-	Confirmed: K2-1 b, WASP-28 b (Anderson et al. 2015)	
246389308	12	17.65	57742.95408	3.17	1.58	-		pFP

Table A.2 continued from previous page

EPIC #	Campaign #	P_{orb} (days)	t_C (days)	t_T (hrs)	Δ F (%)	# of RVs	Comments	Flag*
246441449	12	4.53	57777.27946	2.01	1.11	7	Confirmed: K2-134 b, WASP-151 b (Demangeon et al. 2018)	ConP
246485787	12	4.55	57801.75656	1.23	0.25	-		CandP
246628376	13	4.55	57850.63681	2.63	0.40	-		
246698204	13	14.78	57861.81312	7.48	2.28	-		pFP
246712205	13	3.56	57847.06141	3.29	1.84	4	Ellipsoidal variation in light curve and noisy CCFs – a signal would be difficult to find.	pFP
246769933	13	3.93	57831.61501	31.32	0.55	-		pFP
246851721	13	6.18	57858.93267	2.77	0.52	2	Confirmed: K2-267 b (Yu et al. 2018b)	ConP
246911830	13	2.63	57878.52639	3.19	0.99	6	Confirmed: K2-260 b (Johnson et al. 2018)	ConP
247028425	13	1.38	57838.39807	0.91	0.71	-		
247085413	13	2.42	57878.44431	1.96	0.55	-		pFP
247098361	13	11.16	57836.51856	2.33	0.81	18	Confirmed: K2-232 b (Yu et al. 2018b; Brahm et al. 2018)	ConP
247142564	13	10.91	57850.73965	1.90	0.45	-		
247476672	13	2.33	57831.59449	3.01	0.89	-		

Table A.2 continued from previous page

EPIC #	Campaign #	P_{orb} (days)	t_C (days)	t_T (hrs)	Δ F (%)	# of RVs	Comments	Flag*
247548566	13	3.49	57876.97312	2.06	1.62	20	Undergoing RVFU (three incorrect points)	CandP
247576642	13	6.97	57866.88036	0.98	0.37	-		
247689275	13	3.75	57885.79959	4.90	1.27	-		
247740694	13	48.11	57825.07667	9.78	2.52	-		pFP
247773181	13	2.79	57834.39386	1.03	0.62	-		
247887989	13	11.02	57881.30455	1.65	0.16	-	Confirmed: K2-133 b, K2-133 c, K2-133 d (Wells et al. 2018)	ConP
247956487	13	35.37	57854.66151	6.53	1.06	3	RVs do not match planetary orbit phase	pFP
248545986	14	5.24	57934.39483	0.99	0.07	-	Confirmed: K2-239 b, K2-239 c, K2-239 d (Díez Alonso et al. 2018)	ConP
248874928	14	3.44	57929.61380	2.24	0.23	-		
201498078	14	11.64	57976.64802	4.12	0.29	-	Confirmed: K2-261 b (Johnson et al. 2018)	ConP
248777106	14	11.82	57984.69699	5.36	0.14	-	Confirmed: K2-234 b, HD 89345 b (Yu et al. 2018a; Van Eylen et al. 2018)	ConP
248758353	14	33.56	57909.01828	4.90	0.30	-		
248847494	14	54787.50	57967.12500	56.40	0.25	19	Monotransit candidate. Undergoing RVFU. (Giles et al. 2018b)	CandP

Table A.2 continued from previous page

EPIC #	Campaign #	P_{orb} (days)	t_C (days)	t_T (hrs)	Δ F (%)	# of RVs	Comments	Flag*
248651022	14	5.11	57925.95624	1.22	0.05	-		
248779118	14	11.55	57973.74599	2.16	3.28	1	Resolved as 2 stars in finding image.	pFP
248527709	14	5.75	57926.85486	2.56	0.11	-		
248827616	14	2.57	57947.61340	1.23	0.05	-		
248783679	14	5.95	57953.55913	1.56	0.32	-		pFP
248621597	14	17.27	57954.96964	4.40	0.04	-		pFP
201701882	14	39.65	57983.43140	2.77	2.80	4	Artefacts in CCFs and some RV shifts – SB1/SB2	pFP
248740871	14	26.54	57947.53243	5.53	0.05	-		
248618202	14	32.42	57948.47233	4.43	0.09	3	Strong RV/BIS correlation	pFP
248659495	14	38.84	57911.40870	4.66	2.48	2	Significant movement in RV values – SB1	pFP
249788281	15	5.30	58069.37376	1.44	0.75	1		pFP
249928278	15	4.19	58015.47527	2.34	0.42	19	Undergoing RVFU	
249703125	15	10.31	58000.86661	3.12	0.10	-		
249559552	15	7.82	58043.60985	2.52	0.09	-		
249451861	15	14.89	58016.61975	2.32	0.63	10	Confirmed: K2-287 b (Jordán et al. 2019)	ConP
249833762	15	4.96	58010.55169	4.68	0.03	-		

Table A.2 continued from previous page

EPIC #	Campaign #	P_{orb} (days)	t_C (days)	t_T (hrs)	Δ F (%)	# of RVs	Comments	Flag*
249884266	15	5.76	58021.85059	1.08	0.75	2	Significant movement in RV values – SB1	pFP
249846890	15	2.88	57995.57445	1.17	0.16	-		pFP/CandP
249378363	15	14.87	58032.82215	1.82	0.50	-		pFP/CandP
249707254	15	15.51	58009.97939	3.83	0.10	-		
249401470	15	8.91	57990.99750	2.05	0.11	-		
249447551	15	18.55	58068.02595	2.52	0.16	-		
249921188	15	17.56	58008.07939	2.20	0.38	-		
249541048	15	20.46	58039.29913	5.04	0.04	-		
249259371	15	11.85	58076.52588	1.75	0.15	-		
249865296	15	28.90	58008.40616	5.13	0.17	1	Undergoing RVFU	
249223471	15	22.55	58032.94463	3.66	0.20	3	No RV variation	
249624646	15	48.35	58043.38543	6.34	0.44	1	Confirmed: K2-290 b, K2-290 c (Hjorth et al. 2019)	ConP
249133524	15	2.99	58066.43268	7.17	0.06	-		
204440872	15	7.21	58069.45673	1.29	0.85	1		pFP
249883966	15	10.19	58016.70113	16.09	0.04	-		
249217698	15	5.09	58014.55640	2.85	0.97	1	Artefacts in CCFs – SB3	pFP

Table A.2 continued from previous page

EPIC #	Campaign #	P_{orb} (days)	t_C (days)	t_T (hrs)	Δ F (%)	# of RVs	Comments	Flag*
249675967	15	20.23	58033.43451	5.07	0.13	2	Significant movement in RV values – SB1	
249569027	15	29.20	58056.35932	3.56	0.07	2	Undergoing RVFU	
249401939	15	18.78	58061.44689	2.83	0.14	-		
249483417	15	1.22	58067.04514	0.88	0.30	6	No RV variation	
249252791	15	3.53	58045.59188	7.89	0.10	-		pFP
249344320	15	14.86	58041.36203	2.27	3.00	1	Asymmetric CCF	pFP
249830881	15	1.76	58076.30097	1.64	1.55	-		pFP
249708923	15	4.50	58035.15128	1.76	0.30	-		
249893012	15	15.62	58061.34415	6.15	0.04	-		
212110888	16	3.00	58111.93921	1.75	0.62	-	Confirmed: K2-34 b (Hirano et al. 2016; Lillo-Box et al. 2016; Brahm et al. 2016)	ConP
212036875	16	5.17	58150.37790	1.22	0.27	-		CandP
211432167	16	5.82	58130.94362	2.18	1.26	3	Strong RV/BIS correlation	pFP
212040382	16	4.45	58139.36304	2.71	0.48	-		CandP
211730024	16	5.11	58142.83693	2.17	0.12	1	Undergoing RVFU	CandP
211812935	16	3.61	58173.65365	2.11	0.56	-		CandP
211920604	16	9.48	58106.99339	9.85	0.20	1	Undergoing RVFU	pFP

Table A.2 continued from previous page

EPIC #	Campaign #	P_{orb} (days)	t_C (days)	t_T (hrs)	Δ F (%)	# of RVs	Comments	Flag*
211741619	16	2.79	58141.42730	0.84	0.12	-		CandP
251408535	16	5.17	58166.11320	2.25	0.15	-		
212204403	16	4.69	58162.35333	2.53	0.14	-		CandP
211945201	16	19.49	58152.93217	3.19	0.13	-	Confirmed: K2-236 b (Livingston et al. 2018; Chakraborty et al. 2018)	ConP
211647930	16	14.76	58112.16296	5.50	0.24	3	Undergoing RVFU	CandP
211919004	16	11.72	58110.09971	4.12	0.10	-	Confirmed: K2-273 b (Livingston et al. 2018)	ConP
211830293	16	20.88	58114.67670	4.05	0.80	3	Undergoing RVFU	CandP
211397844	16	16.17	58123.97482	2.77	1.58	-		pFP/CandP
211604981	16	12.43	58125.18032	4.09	1.61	1	Undergoing RVFU	pFP
211816003	16	14.45	58098.79855	2.98	0.11	-	Confirmed: K2-272 b (Livingston et al. 2018)	ConP
211886472	16	19.64	58134.39704	2.33	0.28	2	Undergoing RVFU	pFP/CandP
212048748	16	5.75	58153.01408	0.98	0.33	-		CandP
212165050	16	16.82	58138.34174	8.37	0.22	-		
212651234	17	2.54	58246.35611	2.58	1.37	-		
212697709	17	3.95	58221.99784	1.32	0.61	12	Confirmed: K2-41 b, WASP-157 b (Močnik et al. 2016)	ConP

Table A.2 continued from previous page

EPIC #	Campaign #	P_{orb} (days)	t_C (days)	t_T (hrs)	Δ F (%)	# of RVs	Comments	Flag*
212705192	17	2.27	58215.43797	1.42	0.62	2		
212735333	17	8.36	58187.68640	2.61	0.06	1	Confirmed: K2-197 b (Livingston et al. 2018; Mayo et al. 2018)	ConP
212779563	17	6.00	58209.36828	1.23	0.07	-	Confirmed: K2-262 b, Wolf 503 b (Peterson et al. 2018)	ConP
212803289	17	18.25	58182.72004	11.22	0.19	-	Confirmed: K2-99 b (Smith et al. 2017)	ConP
212628254	17	33.95	58231.23427	3.56	0.04	-	Confirmed: K2-292 b (Luque et al. 2019)	ConP
212689874	17	15.85	58223.93933	4.27	0.09	-	Confirmed: K2-195 b, K2-195c (Livingston et al. 2018; Mayo et al. 2018)	ConP
212672300	17	39.71	58236.03667	6.92	0.05	-	Confirmed: K2-194 b (Mayo et al. 2018)	ConP
212691422	17	50.00	-	-	-	-	Confirmed: K2-196 b (Mayo et al. 2018)	ConP
211309648	18	3.14	58279.59989	3.16	0.94	-		
211317649	18	3.33	58266.93169	2.61	1.40	-		
211391507	18	1.10	58277.59697	1.23	0.58	-		
211393988	18	4.87	58264.48022	3.46	0.56	-		
211417387	18	2.46	58296.82317	1.77	0.85	-		

Table A.2 continued from previous page

EPIC #	Campaign #	P_{orb} (days)	t_C (days)	t_T (hrs)	Δ F (%)	# of RVs	Comments	Flag*
211432167	18	5.82	58288.01765	2.16	1.24	3	Strong RV/BIS correlation	pFP
211480861	18	6.35	58273.61248	1.10	0.27	-		
211705502	18	2.58	58290.52986	1.01	0.14	-		
211713099	18	8.56	58262.82448	2.71	0.47	-	Confirmed: K2-271 b (Livingston et al. 2018)	ConP
211736671	18	4.73	58271.67130	3.17	0.08	-	Confirmed: K2-108 b (Petigura et al. 2017)	ConP
211800191	18	1.11	58265.72638	0.80	0.11	-		
211808055	18	3.38	58282.37801	3.21	0.14	-		pFP/CandP
211817572	18	2.26	58301.54234	1.01	0.41	-		
211818569	18	5.19	58289.61063	1.30	1.08	-	Confirmed: K2-121 b (Dressing et al. 2017)	ConP
211962097	18	5.84	58261.08831	4.23	0.84	-		
211993818	18	8.99	58272.38656	2.43	1.58	-		pFP
212110888	18	3.00	58300.66409	1.64	0.64	-	Confirmed: K2-34 b (Hirano et al. 2016; Lillo-Box et al. 2016; Brahm et al. 2016)	ConP
212099230	18	7.10	58269.30149	2.51	0.06	3	Undergoing RVFU	CandP
211490999	18	9.84	58268.54591	2.43	0.10	-		

Table A.2 continued from previous page

EPIC #	Campaign #	P_{orb} (days)	t_C (days)	t_T (hrs)	Δ F (%)	# of RVs	Comments	Flag*
211424769	18	5.18	58272.91820	1.01	0.43	-		
212164470	18	7.81	58300.62339	3.63	0.05	-	Confirmed: K2-188 b, K2-188 c (Livingston et al. 2018; Mayo et al. 2018)	ConP
211816003	18	14.46	58272.24415	3.96	0.12	-	Confirmed: K2-272 b (Livingston et al. 2018)	ConP
211921220	18	9.50	58296.70077	8.71	0.11	-		
211920604	18	9.48	58258.75890	10.24	0.17	1	Undergoing RVFU	pFP
211506851	18	10.54	58260.39341	2.47	0.10	-		
211442297	18	20.26	58292.45072	3.73	1.48	-	Confirmed: K2-115 b (Shporer et al. 2017; Livingston et al. 2018)	ConP
211342524	18	14.45	58290.83681	2.05	2.97	-		pFP
211919528	18	9.48	58258.73847	10.09	0.48	-		pFP
211730267	18	16.34	58287.81313	3.33	0.12	1	Undergoing RVFU	
211401787	18	13.77	58266.82935	4.52	0.03	5	Undergoing RVFU	
211391664	18	10.13	58271.18130	4.82	0.11	24	Confirmed: K2-98 b (Barragán et al. 2016)	ConP
211733267	18	8.66	58270.48682	0.97	0.52	2	Undergoing RVFU	CandP
211644764	18	23.52	58268.72950	2.63	0.18	1	Undergoing RVFU	
211822389	18	38.40	58262.76356	7.89	0.03	-		

Table A.2 continued from previous page

EPIC #	Campaign #	P_{orb} (days)	t_C (days)	t_T (hrs)	Δ F (%)	# of RVs	Comments	Flag*
211892898	18	-	-	55.20	0.80	-		
211390677	18	-	-	36.00	0.84	-		
212009578	18	-	-	24.00	8.00	-		

* These flags are defined from the ExoFOP-K2 catalog with their definitions as follows:

'pFP' - possible false-positive, 'CandP' - possible planet candidate, 'ConP' - confirmed planet.

Appendix B

Appendix: Other Publications

Here I include other publications which I contributed to in small ways which were outside of the scope of this thesis:

1) 'Ground-based photometry of the 21-day Neptune HD 106315c'
   Lendl et al. (2017)
2) 'Validation and Initial Characterization of the Long-period Planet Kepler-1654 b'
   Beichman et al. (2018)
3) 'An Earth-sized exoplanet with a Mercury-like composition'
   Santerne et al. (2018)
4) 'A Jovian planet in an eccentric 11.5 day orbit around HD 1397 discovered by *TESS*'
   Nielsen et al. (2019)
5) 'HD 213885b: A transiting 1-day-period super-Earth with an Earth-like composition around a bright (V = 7.9) star unveiled by TESS'
   Espinoza et al. (2019)
6) 'The CORALIE survey for southern extrasolar planets XVIII. Three new massive planets and two low mass brown dwarfs at separation larger than 5 AU'
   Rickman et al. (2019)

A&A 603, L5 (2017)
DOI: 10.1051/0004-6361/201731278

Astronomy & Astrophysics

Letter to the Editor

Ground-based photometry of the 21-day Neptune HD 106315c*

M. Lendl[1,2], D. Ehrenreich[2], O. D. Turner[2], D. Bayliss[2], S. Blanco-Cuaresma[2,3], H. Giles[2], F. Bouchy[2], M. Marmier[2], and S. Udry[2]

[1] Space Research Institute, Austrian Academy of Sciences, Schmiedlstr. 6, 8042 Graz, Austria
e-mail: monika.lendl@oeaw.ac.at
[2] Observatoire de Genève, Université de Genève, Chemin des maillettes 51, 1290 Sauverny, Switzerland
[3] Harvard-Smithsonian Center for Astrophysics, 60 Garden Street, Cambridge, MA 02138, USA

Received 30 May 2017 / Accepted 17 June 2017

ABSTRACT

Space-based transit surveys such as K2 and the Transiting Exoplanets Survey Satellite (TESS) allow the detection of small transiting planets with orbital periods greater than 10 days. Few of these warm Neptunes are currently known around stars bright enough to allow for detailed follow-up observations dedicated to their atmospheric characterization. The 21-day period and 3.95 $R_\oplus$ planet HD 106315c has been discovered by K2 based on the observation of two of its transits. We observed HD 106315 using the 1.2 m Euler telescope equipped with the EulerCam camera on two occasions to confirm the transit using broadband photometry and refine the planetary period. Based on two observed transits of HD 106315c, we detect its ~1 mmag transit and obtain a precise measurement of the planetary ephemerides, which are critical for planning further follow-up observations. We used the attained precision together with the predicted yield from the TESS mission to evaluate the potential for ground-based confirmation of Neptune-sized planets found by TESS. We find that one-meter class telescopes on the ground equipped with precise photometers could substantially contribute to the follow-up of 162 TESS candidates orbiting stars with magnitudes of $V \leq 14$. Of these candidates, 74 planets orbit stars with $V \leq 12$ and 12 planets orbit $V \leq 10$, which makes them high-priority objects for atmospheric characterization with high-end instrumentation.

Key words. techniques: photometric – planets and satellites: detection – planets and satellites: individual: HD 106315c

1. Introduction

Since the repurposing of the *Kepler* satellite (Borucki et al. 2009), the K2 mission (Howell et al. 2014) has been surveying a set of fields along the ecliptic for transiting planets. Largely increasing the number of bright stars observed compared to *Kepler's* original mission, K2 has been discovering an increasing number of small transiting planets orbiting bright stars (e.g., Vanderburg et al. 2015, 2016; Armstrong et al. 2015; Crossfield et al. 2015; Petigura et al. 2015). Thanks to their bright hosts, these objects are prime targets for atmospheric studies through optical and near-IR transmission spectroscopy both from the ground (e.g. Bean et al. 2010; Redfield et al. 2008; Lendl et al. 2016; Wyttenbach et al. 2015) and from space (Charbonneau et al. 2002; Deming et al. 2013; Sing et al. 2015), as well as exospheric characterization through UV observations (e.g., Vidal-Madjar et al. 2003; Fossati et al. 2010; Ehrenreich et al. 2015). Radial velocity observations efficiently provide precise planetary masses, and with well-determined stellar properties these objects are key for determining planetary mass-radius relations. After K2, the Transiting Exoplanets Survey Satellite (TESS, Ricker et al. 2015), foreseen for launch in 2018, will perform a nearly all-sky survey of bright stars, surveying 26 fields for at least 30 days each.

Of particular interest are planets at periods longer than ~10 days, which are outside the detection realm of ground-based surveys such as the Next-Generation Transit Survey (NGTS) (Wheatley et al. 2013), and inhabit a position in the parameter space currently ill-populated by objects bright enough for detailed follow-up[1]. One such object is the $V = 8.95$ F5V star HD 106315, which was observed by K2 during campaign 10, and found to be orbited by at least two planetary-mass objects, a 2.23 $R_\oplus$ super-Earth at an orbital period of 9.55 days and a warm 21-day period 3.95 $R_\oplus$ Neptune (Crossfield et al. 2017; Rodriguez et al. 2017, hereafter C17 and R17).

The very nature of warm transiting planets such as HD 106315c, namely their long orbital periods and thus rare transits events, poses a major limitation to their efficient further study because predicted ephemerides are uncertain. In the case of HD 106315c[2], the 3σ timing uncertainty for possible early JWST observations in mid-2019 amounts to 7.1 h, making observations inefficient and challenging to schedule.

In this letter, we present ground-based transit observations HD 106315c, and illustrate how flexible ground-based follow-up can resolve this issue for a large fraction of transiting planets expected from TESS.

2. Observations, data reduction, and analysis

2.1. Transit observations of HD 106315 c

We observed HD 106315 during two transits of planet c with EulerCam at the 1.2 m *Euler*-Swiss telescope at the ESO La Silla site. Both observations were carried out using an I-Cousins filter, applying a substantial telescope defocus to allow for an improved observation efficiency. The main properties of the observations are summarized in Table 1 (see Lendl et al. 2012, for

* The photometric time series data are only available at the CDS via anonymous ftp to cdsarc.u-strasbg.fr (130.79.128.5) or via http://cdsarc.u-strasbg.fr/viz-bin/qcat?J/A+A/603/L5

[1] A query of exoplanet.eu and exoplanets.org on 21 May 2017 reveals only 12 planets with $V < 10$ mag, $R_P < 0.5 R_J$ and $P > 15$ days.
[2] $P = 21.0576^{+0.0020}_{-0.0019}$, $T_0 = 2457611.131 \pm 0.0012$ (C17).

The Astronomical Journal, 155:158 (11pp), 2018 April https://doi.org/10.3847/1538-3881/aaaeb6

Validation and Initial Characterization of the Long-period Planet Kepler-1654 b

C. A. Beichman[1], H. A. C. Giles[2], R. Akeson[1], D. Ciardi[1], J. Christiansen[1], H. Isaacson[3], G. M. Marcy[3], E. Sinukoff[4], T. Greene[5], J. J. Fortney[6], I. Crossfield[7], R. Hu[8], A. W. Howard[9], E. A. Petigura[9], and H. A. Knutson[9]
[1] NASA Exoplanet Science Institute and Infrared Processing and Analysis Center, California Institute of Technology, Jet Propulsion Laboratory, Pasadena, CA 91125, USA
[2] Observatoire Astronomique de l'Université de Genève, Switzerland
[3] University of California at Berkeley, Berkeley, CA, USA
[4] Institute for Astronomy, University of Hawaii, 2680 Woodlawn Drive, Honolulu, HI 96822, USA
[5] NASA Ames Research Center, Mountain View, CA 94035, USA
[6] University of California Santa Cruz, 1156 High Street, Santa Cruz, CA 95064, USA
[7] Massachusetts Institute of Technology, 77 Massachusetts Avenue, Cambridge, MA 02139, USA
[8] Jet Propulsion Laboratory, California Institute of Technology, 4800 Oak Grove Drive, Pasadena, CA 91125, USA
[9] California Institute of Technology, 1200 East California Boulevard, Pasadena, CA 91125, USA
Received 2017 December 27; revised 2018 January 29; accepted 2018 February 8; published 2018 March 20

Abstract

Fewer than 20 transiting *Kepler* planets have periods longer than one year. Our early search of the *Kepler* light curves revealed one such system, Kepler-1654b (originally KIC 8410697b), which shows exactly two transit events and whose second transit occurred only five days before the failure of the second of two reaction wheels brought the primary *Kepler* mission to an end. A number of authors have also examined light curves from the *Kepler* mission searching for long-period planets and identified this candidate. Starting in 2014 September, we began an observational program of imaging, reconnaissance spectroscopy, and precision radial velocity (RV) measurements that confirm with a high degree of confidence that Kepler-1654b is a *bona fide* transiting planet orbiting a mature G5V star ($T_{\rm eff} = 5580$ K, [Fe/H] $= -0.08$) with a semimajor axis of 2.03 au, a period of 1047.84 days, and a radius of 0.82 ± 0.02 $R_{\rm Jup}$. RV measurements using Keck's HIRES spectrometer obtained over 2.5 years set a limit to the planet's mass of <0.5 (3σ) $M_{\rm Jup}$. The bulk density of the planet is similar to that of Saturn or possibly lower. We assess the suitability of temperate gas giants like Kepler-1654b for transit spectroscopy with the *James Webb Space Telescope*, as their relatively cold equilibrium temperatures ($T_{\rm pl} \sim 200$ K) make them interesting from the standpoint of exoplanet atmospheric physics. Unfortunately, these low temperatures also make the atmospheric scale heights small and thus transmission spectroscopy challenging. Finally, the long time between transits can make scheduling *JWST* observations difficult—as is the case with Kepler-1654b.

Key words: planetary systems – planets and satellites: detection

1. Introduction

The *Kepler* mission (Borucki et al. 2010) has revolutionized our understanding of exoplanets, finding over 2300 confirmed planets and almost 4500 candidates[10] (Batalha et al. 2013). These data have improved our knowledge of the constituents of the inner solar system with an inventory that includes planets ranging from less than an Earth radius (Kepler 37b) up to 1.5 Jupiter radii (Kepler 12b), and periods ranging from less than a day (Kepler 78b) up to 1100 days, including Kepler 167 (Kipping et al. 2016) and Kepler 1647 (Kostov et al. 2016). A number of non-transiting *Kepler* planets with longer periods were identified by their radial velocity (RV) signature, e.g., Kepler 407c with a period of order 3000 days (Marcy et al. 2014). The completeness of the *Kepler* catalog is poor for long-period planets. These objects are hard to find a priori, as the transit probability decreases with increasing semimajor axis and because fewer transits are observable in a given observing period. A smaller number of events reduces the total signal-to-noise-ratio (S/N) achievable by averaging multiple transits. Most importantly, the *Kepler* pipeline required three or more potential transits before promoting a star to become a *Kepler* Object of Interest, or KOI, worthy of further investigation. (Jenkins et al. 2010).

To avoid the *Kepler* pipeline's prohibition against planets with one or two transits, we analyzed *Kepler* light curves *not identified* with confirmed planets, *Kepler* candidates, or KOI's. As described below, this search was rewarded with the detection of a Jupiter-sized planet in a 2.87 year (1047.836 day) period orbiting a mid-G star, KIC 8410697, which we now refer to as Kepler-1654. A more complete search for long-period systems was carried out by the Planet Hunters group (Wang et al. 2015) who identified a number of systems with one and two transits. In the case of Kepler-1654, they found only the first of its two transits. Foreman-Mackey et al. (2016) identified seven new transiting systems, showing one or at most two transits, and eight long-period planets identified with known *Kepler* systems having at least one shorter period planet.

This paper describes follow-up observations of Kepler-1654 using the W. M. Keck Observatory that have allowed us to reject a variety of alternative ("false-positive") interpretations, fully characterize the host star, and set an upper limit to its mass to be less than $0.48\,M_{\rm Jup}$ (3σ). Section 2 describes the search through the *Kepler* light curves. Section 3 presents the follow-up observations of the star, and Section 4 presents the characterization of the planet. Section 5 investigates the

[10] As of December 2107 for *Kepler* with an additional 170 confirmed planets for K2, http://exoplanetarchive.ipac.caltech.edu/.

nature astronomy

LETTERS

https://doi.org/10.1038/s41550-018-0420-5

An Earth-sized exoplanet with a Mercury-like composition

A. Santerne[1*], B. Brugger[1], D. J. Armstrong[2], V. Adibekyan[3], J. Lillo-Box[4], H. Gosselin[1,5], A. Aguichine[1,6], J.-M. Almenara[7], D. Barrado[8], S. C. C. Barros[3], D. Bayliss[7], I. Boisse[1], A. S. Bonomo[9], F. Bouchy[7], D. J. A. Brown[2], M. Deleuil[1], E. Delgado Mena[3], O. Demangeon[3], R. F. Díaz[7,10,11], A. Doyle[2], X. Dumusque[7], F. Faedi[2,12], J. P. Faria[3,13], P. Figueira[3,4], E. Foxell[2], H. Giles[7], G. Hébrard[14,15], S. Hojjatpanah[3,13], M. Hobson[1], J. Jackman[2], G. King[2], J. Kirk[2], K. W. F. Lam[2], R. Ligi[1], C. Lovis[7], T. Louden[2], J. McCormac[2], O. Mousis[1], J. J. Neal[3,13], H. P. Osborn[1,2], F. Pepe[7], D. Pollacco[2], N. C. Santos[3,13], S. G. Sousa[3], S. Udry[7] and A. Vigan[1]

Earth, Venus, Mars and some extrasolar terrestrial planets[1] have a mass and radius that is consistent with a mass fraction of about 30% metallic core and 70% silicate mantle[2]. At the inner frontier of the Solar System, Mercury has a completely different composition, with a mass fraction of about 70% metallic core and 30% silicate mantle[3]. Several formation or evolution scenarios are proposed to explain this metal-rich composition, such as a giant impact[4], mantle evaporation[5] or the depletion of silicate at the inner edge of the protoplanetary disk[6]. These scenarios are still strongly debated. Here, we report the discovery of a multiple transiting planetary system (K2-229) in which the inner planet has a radius of 1.165 ± 0.066 Earth radii and a mass of 2.59 ± 0.43 Earth masses. This Earth-sized planet thus has a core-mass fraction that is compatible with that of Mercury, although it was expected to be similar to that of Earth based on host-star chemistry[7]. This larger Mercury analogue either formed with a very peculiar composition or has evolved, for example, by losing part of its mantle. Further characterization of Mercury-like exoplanets such as K2-229 b will help to put the detailed in situ observations of Mercury (with MESSENGER and BepiColombo[8]) into the global context of the formation and evolution of solar and extrasolar terrestrial planets.

The star EPIC 228801451 (TYC 4947-834-1; 2MASS J12272958-0643188; K2-229) was observed in photometry as part of campaign 10 of the K2 mission with the Kepler space telescope, from 2016 July 6 to 2016 September 20 with a 30 min cadence. Analysis of the extracted and reduced light curve using the POLAR (Planet candidates from OptimaL Aperture Reduction) pipeline[9] revealed two sets of periodic planetary transit-like events on periods of about 14 h and 8.3 d. A single transit-like event near the mid-campaign time was also detected (see Fig. 1 and Methods). We refer to these planets as K2-229 b, c and d, respectively. The light curve exhibits a large modulation with a 2% peak-to-peak amplitude and 18 d period variability (see Fig. 1) that is caused by the presence of active regions (spots and/or faculae). The star is a bright (magnitude in the visual wavelength band $V = 11$ mag, following the Vega magnitude system) late-G/early-K dwarf[10], and hence is suitable for precise radial velocity (RV) observations.

We observed EPIC 228801451 with the HARPS (High Accuracy Radial velocity Planet Searcher) spectrograph with the aim of confirming the planetary nature of the transiting candidates and measuring the mass through Doppler spectroscopy. We collected 120 RVs from 2017 January 26 to 2017 May 4 with up to four observations each night. We reduced the spectra using the online pipeline available at the telescope and derived the RV, the full-width at half-maximum (FWHM) and the bisector (BIS) of the averaged line profile, as well as the spectroscopic indices of chromospheric activity in the core of five spectral lines (see Methods and Supplementary Tables 3 and 4). The pipeline automatically rejected one poor-quality spectrum.

To assess the planetary nature of the detected transit signals and rule out the presence of background stellar objects contaminating the light curve, we performed high-resolution imaging observations with the AstraLux lucky-imaging instrument. No background or stellar companion is detected within the sensitivity limits of the data and within the photometric mask (see Methods and Supplementary Fig. 2).

We co-added the HARPS spectra and derived the spectral parameters of the host star[11] (see Methods). We find that the host star has an effective temperature $T_{\rm eff} = 5{,}120 \pm 39$ K, a surface gravity $\log g = 4.51 \pm 0.12$, an iron/hydrogen abundance ratio $[{\rm Fe/H}] = -0.06 \pm 0.02$ decimal exponents (dex), where the square brackets indicate that the ratio is the log relative to solar values, and a microturbulence velocity $v_{\rm mic} = 0.74 \pm 0.08\,{\rm km\,s^{-1}}$. This identifies the host

[1]Aix Marseille Univ., CNRS, LAM, Laboratoire d'Astrophysique de Marseille, Marseille, France. [2]Department of Physics, University of Warwick, Coventry, UK. [3]Instituto de Astrofísica e Ciências do Espaço, Universidade do Porto, CAUP, Porto, Portugal. [4]European Southern Observatory (ESO), Santiago de Chile, Chile. [5]Université de Toulouse, UPS-OMP, IRAP, Toulouse, France. [6]Paris-Saclay Université, ENS Cachan, Cachan, France. [7]Observatoire Astronomique de l'Université de Genève, Versoix, Switzerland. [8]Depto. de Astrofísica, Centro de Astrobiología (CSIC-INTA), Madrid, Spain. [9]INAF—Osservatorio Astrofisico di Torino, Pino Torinese, Italy. [10]Universidad de Buenos Aires, Facultad de Ciencias Exactas y Naturales, Buenos Aires, Argentina. [11]CONICET—Universidad de Buenos Aires, Instituto de Astronomía y Física del Espacio (IAFE), Buenos Aires, Argentina. [12]INAF—Osservatorio Atrofisico di Catania, Catania, Italy. [13]Departamento de Física e Astronomia, Faculdade de Ciencias, Universidade do Porto, Porto, Portugal. [14]Institut d'Astrophysique de Paris, UMR7095 CNRS, Universite Pierre & Marie Curie, Paris, France. [15]Aix Marseille Univ., CNRS, OHP, Observatoire de Haute Provence, Saint Michel l'Observatoire, France. *e-mail: alexandre.santerne@lam.fr

A&A 623, A100 (2019)
https://doi.org/10.1051/0004-6361/201834577

Astronomy & Astrophysics

A Jovian planet in an eccentric 11.5 day orbit around HD 1397 discovered by TESS

L. D. Nielsen[1], F. Bouchy[1], O. Turner[1], H. Giles[1], A. Suárez Mascareño[1], C. Lovis[1], M. Marmier[1], F. Pepe[1], D. Ségransan[1], S. Udry[1], J. F. Otegi[1,2], G. Ottoni[1], M. Stalport[1], G. Ricker[8], R. Vanderspek[8], D. W. Latham[7], S. Seager[8,12], J. N. Winn[13], J. M. Jenkins[14], S. R. Kane[3], R. A. Wittenmyer[4], B. Bowler[18], I. Crossfield[8], J. Horner[4], J. Kielkopf[19], T. Morton[20], P. Plavchan[21], C. G. Tinney[22], Hui Zhang[23], D. J. Wright[4], M. W. Mengel[4], J. T. Clark[4], J. Okumura[4], B. Addison[4], D. A. Caldwell[5,14], S. M. Cartwright[6], K. A. Collins[7], J. Francis[8], N. Guerrero[8], C. X. Huang[8], E. C. Matthews[8], J. Pepper[9], M. Rose[10], J. Villaseñor[8], B. Wohler[5,14], K. Stassun[11], S. Howell[14], D. Ciardi[15], E. Gonzales[16], R. Matson[14], C. Beichman[15], and J. Schlieder[17]

[1] Geneva Observatory, University of Geneva, Chemin des Mailettes 51, 1290 Versoix, Switzerland
e-mail: Louise.Nielsen@unige.ch
[2] Institute for Computational Science, University of Zurich, Winterthurerstrasse 190, 8057 Zurich, Switzerland
[3] Department of Earth Sciences, University of California, Riverside, CA 92521, USA
[4] University of Southern Queensland, Centre for Astrophysics, Toowoomba, QLD 4530, Australia
[5] SETI Institute, Mountain View, CA 94043, USA
[6] Proto-Logic LLC, Washington, DC 20009, USA
[7] Harvard-Smithsonian Center for Astrophysics, 60 Garden Street, Cambridge, MA 02138, USA
[8] Department of Physics and Kavli Institute for Astrophysics and Space Research, MIT, Cambridge, MA 02139, USA
[9] Department of Physics, Lehigh University, 16 Memorial Drive East, Bethlehem, PA 18015, USA
[10] Leidos/NASA Ames Research Center, Moffett Field, CA 94035, USA
[11] Department of Physics & Astronomy, Vanderbilt University, 6301 Stevenson Center Ln., Nashville, TN 37235, USA
[12] Department of Earth, Atmospheric, and Planetary Sciences, and Department of Aeronautics and Astronautics, MIT, 77 Massachusetts Avenue, Cambridge, MA 02139, USA
[13] Department of Astrophysical Sciences, Princeton University, 4 Ivy Lane, Princeton, NJ 08544, USA
[14] NASA Ames Research Center, Moffett Field, CA 94035, USA
[15] Caltech/IPAC-NASA Exoplanet Science Institute, M/S 100-22, 770 S. Wilson Ave, Pasadena, CA 91106, USA
[16] UC Santa Cruz, Department of Astronomy & Astrophysics, 1156 High Street, Santa Cruz, CA 95064, USA
[17] NASA Goddard Space Flight Center, 8800 Greenbelt Rd., Greenbelt, MD 20771, USA
[18] Department of Astronomy, The University of Texas at Austin, 2515 Speedway C1400, Austin, TX 78712, USA
[19] Department of Physics and Astronomy, University of Louisville, Louisville, KY 40292, USA
[20] Astronomy Department, University of Florida, 211 Bryant Space Science Center, PO Box 112055, Gainesville, FL 32611-2055, USA
[21] Department of Physics and Astronomy, George Mason University, Fairfax, VA 22030, USA
[22] Exoplanetary Science at UNSW, School of Physics, UNSW Sydney, NSW 2052, Australia
[23] School of Astronomy and Space Science, Key Laboratory of Ministry of Education, Nanjing University, Nanjing, PR China

Received 5 November 2018 / Accepted 18 February 2019

ABSTRACT

The Transiting Exoplanet Survey Satellite TESS has begun a new age of exoplanet discoveries around bright host stars. We present the discovery of HD 1397b (TOI-120.01), a giant planet in an 11.54-day eccentric orbit around a bright ($V = 7.9$) G-type subgiant. We estimate both host star and planetary parameters consistently using *EXOFASTv2* based on TESS time-series photometry of transits and radial velocity measurements with CORALIE and MINERVA-Australis. We also present high angular resolution imaging with NaCo to rule out any nearby eclipsing binaries. We find that HD 1397b is a Jovian planet, with a mass of $0.415 \pm 0.020\ M_J$ and a radius of $1.026 \pm 0.026\ R_J$. Characterising giant planets in short-period eccentric orbits, such as HD 1397b, is important for understanding and testing theories for the formation and migration of giant planets as well as planet-star interactions.

Key words. planets and satellites: detection – planets and satellites: individual: HD 1397b – planets and satellites: individual: TOI-120 – planets and satellites: individual: 394137592

1. Introduction

Transiting exoplanets offer a unique window into exoplanetology, because we can measure both the mass and radius of the planet, and thereby place constraints on the interior structure. Atmospheric characterisation is also possible through transmission spectroscopy, thus enabling a full understanding of bulk properties and atmosphere.

After the recent end of the NASA *Kepler* and K2 missions, the exoplanet-finding torch has truly been passed on to the Transiting Exoplanet Survey Satellite (TESS; Ricker et al. 2015). Since the start of science operations on July 25, 2018, TESS has

MNRAS 000, 1–19 (2015) Preprint 20 March 2019 Compiled using MNRAS LATEX style file v3.0

HD 213885b: A transiting 1-day-period super-Earth with an Earth-like composition around a bright (V = 7.9) star unveiled by TESS

Néstor Espinoza[1]★†‡, Rafael Brahm[2,3,4], Thomas Henning[1], Andrés Jordán[3,4], Caroline Do
Felipe Rojas[3,4], Paula Sarkis[1], Diana Kossakowski[1] Matías Díaz[6], James S. Jenkins[6],
Claudia Aguilera-Gomez[7], Jon M. Jenkins[8], Joseph D. Twicken[9], Karen A. Collins[10],
Jack Lissauer[8], David J. Armstrong[11,12], Vardan Adibekyan[13], David Barrado[14],
Susana C. C. Barros[13], Matthew Battley[11,12], Daniel Bayliss[11,12], François Bouchy[15],
Edward Bryant[11,12], Benjamin F. Cooke[11,12], Olivier D. S. Demangeon[13], Xavier Dumusqu
Pedro Figueira[16,12], Helen Giles[15], Jorge Lillo-Box[16], Christophe Lovis[15], Louise D. Nielser
Francesco Pepe[15], Don Pollaco[11], Nuno C. Santos[13,17], Sergio G. Sousa[13], Stéphane Udry[15]
Peter J. Wheatley[11,12], Oliver Turner[15], Maxime Marmier[15], Damien Ségransan[15],
George Ricker[18], David Latham[10], Sara Seager[18], Joshua N. Winn[19], John F. Kielkopf[20],
Rhodes Hart[21], Geof Wingham[22], Eric L. N. Jensen[24], Krzysztof G. Hełminiak[24],
A. Tokovinin[25], C. Briceño[25], Carl Ziegler[26], Nicholas M. Law[27], Andrew W. Mann[27],
Tansu Daylan[17]§, John P. Doty[28], Natalia Guerrero[17], Patricia Boyd[29], Ian Crossfield[18],
Robert L. Morris[9,8], Christopher E. Henze[8], Aaron Dean Chacon[30,8]
The authors' affiliations are shown in Appendix A.

Accepted XXX. Received YYY; in original form ZZZ

ABSTRACT

We report the discovery of the 1.008-day, ultra-short period (USP) super-Earth HD 213885b (TOI-141b) orbiting the bright (V = 7.9) star HD 213885 (TOI-141, TIC 403224672), detected using photometry from the recently launched *TESS* mission. Using FEROS, HARPS and CORALIE radial-velocities, we measure a precise mass of $8.83^{+0.66}_{-0.65} M_\oplus$ for this $1.745^{+0.051}_{-0.052} R_\oplus$ exoplanet, which provides enough information to constrain its bulk composition, which is similar to Earth's composition but enriched in iron. The radius, mass and stellar irradiation of HD 213885b are almost indistinguishable from that of 55 Cancri e, making this exoplanet its first "twin" in terms of its physical properties — HD 213885b, however, appears to be denser ($9.15^{+1.1}_{-1.0}$ gr cm^{-3}) than 55 Cancri e. Our precise radial-velocities reveal an additional 4.78-day signal which we interpret as arising from a second, non-transiting planet in the system, HD 213885c, which has a minimum mass of $19.95^{+1.38}_{-1.36} M_\oplus$ and thus is consistent with being a Neptune-mass exoplanet. The HD 213885 system is very interesting from the perspective of future atmospheric characterization, being the second brightest star to host an ultra-short period transiting super-Earth (with the brightest star being, in fact, 55 Cancri). Prospects for characterization with present and future observatories are discussed.

Key words: HD 213885 – TOI-141 – TIC 403224672

★ E-mail: espinoza@mpia.de (NE) † Bernoulli Fellow

Astronomy & Astrophysics manuscript no. main
April 4, 2019

The CORALIE survey for southern extrasolar planets XVIII ⋆ ⋆⋆

Three new massive planets and two low mass brown dwarfs at separation larger than 5 AU

E. L. Rickman[1], D. Ségransan[1], M. Marmier[1], S. Udry[1], F. Bouchy[1], C. Lovis[1], M. Mayor[1], F. Pepe[1], D. Queloz[1], N. C. Santos[2,3], R. Allart[1], V. Bonvin[4], P. Bratschi[1], F. Cersullo[1], B. Chazelas[1], A. Choplin[1], U. Conod[1], A. Deline[1], J.-B. Delisle[1], L. A. Dos Santos[1], P. Figueira[5,2], H. A. C. Giles[1], M. Girard[1], B. Lavie[1], D. Martin[1,6,7], F. Motalebi[1], L. D. Nielsen[1], H. Osborn[8,9], G. Ottoni[1], M. Raimbault[1], J. Rey[1,10], T. Roger[1,11], J. V. Seidel[1], M. Stalport[1], A. Suárez Mascareño[1,12], A. Triaud[13], O. Turner[1], L. Weber[1], A. Wyttenbach[1,14]

(Affiliations can be found after the references)

Received; accepted

ABSTRACT

Context. Since 1998, a planet-search around main sequence stars within 50 pc in the southern hemisphere has been carried out with the CORALIE spectrograph at La Silla Observatory.
Aims. With an observing time span of more than 20 years, the CORALIE survey is able to detect long term trends in data with masses and separations large enough to select ideal targets for direct imaging. Detecting these giant companion candidates will allow us to start bridging the gap between radial velocity detected exoplanets and directly imaged planets and brown dwarfs.
Methods. Long-term precise Doppler measurements with the CORALIE spectrograph reveal radial velocity signatures of massive planetary companions and brown dwarfs on long-period orbits.
Results. In this paper we report the discovery of new companions orbiting HD 181234, HD 13724, HD 25015, HD 92987 and HD 50499. We also report updated orbital parameters for HD 50499b, HD 92788b and HD 98649b. In addition, we confirm the recent detection of HD 92788c. The newly reported companions span a period range of 15.6 to 40.4 years and a mass domain of 2.93 to 26.77 $M_{\rm Jup}$, the latter of which straddles the nominal boundary between planets and brown dwarfs.
Conclusions. We have reported the detection of five new companions and updated parameters of four known extrasolar planets. We identify at least some of these companions to be promising candidates for imaging and further characterisation.

Key words. planetary systems – binaries: visual – planets and satellites: detection – techniques: radial velocities – stars: individual – HD 181234, HD 13724, HD 25015, HD 92987, HD 98649, HD 50499, HD 92788

1. Introduction

Little is known about massive giant planets and brown dwarfs at orbital separations between 5 and 50 AU due to their low occurrence rate (Bowler 2016) and to the lower sensitivity of the different observing methods in this separation range. Indeed, radial velocities and transit techniques are extremely efficient to detect planets around older stars at short separations (Fischer et al. 2014). On the other hand, direct imaging is most efficient at detecting younger planets at separations larger than several times the diffraction limit of the telescope (typically 5 to 10 λ/D). This translates into several tens of astronomical units for the closest young stellar associations (e.g. β Pic and 51 Eri as part of the β Pic moving group (Zuckerman et al. 2001; Feigelson et al. 2006) and HR 8799 as part of the Columba association (Zuckerman et al. 2011)). And yet, the population of massive giant exoplanets at intermediate orbital separations between 5 - 50 AU is an important puzzle piece needed for constraining the uncertainties that exist in planet formation and evolution models.

The historical CORALIE planet-search survey has been ongoing for more than 20 years in the southern hemisphere and monitors a volume limited sample of 1647 main sequence stars from F8 down to K0 located within 50 pc of the Sun (Udry et al. 2000). With an individual measurement precision ranging between 3.5 and 6 $\rm ms^{-1}$, CORALIE has allowed the detection (or has contributed to the detection) of more than 140 extra-solar planet candidates (Pepe et al. 2002; Udry et al. 2002; Tamuz et al. 2008; Ségransan et al. 2010; Marmier et al. 2013). Such a long and contin-

⋆ Based on observations collected with the CORALIE spectrograph mounted on the 1.2 m Swiss telescope at La Silla Observatory and with the HARPS spectrograph on the ESO 3.6 m telescope at La Silla (ESO, Chile).
⋆⋆ The radial velocity measurements and additional data products discussed in this paper are available on the DACE web platform at https://dace.unige.ch/radialVelocities. See the appendix for a direct link to the individual target data products.

Bibliography

Abetti, G. 1957, The Sun. (Faber & Faber)

Abubekerov, M. K. & Gostev, N. Y. 2013, MNRAS, 432, 2216

Agol, E., Steffen, J., Sari, R., & Clarkson, W. 2005, MNRAS, 359, 567

Aigrain, S., Pont, F., & Zucker, S. 2012, MNRAS, 419, 3147

Alonso, R., Brown, T. M., Torres, G., et al. 2004, ApJ, 613, L153

Anderson, D. R., Collier Cameron, A., Hellier, C., et al. 2015, A&A, 575, A61

Armstrong, D. J., Pollacco, D., & Santerne, A. 2017, MNRAS, 465, 2634

Auvergne, M., Bodin, P., Boisnard, L., et al. 2009, A&A, 506, 411

Bakos, G. Á., Torres, G., Pál, A., et al. 2010, ApJ, 710, 1724

Ballard, S., Fabrycky, D., Fressin, F., et al. 2011, ApJ, 743, 200

Balthasar, H. & Woehl, H. 1983, Sol. Phys., 88, 71

Baraffe, I., Chabrier, G., & Barman, T. 2010, Reports on Progress in Physics, 73, 016901

Baranne, A., Queloz, D., Mayor, M., et al. 1996, A&AS, 119, 373

Barclay, T., Pepper, J., & Quintana, E. V. 2018, ApJS, 239, 2

Barragán, O., Grziwa, S., Gandolfi, D., et al. 2016, AJ, 152, 193

Bastien, F. A., Stassun, K. G., Basri, G., & Pepper, J. 2013, Nature, 500, 427

Bayliss, D. D. R., Weldrake, D. T. F., Sackett, P. D., Tingley, B. W., & Lewis, K. M. 2009, AJ, 137, 4368

Beichman, C. A., Giles, H. A. C., Akeson, R., et al. 2018, AJ, 155, 158

Berdiñas, Z. M., Amado, P. J., Anglada-Escudé, G., Rodríguez-López, C., & Barnes, J. 2016, MNRAS, 459, 3551

Berdyugina, S. V. 2002, Astronomische Nachrichten, 323, 192

Berdyugina, S. V. & Solanki, S. K. 2002, A&A, 385, 701

Berdyugina, S. V., Solanki, S. K., & Frutiger, C. 2003, A&A, 412, 513

Biermann, L. 1941, Vierteljahresschrift der Astronomischen Gesellschaft, 76, 194

Bogdan, T. J., Gilman, P. A., Lerche, I., & Howard, R. 1988, ApJ, 327, 451

Boisse, I., Bonfils, X., & Santos, N. C. 2012, A&A, 545, A109

Boisse, I., Bouchy, F., Hébrard, G., et al. 2011, A&A, 528, A4

Bond, I. A., Udalski, A., Jaroszyński, M., et al. 2004, ApJ, 606, L155

Bonomo, A. S. & Lanza, A. F. 2012, A&A, 547, A37

Bopp, B. W. & Evans, D. S. 1973, MNRAS, 164, 343

Borucki, W. J., Koch, D., Basri, G., et al. 2010, Science, 327, 977

Bouchy, F., Hébrard, G., Udry, S., et al. 2009, A&A, 505, 853

Bradshaw, S. J. & Hartigan, P. 2014, ApJ, 795, 79

Brahm, R., Espinoza, N., Jordán, A., et al. 2018, MNRAS, 477, 2572

Brahm, R., Jones, M., Espinoza, N., et al. 2016, PASP, 128, 124402

Bray, R. J. & Loughhead, R. E. 1964, Sunspots (Chapman & Hall)

Broeg, C., Fortier, A., Ehrenreich, D., et al. 2013, in European Physical Journal Web of Conferences, Vol. 47, European Physical Journal Web of Conferences, 03005

Budding, E. 1977, Ap&SS, 48, 207

Carter, J. A., Winn, J. N., Holman, M. J., et al. 2011, ApJ, 730, 82

Casanovas, J. 1997, in Astronomical Society of the Pacific Conference Series, Vol. 118, 1st Advances in Solar Physics Euroconference. Advances in Physics of Sunspots, ed. B. Schmieder, J. C. del Toro Iniesta, & M. Vazquez, 3

Catalano, S., Biazzo, K., Frasca, A., & Marilli, E. 2002, A&A, 394, 1009

Catalano, S. & Rodonò, M. 1967, Mem. Soc. Astron. Italiana, 38, 395

Cegla, H. M., Shelyag, S., Watson, C. A., & Mathioudakis, M. 2013, ApJ, 763, 95

Cegla, H. M., Watson, C. A., Marsh, T. R., et al. 2012, MNRAS, 421, L54

Cegla, H. M., Watson, C. A., Shelyag, S., Mathioudakis, M., & Moutari, S. 2019, ApJ, 879, 55

Chakraborty, A., Roy, A., Sharma, R., et al. 2018, AJ, 156, 3

Charbonneau, D., Brown, T. M., Latham, D. W., & Mayor, M. 2000, ApJ, 529, L45

Chauvin, G., Lagrange, A.-M., Dumas, C., et al. 2004, A&A, 425, L29

Chugainov, P. F. 1966, Information Bulletin on Variable Stars, 122

Claret, A. & Bloemen, S. 2011, A&A, 529, A75

Cosentino, R., Lovis, C., Pepe, F., et al. 2012, in Proc. SPIE, Vol. 8446, Ground-based and Airborne Instrumentation for Astronomy IV, 84461V

Cranmer, S. R., Bastien, F. A., Stassun, K. G., & Saar, S. H. 2014, ApJ, 781, 124

Czesla, S., Huber, K. F., Wolter, U., Schröter, S., & Schmitt, J. H. M. M. 2009, A&A, 505, 1277

Davenport, J. 2015, PhD thesis, University of Washington

Davenport, J. R. A., Hebb, L., & Hawley, S. L. 2015, ApJ, 806, 212

Davies, R. & Kasper, M. 2012, ARA&A, 50, 305

Demangeon, O. D. S., Faedi, F., Hébrard, G., et al. 2018, A&A, 610, A63

Deutsch, A. J. 1958, in IAU Symposium, Vol. 6, Electromagnetic Phenomena in Cosmical

Physics, ed. B. Lehnert, 209

Deutsch, A. J. 1970, ApJ, 159, 985

Díez Alonso, E., González Hernández, J. I., Suárez Gómez, S. L., et al. 2018, MNRAS, 480, L1

Donati, J.-F. & Brown, S. F. 1997, A&A, 326, 1135

Donati, J.-F. & Collier Cameron, A. 1997, MNRAS, 291, 1

Dorren, J. D. 1987, ApJ, 320, 756

Doyle, L. R., Carter, J. A., Fabrycky, D. C., et al. 2011, Science, 333, 1602

Dressing, C. D., Vanderburg, A., Schlieder, J. E., et al. 2017, AJ, 154, 207

Dumusque, X., Boisse, I., & Santos, N. C. 2014, ApJ, 796, 132

Dumusque, X., Santos, N. C., Udry, S., Lovis, C., & Bonfils, X. 2011a, A&A, 527, A82

Dumusque, X., Udry, S., Lovis, C., Santos, N. C., & Monteiro, M. J. P. F. G. 2011b, A&A, 525, A140

Dunn, R. B. & Zirker, J. B. 1973, Sol. Phys., 33, 281

Eastman, J. 2017, EXOFASTv2: Generalized publication-quality exoplanet modeling code, Astrophysics Source Code Library

Eastman, J., Gaudi, B. S., & Agol, E. 2013, PASP, 125, 83

Eaton, J. A. & Hall, D. S. 1979, ApJ, 227, 907

Eberhard, G. & Schwarzschild, K. 1913, ApJ, 38

Eddy, J. A. 1976, Science, 192, 1189

Espinoza, N., Brahm, R., Henning, T., et al. 2019, arXiv e-prints

Espinoza, N., Brahm, R., Jordán, A., et al. 2016, ApJ, 830, 43

Evans, D. S. 1959, MNRAS, 119, 526

Fabricius, J. 1611, Narratio de maculis in sole observatis et apparente earum cum sole conversione (Wittenberg)

Falk, A. E. & Wehlau, W. H. 1974, ApJ, 192, 409

Faria, J. P., Haywood, R. D., Brewer, B. J., et al. 2016, A&A, 588, A31

Fischer, D. A., Anglada-Escude, G., Arriagada, P., et al. 2016, PASP, 128, 066001

Fischer, D. A., Marcy, G. W., & Spronck, J. F. P. 2014, ApJS, 210, 5

Fischer, D. A., Schwamb, M. E., Schawinski, K., et al. 2012, MNRAS, 419, 2900

Foreman-Mackey, D., Hogg, D. W., Lang, D., & Goodman, J. 2013, PASP, 125, 306

Foreman-Mackey, D., Morton, T. D., Hogg, D. W., Agol, E., & Schölkopf, B. 2016, AJ, 152, 206

Fulton, B. J., Petigura, E. A., Blunt, S., & Sinukoff, E. 2018, PASP, 130, 044504

Gaia Collaboration, Brown, A. G. A., Vallenari, A., et al. 2018, A&A, 616, A1

Gaia Collaboration, Brown, A. G. A., Vallenari, A., et al. 2016a, A&A, 595, A2

Gaia Collaboration, Prusti, T., de Bruijne, J. H. J., et al. 2016b, A&A, 595, A1

Galilei, G., Welser, M., & Filiis, A. 1613, Istoria e dimostrazioni intorno alle macchie solari e loro accidenti comprese in tre lettere scritte all'illvstrissimo signor Marco Velseri (G. Mascadi)

Giles, H. A. C., Bayliss, D., Espinoza, N., et al. 2018a, MNRAS, 475, 1809

Giles, H. A. C., Collier Cameron, A., & Haywood, R. D. 2017, MNRAS, 472, 1618

Giles, H. A. C., Osborn, H. P., Blanco-Cuaresma, S., et al. 2018b, A&A, 615, L13

Giménez, A. 2006, A&A, 450, 1231

Godoli, G. 1968, in Mass Motions in Solar Flares and Related Phenomena, ed. Y. Oehman, 211

Gokhale, M. H. & Zwaan, C. 1972, Sol. Phys., 26, 52

Goncharskii, A. V., Stepanov, V. V., Kokhlova, V. L., & Yagola, A. G. 1977, Soviet Astronomy Letters, 3, 147

Gray, D. F. 1994, PASP, 106, 1248

Gray, D. F. 1996, in IAU Symposium, Vol. 176, Stellar Surface Structure, ed. K. G. Strassmeier & J. L. Linsky, 227

Gray, D. F., Baliunas, S. L., Lockwood, G. W., & Skiff, B. A. 1996, ApJ, 465, 945

Gregory, P. C. 2011, MNRAS, 415, 2523

Hall, D. S. 1972, PASP, 84, 323

Hardy, R. 1991, Journal of the British Astronomical Association, 101, 261

Hathaway, D. H. & Choudhary, D. P. 2008, Sol. Phys., 250, 269

Hatzes, A. P. 2002, Astronomische Nachrichten, 323, 392

Haywood, R. D. 2015, PhD thesis, University of St Andrews

Haywood, R. D., Collier Cameron, A., Queloz, D., et al. 2014, MNRAS, 443, 2517

Haywood, R. D., Vanderburg, A., Mortier, A., et al. 2018, AJ, 155, 203

Hébrard, G., Almenara, J.-M., Santerne, A., et al. 2013, A&A, 554, A114

Henry, G. W., Marcy, G. W., Butler, R. P., & Vogt, S. S. 2000, ApJ, 529, L41

Hershey, J. L. 1973, AJ, 78, 421

Hirano, T., Nowak, G., Kuzuhara, M., et al. 2016, ApJ, 825, 53

Hjorth, M., Justesen, A. B., Hirano, T., et al. 2019, MNRAS, 484, 3522

Holman, M. J., Fabrycky, D. C., Ragozzine, D., et al. 2010, Science, 330, 51

Holman, M. J. & Murray, N. W. 2005, Science, 307, 1288

Howard, R., Gilman, P. I., & Gilman, P. A. 1984, ApJ, 283, 373

Howell, S. B., Rowe, J. F., Bryson, S. T., et al. 2012, ApJ, 746, 123

Howell, S. B., Sobeck, C., Haas, M., et al. 2014, PASP, 126, 398

Hoyt, D. V. & Schatten, K. H. 1997, The role of the sun in climate change (Oxford University Press)

Huber, D., Bryson, S. T., Haas, M. R., et al. 2016, ApJS, 224, 2

Huenemoerder, D. P. & Ramsey, L. W. 1987, ApJ, 319, 392

Huenemoerder, D. P., Ramsey, L. W., & Buzasi, D. L. 1989, AJ, 98, 2264

Irwin, J., Charbonneau, D., Nutzman, P., & Falco, E. 2009, in IAU Symposium, Vol. 253, Transiting Planets, ed. F. Pont, D. Sasselov, & M. J. Holman, 37–43

Johnson, M. C., Dai, F., Justesen, A. B., et al. 2018, MNRAS, 481, 596

Jordán, A., Brahm, R., Espinoza, N., et al. 2019, AJ, 157, 100

Joy, A. H. & Wilson, R. E. 1949, ApJ, 109, 231

Keller, C. U. & von der Luehe, O. 1992, A&A, 261, 321

Keppens, R. & Martinez Pillet, V. 1996, A&A, 316, 229

Koch, D. G., Borucki, W. J., Basri, G., et al. 2010, ApJ, 713, L79

Konacki, M., Torres, G., Jha, S., & Sasselov, D. D. 2003, Nature, 421, 507

Kovács, G., Zucker, S., & Mazeh, T. 2002, A&A, 391, 369

Kreidberg, L. 2015, PASP, 127, 1161

Kron, G. E. 1947, PASP, 59, 261

Kron, G. E. 1950, Leaflet of the Astronomical Society of the Pacific, 6, 52

Krzeminski, W. 1969, in Low-Luminosity Stars, ed. S. S. Kumar, 57

Krzeminski, W. & Kraft, R. P. 1967, AJ, 72, 307

LaCourse, D. M. & Jacobs, T. L. 2018, Research Notes of the American Astronomical Society, 2, 28

Langhans, K., Scharmer, G. B., Kiselman, D., Löfdahl, M. G., & Berger, T. E. 2005, A&A, 436, 1087

Lanza, A. F., Bonomo, A. S., Pagano, I., et al. 2011, A&A, 525, A14

Latham, D. W. & HARPS-N Collaboration. 2013, in American Astronomical Society Meeting Abstracts, Vol. 221, American Astronomical Society Meeting Abstracts #221, 231.02

Leka, K. D. & Skumanich, A. 1998, ApJ, 507, 454

Lendl, M., Ehrenreich, D., Turner, O. D., et al. 2017, A&A, 603, L5

Lillo-Box, J., Demangeon, O., Santerne, A., et al. 2016, A&A, 594, A50

Litvinenko, Y. E. & Wheatland, M. S. 2015, ApJ, 800, 130

Litvinenko, Y. E. & Wheatland, M. S. 2017, ApJ, 834, 108

Livingston, J. H., Crossfield, I. J. M., Petigura, E. A., et al. 2018, AJ, 156, 277

Loeb, A. 2009, New A, 14, 363

Lomb, N. R. 1976, Ap&SS, 39, 447

López-Morales, M., Haywood, R. D., Coughlin, J. L., et al. 2016, AJ, 152, 204

Ludwig, H.-G. 2006, A&A, 445, 661

Luque, R., Nowak, G., Pallé, E., et al. 2019, A&A, 623, A114

Macintosh, B., Graham, J. R., Barman, T., et al. 2015, Science, 350, 64
Malavolta, L., Borsato, L., Granata, V., et al. 2017, AJ, 153, 224
Mandel, K. & Agol, E. 2002, ApJ, 580, L171
Marcy, G. W. & Butler, R. P. 1996, ApJ, 464, L147
Martinez Pillet, V., Moreno-Insertis, F., & Vazquez, M. 1993, A&A, 274, 521
Maunder, E. W. 1922, MNRAS, 82, 534
Maxted, P. F. L. 2016, A&A, 591, A111
Mayo, A. W., Vanderburg, A., Latham, D. W., et al. 2018, AJ, 155, 136
Mayor, M. & Queloz, D. 1995, Nature, 378, 355
McQuillan, A., Aigrain, S., & Mazeh, T. 2013, MNRAS, 432, 1203
McQuillan, A., Mazeh, T., & Aigrain, S. 2014, ApJS, 211, 24
Meunier, N., Lagrange, A. M., Borgniet, S., & Rieutord, M. 2015, A&A, 583, A118
Miralda-Escudé, J. 2002, ApJ, 564, 1019
Moreno-Insertis, F. & Vazquez, M. 1988, A&A, 205, 289
Morris, B. M., Davenport, J. R. A., Giles, H. A. C., et al. 2019, MNRAS, 484, 3244
Morris, B. M., Hebb, L., Davenport, J. R. A., Rohn, G., & Hawley, S. L. 2017, ApJ, 846, 99
Močnik, T., Anderson, D. R., Brown, D. J. A., et al. 2016, PASP, 128, 124403
Namekata, K., Maehara, H., Notsu, Y., et al. 2019, ApJ, 871, 187
Neff, J. E., O'Neal, D., & Saar, S. H. 1995, ApJ, 452, 879
Newton, H. W. 1955, Vistas in Astronomy, 1, 666
Nielsen, L. D., Bouchy, F., Turner, O., et al. 2019, A&A, 623, A100
Norris, C. M., Beeck, B., Unruh, Y. C., et al. 2017, A&A, 605, A45
Nutzman, P. & Charbonneau, D. 2008, PASP, 120, 317
O'Neal, D. & Neff, J. E. 1997, AJ, 113, 1129
O'Neal, D., Neff, J. E., & Saar, S. H. 1998, ApJ, 507, 919
O'Neal, D., Neff, J. E., Saar, S. H., & Cuntz, M. 2004, AJ, 128, 1802
O'Neal, D., Saar, S. H., & Neff, J. E. 1996, ApJ, 463, 766
Osborn, H. P., Ansdell, M., Ioannou, Y., et al. 2019, arXiv e-prints
Osborn, H. P., Armstrong, D. J., Brown, D. J. A., et al. 2016, MNRAS, 457, 2273
Oshagh, M., Boisse, I., Boué, G., et al. 2013a, A&A, 549, A35
Oshagh, M., Dreizler, S., Santos, N. C., Figueira, P., & Reiners, A. 2016, A&A, 593, A25
Oshagh, M., Santos, N. C., Boisse, I., et al. 2013b, A&A, 556, A19
Pepe, F., Lovis, C., Ségransan, D., et al. 2011, A&A, 534, A58
Pepe, F., Mayor, M., Queloz, D., et al. 2004, A&A, 423, 385
Perrier, C., Sivan, J. P., Naef, D., et al. 2003, A&A, 410, 1039
Perryman, M. 2018, The Exoplanet Handbook, 2nd edn. (Cambridge University Press)

Perryman, M., Hartman, J., Bakos, G. Á., & Lindegren, L. 2014, ApJ, 797, 14
Perryman, M. A. C., de Boer, K. S., Gilmore, G., et al. 2001, A&A, 369, 339
Peterson, M. S., Benneke, B., David, T. J., et al. 2018, AJ, 156, 188
Petigura, E. A., Sinukoff, E., Lopez, E. D., et al. 2017, AJ, 153, 142
Petrovay, K., Martínez Pillet, V., & van Driel-Gesztelyi, L. 1999, Sol. Phys., 188, 315
Petrovay, K. & Moreno-Insertis, F. 1997, ApJ, 485, 398
Petrovay, K. & van Driel-Gesztelyi, L. 1997, Sol. Phys., 176, 249
Pickering, E. C. 1880, Proc. Am. Acad. Arts Sci., 16, 257
Poe, C. H. & Eaton, J. A. 1985, ApJ, 289, 644
Pollacco, D. L., Skillen, I., Collier Cameron, A., et al. 2006, PASP, 118, 1407
Queloz, D., Mayor, M., Weber, L., et al. 2000, A&A, 354, 99
Rajpaul, V., Aigrain, S., Osborne, M. A., Reece, S., & Roberts, S. 2015, MNRAS, 452, 2269
Ramsey, L. W. & Nations, H. L. 1980, ApJ, 239, L121
Rauer, H., Catala, C., Aerts, C., et al. 2014, Experimental Astronomy, 38, 249
Ribárik, G., Oláh, K., & Strassmeier, K. G. 2003, Astronomische Nachrichten, 324, 202
Ribas, I., Tuomi, M., Reiners, A., et al. 2018, Nature, 563, 365
Ricker, G. R., Winn, J. N., Vanderspek, R., et al. 2015, Journal of Astronomical Telescopes, Instruments, and Systems, 1, 014003
Rickman, E. L., Ségransan, D., Marmier, M., et al. 2019, A&A, 625, A71
Rouppe van der Voort, L. H. M., Löfdahl, M. G., Kiselman, D., & Scharmer, G. B. 2004, A&A, 414, 717
Saar, S. H., Butler, R. P., & Marcy, G. W. 1998, ApJ, 498, L153
Saar, S. H. & Donahue, R. A. 1997, ApJ, 485, 319
Sahlmann, J., Lazorenko, P. F., Ségransan, D., et al. 2013, A&A, 556, A133
Sanchis-Ojeda, R. & Winn, J. N. 2011, ApJ, 743, 61
Santerne, A., Brugger, B., Armstrong, D. J., et al. 2018, Nature Astronomy, 2, 393
Santos, N. C., Mayor, M., Naef, D., et al. 2000, A&A, 356, 599
Scargle, J. D. 1982, ApJ, 263, 835
Scharmer, G. B., Gudiksen, B. V., Kiselman, D., Löfdahl, M. G., & Rouppe van der Voort, L. H. M. 2002, Nature, 420, 151
Scheiner, C. 1630, Rosa Ursina sive Sol (Bracciano: Andreas Phaeus)
Schmitt, J. R., Wang, J., Fischer, D. A., et al. 2014, AJ, 148, 28
Schwabe, M. 1843, Astronomische Nachrichten, 20, 283
Schwarzschild, K. & Villiger, W. 1906, ApJ, 23, 284
Seager, S. & Mallén-Ornelas, G. 2003, ApJ, 585, 1038
Semel, M. 1989, A&A, 225, 456

Shporer, A., Zhou, G., Fulton, B. J., et al. 2017, AJ, 154, 188

Silva-Valio, A., Lanza, A. F., Alonso, R., & Barge, P. 2010, A&A, 510, A25

Simon, G. W. & Leighton, R. B. 1964, ApJ, 140, 1120

Smith, A. M. S., Gandolfi, D., Barragán, O., et al. 2017, MNRAS, 464, 2708

Solanki, S. K. & Montavon, C. A. P. 1994, in NATO Advanced Science Institutes (ASI) Series C, Vol. 433, NATO Advanced Science Institutes (ASI) Series C, ed. R. J. Rutten & C. J. Schrijver, 239

Solanki, S. K. & Unruh, Y. C. 2004, MNRAS, 348, 307

Soto, M. G., Díaz, M. R., Jenkins, J. S., et al. 2018, MNRAS, 478, 5356

Southworth, J. 2011, MNRAS, 417, 2166

Spörer, F. W. G. & Maunder, E. W. 1890, MNRAS, 50, 251

Spörer, G. 1889, Nova Acta der Ksl. Leop.-Carol. Deutschen Akademie der Naturforscher, 8, 283

Stassun, K. G., Oelkers, R. J., Pepper, J., et al. 2018, AJ, 156, 102

Stix, M. 2002, The sun: an introduction (Springer)

Sütterlin, P. 2001, A&A, 374, L21

Svensson, F. & Ludwig, H.-G. 2005, in ESA Special Publication, Vol. 560, 13th Cambridge Workshop on Cool Stars, Stellar Systems and the Sun, ed. F. Favata, G. A. J. Hussain, & B. Battrick, 979

Tassoul, J.-L. & Tassoul, M. 2006, Astronomy & Geophysics, 47

Thomas, J. H. & Weiss, N. O., eds. 1992, NATO Advanced Science Institutes (ASI) Series C, Vol. 375, Sunspots: Theory and observations; Proceedings of the NATO Advanced Research Workshop on the Theory of Sunspots, Cambridge, United Kingdom, Sept. 22-27, 1991

Toner, C. G. & Gray, D. F. 1988, ApJ, 334, 1008

Torres, G., Andersen, J., & Giménez, A. 2010, A&A Rev., 18, 67

Tuomi, M., Anglada-Escudé, G., Gerlach, E., et al. 2013, A&A, 549, A48

Udalski, A., Paczynski, B., Zebrun, K., et al. 2002, Acta Astron., 52, 1

Udry, S. & Mayor, M. 2008, in Astronomical Society of the Pacific Conference Series, Vol. 398, Extreme Solar Systems, ed. D. Fischer, F. A. Rasio, S. E. Thorsett, & A. Wolszczan, 13

Udry, S., Mayor, M., Naef, D., et al. 2000, A&A, 356, 590

Uehara, S., Kawahara, H., Masuda, K., Yamada, S., & Aizawa, M. 2016, ApJ, 822, 2

Unruh, Y. C., Collier Cameron, A., & Cutispoto, G. 1995, MNRAS, 277, 1145

van de Kamp, P. 1963, AJ, 68, 515

Van Eylen, V., Dai, F., Mathur, S., et al. 2018, MNRAS, 478, 4866

Vanderburg, A., Becker, J. C., Kristiansen, M. H., et al. 2016, ApJ, 827, L10

Vanderburg, A., Mann, A. W., Rizzuto, A., et al. 2018, AJ, 156, 46

Vanderburg, A., Montet, B. T., Johnson, J. A., et al. 2015, ApJ, 800, 59

Villanueva, Jr., S., Dragomir, D., & Gaudi, B. S. 2019, AJ, 157, 84

Vogt, S. S. 1979, PASP, 91, 616

Vogt, S. S. 1981a, ApJ, 250, 327

Vogt, S. S. 1981b, ApJ, 247, 975

Vogt, S. S. 1981c, in The Physics of Sunspots, ed. L. E. Cram & J. H. Thomas, 455–479

Vogt, S. S., Allen, S. L., Bigelow, B. C., et al. 1994, in Proc. SPIE, Vol. 2198, Instrumentation in Astronomy VIII, ed. D. L. Crawford & E. R. Craine, 362

Vogt, S. S., Marcy, G. W., Butler, R. P., & Apps, K. 2000, ApJ, 536, 902

Vogt, S. S. & Penrod, G. D. 1983, PASP, 95, 565

Vogt, S. S., Penrod, G. D., & Hatzes, A. P. 1987, ApJ, 321, 496

Walkowicz, L. M., Basri, G., & Valenti, J. A. 2013, ApJS, 205, 17

Wang, J., Fischer, D. A., Barclay, T., et al. 2013, ApJ, 776, 10

Wang, J., Fischer, D. A., Barclay, T., et al. 2015, ApJ, 815, 127

Wells, R., Poppenhaeger, K., & Watson, C. A. 2018, MNRAS, 473, L131

Wheatley, P. J., Pollacco, D. L., Queloz, D., et al. 2013, in European Physical Journal Web of Conferences, Vol. 47, European Physical Journal Web of Conferences, 13002

Wilson, O. C. 1978, ApJ, 226, 379

Wilson, P. R. & Cannon, C. J. 1968, Sol. Phys., 4, 3

Wilson, P. R. & McIntosh, P. S. 1969, Sol. Phys., 10, 370

Wittmann, A. D. & Xu, Z. T. 1987, A&AS, 70, 83

Wolszczan, A. & Frail, D. A. 1992, Nature, 355, 145

Wright, J. T. 2005, PASP, 117, 657

Yau, K. K. C. & Stephenson, F. R. 1988, QJRAS, 29, 175

Yu, L., Rodriguez, J. E., Eastman, J. D., et al. 2018a, AJ, 156, 127

Yu, L., Zhou, G., Rodriguez, J. E., et al. 2018b, AJ, 156, 250

Zwaan, C. 1978, Sol. Phys., 60, 213

Zwaan, C. 1992, in NATO Advanced Science Institutes (ASI) Series C, Vol. 375, NATO Advanced Science Institutes (ASI) Series C, ed. J. H. Thomas & N. O. Weiss, 75–100